

UiO : Department of Geosciences
University of Oslo

**Reservoir Characterization of Triassic and Jurassic
sandstones of Snorre Field, the northern North Sea**

Owais Hameed
Master Thesis, Autumn 2016



Reservoir Characterization of Triassic and Jurassic sandstones of Snorre Field, the northern North Sea

Owais Hameed



Thesis submitted for degree of Master in Geology
60 credits

Department of Mathematics and Natural Science
UNIVERSITY OF OSLO

December / 2016

© Owais Hameed, 2016

Tutor(s): Nazmul Haque Mondol (UiO)

This work is published digitally through DUO – Digital Utgivelser ved UiO

<http://www.duo.uio.no>

It is catalogued in BIBSYS (<http://www.bibsys.no/English>)

All rights reserved. No part of this publication may be reproduced or transmitted, in any form or by any means, without permission.

Preface

This thesis is submitted to the Department of Geosciences, University of Oslo (UiO) in candidacy of M.Sc. degree in Geology.

The research has been performed at Department of Geosciences, University of Oslo during the period of January 2016 to December 2016 under supervision of Dr. Nazmul Haque Mondol, Associate Professor, Department of Geosciences, UiO.

Acknowledgement

I would like to express my gratitude to my supervisor Dr. Nazmul Haque Mondol, Associate Professor, Department of Geosciences, University of Oslo, for giving me the opportunity to work under his supervision and learn from his immense knowledge and experience. His guidance, patience and encouragement throughout the study helped me to complete this thesis.

I am grateful to PhD candidate Mohammad Nooraipour and Irfan Baig for their precious time and help. Special thanks to Manzar Fawad and Mohammad Koochak Zadeh for their help and time when it was needed.

I would like to thanks my fellow Hans-Martin, Jørgen Andre Hansen and Manvydas Saltis for our useful discussion and exchange of ideas to improve thesis. I am grateful to Tímea Gyenis for her support and encouragement during the thesis. Special thanks to all of my friends for their support.

In the end, I would like to thanks my parents for their continuous support and encouragement during my study and stay in Norway.

O. Hameed

Abstract

Reservoir characterization is one of the vital steps for hydrocarbon exploration and prospect evaluation. It improves the reservoir understanding and reduces risk during exploration. In this study a combined approach of petrophysical analysis, compaction study and rock physics diagnostic is used to understand reservoir properties and its variation with respect to burial diagenesis. The Triassic Lunde Formation and the Lower Jurassic Statfjord Formation of the Snorre field northern North Sea are investigated in this study. The Lunde Formation is principal reservoir of the Snorre field, while the Statfjord Formation is secondary reservoir due to its limited occurrence and lower thickness. A suit of well log data from 20 exploration wells was utilized to conduct this study.

The Snorre field is located on the Tampen Spur area, northwest of Viking Graben in northern North Sea. The Tampen Spur is a structural high and consists of rotated fault blocks. The Lunde and Statfjord Formations are deposited on large alluvial plain during thermal subsidence phase of permo-triassic rifting phase of northern North Sea. The reservoirs consist of braided stream, single and multi-storey channel sandstones. Associated facies are fine grained overbank deposits and floodplain mudstones.

Petrophysical analysis includes calculation of shale content, porosity and saturation. Petrophysical analysis shows channel sandstones have good porosity up to 23% in the Statfjord Formation and up to 18% in the Lunde Formation. The fine grained overbank deposits show less porosity. Average shale volume is observed higher in the Statfjord Formation as compared to the Lunde Formation.

The rock physical properties as a function of burial depth were plotted to identify the transition of mechanical compaction to chemical compaction. The transition from mechanical compaction domain to chemical compaction domain occur between 70-90 °C temperature at depth range between 2-2.5 km (BSF). The transition zone is marked on the basis of sharp increase in velocity which correspond grain framework stiffening due to imitiation of cement. The present day temperature and geothermal gradient used to identify the transition zone. The transition occurs in same stratigraphic horizon (Lunde Formation) in most of the studied wells. The studied area is progressively subsiding basin and no regional uplift is observed. The estimated uplift along few wells is associated with rotated fault blocks and footwall uplift.

Rock physics diagnostic was used to observe the effect of rock microstructures (cement and sorting) for rock properties of reservoir sandstones. The different trends of shallow buried sandstone and deeply buried sandstone are observed in rock physics effective medium models. The carbonate cement (e.g. calcite, siderite, and dolomite) also effect on rock physical properties which is observed during rock physics diagnostics. The lithology effect is observed by utilizing crossplots of V_p/V_s versus AI and LMR (Lambda-Rho versus Mu-rho). The different trends of sands and shales in V_p/V_s versus AI crossplot show good discrimination of lithology. The impact of cement is also observed in LMR crossplot, which drag data points in high rigidity area.

Table of contents

Preface	i
Acknowledgement.....	iii
Abstract	v
Table of contents	vii
List of Figures	xi
List of tables	xvii
List of Appendices	xix
Nomenclature	xxi
1. Chapter 1: Introduction	1
1.1 Background and motivation	1
1.2 Research objectives	1
1.3 Study area	2
1.4 Database	3
1.5 Chapter description	4
1.6 Limitations and future work	4
2. Chapter 2: Geology of the study area	6
2.1 Geological Evolution.....	6
2.2 Structural Elements	9
2.3 General stratigraphy of the Tampen Spur	11
2.3.1 Hegre Group	13
2.3.2 Statfjord Formation.....	14
2.3.3 Dunlin Group	15
2.3.4 Brent Group	15
2.3.5 Viking Group	17
2.3.6 Cromer Knoll Group.....	18
2.3.7 Shetland Group	18
2.3.8 Rogaland Group.....	18
2.3.9 Hordaland Group	18
2.3.10 Nordland Group.....	18
3. Chapter 3: Research methodologies and theoretical background	19
3.1 Work Flow.....	19

3.2	Data Handling	20
3.2.1	Log editing and quality check	20
3.3	Petrophysical Analysis	21
3.3.1	Shale Volume Calculation	21
3.3.2	Lithology Discrimination	26
3.3.3	Porosity Estimation.....	27
3.3.4	Water saturation.....	30
3.3.5	Net-to-Gross and pay zone	31
3.3.6	Permeability prediction.....	31
3.3.7	Facies Interpretation from Well logs	32
3.4	Compaction Study	33
3.4.1	Mechanical Compaction	33
3.4.2	Chemical Compaction	34
3.4.3	Porosity preservation	35
3.4.4	Transition Zone.....	35
3.4.5	Present day temperature/Temperature gradient	36
3.4.6	Comparison with published trends	36
3.4.7	Exhumation Estimation	38
3.4.8	Uncertainties in exhumation studies	38
3.5	Rock Physics Diagnostics	39
3.5.1	Vs Estimation	39
3.5.2	Relationship between P and S – wave velocities.....	43
3.5.3	Relationship between velocity, porosity and clay	43
3.5.4	Rock physics diagnostics	44
3.5.5	Rock physics effective medium models	45
3.5.6	Estimation of cement volume	49
3.5.7	Rock physics templates of V_p/V_s versus AI	49
3.5.8	Lamda-rho versus Muo-rho	50
4.	Chapter 4: Petrophysical analysis	52
4.1	Reservoir Rocks	52
4.1.1	Thickness and correlation of the reservoir rock	52
4.1.2	Shale Content in Reservoir rocks	56
4.1.3	Porosity in Reservoir Sandstones	57

4.1.4	Saturation in Reservoir Sandstones	60
4.1.5	Permeability estimation	62
4.1.6	Net-to-Gross and pay thickness estimation	62
4.1.7	Facies interpretation of reservoir rocks	64
4.2	Cap rocks.....	66
4.2.1	Identification of Cap rock.....	66
4.2.2	Shale volume in cap rock.....	67
4.2.3	Porosity in seal rock intervals.....	67
4.3	Discussion	68
4.3.1	Overview of the data and reservoirs	68
4.3.2	Source rock.....	68
4.3.3	Reservoir rock.....	68
5.	Chapter 5: Compaction Study	72
5.1	General Velocity versus depth trends.....	72
5.2	Density versus depth trend	74
5.3	Velocity versus density trend	75
5.4	Trends from individual wells	76
5.5	Transition from mechanical to chemical compaction	77
5.6	Shale and Sand Compaction trend	79
5.7	Analysis of reservoir rock	82
5.8	Time-temperature effect on compaction	83
5.9	Compaction of reservoir rocks	85
5.10	Exhumation studies.....	87
5.11	Discussion.....	91
5.11.1	Velocity, density trends with depth.....	91
5.11.2	Temperature and transition zone within the studied wells.....	93
5.11.3	Effect of overpressure	95
5.11.4	Uplift estimation.....	96
5.12	Uncertainties	96
6.	Chapter 6: Rock Physics Diagnostics.....	97
6.1	Effect of clay on V_p	97
6.2	V_p/V_s versus AI	100
6.3	Rock physics cement models	108

6.4	Lamda-Rho versus Mu-Rho (LMR).....	114
6.5	Discussion	118
6.5.1	Effect of clay on porosity and velocity.....	118
6.5.2	Rock physics cement models.....	120
6.5.3	Effect of lithology and fluid sensitivity	124
6.5.4	LMR ($\lambda\rho$ versus $\mu\rho$) crossplot.....	125
6.6	Uncertainties in rock physics diagnostics	125
7.	Chapter 7: Summary and Conclusions	127
	Reference list.....	130
	Appendix A. Composite log displays.....	137
	Appendix B. Interpreted facies from published literature	153
	Appendix C. Velocity-depth trend	156
	Appendic D. Rock physics plots	159

List of Figures

Figure 1.1: Location of the Snorre field on NCS in the northern North Sea (adapted from NPD, 2016).....	2
Figure 2.1: Schematic illustration of the events that shaped the North Sea basin; (A) Plate tectonic setting during late Proterozoic; (B) The opening of the Iapetus Ocean during early Palaeozoic; (C) Caledonian Orogeny due to closure of the Iapetus Ocean in the end of the Silurian; and (D) Laurussian continent separated from Gondwana by Rheic Ocean in Devonian. The figure is adapted and redrawn from Glennie, (2009).	6
Figure 2.2: Subsurface profile from northern North Sea, showing pre, syn and post rift strata of different rifting events; Permo-Triassic post rift strata overlies the basement rock. The figure is adapted from Christiansson et al. (2000).	8
Figure 2.3: The main structural elements of the northern North Sea and adjacent areas. The figure is adapted from Faleide et al. (2015).	10
Figure 2.4: The regional seismic profile from northern North Sea area. The location of the seismic line is marked on Figure 2.3 (Red and black line). The line is interpreted by Christiansson et al. (2000) and cited in Faleide et al. (2015). The study area is marked by red rectangle on figure. In this study the figure is adapted from Faleide et al. (2015).	11
Figure 2.5: The general stratigraphic column of Tampen Spur area. The Lunde Formation and Statfjord Formation are marked by red rectangle in the figure. The figure is adapted from Ketzer et al. (2002).	12
Figure 2.6: Core photograph of Lomvi Formation from interval 3560-3567 m (MDKB). The core is taken in well 34/7-6. The figure is adapted from NPD, (2016).	13
Figure 2.7: Core photograph of Lunde Formation from interval 2448-2454 m (MDKB). The core is taken in well 34/4-4. The figure is adapted from NPD, (2016).	14
Figure 2.8: Core photograph of Dunlin Group from interval 2873-2888 m (MDKB). The core is taken in well 34/7-13. The figure is adapted from NPD, (2016).	15
Figure 2.9: Core photographs of Brent Group. The core is taken in Well 34/7-12; (a) Tarbert Fm interval 2169-2174 m (b) Ness Fm interval 2238-2242 m (c) Etive Fm interval 2257-2261 m and (d) Rannoch Fm interval 2290-2295 m (MDKB). The figure is adapted from NPD, (2016).	16
Figure 2.10: Core photographs of Heather Fm interval 2581-2589 m (MDKB) from well 34/7-20. The figure is adapted from NPD, (2016).	17
Figure 3.1: The overall workflow chart for the study.	19
Figure 3.2: The GR histogram with GR_{min} (red colour, sand line) and GR_{max} (green colour shale line). The data points are plotted from well 34/4-1 for Lunde Formation.	22
Figure 3.3: The chart for shale volume correction by non-linear equations suggested by different authors. The figure is adapted and modified from Mondol, (2015).	23
Figure 3.4: Neutron-density cross plot for defining clean sand and shale lines for estimation of the shale volume. The data points are plotted from well 34/4-1 for Lunde Formation.	25
Figure 3.5: The well log section from well 34/7-3 over interval in the Statfjord and Amundsen Formations. The depth is given in MDKB (Measured depth from Kelly bushing). GR –	

Gamma Ray log, SWU – water saturation, PHIT – total porosity, PHIE – effective porosity, NPHI – neutron porosity. Clay, silt and sand are three lithology types.	26
Figure 3.6: Pickett plot with data points of the Statfjord Formation from well 34/7-10; RD – Deep/true resistivity and PHIE – Effective porosity.	30
Figure 3.7: Generalized illustration of the log trends. The figure is adapted and modified from Emery and Myres, (2009).	32
Figure 3.8: An illustration of the overburden stress carried by solid phase mineral grain framework on grain to grain contact and by pore pressure. The figure is adapted from Bjorlykke et al. (2010).	34
Figure 3.9: The porosity preservation mechanism in chemical compaction regime due to grains coating. The figure is adapted from Bjørlykke and Jahren, (2010).	35
Figure 3.10: Compaction and burial diagenesis as a function of time and temperature. The figure is adapted from Bjørlykke and Jahren, (2010).	36
Figure 3.11: Published velocity-depth trends from literature.	37
Figure 3.12: The Vp versus Vs crossplot of well 34/7-27. The high velocity data marked by light blue ellipses are carbonate intervals.	39
Figure 3.13: The log section from well 34/7-27. The high velocity carbonate intervals discussed in text are marked with light blue shading.	40
Figure 3.14: The Vp-Vs cross plot from well 34/7-27; (a) $V_{sh} \leq 0.5$, and (b) $V_{sh} > 0.5$	40
Figure 3.15: The linear Vp versus Vs trends of well 34/7-27. The Vs is estimated with linear equations from literature.	41
Figure 3.16: The Vp versus Vs crossplot overlaid by linear trend from literature data. The data is plotted from well 34/7-27 and categorized with shale volume as; (a) $V_{sh} \leq 0.5$; (b) $V_{sh} \geq 0.5$	42
Figure 3.17: The Han et al. (1986) models for varying clay percentage in sandstones at 30 MPa effective pressure.	44
Figure 3.18: Schematic illustration of the effective medium models. The figure is adapted and modified from Avseth et al. (2005).	45
Figure 3.19: The effective medium models used in this study; (a) Friable sand model (black dotted lines) are produced for pure quartz sand at different effective pressure (1 MPa, 10 Mpa & 20 MPa). Sediments of varying sorting will fall along black dotted line. The constant cement model line (red line, assuming 2 % quartz cement) is digitized from Avseth et al. (2005). The contact cement model line (continuous black line) is also digitized from Avseth et al. (2005). (b) The model lines are digitized from Avseth et al. (2010).	48
Figure 3.20: The conceptual rock physics template in term of Vp/Vs and AI. The template is modelled for well sorted, compacted arenite with effective pressure of 20 MPa. The arrows show various geologic trends; (1): increasing shaliness, (2): increasing cement volume, (3): increasing porosity, (4): decreasing effective pressure and (5): increasing gas saturation. The figure is adapted from Ødegaard and Avseth, (2003).	50
Figure 3.21: The LMR rock physics template for lithology discrimination and fluid identification. The figure is adapted from Goodway et al. (1997).	51
Figure 4.1: The thickness contour map of the Lunde Formation.	52
Figure 4.2: The thickness contour map of the Statfjord Formation.	53

Figure 4.3: The stratigraphic correlation from N-S direction over the Snorre field; (A) shows the correlation using Gamma Ray log and formation top; (B) Schematic illustration of the thickness variation of the Lunde FM, Statfjord FM, Dunlin Gp, Shetland GP and Rogaland GP along N-S direction in the Snorre field; (C) The wells highlighted with green are used for correlation.....	54
Figure 4.4: The stratigraphic correlation from NE to SW direction of the Snorre field; (A) The thickness of reservoir (Lunde and Statfjord Formations) and seal/cap rock (Shetland/Rogaland Groups) are shown by using gamma ray log and formation top information; (B) The schematic illustration of thickness variation along NE to SW direction; (C) The wells highlighted by green colour are used for NE-SW correlation starting from well 34/4-6 to well 34/7-13.	55
Figure 4.5: The shale volume histogram; (a) Lunde Formation, (b) Statfjord Formation. The mean and mode value are shown on histograms.	57
Figure 4.6: The porosity histograms for Lunde Formation; Φ_i T – True porosity, Φ_i E – Effective porosity.	59
Figure 4.7: The porosity histograms for Statfjord Formation; Φ_i T – True porosity, Φ_i E – Effective porosity.	60
Figure 4.8: Log plot over hydrocarbon saturated zone from Statfjord Formation in well 34/7-3. The hydrocarbon saturated zones are marked by blue rectangle.	61
Figure 4.9: The permeability versus effective porosity crossplot of Lunde Formation of well 34/4-1. The permeability estimated by Morris-Biggs equation (left) and the estimated by Timur equation (right).	62
Figure 4.10: The facies marked along 3 wells (34/4-1, 34/4-2 and 34/7-4 from left to right respectively) for Lunde Formation. The red arrows shows individual sequence of coarsening upward and fining upward while the blue symbol show the major coarsening upward and fining upward along Gamma Ray log trend.	65
Figure 4.11: Gamma Ray log from Statfjord Formation for well 34/7-13. The different facies are marked along the log responses.....	65
Figure 4.12: The composite log display of wells 34/4-7 (left) and 34/7-3 (right), show different reservoir sections (light blue colour) and their potential seals/cap rock (light red and light green colour).	66
Figure 4.13: The shale volume histogram; (a) Amasuden Fm (Dunlin Gp), (b) Kyree Fm (Sheetland Gp).....	67
Figure 5.1: Velocity-depth trend for mudstones and shales ($V_{sh} \geq 75\%$) for studied 19 wells colour coded by present day temperature. One well (34/7-32) excluded due to absence of V_p data (Table 3.1).	73
Figure 5.2: Density-depth plot from 19 wells. Data is colour coded by present day temperature.....	74
Figure 5.3: Velocity versus bulk density plot. Only for shales and mudstones data ($V_{sh} \geq 75\%$) are plotted from 19 wells and colour coded by present day temperature.	75
Figure 5.4: The V_p -depth trend of well 34/4-4; (a) GR-depth (b) V_p -depth colour coded by stratigraphic formations, (c) V_p log signature along the well. The zones are marked with	

different colour shading; TZ – transition zone, MC – mechanical compaction, CC – chemical compaction.	76
Figure 5.5: The Vp-depth data from well 34/4-1 and 34/4-7. The data plotted parallel with reference curves and colour coded by the present day temperature. The transition zone is marked with light yellow shading; MC – Mechanical compaction, CC – Chemical compaction, TZ – Transition zone.	78
Figure 5.6: The zoomed view of the transition zone from well 34/4-1 and 34/4-7 with Gamma Ray log and density log; MC – Mechanical compaction, CC – Chemical Compaction.	79
Figure 5.7: Velocity-depth trend of 19 wells sand data points. The data plotted only for sand lithology ($V_{sh} \text{ cutt-off} \leq 0.25$).	80
Figure 5.8: The velocity-depth trend for shale lithology ($V_{sh} \geq 0.75$). Data plotted from 19 wells.	81
Figure 5.9: The velocity-depth data for reservoir interval (Lunde and Statfjord Formations). The reference sand trend from Marcussen et al. (2010) is also plotted. Data is plotted from 13 wells. The light yellow shading shows the presence of hydrocarbons. Data is colour coded by present day temperature.	82
Figure 5.10: Vp-depth data for reservoir interval (Lunde and Statfjord Formations). Data colour coded by S_w (water saturation).	83
Figure 5.11: Vp, density and depth cross-plots colour coded by temperature from well 34/7-1. On right side the Vp signature from well 34/7-1 is also shown.	85
Figure 5.12: Vp-depth data of Statfjord Formation from well 34/7-3 (left) and Lunde Formation from well 34/7-1 (right). The data is plotted for sandstone ($V_{sh} < 0.25$).	87
Figure 5.13: The Vp-depth data plotted from 11 wells with different published reference curves; (a) before exhumation (b) after exhumation. The uplift correction is applied from Mondol, (2009) kaolinite-silt 50:50.	88
Figure 5.14: The Vp-depth data of Well 34/7-1; (a) data before exhumation correction (b) data after exhumation correction.	89
Figure 5.15: The Vp-depth data plotted from four wells. The data before exhumation and after exhumation are plotted. The correction is applied by kaolinite-silt (50:50) curve (Mondol, 2009).	90
Figure 5.16: Present day transition zone depth map in the study area.	93
Figure 5.17: Geothermal gradient map within study area.	94
Figure 5.18: The possible present day temperature at transition zone within the study area...	95
Figure 6.1: The porosity and velocity (Vp) crossplot for Lunde Formation (left) and Statfjord Formation (right). The crossplot is colour coded by shale volume to observe the effect of shale on porosity and velocity. The overlaid upper curve is clean sandstone line (2 % quartz cement) and lower curve is clay line assuming 80% clay and 20 % quartz. The overlaid curves are digitized from Avseth et al. (2005).	97
Figure 6.2: The Vp-porosity crossplot overlaid by empirical line suggested by Han et al. (1986) for 30 MPa confining pressure. On left the Lunde Formation from 14 wells is plotted, while on right Statfjord Formation from 8 wells is plotted.	98
Figure 6.3: The Vp-porosity crossplot overlaid by Han et al. (1986) clay line for 30 MPa confining pressure. Crossplot is colour coded with S_w (upper) and burial depth (lower).	99

Figure 6.4: Crossplot of V_p/V_s versus IP (P-impedance) of data points from well 34/7-27, overlying the rock physics template modelled for 25 MPa pressure (assumed from depth as 1MPa/100m). The log section of neutron-density is also shown to discriminate between sand and shales.....	100
Figure 6.5: The V_p/V_s versus AI crossplot of well 34/7-27; (a) data points colour coded by shale volume overlaid on quartz sand model, (b) data points colour coded by porosity and overlaid on quartz sand model, (c) data points colour coded by shale volume and overlaid on pure shale model line, (d) data points are colour coded by porosity and overlaid on pure shale model line.....	101
Figure 6.6: The V_p/V_s versus AI crossplot of the Etive Formation from well 34/7-27. The crossplot is colour coded by shale volume (left) and porosity (right).....	102
Figure 6.7: The V_p/V_s versus AI crossplot of Etive Formation after performing fluid substitution from well 34/7-27;(a & b) 100 % oil saturated scenario, (c & d) 100 % gas saturated scenario.	103
Figure 6.8: The V_p/V_s crossplot of the Statfjord Fm. Data from four wells is plotted.	104
Figure 6.9: The V_p/V_s crossplot of Statfjord Formation from well 34/4-8. The crossplot is overlaid by rock physics template; (a) the model line is generated for 100 % quartz sand, (b) the model line is generated for 80% quartz and 20% clay.	105
Figure 6.10: The V_p/V_s versus AI crossplotted from Statfjord Formation for well 34/4-8. The data is sorted by shale volume ≤ 0.25 . The data is colour coded with porosity (left) and cement volume (right).	106
Figure 6.11: The V_p/V_s and AI crossplot of Statfjord Formation of well 34/7-8. The data points are sorted by shale volume ($V_{sh} \leq 0.25$). The colour coding is V_{sh} (left) and porosity (right).....	106
Figure 6.12: The V_p/V_s versus AI crossplot for the Lunde Fm from 34/7-6. The data is colour coded with shale volume (V_{sh}).	107
Figure 6.13: V_p/V_s and AI crossplot of Lunde Formation of well 34/7-6; colour coded by burial depth (left) and cement volume (right). The data is plotted for only sandstone ($V_{sh} \leq 0.25$).....	108
Figure 6.14: The V_p -porosity crossplot (upper) and V_s -porosity crossplot (lower) of Lunde Formation with overlying rock physics effective medium models. The data is plotted from six selected wells (34/4-7, 34/4-8, 34/7-1, 34/7-3, 34/7-4, 34/7-6 and 34/7-8) across the Snorre field. The data is filtered by using shale volume ($V_{sh} \leq 0.5$). The colour coding in both plots is shale volume.	109
Figure 6.15: The V_p versus porosity (left) and V_s versus porosity (right) crossplots of Lunde Formation from well 34/7-1. The crossplots are overlaid with rock physics cement models. The colour coding used is V_{sh} (upper) and burial depth (lower).....	110
Figure 6.16: The V_p versus porosity (left) and V_s versus porosity (right) crossplot for Lunde Formation from well 34/7-6. The crossplot overlaid by rock physics cement model and data points are colour coded with V_{sh} (upper) and burial depth (lower).	111
Figure 6.17: The V_p -porosity (left)) and V_s -porosity crossplot of the Statfjord Formation overlaid by rock physics cement models. Data is plotted from six wells (34/4-8, 34/7-3, 34/7-4, 34/7-6, 34/7-8 and 34/7-13).	112

Figure 6.18: The Vp-porosity (left) and Vs-porosity (right) crossplot for Statfjord Formation from six wells. Data is sorted by $V_{sh} \leq 0.25$ and colour coded with depth (MDKB).	113
Figure 6.19: The Vp versus porosity (left) and Vs versus porosity (right) plots of the Statfjord Formation from six selected wells are plotted with rock physics effective medium models. The crossplots are colour coded by cement volume.	114
Figure 6.20 The Lamda-Rho versus Mu-Rho crossplot of the Lunde Formation from well 34/7-6. The red line on the left side of the each plot is threshold line for gas saturated zone from Goodway et al, (1997). The crossplots are colour coded by; (A) Shale volume, (B) burial depth (MDKB), (C) cement volume and (D) porosity.	115
Figure 6.21: The LMR crossplot of Lunde Formation from 34/7-1, colour coded by; (A) shale volume, (B) water saturation, (C) cement volume and (D) burial depth.	116
Figure 6.22: The LMR crossplot of Statfjord Formation from well 34/4-8. The crossplots are colour coded by; (A) Vsh, (B) burial depth, (C) cement volume and (D) porosity.	117
Figure 6.23: Schematic illustration of the grain supported to clay-supported sediments (left). The inverted V-shaped model for shaly sand and sandy shale (right) is suggested by Marion et al. (1992). The model shows increase in velocity with decreasing porosity from sand to shaly sand due to settlement of fine clay particles in pore spaces of sand and decrease in velocity after transition from shaly sand to sandy shale and pure shales. The figure is adapted from Marion et al. (1992).	119
Figure 6.24: Pore filling kaolinite in Lunde Formation from well 34/7-A5H at burial depth of 2936.82 m. The figure is adapted from Khanna, (1997).	120
Figure 6.25: The SEM picture showing pore filling kaolinite in Lunde Formation from well 34/4-1 at burial depth 2575 m (left) and at burial depth 2524 m (right); Kao – kaolinite, Plag – plagioclase, Sid – siderite, Dol – dolomite, Fsp – feldspar, Ank – ankerite. The figure is adapted from Muller, (1996).	121
Figure 6.26: The geothermal gradient map of the Snorre field (left) and Velocity-depth trend of Lunde Formation from well 347-1(right). The light green shaded data (right) is plotting on friable sand model line in Figure 6.15, while the light grey shaded data plotting close to constant cement model line.	122
Figure 6.27: Backscatter image of calcite cement in Statfjord Fm (left) from well 34/7-8 (2341 m burial depth) and Lunde Formation (right) from well 34/7-P13 (3684 m burial depth) in Snorre field. The figure is adapted from Khanna, (1997).	123
Figure 6.28 SEM images of Lunde Formation from well 34/7-7 at burial depth of 3329 m (left) and 34/4-7 at burial depth of 3328 (right) showing quartz overgrowth; Qtz – quartz grain, Qtzp – quartz overgrowth, Kao – kaolinite and Ilm – ilmenite. The figure is adapted from Muller, (1996).	123

List of tables

Table 1.1: Detail information of wells included this study (adapted from NPD, 2016).	3
Table 3.1: A summary of available well logs. The true vertical depth and bottom hole temperature of all studied wells are also shown.....	20
Table 3.2: The non-linear relations suggested by different authors for shale volume calculation from Gamma Ray log.	23
Table 3.3: Estimated average shale volume from GR log; GR_{min} – Sand line, GR_{max} – Shale line and Larinov – Larionov, (1969) older rock.....	24
Table 3.4: The different minerals densities that form rock matrix adapted from Mondol, (2015).	28
Table 3.5: The porosity estimation from different logs for Lunde Fm in well 34/4-4.....	29
Table 3.6: Vp-Vs linear relations for two scenarios obtained from regression.....	40
Table 3.7: The published empirical relations for Vs estimation from Vp.....	41
Table 3.8: The empirical relations for velocity for different clay content suggested by Han et al. (1986); ϕ – porosity and C – clay content. The velocity is in km/s.	44
Table 3.9: The elastic properties of minerals from published literature, adapted from Hansen, (2016).	49
Table 4.1: The shale volume calculated from 14 wells; Vsh – Shale volume, R.Top – Reservoir top (m), R.Bottom – Reservoir bottom (m).	56
Table 4.2: The shale volume calculated from 8 wells containing Statfjord Formation; VshND – Shale volume, R.T – Reservoir Top (m), R.B – Reservoir Base (m).....	57
Table 4.3: The porosity calculated for Lunde Formation; Φ_iT – True porosity, Φ_iE – Effective porosity.	59
Table 4.4: The calculated porosity of the Statfjord Formation; Φ_iT – true porosity, Φ_iE – effective porosity.....	60
Table 4.5: The porosity and water saturation (S_w) of four hydrocarbon zones in well 34/7-13.	61
Table 4.6: The estimated N/G values for Lunde Formation; Net(r) – Net reservoir interval, N/G – Net-to-gross ratio, $\phi(r)$ – average porosity in reservoir zone, $\phi(p)$ – porosity in pay zone, $S_w(R)$ – water saturation in reservoir zone in percentage, $S_w(P)$ – water saturation in pay zone in percentage.	63
Table 4.7: The Net-to-gross value for Statfjord Formation; Net(r) – net reservoir interval, N/G – Net-to-gross ratio, $\phi(r)$ – average porosity in reservoir interval, $\phi(p)$ – average porosity in pay interval, $S_w(R)$ – water saturation in reservoir interval, $S_w(P)$ – water saturation in pay interval.....	63
Table 5.1: Approximate transition depth in the study area in different wells.....	77
Table 5.2: Temperature in the transition zone in 14 wells utilized in Vp-depth plot.....	84
Table 5.3: The present locations of studied reservoir units (Lunde and Statfjord Formations) with respect to compaction processes.	86
Table 5.4: The total estimated uplift (m) in different wells by using reference curve from Mondol, (2009).....	89

List of Appendices

A.1: Composite log display of Lunde Formation, well 34/4-1.....	137
A.2: Composite log display of Lunde Formation, well 34/4-2.....	138
A.3: Composite log display of Lunde Formation, well 34/4-4.....	139
A.4: Composite log display of Lunde Formation, well 34/4-6.....	140
A.5: Composite log display of Lunde Formation, well 34/4-7.....	141
A.6: Composite log display of Lunde Formation, well 34/4-8.....	142
A.7: Composite log display of Lunde Formation, well 34/7-1.....	143
A.8: Composite log display of Lunde Formation, well 34/7-3.....	144
A.9: Composite log display of Lunde Formation, well 34/7-4.....	145
A.10: Composite log display of Lunde Formation, well 34/7-6.....	146
A.11: Composite log display of Statfjord Formation, well 34/4-8.....	147
A.12: Composite log display of Statfjord Formation, well 34/7-3.....	148
A.13: Composite log display of Statfjord Formation, well 34/7-4.....	149
A.14: Composite log display of Statfjord Formation, well 34/7-6.....	150
A.15: Composite log display of Statfjord Formation, well 34/7-10.....	151
A.16: Composite log display of Statfjord Formation, well 34/7-13.....	152
B.1: The facies in Lunde Formation from well 34/4-7. Figure adapted from Nystuen and Fält, (1995).....	153
B.2: The facies in Lunde Formation from well 34/7-9. Figure adapted from Nystuen and Fält, (1995).....	154
B.3: The facies in Lunde Formation from well 34/4-1. Figure adapted from Nystuen and Fält, (1995).....	154
B.4: The facies in Statfjord Formation from well 34/7-10. Figure adapted from Nystuen and Fält, (1995).....	155
C.1: The velocity-depth trend from well 34/4-1, 34/4-2, 34/4-4 and 34/4-6; MC – mechanical compaction, CC – chemical compaction and TZ – transition zone.....	156
C.2: The velocity-depth trend from well 34/4-7, 34/4-8, 34/7-1 and 34/7-3; MC – mechanical compaction, CC – chemical compaction and TZ – transition zone.....	157
C.3: The velocity-depth trend from well 34/7-9, 34/7-10, 34/7-13 and 34/7-19; MC – mechanical compaction, CC – chemical compaction and TZ – transition zone.....	158
D.1: Vp – porosity crossplot for Lunde Formation with rock physics cement model from well 34/4-4.....	159
D.2: Vp – porosity crossplot for Lunde Formation with rock physics cement model from well 34/4-6.....	159
D.3: Vp – porosity crossplot for Lunde Formation with rock physics cement model from well 34/7-8.....	160
D.4: Vp – porosity crossplot for Lunde Formation with rock physics cement model from well 34/7-9.....	160
D.5: Vp – porosity crossplot of Statfjord Formation from well 34/7-4, overlaid with rock physics cement model.....	161

D.6: Vp – porosity crossplot of Statfjord Formation from well 34/7-8, overlaid with rock physics cement model.....	161
--	-----

Nomenclature

NCS – Norwegian Continental Shelf

BHT – Bottom hole temperature

MD – Measured depth

TVD – True vertical depth

BSF – Bottom sea floor

GR – Gamma ray

MC – Mechanical compaction

CC – Chemical compaction

TZ – Transition zone

Phi – Porosity

PhiT – True porosity

PhiE – Effective porosity

I_{GR} - Gamma ray index

m – Meter

S_w – Water saturation

V_p – P-wave (Compressional wave velocity)

V_s – S-wave (Shear wave velocity)

ND – Neutron-density combination

RPT – Rock physic template

V_{sh} – Shale volume

Frac – Fraction

GPa – Giga pascal

MPa – Mega pascal

g/cc – gram per cubic centimetre

VshGR – Shale volume from GR log

VshND – Shale volume from neutron-density

NPD – Norwegian Petroleum Directorate

Chapter 1: Introduction

1.1 Background and motivation

The Norwegian Continental Shelf (NCS) is well studied, most explored offshore region in Europe continent and divided into three petroleum provinces; North Sea, Norwegian Sea and Barents Sea. The discovery of Groningen field in the Netherland in 1958 generated interest about North Sea to explore for hydrocarbons (Faleide et al., 2015). The first well was drilled on the Norwegian Continental Shelf (NCS) in 1966 but it was dry, later the Ekofisk discovery in 1969 revealed high petroleum potential of the Norwegian Continental Shelf (NCS). In subsequent years, number of discoveries were made and laid a foundation for new and important industry in Norway (Mohn and Osmundsen, 2008).

This study is conducted to understand the reservoir properties of the Snorre field on Tampen Spur, in northern part of the North Sea. The North Sea with extensive well data-base and 3D seismic coverage is one of the well-studied rift system in the world (Erratt et al., 1999). The Tampen Spur area is located between Viking Graben and Shetland Basin with several giant oilfields such as Statfjord, Gullfaks and Snorre (Horstad et al., 1995). The Snorre field was discovered by Saga Petroleum in 1979 and production started in 1992 (Horstad et al., 1995; Hoversten et al., 2001; Smith et al., 2001). The Snorre field has two reservoir intervals, the Triassic Lunde Formation and the Jurassic Statfjord Formation (Nystuen and Fält, 1995; Smith et al., 2001). The fluvial deposited reservoir of the Snorre field contains sand channels with internal flow barrier make the field very challenging to produce hydrocarbon.

1.2 Research objectives

The aim of research is to characterize the complex Lunde and Statfjord reservoirs of the Snorre field. By using the standard well log data, the reservoir characterization has performed. To get better understanding of the reservoir, a detail compaction study is also performed. The overall objectives of the thesis are listed below:

- Detail literature review of the study area to understand the geological evolution, structure and tectonic history.
- Reservoir properties estimation such as porosity and shale volume calculation, net-to-gross estimation, permeability prediction and calculation of hydrocarbon saturation.
- Study rock physical depth trends (velocity-depth, density-depth) to identify mechanical and chemical compaction zones.
- Mark transition zone and study the effect of compaction on the reservoir rocks.
- Rock physics diagnostics to characterize the target reservoirs.
- Discussion of the uncertainties related to the results and interpretations.

1.3 Study area

The Snorre field is located in the Norwegian sector of the northern North Sea, on the Tampen Spur area. It is about 200 km northwest of Bergen city, in west Norway. The water depth is 300-350 meters and the reservoir depth is 2000-3500 meters with an aerial extent of 100 km². The field is located in block 34/4 and 34/7, under production license of PL 057 and PL 089 (adapted from NPD, 2016). The location of the Snorre field is shown in Figure 1.1.

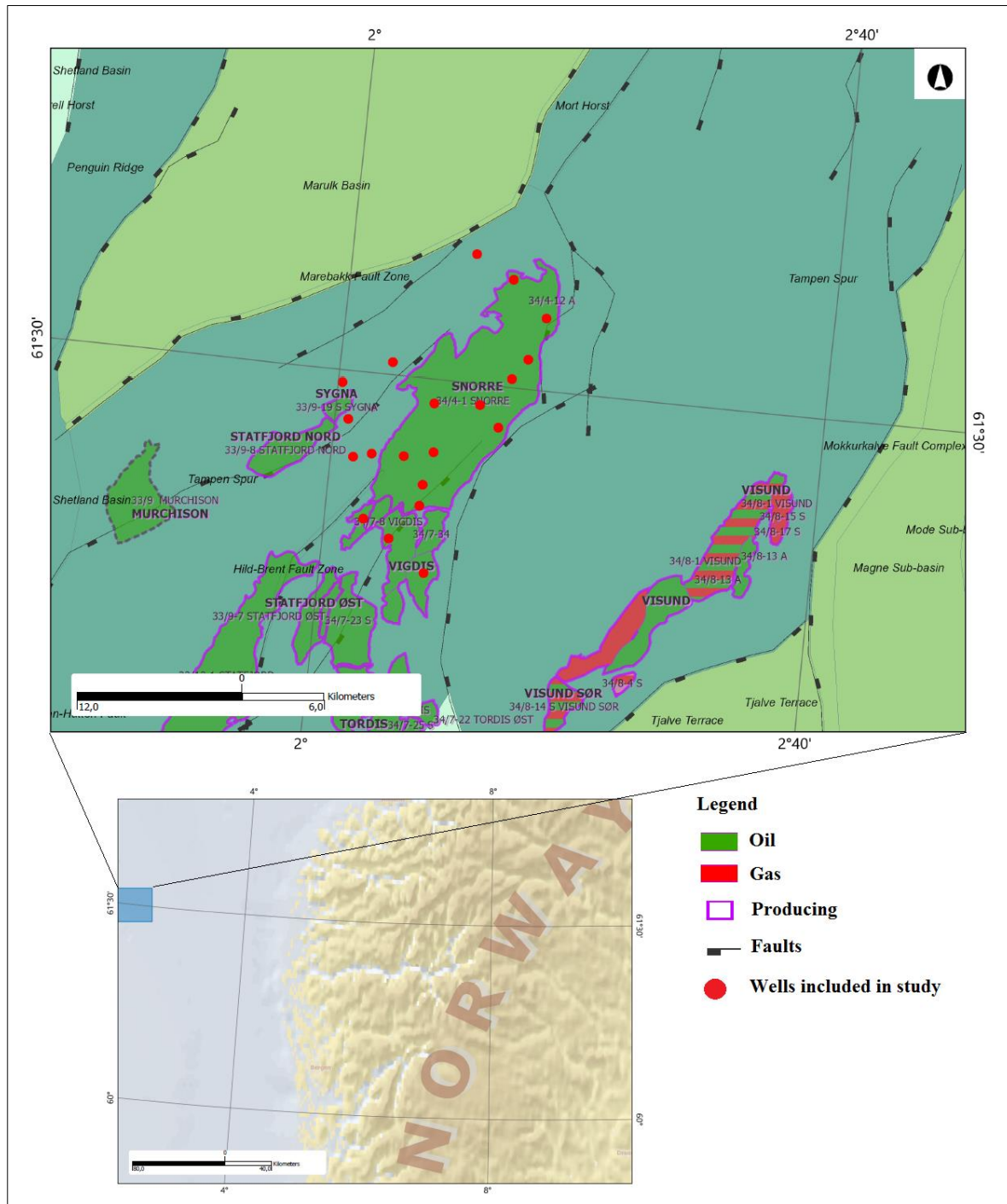


Figure 1.1: Location of the Snorre field on NCS in the northern North Sea (adapted from NPD, 2016).

The reservoirs of the Snorre field consist of several large fault blocks and producing with water injection, gas injection and water alternating gas injection (WAG) (Smith et al., 2001). The first well in Snorre field 34/4-1 was drilled in 1979 and oil was encountered in Lunde Formation (Jorde and Diesen, 1990). To understand the reservoir properties of Snorre field, twenty exploration wells from block 34/4 and 34/7 have been included in this study (Table 1.1). The current owners of Snorre field are Statoil Petroleum ASA (33.27%, operator), Petoro AS (30%), ExxonMobil (17.44%), Idemitsu Petroleum Norge AS (9.60%), DEA Norge AS (8.57%), Core Energy AS (1.10%) (adapted from NPD, 2016).

1.4 Database

As mentioned earlier total 20 exploration wells from blocks 34/4 and 34/7 are included in the study (Table 1.1). Only six wells are from block 34/4, out of which three are planned as wildcat and other three as appraisal wells. The fourteen wells are from block 34/7 with five wildcat and 9 appraisal wells. Only five wells in the studied area are dry while rest of the wells contain oil.

Table 1.1: Detail information of wells included this study (adapted from NPD, 2016).

Sr. No	Well Name	Water Depth (m)	Res. Depth (m)	Purpose	Status	Content	Reservoirs
1.	34/4-1	377	2508	Wildcat	P&A	Oil	Lunde Fm
2.	34/4-2	322	2697	Wildcat	P&A	Dry	Lunde, Statfjord Fms
3.	34/4-4	345	2425	Appraisal	P&A	Oil	Lunde Fm
4.	34/4-6	373	2577	Appraisal	P&A	Oil	Lunde Fm
5.	34/4-7	354	2502	Appraisal	P&A	Oil	Lunde Fm
6.	34/4-8	363	2799	Wildcat	P&A	Dry	Lunde, Statfjord Fms
7.	34/7-1	328	2392	Appraisal	P&A	Oil	Lunde Fm
8.	34/7-3	303	2414	Appraisal	P&A	Oil	Lunde, Statfjord Fms
9.	34/7-4	319	2536	Appraisal	P&A	Oil	Lunde, Statfjord Fms
10.	34/7-6	307	2510	Appraisal	P&A	Oil	Lunde, Statfjord Fms
11.	34/7-8	286	2299	Wildcat	P&A	Oil	Lunde, Statfjord Fms
12.	34/7-9	330	2443	Appraisal	P&A	Oil	Lunde Fm
13.	34/7-10	300	2531	Appraisal	P&A	Oil	Lunde, Statfjord Fms
14.	34/7-13	282	2493	Appraisal	P&A	Oil	Lunde, Statfjord Fms
15.	34/7-16	286	2390	Appraisal	SUSP	Oil	Etive, Rannoch Fms
16.	34/7-19	285	2456	Appraisal	SUSP	Oil	Brent Gp
17.	34/7-20	295	3128	Wildcat	P&A	Oil	Statfjord, Lunde Fms
18.	34/7-27	311	2837	Wildcat	P&A	Dry	Brent Gp
19.	34/7-28	304	2729	Wildcat	P&A	Dry	Brent Gp
20.	34/7-32	297	2535	Wildcat	P&A	Dry	Brent Gp

1.5 Chapter description

The study is organized in seven different chapters and the description of the each chapter is given below.

Chapter 1- “Introduction” The first chapter gives a general introduction of the thesis includes research motivation, objectives and background. In addition, the general introduction of the study area and well log database used in this study are discussed in chapter 1.

Chapter 2- “Geology of the study area” The second chapter focuses on the detail tectonic and geological evolution of the northern North Sea. The chapter also includes the main structural elements of the northern North Sea and the stratigraphic overview of the Tampen Spur area.

Chapter 3- “Research methodologies and theoretical background” The third chapter discusses the work flow to conduct this research with theoretical background of all three methods: Petrophysical Analysis, Compaction Study and Rock Physics Diagnostics. The theories are discussed in sub headings under the main heading of Petrophysics, Compaction and Rock physics respectively.

Chapter 4- “Petrophysical Analysis” In chapter four the results and interpretation from petrophysical analysis of the Lunde and Statfjord Formations are discussed. The chapter is started with stratigraphic correlation of the Lunde and Statfjord Formations. Furthermore, shale volume calculation, Net-to-Gross, porosity estimation, water saturation calculation and permeability prediction are included. The discussion of the results is included at the end of the chapter.

Chapter 5- “Compaction Study” The chapter five covers the analysis of compaction study of the Snorre field. Different trends like velocity-depth, density-depth and velocity-density are discussed initially. The trends are also compared with reference curves from published literature like Mondol et al. (2007), Mondol, (2009), and Marcussen et al. (2010). Furthermore, the transition zone of mechanical compaction and chemical compaction is identified and geothermal gradient of the area is discussed with respect to present day temperature. Finally, the possible uplift in the study area is investigated.

Chapter 6- “Rock Physics Diagnostics” Chapter six covers the results and discussion of ‘Rock Physics Diagnostics’. In this study four rock physics models/templates of V_p/V_s versus AI , Cement Model, Velocity versus Porosity and Lambda-Rho versus Mu-Rho are used and results are described accordingly.

Chapter 7- “Summary and Conclusion” The chapter seven is the last chapter and include summary of the research and conclusions of the study.

1.6 Limitations and future work

- The available data for this study is geophysical well logs. The absence of thin section analysis and core examination lacks the mineralogical information about the reservoir rocks in this study.

- The absence of sedimentological core logging makes difficult to correlate the facies along wells. The facies interpretation from core logging along with the well log analysis can be useful for reservoir understanding.
- The unavailability of mineralogical information evolves uncertainties in rock physics models used for rock physics diagnostics.
- The unavailability of pressure data in the reservoir zones makes it difficult to explain overpressure in the reservoir and its effect on fluid flow.
- The absence of shear sonic data in all wells make it difficult to extract more information about reservoir from rock physics crossplots e.g. V_p/V_s versus AI and LMR.
- The presence of seismic data can be advantageous for large scale correlation of seismic attributes.
- Future research can be considered rock physics diagnostics of the reservoir by using mineralogical and cement observation from thin section analysis. The rock physics diagnostics by using inverted elastic parameters from seismic data and its verification from well log data will add extra value of the study.

Chapter 2: Geology of the study area

This chapter focuses on geological and structural evolution of the study area by utilizing published literature. The stratigraphy of the study area is also discussed.

2.1 Geological Evolution

The hydrocarbon rich North Sea basin is an extensional rifted basin and has complex tectonic and geological history. The thick sedimentary sequence with sediments ranging from lower Palaeozoic to Quaternary age underlie in the North Sea (Ziegler, 1977). The complex geological evolution from Cambrian to Recent formed different tectonic elements and sedimentary basins of the North Sea (Ziegler, 1975). Different basins formed and destroyed in time and space during geological evolution. Some basins stacked on the top of other. The tectonic evolution of the North Sea related to major plate-margin effects are; Caledonian plate cycle and Variscan plate cycle (Glennie, 2009; Ziegler, 1977). Ahead from continental collision during Caledonian Orogeny North Sea area was widely separated continental fragments in Early Palaeozoic Iapetus Ocean and Tornquist Sea (Figure 2.1) (Glennie, 2009). The Caledonian cycle from Cambrian to Silurian ended after the closure of Iapetus Ocean due to collision between Laurentia, Baltica and Avalonia. The Caledonian Orogeny affected much of North Sea area.

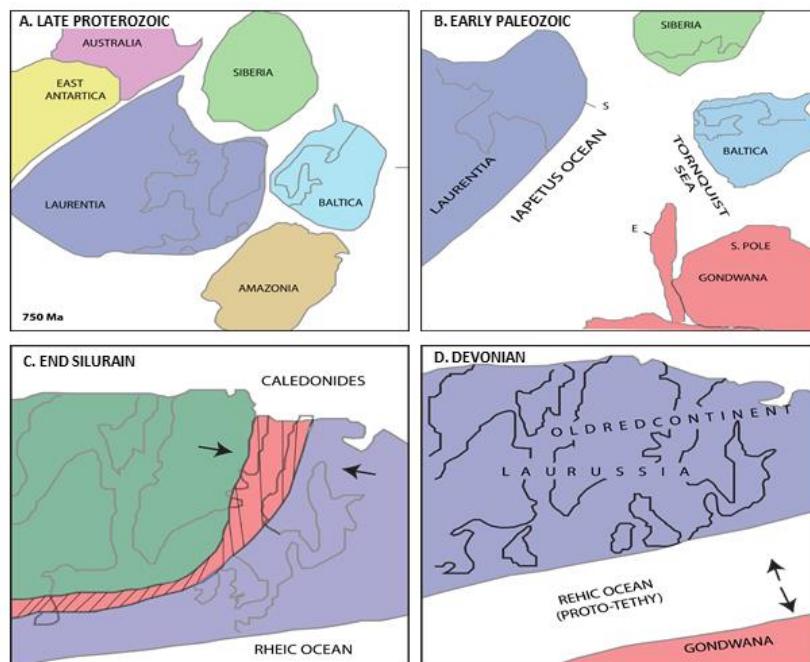


Figure 2.1: Schematic illustration of the events that shaped the North Sea basin; (A) Plate tectonic setting during late Proterozoic; (B) The opening of the Iapetus Ocean during early Palaeozoic; (C) Caledonian Orogeny due to closure of the Iapetus Ocean in the end of the Silurian; and (D) Laurussian continent separated from Gondwana by Rheic Ocean in Devonian. The figure is adapted and redrawn from Glennie, (2009).

In Late Devonian time North Sea basin had hot arid continental depositional environment which lead to deposition of old red sandstone (ORS) that form bulk of Devonian strata within the North Sea Basin (Downie, 2009; Torsvik et al., 2002). The Variscan tectonic cycle from Devonian to Late Carboniferous times and ended with Variscan orogeny in late Carboniferous (Glennie, 2009; Ziegler, 1977). The Variscan Orogeny was the result of collision between Gondwana and Laurussia created supercontinent called Pangea (Glennie, 2009). Southern and central North Sea became part of large clastic and carbonate shelf during Late Devonian and Early Carboniferous which later destroyed during late Carboniferous Variscan Orogeny (Ziegler, 1992).

These events were followed by the intracratonic extensional phases of the North Sea during Permian and early Triassic and Middle-Late Jurassic producing rift system (Færseth et al., 1995). The Late Permian Early Triassic rifting and Middle-Late Jurassic rifting referred as Permo-Triassic and Middle-Late Jurassic rifting in published literature and following terminology will be used for this thesis.

Several authors (Badley et al., 1988; Bukovics and Ziegler, 1985; Christiansson et al., 2000; Faleide et al., 2015; Faleide et al., 2002; Færseth, 1996; Færseth et al., 1995; Gabrielsen et al., 2010; Glennie, 2009; Jackson et al., 2010; Ravnås et al., 2000; Ziegler, 1992) explained the Permo-Triassic and Middle-Late Jurassic rifting episodes of the North Sea followed by thermal subsidence. The subsurface profile of northern North Sea is shown in Figure 2.2. The rifting of North Sea spanning from early Triassic to Palaeocene when crustal separation between Europe and Greenland achieved (Ziegler, 1992). The Permo-Triassic and mid-late Jurassic rifting directed E-W to NW-SE and result of regional stress regime (Færseth et al., 1995). As a result of extensional stress tilted fault-blocks formed in basin with planer and listric faults.

The most of basement rock of the North Sea belong to Caledonian Orogeny (Faleide et al., 2002; Færseth et al., 1995; Sclater and Christie, 1980; Ziegler, 1992). The sediments overlain the crystalline basement of the North Sea are deposited in different types of sedimentary basins in response of different tectonic settings (Ziegler, 1977). The several rifting events and peak magmatism of Oslo region in Early Permian time highly affected the North Sea (Torsvik et al., 2002). In northwest Europe wrench fault system developed during Early Permian and in North Sea the wrench faulting deformed the sedimentary fill of the Variscan foreland basin (Ziegler, 1992). The faulting sized in Late Permian with initiation of subsidence of Permian basin due to thermal relaxation of lithosphere that later become Viking and Central Grabens (Glennie, 2009; Ziegler, 1992). Rifting along Viking Graben and sea level rise led to deposition of black shale on Aeolian sand dune of Rotliegend Group (Torsvik et al., 2002). The carbonates, sulphates and halite's of Zechstein Group overlain the continental clast of Rotliegend Group (Ziegler, 1992)

The rifting started during earliest Triassic cross-cut the Caledonian basement and pre-existing crustal discontinuities such as Horn Graben (Ziegler, 1992). The post-rift sediments encountered from borehole in northern part of the North Sea also indicates that the age of rift is Permian to early Triassic (Badley et al., 1988). The Permo-Triassic rift axis is believed to be centred beneath Horda Platform (Christiansson et al., 2000; Faleide et al., 2015; Whipp et al., 2014). The Permo-Triassic lithospheric extension is overprinted by later deformation and it has proved difficult to compute precisely the block rotation and graben infilling in North Sea (Fisher and Mudge, 1998). The rifting is well documented in the marginal areas of Viking Graben because this area is less deformed by Jurassic overprints (Christiansson et al., 2000).

During Triassic the North Sea had still arid climate leads to deposition of continental red sand stone (Faleide et al., 2015; Yielding et al., 1992). The Triassic rift of North Sea involve small amount of crustal stretching as there is not any significant volcanic activity noted during that time and basin continue to subside during early Jurassic (Ziegler, 1992).

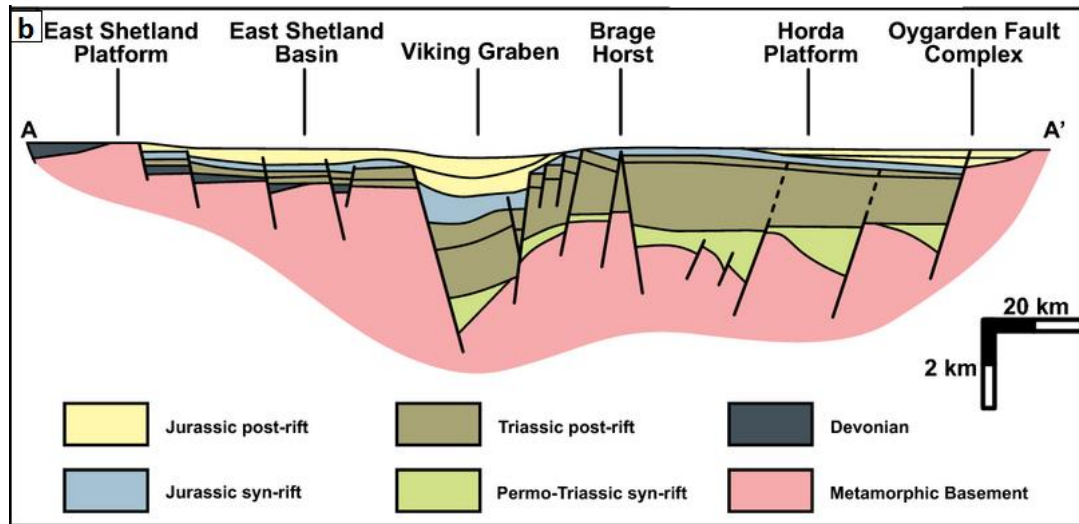


Figure 2.2: Subsurface profile from northern North Sea, showing pre, syn and post rift strata of different rifting events; Permo-Triassic post rift strata overlies the basement rock. The figure is adapted from Christiansson et al. (2000).

In mid-Jurassic (Aalenian and Bajocian) the lithospheric up doming of the North Sea started that leads to next rifting episode followed by thermal subsidence. The present architecture, the main graben structures and rotated fault blocks formed during Mid-Jurassic to Cretaceous extension of the North Sea. Master faults that associated with Permo-Triassic rifting were reactivated in the Jurassic rifting (Odinsen et al., 2000). The Mid-Jurassic doming that extended in W-E and in N-S direction, provoked the truncation of Early Jurassic, Triassic and even Permian sediments (Ziegler, 1992). Extensive volcanic activity is also associated with up doming of North Sea in Mid Jurassic. The uplifted area caused continuous erosion and product were deposited in adjacent subsiding basin such as Brent group in Viking Graben (Ziegler, 1992). The thickness of Brent Group increase toward the centre of basin which shows the thermal subsidence that affected the area during early rifting episode (Badley et al., 1988).

The crustal extension increased from Late Jurassic to Early Cretaceous during second rifting episode of the North Sea. The rifting phase overprinted the earlier phase of rifting. The rifting followed by thermal subsidence and the post rift subsidence period lasted over a period of 70 Ma (Gabrielsen et al., 2010). The late Jurassic-Early Cretaceous rift phase followed by major transgression but the uplifted fault blocks caused erosion which form a major unconformity between Cretaceous and Jurassic (Faleide et al., 2015). The unconformity called ‘late Kimmerian unconformity’ and marked regionally the entire north sea (Ziegler, 1977). The tectonic activity were concentrated on Viking Graben, Central Graben and Moray Firth-Witch Ground Graben system during Kimmeridgian to Berriasian (Ziegler, 1992). The small tilted fault blocks with compartment that act as main hydrocarbon trap system in northern north sea formed during Jurassic rifting (Færseth, 1996). Viking Graben and Central Graben contain major oil provinces of the North Sea and sediments deposited during Jurassic-Cretaceous stage of rift system contain source rock as well as reservoir rocks (Ziegler, 1977). The

Heather Formation and Draupne Formation (potential source rocks) deposited during rifting phase of Late Jurassic to Early Cretaceous (Badley et al., 1988). The tilted fault blocks and rifted topography produced basins with poor bottom water circulation caused the deposition of organic rich source rock of the North Sea after late Jurassic transgression (Faleide et al., 2015).

The Early Cenozoic was time of thermal subsidence after Jurassic-Early Cretaceous rifting with deep marine environment in basin axis that form on lap of post rift strata against basin margins (Nottvedt et al., 1995). After Late Jurassic the crustal extension decrease and most of faults die out with few master faults that still remain active throughout Cretaceous time (Faleide et al., 2015; Ziegler, 1992). In the late Cretaceous rifting terminated in the North Sea and the subsidence caused by crustal cooling and loading of sediments (Bukovics and Ziegler, 1985) but Norwegian-Greenland rifting remained active until the crustal separation between Greenland and Europe in the end of Palaeocene (Ziegler, 1992). The maximum transgression in Late Cretaceous leads to deposition of planktonic carbonate algae (coccolithoporids), the main component of chalk on the large area of northwest Europe (Faleide et al., 2015). In the North Sea the central and southern part covers thick upper Cretaceous chalk while the northern part dominates mudstone (Christiansson et al., 2000; Ziegler, 1977, 1992).

The North Sea became tectonically stable during early Eocene and the evolution is driven by thermal relaxation of lithosphere and sediment loading (Ziegler, 1992). During Palaeocene and Eocene the Shetland Platform and Norwegian mainland were source area for deep marine turbidity sand for the North Sea basin (Løseth et al., 2013). In the early Palaeocene the East Shetland platform thermally uplifted due to rifting of Greenland-European plate and supplied clastic sediments to starved basin of Late Cretaceous by deltaic and submarine-fan system (Bowman, 2009). There is no indication for post-Palaeocene rejuvenation of Graben (Ziegler, 1992).

2.2 Structural Elements

The present architecture with rotated fault blocks and graben structure of the North Sea resulted mainly from Mid-late Jurassic rifting followed by thermal subsidence in cretaceous and partially from earlier rift phases which are discussed in detail in previous section of this chapter. The most of the North Sea area are underlined by crystalline basement rock that solidifies during Caledonian Orogeny. The main structural elements in the northern North Sea province are Viking Graben, Sogn Graben towards north and both are flanked by the East Shetland Basin and Tampen Spur to the west and in the East Horda Platform (Faleide et al., 2015). These structural elements are formed due to Jurassic-Cretaceous rifting followed by thermal subsidence and sediments loading in the Cretaceous but the Viking Graben and its margins underline old rift basin of Permian-Early Triassic (Faleide et al., 2015).

The study area “Snorre field” is located on eastern margin of the Tampen Spur towards Viking Graben and the area was part of a large sedimentary basin from Permian to Middle Jurassic (Hollander, 1987; Jorde and Diesen, 1990). The main structural elements of the northern North Sea are shown in Figure 2.3 adapted from Faleide et al. (2015).

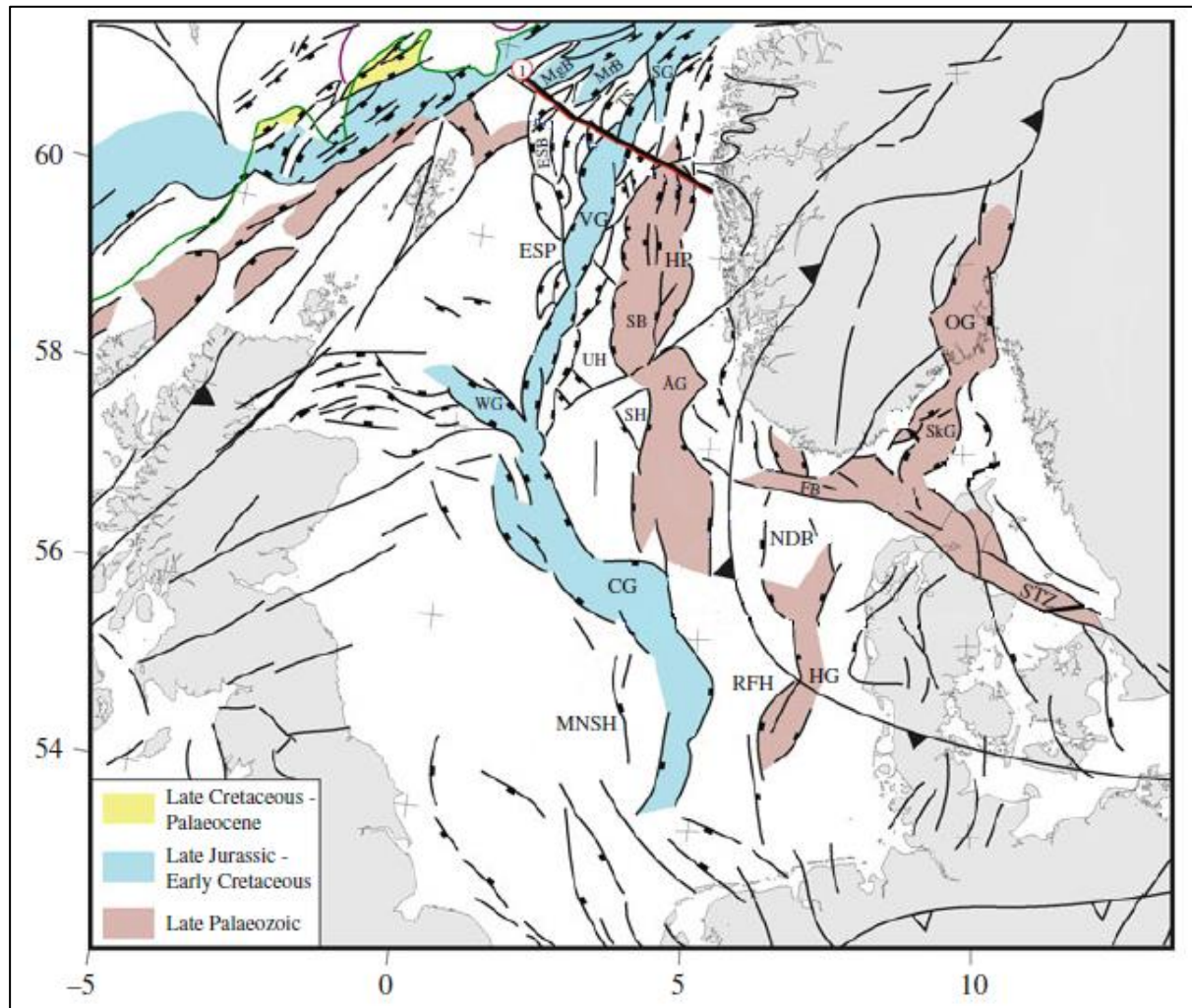


Figure 2.3: The main structural elements of the northern North Sea and adjacent areas. The figure is adapted from Faleide et al. (2015).

Tampen spur is structural high with series of the rotated fault blocks and located between the Viking Graben in the east and south east and the Møre Basin in the north and northwest (Nystuen and Fält, 1995). During early Cretaceous the margins of Tampen spur strongly affected by erosion due to Late Jurassic major uplift of the area (Jorde and Diesen, 1990). In Figure 2.4 the regional seismic profile from northern North Sea is shown and Tampen Spur is marked by red rectangle.

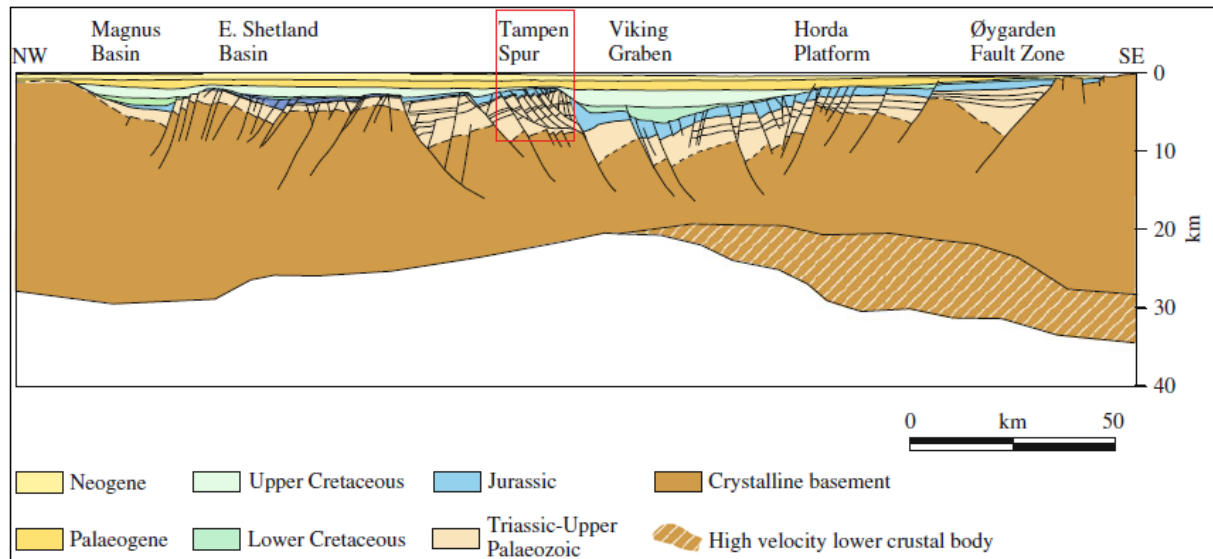


Figure 2.4: The regional seismic profile from northern North Sea area. The location of the seismic line is marked on Figure 2.3 (Red and black line). The line is interpreted by Christiansson et al. (2000) and cited in Faleide et al. (2015). The study area is marked by red rectangle on figure. In this study the figure is adapted from Faleide et al. (2015).

2.3 General stratigraphy of the Tampen Spur

The Snorre field comprises of different stratigraphic formations and the oldest formation penetrated along Snorre wells is Scythian-Anisian Tiest Formation (Jorde and Diesen, 1990). The reservoir rock in Snorre field belongs to Triassic Lunde and Jurassic Statfjord Formations of Hegre Group. The thick shale sequence of Upper Cretaceous Shetland Group and Palaeocene Rogaland Group are efficient seal rocks for the Snorre field (Caillet, 1993). The shale from Dunlin group of the Jurassic age is efficient cap/seal rock in North Sea but the restricted stratigraphic occurrence in the Snorre field concludes as less efficient for Snorre reservoirs. The limestone and marl of the lower Cretaceous Cromer Knoll group does not exceed more than 20 m in the Snorre area.

The reservoir section of the Snorre field comprise of approximately 1300 m of strata (Hollander, 1987). Lunde Formation with 75 % of the total hydrocarbons is the main reservoir unit in the Snorre field while the rest of the hydrocarbons are accumulated in the Statfjord formation (Horstad et al., 1995). The Lunde Formation is subdivided into lower, middle and upper members (Hollander, 1987; Nystuen and Fält, 1995; Nystuen et al., 1989). A general stratigraphic succession of the Tampen Spur area is shown in Figure 2.5.

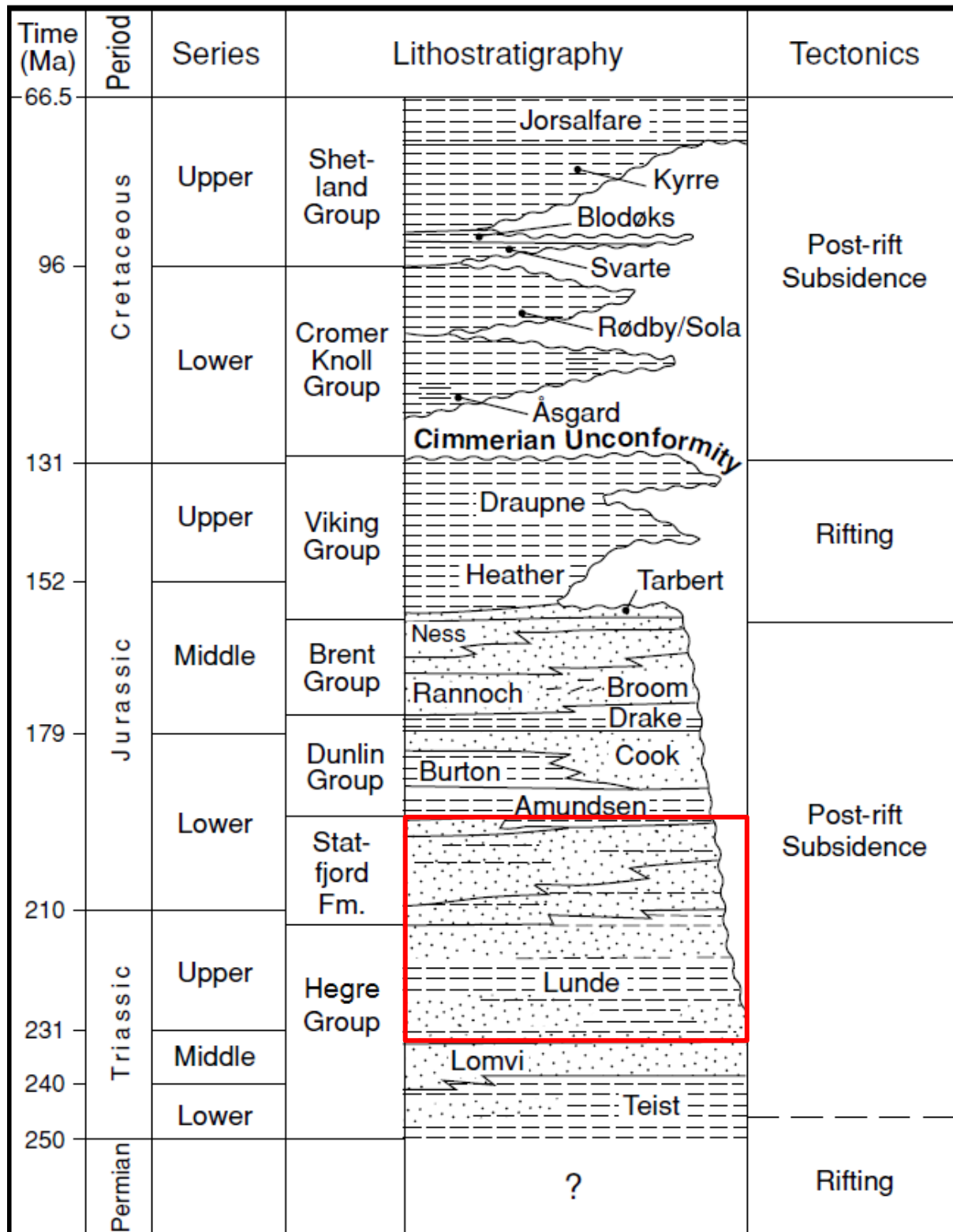


Figure 2.5: The general stratigraphic column of Tampen Spur area. The Lunde Formation and Statfjord Formation are marked by red rectangle in the figure. The figure is adapted from Ketzer et al. (2002).

2.3.1 Hegre Group

The Hegre Group is of Triassic age (Figure 2.5). In northern North Sea the Triassic sequence is the thickest and geographically extensive of the Mesozoic system (Lervik et al., 1989). The Triassic Hegre Group conformably overlying Statfjord Formation of Lower Jurassic age in the northernmost North Sea (Nystuen and Fält, 1995). The major lithology of the Hegre Group consist of interbedded sandstones, claystones and shales combined with sequences of largely sandstone or shale/claystone (Lervik, 2006). The Hegre Group is not completely penetrated by any well that included in this study on Tampen spur area. The Hegre Group is subdivided into three formations: Teist Formation in the base, Lomvi Formation in the middle and Lunde Formation on the Top (Figure 2.5).

Teist Formation

The Scythian-Anisian Teist Formation of the Hegre Group is oldest geological unit penetrated in the Snorre wells (Jorde and Diesen, 1990). The Teist Formation consists of very fine to fine-grained sandstones interbedded with claystones, mudstones and marl (Lervik, 2006). The base of the Teist Formation in the Snorre area has not penetrated and thickness is unknown but in well 34/4-4 it exceeds 576 m (Jorde and Diesen, 1990). The Teist formation deposited on distal alluvial plain with lacustrine and fluvial environment (Jorde and Diesen, 1990). Rocks beneath Teist Formation is unknown on Tampen Spur area but possibly resting unconformably on basement rock (Nystuen and Fält, 1995).

Lomvi Formation

The Lomvi Formation of the fluvial origin contains fine to coarse-grained light brown to grey or white sandstone with red marls and claystone (Vollset and Doré, 1984). The formation contains massive blocky pattern with fine-to coarse-grained kaolinitic sandstones with subordinate marls with claystones (Lervik, 2006). The core photograph of Lomvi Formation from well 34/7-6 is shown in Figure 2.6.

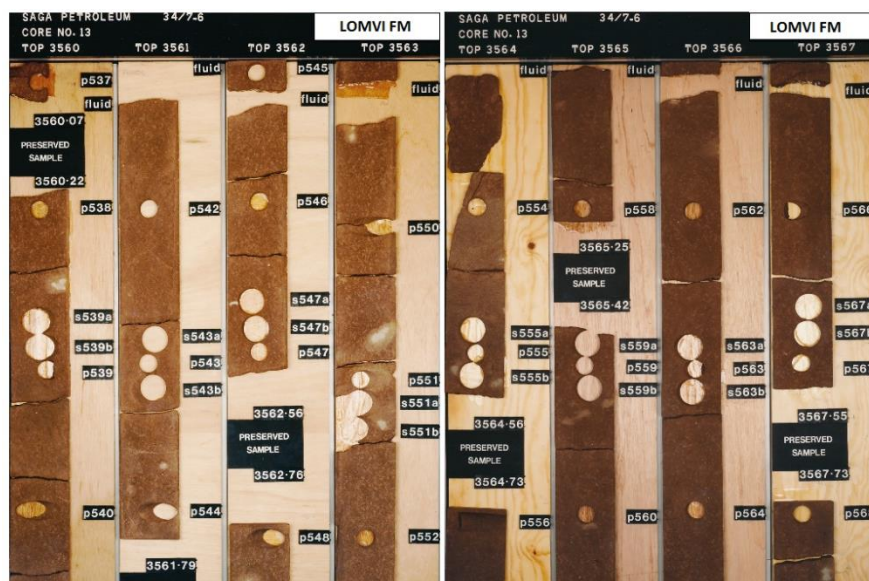


Figure 2.6: Core photograph of Lomvi Formation from interval 3560-3567 m (MDKB). The core is taken in well 34/7-6. The figure is adapted from NPD, (2016).

Lunde Formation

Lunde Formation is the main reservoir in the Snorre field. Vollset and Doré, (1984), suggested Lunde Formation is of continental origin which deposited in lacustrine and fluvial environments and consists of interbedded sequences of very fine to coarse grained sandstones, claystones, marls and shales. The Lunde Formation informally subdivided into three members: lower, middle and upper members (Jorde and Diesen, 1990; Nystuen and Fält, 1995). The lower and middle members consist of claystones, mudstones and thin fine grained sandstones whether the upper member is rich in fluvial channel sandstones apart from uppermost mudstone dominated part (Nystuen and Fält, 1995). The sandstone are white, pink or grey with variable degree of Kaolinite cementation, anhydrite and carbonate (Vollset and Doré, 1984). The core photographs of Lunde Formation from well 34/4-4 are shown in Figure 2.7.

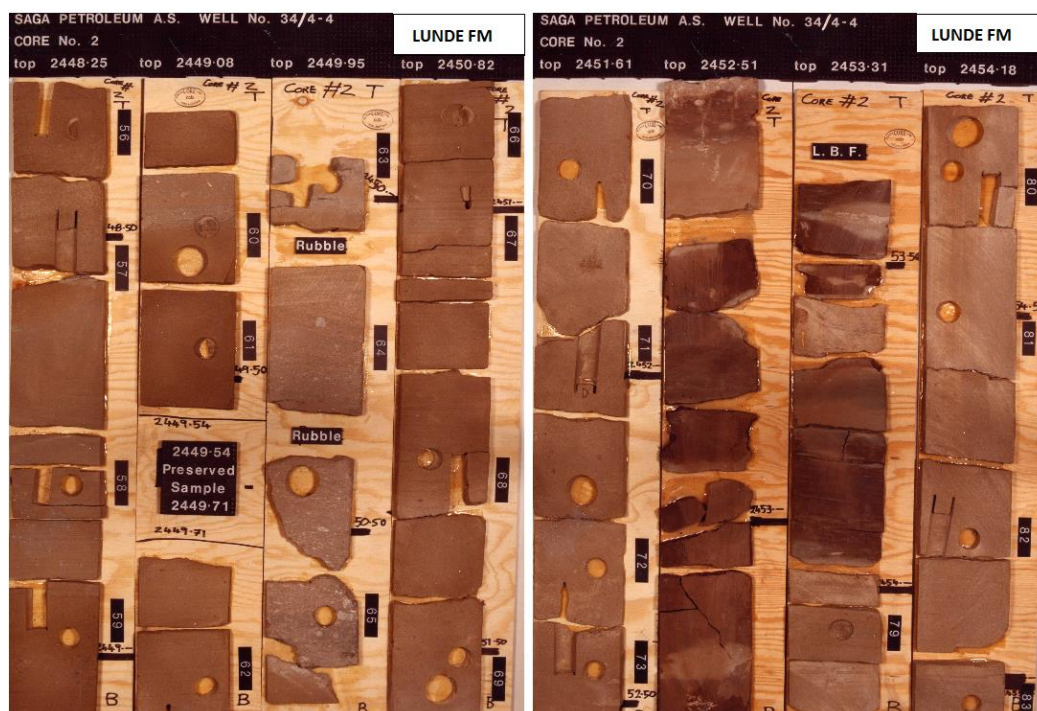


Figure 2.7: Core photograph of Lunde Formation from interval 2448-2454 m (MDKB). The core is taken in well 34/4-4. The figure is adapted from NPD, (2016).

2.3.2 Statfjord Formation

The sandstones and mudrocks of the Statfjord Formation are extensively distributed throughout the North Sea (Ryseth, 2001). The Rhaetian-Sinemurian Statfjord Formation consists of fluvial sandstone and mudstone deposited by braided river on alluvial plain (Jorde and Diesen, 1990). Statfjord Formation is part of Triassic to Early Jurassic continental/paralic deposits and mark transition from continental to marine environments (Vollset and Doré, 1984). The marine deposition of the Statfjord Formation that noticed on the Statfjord Field does not extended into Snorre Field area (Jorde and Diesen, 1990; Nystuen and Fält, 1995). The basal part of the Statfjord Formation shows coarsening upward sequence and consist of grey, green and sometimes red shales interbedded with thin siltstone, sandstone and dolomitic limestones (Vollset and Doré, 1984). The lower part of Statfjord Formation has high

resemblance with upper part of Lunde Formation and show gradational change (Jorde and Diesen, 1990). The uppermost part of the Statfjord Formation contains coarse grain glauconitic sandstone with marine fossils suggest a shallow marine environment (Nystuen and Fält, 1995; Vollset and Doré, 1984).

2.3.3 Dunlin Group

The Dunlin Group is of Jurassic age and of marine origin (Figure 2.5). The group ranges from Hettangian to Bajocian and divided into five formations: Amundsen, Johansen, Burton, Cook and Drake Formations (Vollset and Doré, 1984). The lithology of the Dunlin Group mainly consist of the marine argillaceous sediments with white to light grey, very fine to medium grained marine sandstone on marginal areas (Vollset and Doré, 1984). The boundary between Dunlin Group and underlying Statfjord Formation mark change in depositional environment from alluvial to marginal marine to deep marine conditions in lowermost part of Dunlin Group (Chamock et al., 2001). The core photographs of Dunlin Group from well 34/7-13 are shown in Figure 2.8.

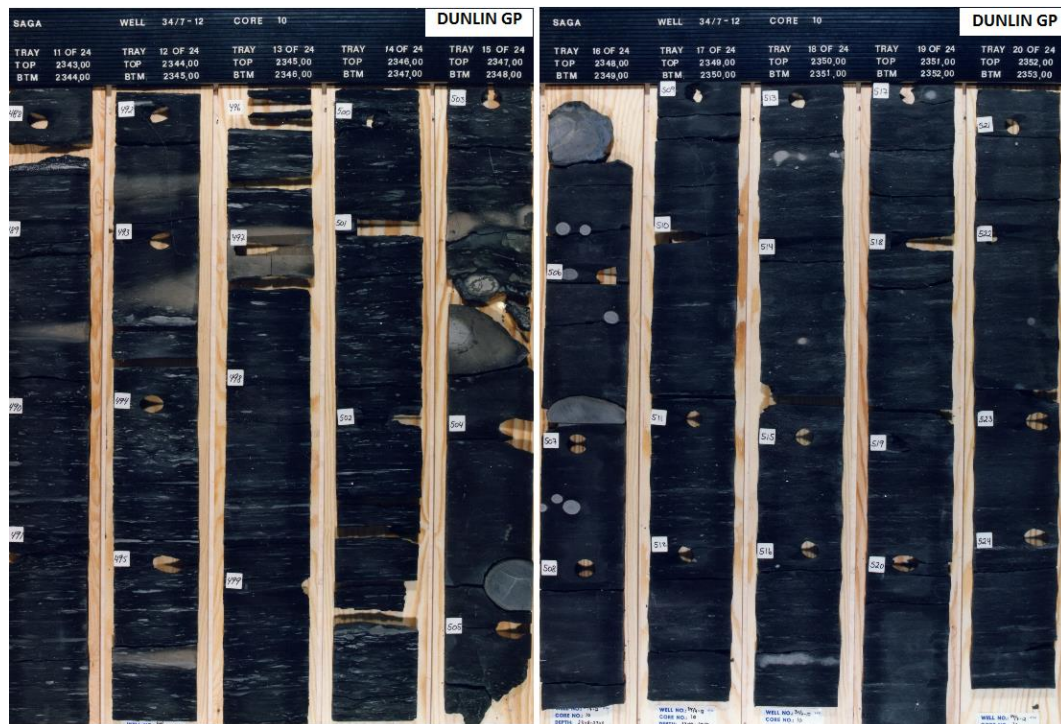


Figure 2.8: Core photograph of Dunlin Group from interval 2873-2888 m (MDKB). The core is taken in well 34/7-13. The figure is adapted from NPD, (2016).

2.3.4 Brent Group

The age of the Brent Group is Middle Jurassic (Figure 2.5). The Brent Group is economically important succession in North Sea and contains most of Britain oil reserves and around 200 papers are published on different aspects of the Brent Group (Fjellanger et al., 1996; Richards, 1992). The major lithology of the Brent Group consists of grey to brown sandstones, siltstones and shales with subordinate coal beds and conglomerates (Vollset and Doré, 1984). The Brent group is subdivided into: Broom, Rannoch, Etive, Ness and Tarbert Formations. The detail discussion of the subdivisions is beyond the scope of this study and

reader is referred to Vollset and Doré, (1984). The core photographs of Brent Group from well 34/7-12 are shown in Figure 2.9.

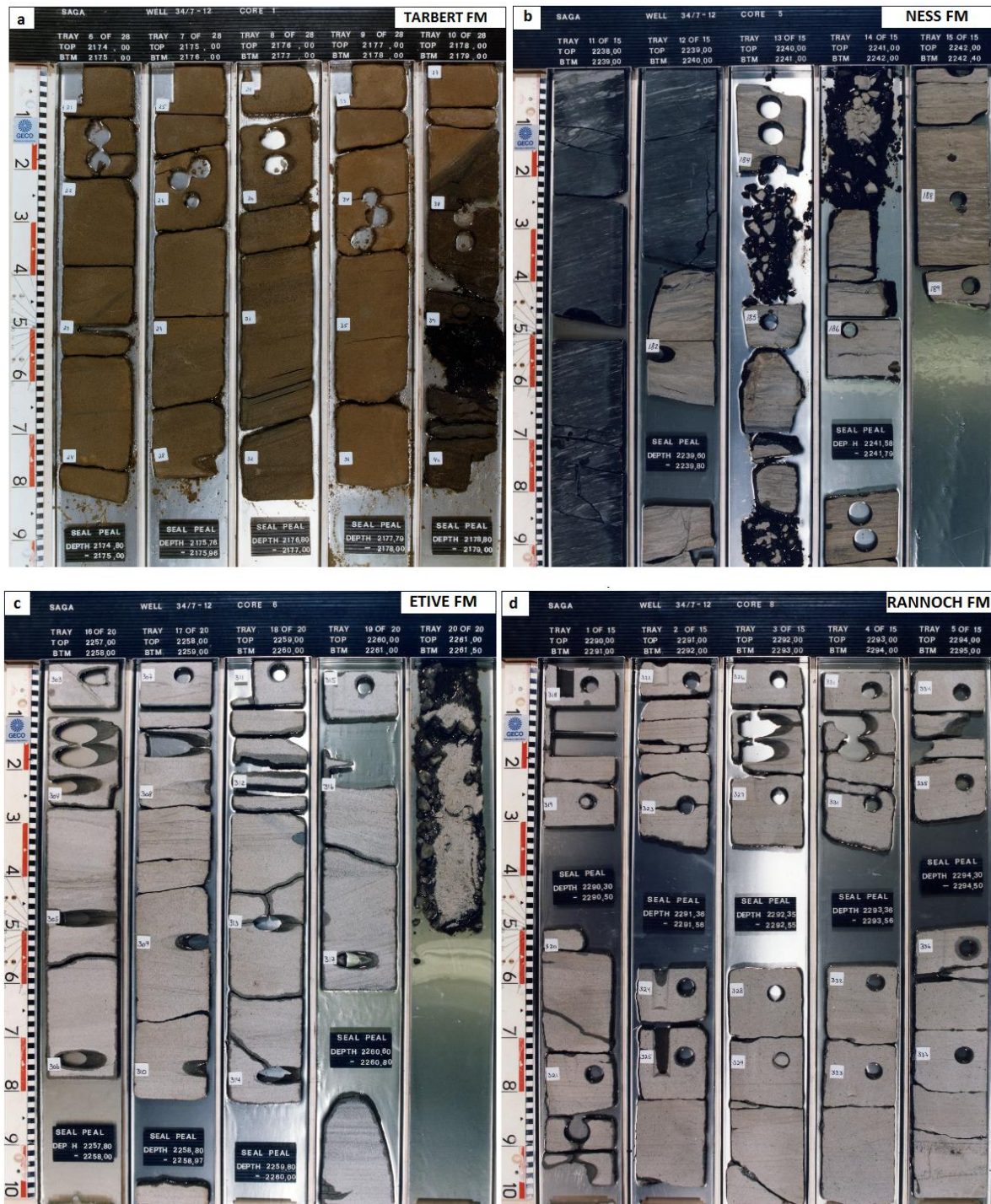


Figure 2.9: Core photographs of Brent Group. The core is taken in Well 34/7-12; (a) Tarbert Fm interval 2169-2174 m (b) Ness Fm interval 2238-2242 m (c) Etive Fm interval 2257-2261 m and (d) Rannoch Fm interval 2290-2295 m (MDKB). The figure is adapted from NPD, (2016).

2.3.5 Viking Group

The Upper Jurassic Viking Group consists of the two subdivisions: Heather Formation and Draupane Formation (Figure 2.5). The group range from Bathonian to Ryazanian in age and mainly consists of dark, grey to black, marine mudstones, claystones and shales (Vollset and Doré, 1984).

Heather Formation

The age of the Heather Formation is Bathonian to Kimmeridgian and mainly consists of grey silty claystones with thin layers of limestone with open marine depositional environment (Vollset and Doré, 1984). The Heather Formation deposited as synrift deposits during Bathonian to Kimmeridgian stretching interval of the North Sea rifting (Justwan and Dahl, 2005). The core photographs of Heather Formation from well 34/7-20 are shown in Figure 2.10.

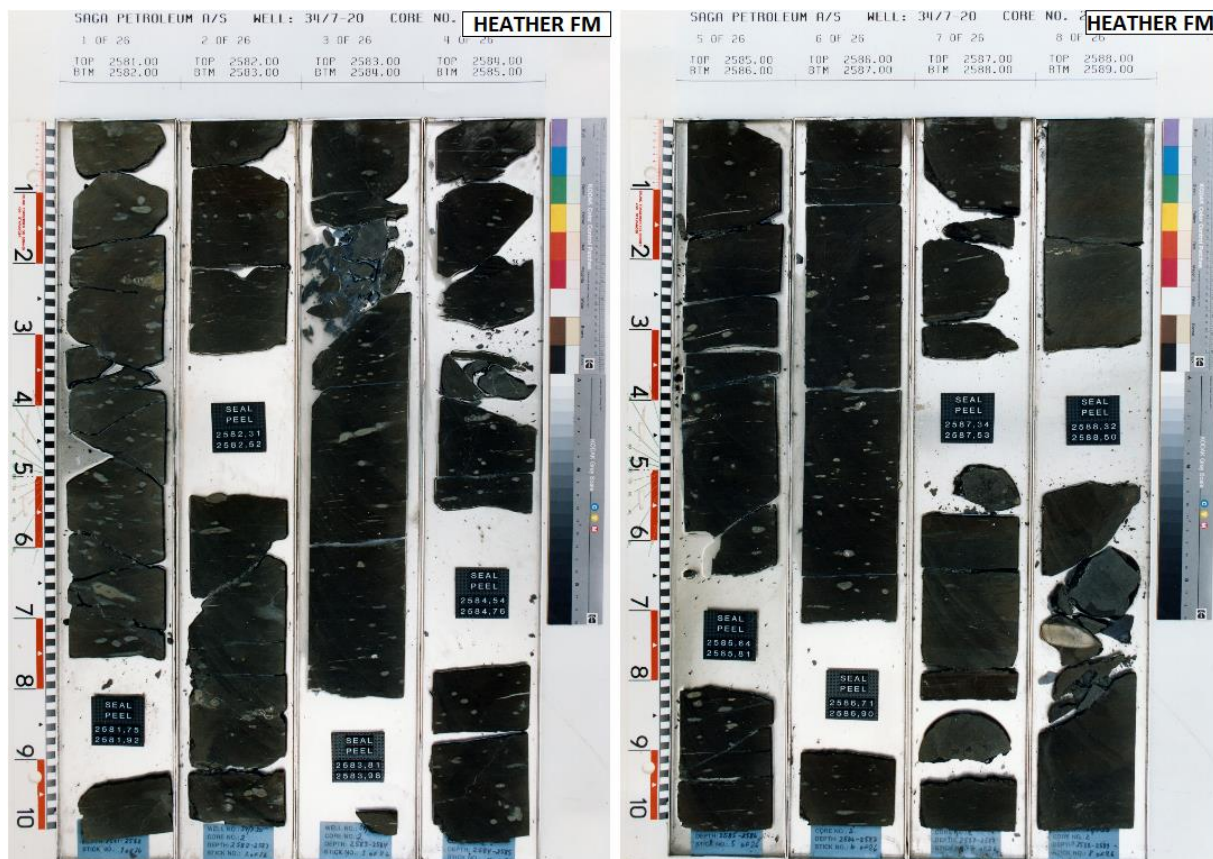


Figure 2.10: Core photographs of Heather Fm interval 2581-2589 m (MDKB) from well 34/7-20. The figure is adapted from NPD, (2016).

Draupane Formation

The Draupane Formation is the main source rock in the northern North Sea and equivalent of the Kimmeridge Clay Formation (Justwan and Dahl, 2005). The age of the Draupane Formation is from Oxfordian to Ryazanian and consists of dark grey-brown to black claystone deposited in restricted bottom circulation marine environment (Vollset and Doré, 1984).

2.3.6 Cromer Knoll Group

The Cromer Knoll Group was deposited in open marine environment and consists of calcareous claystones, siltstones and marls with subordinate layers of limestone and sandstone as main lithology (Isaksen and Tonstad, 1989). The age of the Cromer Knoll Group is Cretaceous usually Ryazanian to Albian/Early Cenomanian (Isaksen and Tonstad, 1989). The Cromer Knoll Group comprises of the three formations: Lange Formation, Lyr Formation and Lysing Formation (Dalland et al., 1988).

2.3.7 Shetland Group

The age of the Shetland Group is Upper Cretaceous. The lithology of the Shetland Group is chalky facies of limestone, marls, calcareous shales and mudstones and deposited in open marine environment (Isaksen and Tonstad, 1989). On the Tampen Spur area the four subdivisions of the Shetland Group are suggested: Svarte Fm, Blodøks Fm, Kyree Fm and Jorsalfare Fm (Figure 2.5).

2.3.8 Rogaland Group

The age of the Rogaland Group is Palaeocene. The lithology in Norwegian sector of the North Sea mainly consist of argillaceous sediments of the marine origin with reworked limestone and marls in basal part (Isaksen and Tonstad, 1989).

2.3.9 Hordaland Group

The Hordaland group is of Eocene age. The major lithology consist of marine claystone, minor very fine to medium grained sandstone and thin streaks of limestone and dolomite (Isaksen and Tonstad, 1989).

2.3.10 Nordland Group

The age of the Nordland Group is Miocene. The lithology is dominated by grey, greenish grey and grey-brown marine claystone with glacial deposits in uppermost part and sandy Utsira formation in the lower part of the group (Isaksen and Tonstad, 1989). The sandstone of Utsira Formation is of marine origin with very fine to fine grain size.

Chapter 3: Research methodologies and theoretical background

The aim of this chapter is to introduce the reader with the methods that are utilized to conduct this study and the theoretical background of all analyses.

3.1 Work Flow

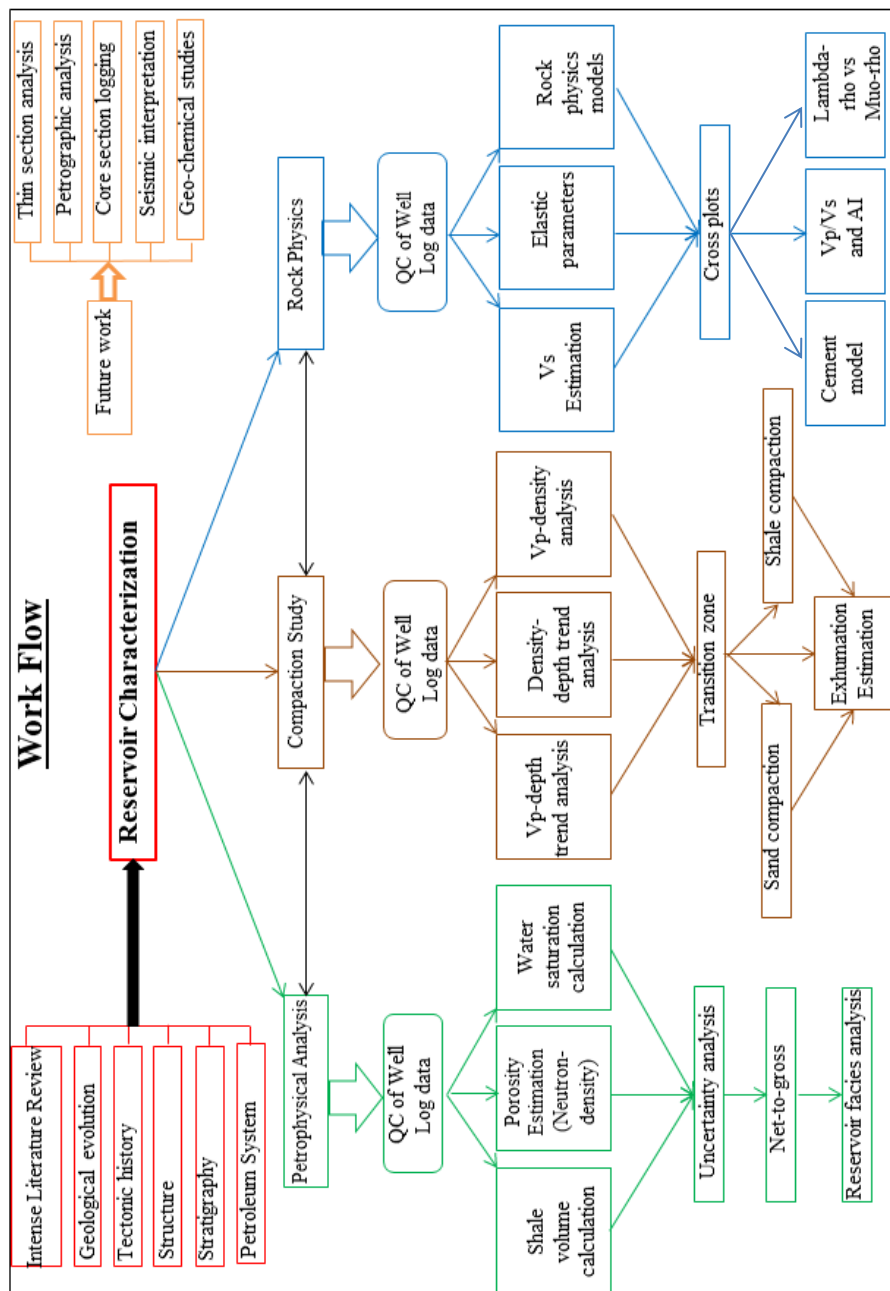


Figure 3.1: The overall workflow chart for the study.

3.2 Data Handling

As mentioned before a suit of well log data from 20 wells were utilized in this study for detailed petrophysical analysis, compaction study and rock physics diagnostics to characterize the reservoirs of the Snorre field. Microsoft Excel, Interactive Petrophysics, Petrel and Hampson Russell softwares were used in this study to perform the target analysis. The first step is to QC the well log data to sort out limitation and uncertainties of the available data. For data handling several steps described below considered seriously in the research tasks.

3.2.1 Log editing and quality check

The first step in log editing was to compare the measured depth (MD) with the true vertical depth (TVD) given by Norwegian Petroleum Directorate (NPD). The deviation of bore hole during drilling caused significant difference between TVD and MD of bore hole. The difference in TVD and MD cause the incorrect stratigraphic position along the well log during interpretation. The shear sonic is missing in all of the wells except Well 34/7-27 (Table 3.1). Additionally, bulk density log and neutron porosity log are partially available in some of the wells.

Table 3.1: A summary of available well logs. The true vertical depth and bottom hole temperature of all studied wells are also shown.

Well	Depth (m) TVD	BHT °C	GR	R _D	Density	NPHI	DT	DTS
34/4-1	2912	103	✓	✓	*	*	✓	×
34/4-2	3599	120	✓	✓	*	*	✓	×
34/4-4	3800	122	✓	✓	✓	*	✓	×
34/4-6	3281	113	✓	✓	✓	*	✓	×
34/4-7	2950	110	✓	✓	*	*	*	×
34/4-8	3108	104	✓	✓	*	*	*	×
34/7-1	2905	105	*	✓	*	*	✓	×
34/7-3	3413	113	✓	✓	✓	*	✓	×
34/7-4	3115	75	✓	✓	*	*	✓	×
34/7-6	3683	125	✓	✓	*	*	✓	×
34/7-8	2766	96	✓	✓	✓	*	✓	×
34/7-9	3239	93	✓	✓	✓	*	✓	×
34/7-10	3000	109	✓	✓	*	*	✓	×
34/713	2994	103	✓	✓	*	*	✓	×
34/7-16	2700	98	✓	✓	*	*	✓	×
34/7-19	2800	91	✓	✓	*	*	✓	×
34/7-20	3177	100	✓	✓	*	*	✓	×
34/7-27	300	103	✓	✓	*	*	✓	*
34/7-28	3005	104	✓	✓	*	*	✓	×
34/7-32	3651	79	✓	✓	×	×	×	×

✓ Available, × Not Available and * Partially available

3.3 Petrophysical Analysis

Petrophysical analysis includes the study of the properties of rock such as porosity (the ratio of volume of available pore spaces to total volume of the rock), saturation (the amount and type of the fluid stored in the rock pores) and interconnectivity of the pores which called permeability. These properties are more desired in hydrocarbon exploration and exploitation phases. The rock composition affects the physical properties of the rock with respect to burial history and diagenesis. Petrophysics help to understand the change in physical properties with change in mineralogy and composition history.

The physical properties are often measured by using various logging tools and displayed in the form of logs called petrophysical logs. The focus of this section is to give the basic overview and theoretical background of petrophysical analysis.

3.3.1 Shale Volume Calculation

The shale volume is one of the basic and important parameter for the petrophysical analysis of the reservoir and can be calculated by using different logs such as SP, Gamma Ray, Resistivity, Neutron-Density logs. Every log has its certain limitations and advantages therefore during well log interpretation confine on single log are not a wise approach. A combination of logs will give more confidence on results. In this study, the shale volume is calculated by using Gamma Ray and Neutron-Density logs by utilizing Interactive Petrophysics (IP) software. For further calculations (e.g. porosity, water saturation and net-to-gross) the shale volume from neutron-density is used in this study.

Shale Volume from GR log

Gamma Ray log measure the natural radioactivity of the rock induced from natural radioactive elements Uranium, Potassium and Thorium. Shales contain significant amount of Uranium and Potassium and give high gamma ray reading but in sandstone the presence of heavy minerals and K-Feldspar can also give high Gamma ray values. Besides quantitative shale volume calculation, Gamma ray log is useful for lithology identification. Gamma ray log is particularly useful in cased wells, non-conductive mud and in absence of SP log (Dresser Atlas, 1982).

By using Gamma Ray log the shale volume can be calculated by linear relation between Gamma ray Index (I_{GR}) and shale volume but several nonlinear relations also suggested. The shale volume is calculated by using linear the following relation (Eq 3.1 and 3.2) (Dresser Atlas, 1982; Mondol, 2015).

$$I_{GR} = \frac{GR_{log} - GR_{min}}{GR_{max} - GR_{min}} \dots\dots\dots (3.1)$$

$$V_{sh} = I_{GR} \dots\dots\dots (3.2)$$

The gamma ray index (I_{GR}) and shale volume (V_{sh}) are assumed to have linear relation but there is no scientific basis for this assumption (Mondol, 2015). The GR_{log} is the desired value from the Gamma ray log in zone of interest while GR_{min} and GR_{max} are the minimum and maximum values along the Gamma Ray log. The GR_{min} referred to as sand line and GR_{max} called shale line. The selection of sand line and shale line depends on interpreter own observation and experience. The histogram shown in Figure 3.2 is quiet simple but useful for

selection of the sand line and shale line. The linear relation of I_{GR} and V_{sh} is not very accurate and mostly overestimated shale volume (Rider and Kennedy, 2011).

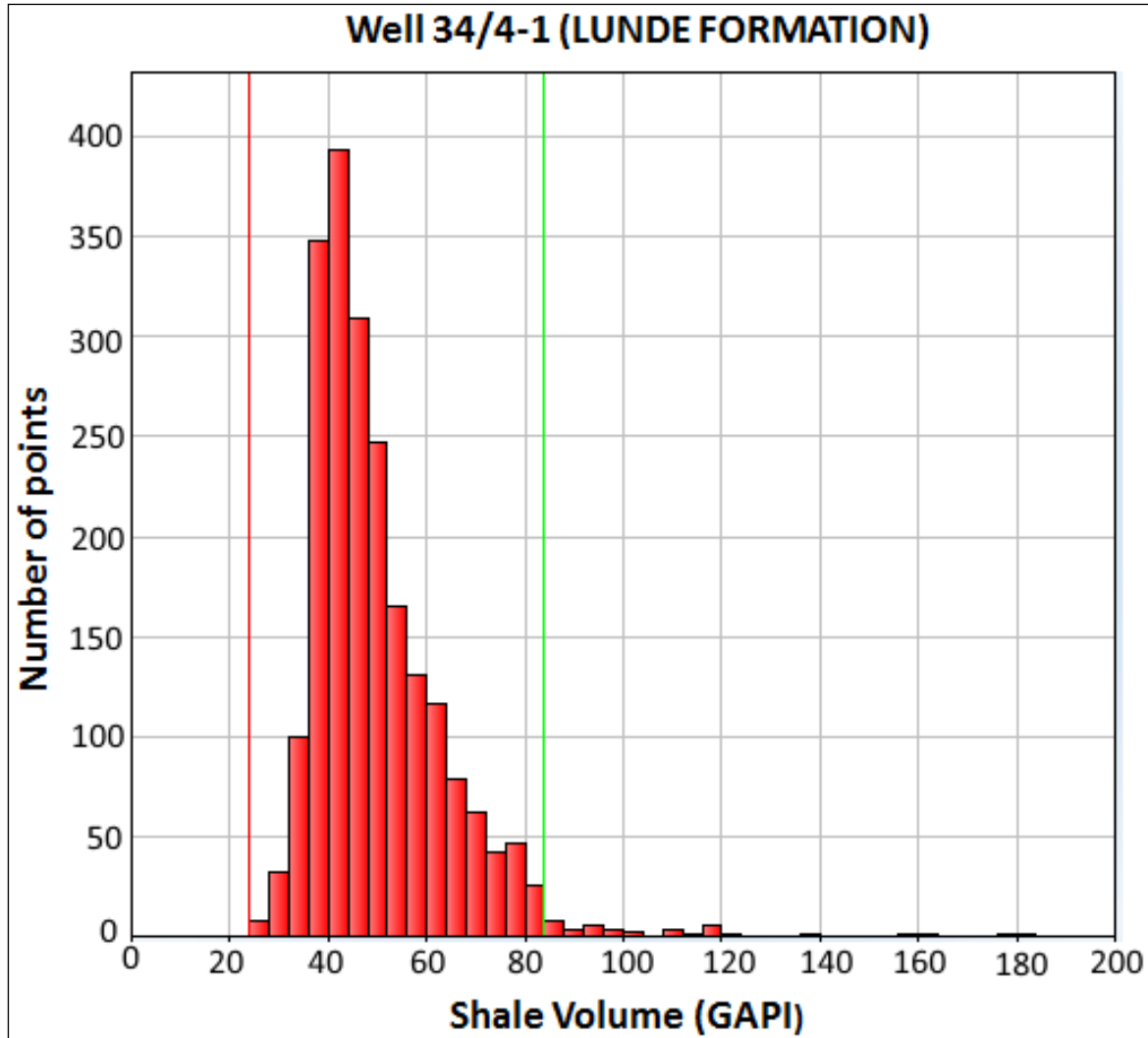


Figure 3.2: The GR histogram with GR_{min} (red colour, sand line) and GR_{max} (green colour shale line). The data points are plotted from well 34/4-1 for Lunde Formation.

Several non-linear relations are suggested over years by different authors (Figure 3.3 and Table 3.2). In order to avoid the overestimation of the shale volume by linear relation, the correction is applied from Larionov older rocks (Larionov, 1969) (Table 3.2) to calculate shale volume from Gamma Ray log. The equations are defined in (Dresser Atlas, 1982; Rider and Kennedy, 2011). The shale volume calculated from non-linear relations is lower than the shale volume calculated by the linear relation of the I_{GR} (Gamma Ray Index).

Table 3.2: The non-linear relations suggested by different authors for shale volume calculation from Gamma Ray log.

Author(s)	Equation
Larionov (1969) Young rocks	$V_{sh} = 0.083 \times (2^{3.71 \times I_{GR}} - 1)$
Larionov (1969) Older rocks	$V_{sh} = 0.33 \times (2^{I_{GR}} - 1)$
Stieber (1970)	$V_{sh} = I_{GR} \div (3 - 2 \times I_{GR})$
Clavier et al. (1971)	$V_{sh} = 1.7 - [3.38 - (I_{GR} + 0.7)^2]^{1/2}$

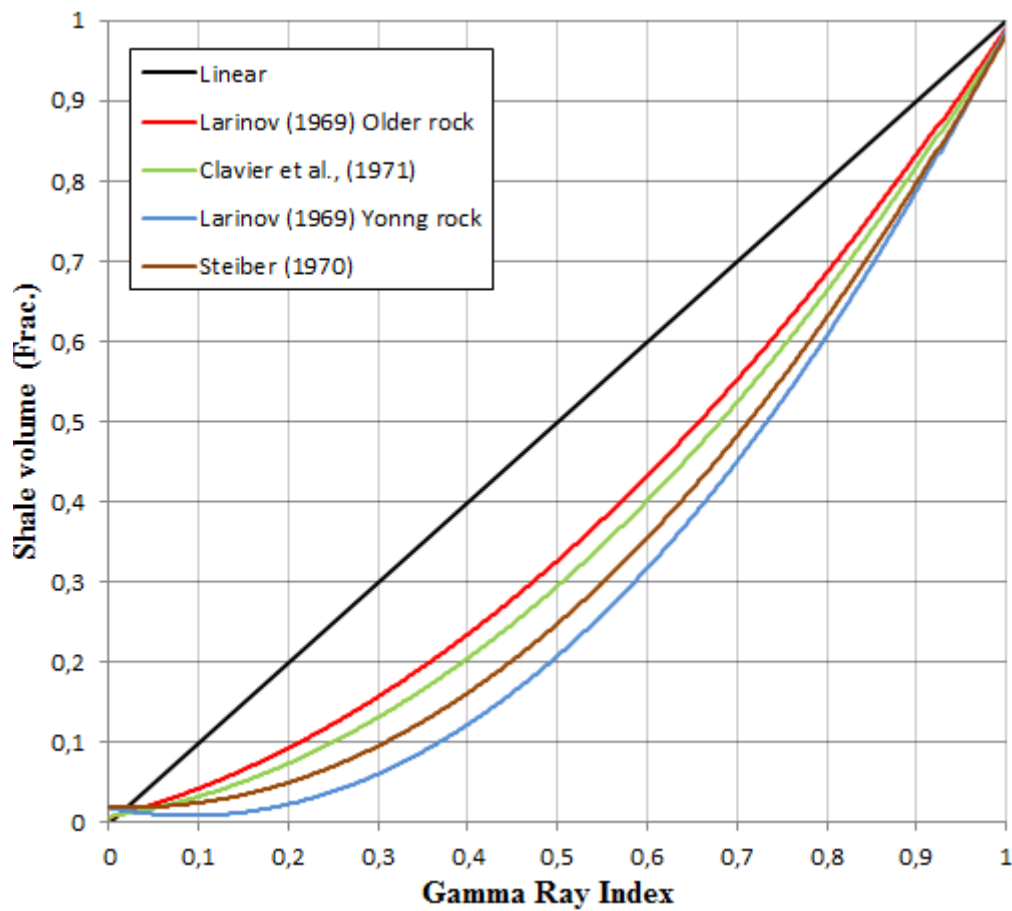


Figure 3.3: The chart for shale volume correction by non-linear equations suggested by different authors. The figure is adapted and modified from Mondol, (2015).

The Table 3.3 shows the GR_{min} and GR_{max} values with the calculated shale volume by linear relation (Eq 3.1 & 3.2) and non-linear relation Larionov, (1969) “Older rock” for Lunde and Statfjord Formations from all the wells included in this study. The overestimation of the shale volume by linear relation is observed for all the wells.

Table 3.3: Estimated average shale volume from GR log; GR_{min} – Sand line, GR_{max} – Shale line and Larinov – Larionov, (1969) older rock.

LUNDE FORMATION				
Well Name	GR _{min} (API)	GR _{max} (API)	Linear	Larinov
34/4-1	24	84	0.41	0.28
34/4-2	17	100	0.44	0.30
34/4-4	24	100	0.42	0.29
34/4-6	20	85	0.43	0.30
34/4-7	46	107	0.35	0.22
34/4-8	42	130	0.53	0.39
34/7-1	46	107	0.34	0.37
34/7-3	30	118	0.39	0.25
34/7-4	17	90	0.43	0.29
34/7-6	22	98	0.39	0.27
34/7-8	22	80	0.32	0.20
34/7-9	28	85	0.33	0.21
34/7-10	45	97	0.40	0.27

STATEFJORD FORMATION				
Well Name	GRmin (API)	GRmax (API)	Vsh (Linear)	Larinov
34/4-2	17	80	0.43	0.29
34/4-8	42	121	0.50	0.40
34/7-3	36	90	0.37	0.25
34/7-4	15	75	0.39	0.25
34/7-6	21	62	0.43	0.30
34/7-8	20	75	0.40	0.26
34/7-10	47	91	0.54	0.40
34/7-13	28	94	0.44	0.32
34/7-20	71	133	0.50	0.37

Limitations in Shale volume from Gamma Ray log

The shale volume calculation from Gamma Ray log is most common technique but approach is not completely reliable due to following reason:

- The caving in the borehole badly effects the Gamma Ray log and leads to underestimation of Gamma Ray reading (Mondol, 2015). The Calliper log in most cases uses to observe the borehole condition.
- The presence of K-feldspar (KAlSi_3O_8) in sandstone. Potassium (K) is radioactive itself and its presence gives high Gamma ray value in sandstone. Due to high Gamma ray value the clean sand appear to be shaly. The Spectral Gamma Ray log could be useful in such case because it gives separate values for Uranium, Potassium and Thorium.
- Presence of heavy minerals, clay filling, volcanic clast or rock fragments leads to high Gamma Ray value in sandstone.

- The drilling mud can also effect Gamma Ray reading such as high density mud effect Gamma Ray and cause low reading while the KCl-based mud can give high reading due to potassium (K) (Mondol, 2015).
- In case the whole clastic formation is shaly, the clean sandline pickup is not simple. In this study the reservoir is shaly and evolves uncertainty in picking up the clean sandline. In mostly wells used in this study the GR_{min} value is relatively high (Table 3.3).

Shale Volume from neutron-density logs

The double clay indicators ‘density-neutron combination’ is reliable method to find shaliness of the reservoir in the presence of uncertainties associated with Gamma Ray log. The Equation 3.3 is used for shale volume calculation from neutron-density (Adeoti et al., 2009).

$$V_{sh} = \frac{\phi_N - \phi_D}{\phi_{NSH} - \phi_{DSH}} \dots \dots \dots (3.3)$$

Where, ϕ_N and ϕ_D represent neutron porosity in sand and density porosity in sand respectively. While ϕ_{NSH} is neutron porosity in shale and ϕ_{DSH} is density porosity in shale.

In Interactive Petrophysics software the double clay indicator works on the principle of defining clean line (sand line) and clay line (Figure 3.4).

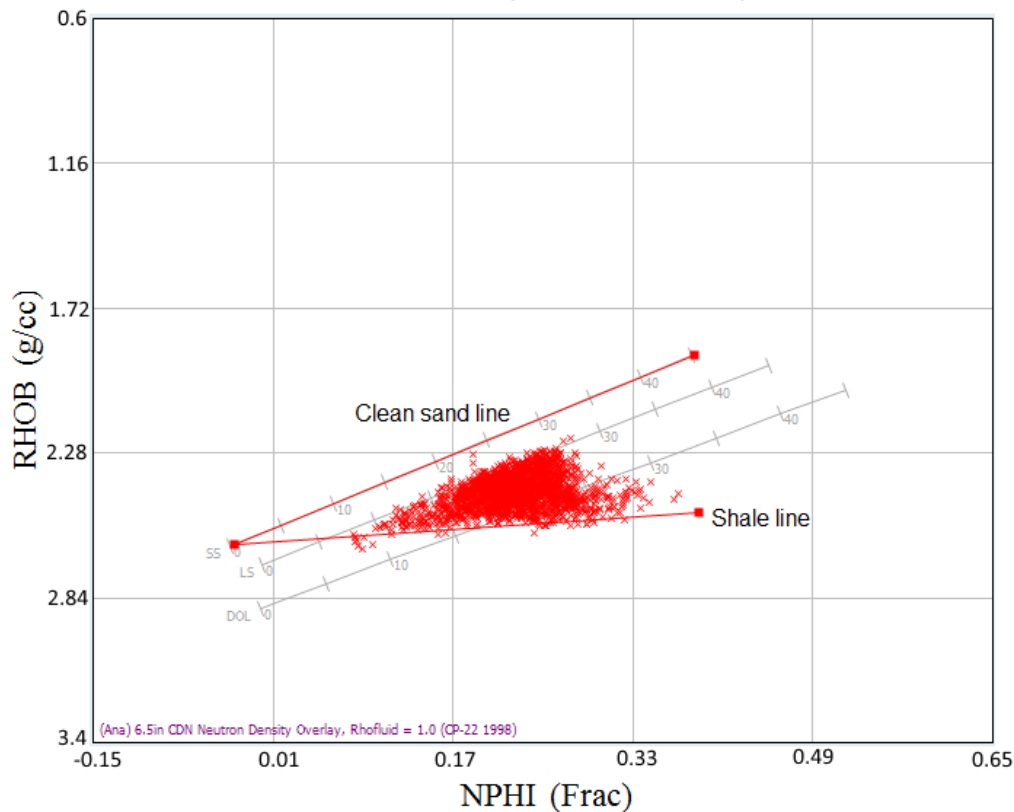


Figure 3.4: Neutron-density cross plot for defining clean sand and shale lines for estimation of the shale volume. The data points are plotted from well 34/4-1 for Lunde Formation.

3.3.2 Lithology Discrimination

Along the well section various lithologies are present and identifying different lithologies are important aspect of the well log interpretation. The most useful and common logs for lithology identification are Gamma Ray log and combination of Neutron-Density logs. Calliper log can also help to identify the sand zone and shale zone along well section due to caving and formation of the mudcake in porous permeable zone. During well log interpretation always set of well logs are necessary to get better control and understandings because a single log can contain lot of uncertainties and pitfalls which leads to misinterpretation of data. For this study the Gamma Ray log with neutron-density crossover is used to discriminate between sandstone and shales (Figure 3.5). Further Calliper log is used to take into consideration the bad borehole effect due to caving in shales.

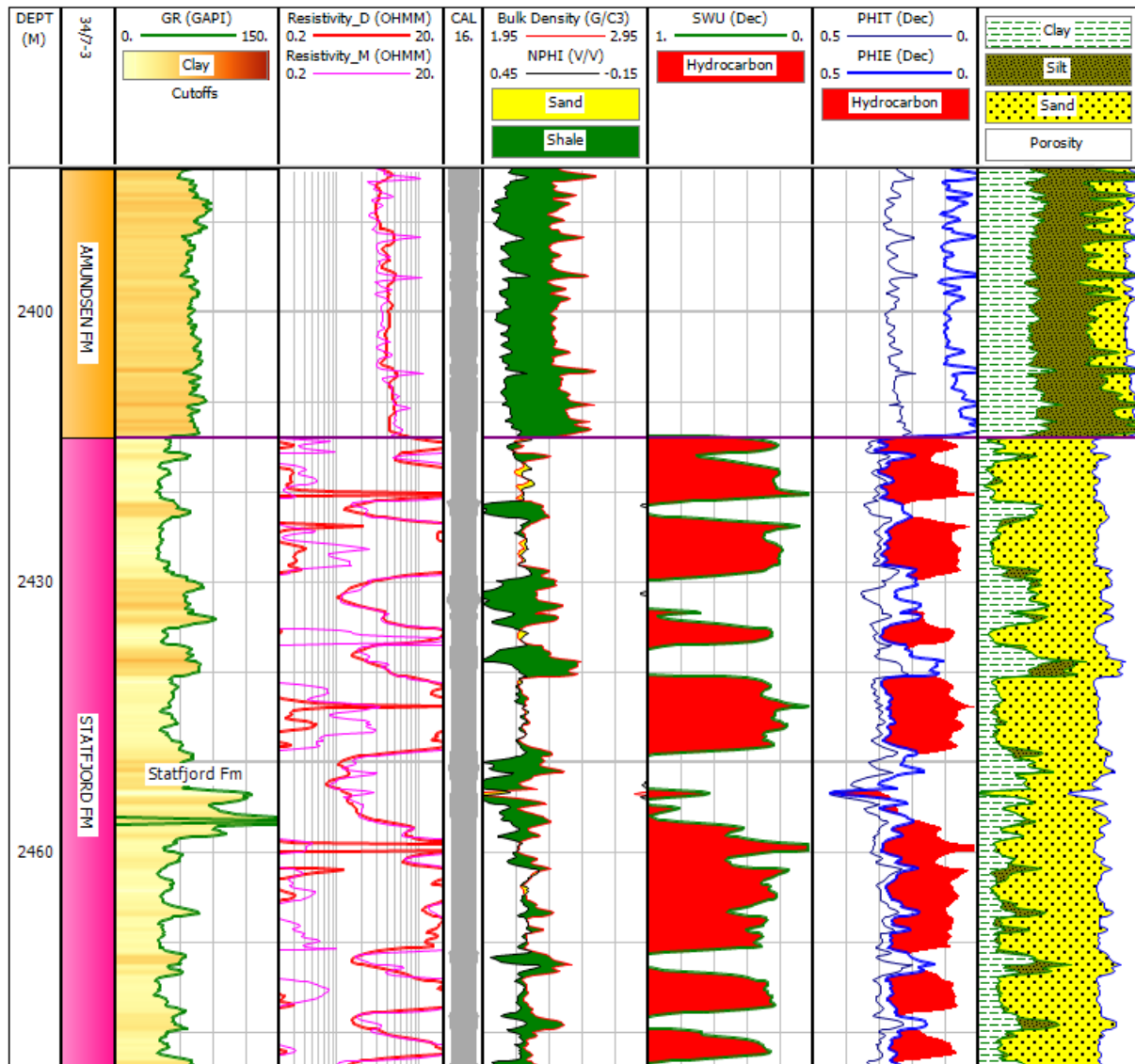


Figure 3.5: The well log section from well 34/7-3 over interval in the Statfjord and Amundsen Formations. The depth is given in MDKB (Measured depth from Kelly bushing). GR – Gamma Ray log, SWU – water saturation, PHIT – total porosity, PHIE – effective porosity, NPHI – neutron porosity. Clay, silt and sand are three lithology types.

3.3.3 Porosity Estimation

Porosity is the pore space between the grains of the rock which can be filled with water, hydrocarbons or air. The actual definition of porosity is the ratio of pore volume to bulk volume of the rock. The porosity is the most important property of siliciclastic rock in hydrocarbon exploration aspect. For the reservoir estimation, reservoir simulation, pore pressure prediction porosity is the parameter that is most applicable (Dvorkin and Nur, 2002). Different logs calculate porosity such as Neutron Porosity (NPHI), Bulk Density Porosity (DPHI), and Sonic Porosity (SPHI) but still stand limitations with each log. In this study, the average porosity from Neutron and Density logs is used to calculate porosity.

Neutron Porosity

Neutron log measure the porosity in the formation as a function of hydrogen present in the rock called hydrogen index (HI). Hydrogen is present in water or hydrocarbon that occupied pore spaces. The formation is bombarded with fast moving neutrons and return of neutrons at low energy level due to interaction with hydrogen atom is counted at neutron tool. The hydrogen has efficiency to slow-down fast neutrons that is widely scattered in rock (Ellis and Singer, 2007). The neutron tool gives accurate porosity calculation in pure limestone because of absence of the hydrogen in limestone mineralogy. The neutron log overestimate porosity in lithologies that contain water such as clay minerals in shales. The calibration of neutron tool effects the calculated porosity such as the tool calibrated against pure limestone with fresh water gives different value for pure sandstone with fresh water. The simplest equation (Eq 3.4) used to measure porosity from neutron expressed by Rider and Kennedy, (2011).

$$\text{Log}_{10}\phi = aN + B \dots \dots \dots (3.4)$$

where, ϕ is true porosity, a, b are constants and N is neutron tool count rate. The constants a and b depend on the nature of the formation (Rider and Kennedy, 2011).

The neutron porosity in Interactive Petrophysics Software is calculated by using equation 3.5:

$$\phi = \frac{(\phi_{neu} - V_{cl} \times \text{Neu}_{cl} + \text{Neu}_{matrix} + \text{Exfact} + \text{Neu}_{sal})}{[S_{xo} + (1 - S_{xo}) \times \text{NeuHyHI}] \dots \dots \dots (3.5)}$$

ϕ_{neu} = Input neutron log

V_{cl} = Wet Clay Volume

Neu_{CL} = Neutron wet clay value

Neu_{matrix} = Neutron Matrix correction

Exfact = Neutron excavation factor

NeuSal = Neutron formation salinity correction

S_{xo} = Flushed zone water saturation

NeuHyHI = Neutron hydrocarbon apparent hydrogen index

Density porosity

The Density Log measures the bulk density of rock which in turn used to find the porosity of the rock and also for lithology identification. The bulk density of rock is function of density of matrix forming the rock volume. The simple equation (Eq 3.6) used to measure porosity by using density log (Dresser Atlas, 1982; Rider and Kennedy, 2011).

$$\phi = \frac{(\rho_{ma} - \rho_b)}{(\rho_{ma} - \rho_f)} \dots \dots \dots (3.6)$$

ρ_{ma} = Density of rock matrix

ρ_f = Pore fluid density

ρ_b = Density reading from log

The density of matrix is typically dependent on density of the minerals forming the rock matrix. The Table 3.4 gives typical rock forming minerals (Mondol, 2015).

Table 3.4: The different minerals densities that form rock matrix adapted from Mondol, (2015).

Lithology	Density Range (g/cm ³)
Quartz	2.65
Calcite	2.71
Dolomite	2.87
Biotite	2.90
Chlorite	2.80
Illite	2.66
Kaolinite	2.59

The fluid density depends on type of fluid either water or hydrocarbons. For a water bearing formation the density of water can vary from 0.95 g/cm³ to 1.25 g/cm³ but also depending on water salinity, pressure and temperature (Kennedy, 2015). The porosity calculated from core sample by using laboratory technique/measurement is most authentic and it is always fortunate to plot core porosity against density porosity if core porosity database is available (Mondol, 2015).

Average porosity

The limitations of the porosity log due to different lithology and fluid content leads to misjudgement of rock porosity. As stated earlier the most accurate porosity calculation is only possible from core samples by using laboratory techniques. In the absence of core data the average porosity of the density-neutron porosity is reliable. In this study the neutron-density porosity is used for whole interpretations. The porosity from combination of density and neutron log is primarily free of the lithology effect (Mondol, 2015). The average porosity calculation is shown in Equation 3.7.

$$\phi = \sqrt{\frac{\phi_N^2 + \phi_D^2}{2}} \dots \dots \dots (3.7)$$

Effective Porosity

Porosity is the ratio of volume of pores to the total volume of the rock but effective porosity is the volume of interconnected pores without any clay or clay-bound water content, along with free fluid that can easily flow. In a clean sand reservoir the effective porosity is almost equal to total porosity (Cluff and Cluff, 2004; Ezekwe, 2010). The interconnected pores provide a path for fluid to flow along the reservoir interval. The effective porosity helps to mark the reservoir pay interval from the whole volume. The presence of shale layers within reservoir effect the effective porosity as it form internal flow barrier additionally decrease net to gross of reservoir. The significant portion of the porosity clocked up with immobile clay bound water in shaly reservoir and therefore is not part of effective porosity (Cluff and Cluff, 2004).

The relationship between effective porosity ($PHIE$), total porosity ($PHIT$), shale volume (V_{shale}) and shale porosity ($PHIT_{shale}$) is defined by Cluff and Cluff, (2004) and expressed by Equation 3.8.

$$PHIE = PHIT - (V_{shale} \times PHIT_{shale}) \dots \dots \dots (3.8)$$

Uncertainties in porosity calculation

All the geophysical logging tools work on different principal with respect to different parameters. Neutron porosity is function of hydrogen index while density porosity depends on matrix density and pore fluid density. Moreover uncertainties arise in well logs during logging due to bad borehole conditions. Additionally the effect of different lithologies and pore fluids contribute in evolution of uncertainties.

In case of neutron-porosity (NPHI), two effective uncertainties/limitations are ‘‘gas effect’’ and ‘‘shale effect’’.

- In a sedimentary basin the most common lithologies are sandstones, limestones and shales. The clay minerals in shales contain clay bound water in their structure. The neutron tool measure the hydrogen from structure of clay minerals and other hand porosity which is actually not true. Therefore, the neutron tool overestimate porosity in the shale and this is called lithology effect or ‘‘shale effect’’.
- The presence of gas in zone of interest evolves another uncertainty which leads to underestimation of porosity from Neutron tool. The amount of hydrogen present in gas per volume is less as compared to oil (Mondol, 2015), therefore Neutron tool underestimate porosity. The example of porosity difference from different logs is shown in Table 3.5.

Table 3.5: The porosity estimation from different logs for Lunde Fm in well 34/4-4.

Lunde Formation				
Well Name	NPHI	DPHI	SPHI	PhiND (Avg)
34/4-4	0.22	0.18	0.33	0.20
34/4-6	0.17	0.11	0.33	0.14
34/7-9	0.13	0.12	0.35	0.12

where the NPHI is porosity calculated from neutron log, DPHI is porosity from density log, SPHI is porosity from sonic log and PhiND is average porosity from neutron-density porosity.

3.3.4 Water saturation

Water saturation is the amount of water excluding clay-bound water present in reservoir along with or without hydrocarbons. The water saturation is expressed in percent or fraction. The water saturation is used to quantify the hydrocarbon saturation in reservoir. The reservoir contains only water at the time of deposition but later the migrated hydrocarbon input from source rock change the water saturation of the reservoir. The different factors such as pore throat size and shape, capillary pressure, buoyancy effect the migration of hydrocarbons into the reservoir.

The water saturation is calculate by using Archie's equation (Archie (1942), which use resistivity of water (R_w), formation true resistivity (R_t), effective porosity (ϕ_e), tortuosity factor (n) and cementation factor (m) (Eq 3.9). The true resistivity of formation is calculated by deep resistivity log. The absence of the core data and reservoir fluid sample build portion of the uncertainties because the resistivity of the water varies with the salinity and temperature.

$$S_w = \sqrt[n]{\frac{(a \times R_w)}{(R_t \times \phi^m)}} \dots\dots\dots (3.9)$$

The total water saturation is calculated by using Equation 3.10 in IP software. The Pickett plot shown in Figure 3.6 is used to find R_w , n , a and m .

$$S_w T = S_w (1 - S_{wb}) + S_{wb} \dots\dots\dots (3.10)$$

where, $S_w T$ – total water saturation, S_{wb} – bound water saturation and S_w – effective water saturation

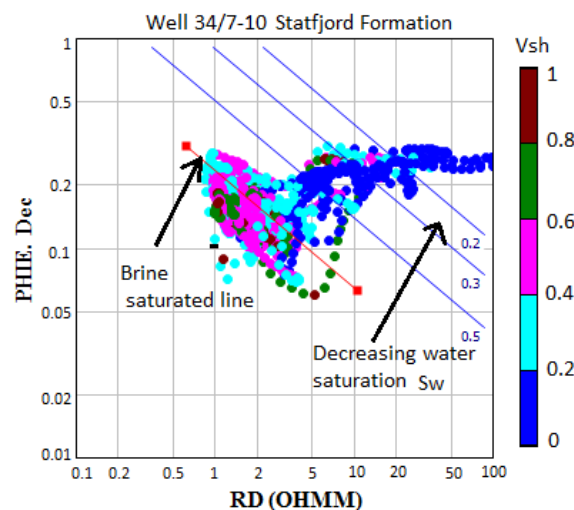


Figure 3.6: Pickett plot with data points of the Statfjord Formation from well 34/7-10; RD – Deep/true resistivity and PHIE – Effective porosity.

3.3.5 Net-to-Gross and pay zone

Net-to-gross is ratio of the thickness interval with good reservoir parameters to the total thickness of the reservoir. Net pay zone contain the thickness with economically producible hydrocarbon. The cut-off values for porosity, shale volume and water saturation are usually apply to exclude the poor, unproductive/unprofitable reservoir interval from net-pay thickness. Cut-off defined for porosity are lower limit and for shale are the upper limit in net thickness, at the same time the upper limit of water saturation are defined for pay zone (Kennedy, 2015). A good quality reservoir usually contains high N/G value.

3.3.6 Permeability prediction

Permeability is defined as the ability of the rock which allows fluids to pass through it in a porous media. The ability to flow fluids through a rock depends on interconnectivity of the pore spaces. The less porous rock could contain high permeability due to fracturing. Similarly it is possible for rock formations contain high porosity but very low permeability. In reservoir characterization permeability is one of the most important but least predictable property of the reservoir rock (Torskaya et al., 2007). The main factor influencing fluid flow or permeability is porosity but several other factors also affect such as pore throat size and shape, wetting angle, capillary pressure and presence of impermeable shale layers which act as flow barrier. The geological aspect of rock such as grain size, shape, geometry and sorting, clay content, fluid type has an influence on ability of rock to allow fluids flow. The poorly sorted sand contained small grains that can fill spaces between large grains and reduce permeability. Permeability is measured by core analysis and well testing but both methods are costly and time consuming therefore not used widely (Mohebbi et al., 2012; Torskaya et al., 2007). The alternative to core analysis and well testing is prediction of permeability from geo-physical logs. The SI unit of permeability is m^2 but in oil field the unit called Darcy (D) or milidarcy (mD) is used. Wyllie and Rose (1950) suggested general empirical relation (Eq 3.11) to calculate permeability from porosity and water saturation of porous media (Torskaya et al., 2007).

$$k = a \frac{\phi^b}{S_{wi}^c} \dots\dots\dots (3.11)$$

where, k – permeability; S_{wi} – irreducible water saturation; a , b and c – model parameters.

Based on Wyllie and Rose, (1950) different empirical relations are suggested from different authors for permeability calculation.

Morris-Biggs Equation

The Equation 3.12, for permeability in oil reservoir is suggested by Morris and Biggs, (1967).

$$k = 62.5 \left[\frac{\phi^3}{S_{wi}} \right]^2 \dots\dots\dots (3.12)$$

Timur Equation

The Equation 3.13 is suggested by Timur, (1968) for permeability calculation.

$$k = 8.58 \frac{\phi^{4.4}}{S_{wi}^2} \dots\dots\dots (3.13)$$

The empirical relations to calculate permeability depends on water saturation which is not directly measured during well logging. The water saturation is calculated by using deep resistivity log and Archie's law.

3.3.7 Facies Interpretation from Well logs

Facies analysis from well logs is a useful understanding in reservoir characterization. The facies interpretation aids to understand the depositional environment of the zone of interest. In reservoir characterization the facies interpretation helps to understand the variation of reservoir parameters with respect to depositional environment. The lithology and depositional environment possibly place on seismic data by using well data, hence linking sedimentological facies to seismic facies (Emery and Myers, 2009). The most accurate subsurface facies interpretation is credible from core section only. The lithologging from core sections is identical to the observation of outcrop sections (Cant, 1992).

In this study the facies interpretation is performed by using Gamma Ray Log. Gamma ray is the most reliable for sequence stratigraphic analysis and used to presume depositional environment by increasing or decreasing clay content (Emery and Myers, 2009). Due to presence of heavy minerals in sandstone certain limitations are associated with Gamma Ray Log but with the aid of Spectral Gamma Ray, the limitations can be overcome. The trends in well log relates to different depositional trends and sedimentary infill patterns (Emery and Myers, 2009). The general illustration of typical log trends is shown in Figure 3.7. The cleaning upward trend represents the upward decrease in clay content with increasing sand. The cleaning upward or coarsening upward sequence in Gamma Ray Log interpreted as barrier bar, beach sand, crevasse splay, mouth bar and deep sea fan deposits (Mondol, 2015). The dirtying upward trend shows increase in clay content and indicate decrease in depositional energy (Emery and Myers, 2009). The upward finning represent meandering or tidal channel deposits whereas in shallow marine environment reflects decrease in depositional energy with increase water depth (Emery and Myers, 2009). The boxcar trend or cylindrical trend show uniform deposition. The irregular trends show

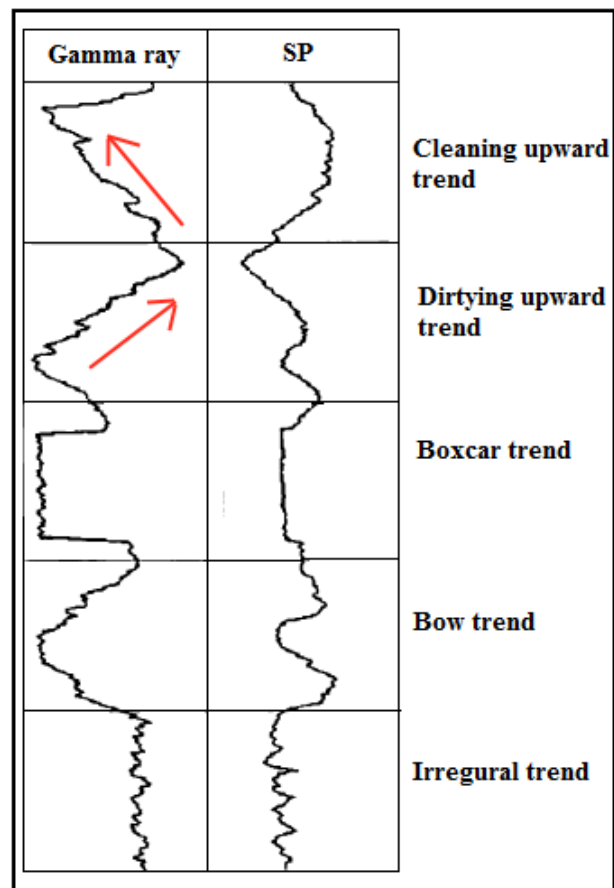


Figure 3.7: Generalized illustration of the log trends. The figure is adapted and modified from Emery and Myres, (2009).

aggradation of shaly or silty lithology and represent muddy alluvial overbank facies, shelf or deep water settings, or lacustrine settings (Emery and Myers, 2009).

3.4 Compaction Study

The compaction rock properties of sedimentary rocks vary significantly with change in rock composition, (e.g. mineralogy, sorting, size and shape), temperature and burial history. The different mineralogy, grain size, grain sorting, grain shape behave differently to varying compactional process (Storvoll et al., 2005). In basin modelling the compaction of sediments is critical since it greatly affect the density and velocity with increase in burial depth for different lithology's (Bjørlykke et al., 2009). The compaction of sedimentary rock is driven by two types of process such as mechanical compaction and chemical compactions.

3.4.1 Mechanical Compaction

The compaction of the sedimentary rock driven by vertical effective stress due to overburden weight of the rocks with depth is called mechanical compaction. Various factors essentially mineralogy, grain size, grain shape, sorting influence mechanical compaction of siliciclastic rocks. The mechanical compaction involves only physical change beyond any chemical changes in mineralogy. During mechanical compaction the bulk volume reduction of siliciclastic rock corresponding to porosity loss because solid remain constant (Bjørlykke, 2010). The most effective porosity reduction process in quartzose sandstone is mechanical compaction (Marcussen et al., 2010). Clays and muds being more porous at the time of deposition are affected significantly by mechanical compaction than other sediments (Mondol et al., 2007). The mechanical compaction started from shallow depth within few meters of burial depth but in case of carbonate it is different because the carbonate cementation is effective from shallow depth. Depending on geothermal gradient the mechanical compaction influence in the shallow part of basin up to 2-4 km depth (80-100°C) (Mondol et al., 2007).

Besides rock composition, grain size, shape and sorting, pore-fluid pressure is another factor that is required to consider in mechanical compaction mechanism. The part of the overburden stress is sustained by pore (fluid) pressure (U) (Chuhan et al., 2002). The mechanical compaction is driven by effective vertical stress which is difference of total vertical stress and pore pressure, by the reason the total overburden weight is carried by mineral grain framework and the pore pressure (Eq 3.14 and Figure 3.8) (Bjørlykke et al., 2010; Chuhan et al., 2002).

$$\sigma'_v = \sigma_v - u \dots\dots\dots (3. 14)$$

σ' = Effective vertical stress

σ_v = Total vertical stress

u = Pore pressure

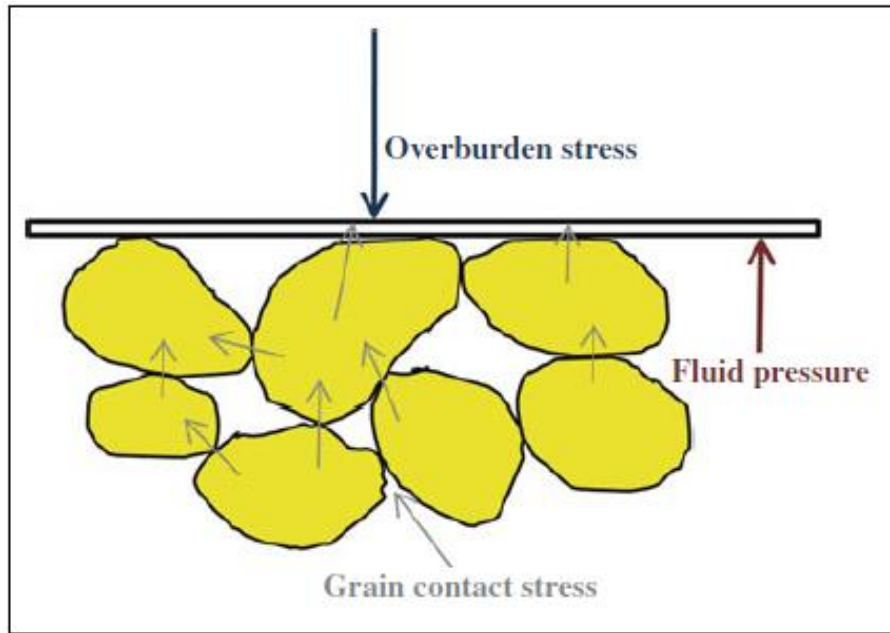


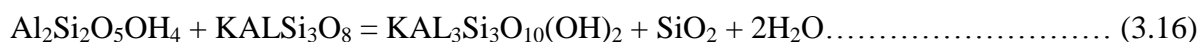
Figure 3.8: An illustration of the overburden stress carried by solid phase mineral grain framework on grain to grain contact and by pore pressure. The figure is adapted from Bjørlykke et al. (2010).

3.4.2 Chemical Compaction

The chemical compaction is driven thermodynamically; less stable minerals undergo dissolution leads to precipitation of new stable minerals which act as source of mineral cement for siliciclastic rocks. The silicate reaction are excessively slow and temperature play an important role (Bjørlykke and Jahren, 2010). The mineralogy, time, temperature and burial depth are important for chemical compaction. The major lithologies in sedimentary basins are shales, sandstone and carbonates and each lithology has a different compaction curve as a function of burial depth (Bjørlykke, 2010). After transition to chemical compaction depth and temperature, the mechanical compaction has no more influence because the initial cement precipitation strengthened the grain framework. In deeply buried sandstone quartz cement is one of the major porosity decline factor (Chuhan et al., 2002). In normally compacted basin the chemical compaction starts at about 2 km burial depth (60-80°C) with normal geothermal gradient (30°C/km) but in cold sedimentary basin it may not start before 4-6 km burial depth (Bjørlykke and Jahren, 2010). The carbonate mineral like aragonite and gypsum are different and can cause dissolution and precipitation shortly after burial at very low temperature (Storvoll et al., 2005). The continuous burial maintain quartz cementation until all the porosity loss and after exposure to 200-300°C the sandstone become well cemented quartzite (Bjørlykke and Jahren, 2010).

There are different sources for quartz cement in siliciclastic rock at different temperature with burial depth. The most common quartz cement sources are formation of amorphous silica due to conversion from Opal A to Opal CT, smectite dissolution (70-80°C), kaolinite dissolution (100-120°C) and dissolution along stylolite (Bjørlykke and Jahren, 2010). Smectite dissolution with precipitation of quartz and illite cause sharp rise in seismic velocity (Bjørlykke and Jahren, 2010). During uplift the chemical compaction in siliceous rock remain effective as long as the temperature is more than 70-80°C (Bjørlykke, 2010). The Equation

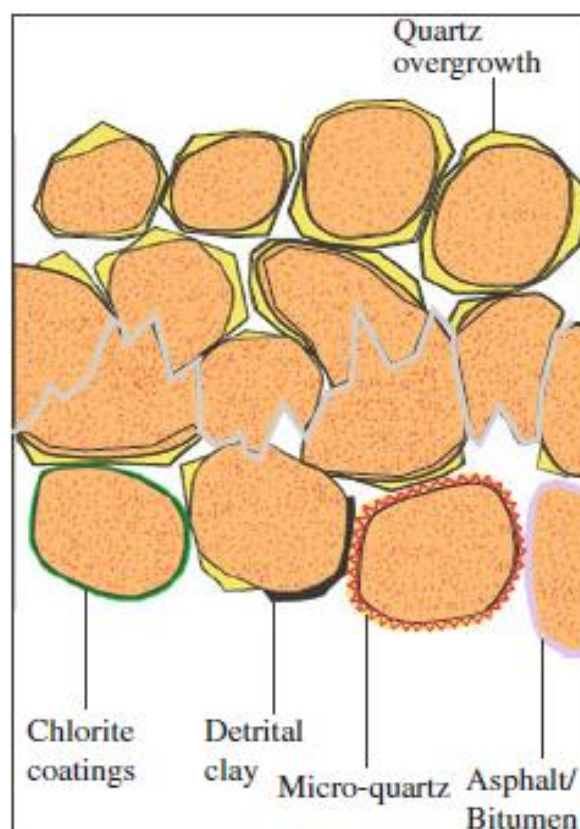
3.15 for smectite to illite transformation and Equation 3.16 for formation of the quartz from kaolinite are described in Bjørlykke, (2010).



3.4.3 Porosity preservation

During shallow depth the porosity loss is function of mechanical compaction due to rearrangement, crushing of mineral grains but at deeper burial depth the quartz cementation cause porosity loss. The fine grained, well sorted sand preserve more porosity because the grain crushing is limited and more grain to grain contact influence the vertical effective stress. The coarse grained poorly sorted sand preserve less porosity due to grain crushing and rearrangement.

Sandstone buried to deeper depth will not preserve enough porosity if the conditions are favourable for quartz cementation. The quartz cementation is absolutely dependent on temperature, time the surface area available (Bjørlykke and Jahren, 2010; Chuhan et al., 2002). Initially quartz cementation assists porosity preservation by strengthening mineral grain framework and ceases the response of the vertical effective stress. The precipitation of micro-quartz coating along mineral grain decrease the surface area along pore space and hinder the quartz precipitation until the solution is getting supersaturated. The surface coating of sand grain with other minerals (petroleum or bitumen, quartz overgrowth, chlorite iron oxide, illite, micro quartz, detrital clay) hinder quartz cementation (Figure 3.9) (Bjørlykke and Jahren, 2010). Chuhan et al. (2002) suggested that the delay in quartz cementation due to grain coating leads to grain fracturing due to vertical stress.



3.4.4 Transition Zone

In basin modelling the starting point of the chemical compaction of siliciclastic rock refers to transition zone and depends on geothermal gradient of basin (Figure 3.10). Depending on geo-thermal gradient, the depth of transition zone varies from basin to basin. After transition zone the initial quartz cement strengthens the grain framework and mechanical compaction will no more effective. The effect of the cementation is completely temperature dependent and immediately starts when temperature reaches to 60-80 °C as it is the lower threshold for activation of the quartz cementation. After meeting transition zone sharp increase appear in velocity. During basin inversion and uplift the quartz cementation

Figure 3.9: The porosity preservation mechanism in chemical compaction regime due to grains coating. The figure is adapted from Bjørlykke and Jahren, (2010).

will continue with slower rate until temperature is higher than 70-80°C (Bjørlykke and Jahren, 2010). The presence of salt in sedimentary basin lower the geothermal gradient because salt is good conductor of heat and transition zone appear at greater depth. The continuous effect of mechanical compaction (due to lack of quartz cement because of low geothermal gradient) results considerable grain crushing and grain fracturing.

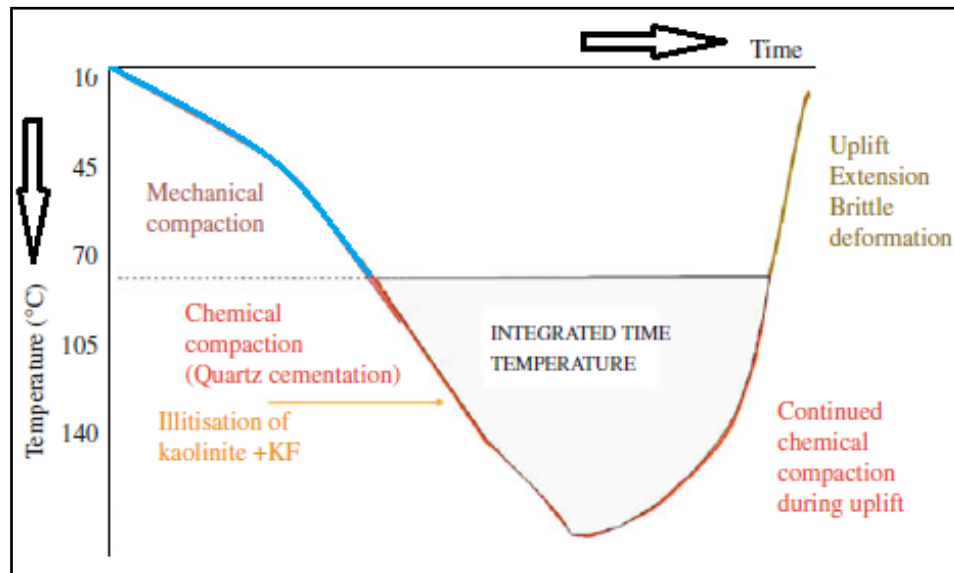


Figure 3.10: Compaction and burial diagenesis as a function of time and temperature. The figure is adapted from Bjørlykke and Jahren, (2010).

3.4.5 Present day temperature/Temperature gradient

The estimation of geothermal gradient is important to predict the transition zone between mechanical and chemical compactions. Temperature log is a tool for measuring borehole temperature (bottom hole temperature, BHT) (Mondol, 2015). The database used to conduct current study lack the temperature log data, therefore Equation 3.17 used to calculate the geothermal gradient of the study area. The Equation 3.17 is adapted from Mondol, (2015). The bottom hole temperature is adapted from NPD (2016).

$$\text{Geothermal Gradient} = \left(\frac{BHT - T_{ms}}{TD} \right) \times 100 \dots \dots \dots (3.17)$$

where, BHT – Bottom hole temperature,

TD – total depth,

T_{ms} – mean surface temperature

3.4.6 Comparison with published trends

The sonic transit time and density are sensitive to various diagenetic processes that results the compaction of rocks in a sedimentary basin. In present study the velocity-depth and density-depth trends are utilized to understand the compaction trend of the study area. As explained earlier mechanical compaction is stress dependent while chemical compaction relies on mineral dissolution and precipitation as a function of temperature and time. The mechanical

compaction and its effect on rock properties with different lithology, grain size and composition are well studied and documented by several authors (Chuhan et al., 2002, 2003; Marcussen et al., 2010; Mondol, 2009; Mondol et al., 2008a; Mondol et al., 2007). These studies are performed by using laboratory data set and only for mechanical compaction. The quartz cementation is main component of chemical compaction process; extremely temperature dependent and significantly slow process; therefore it cannot be studied by laboratory experimental technique. In this study the reference curves from Mondol et al. (2007), Mondol, (2009) and Marcussen et al. (2010) are used for comparison with data from study area (Figure 3.11).

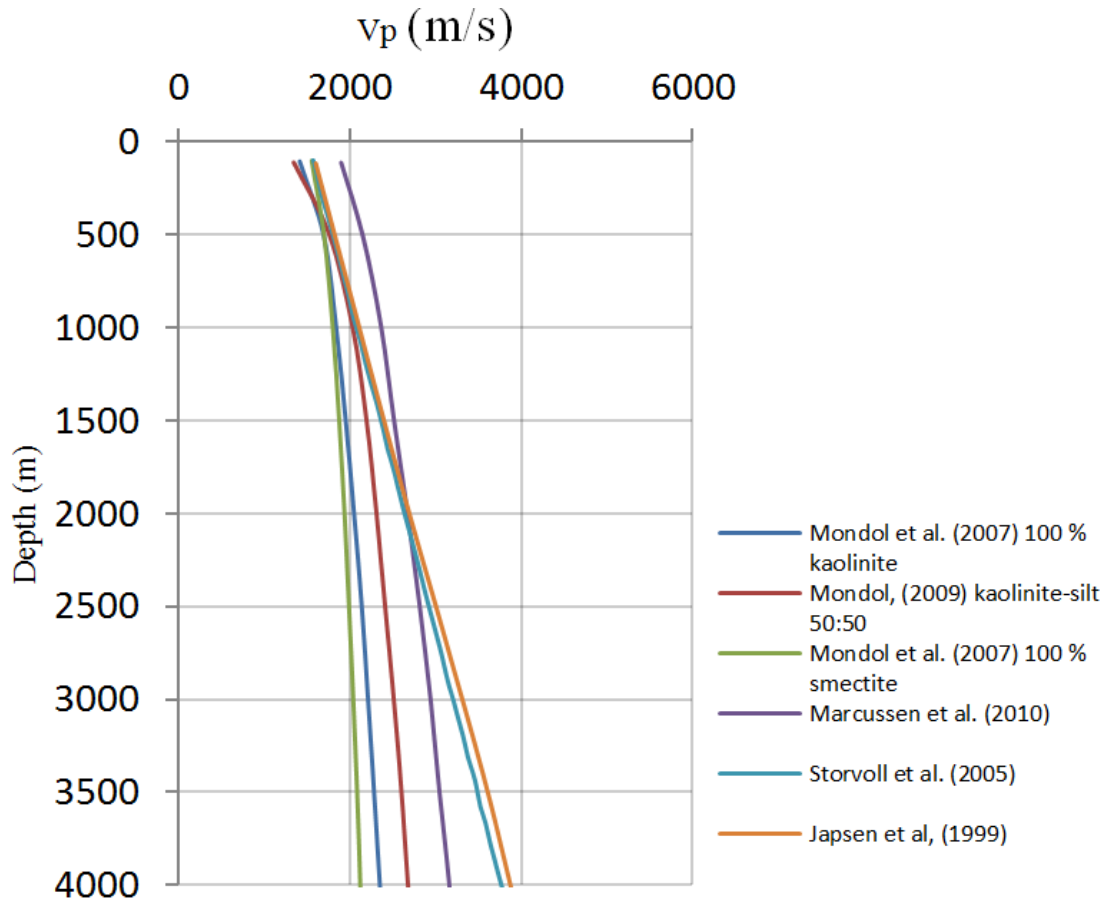


Figure 3.11: Published velocity-depth trends from literature.

The published curves from Mondol et al. (2007), Mondol, (2009) are generated by experimental compaction of the brine-saturated pure smectite clay (100% smectite), pure kaolinite clay (100% kaolinite) and kaolinite-silt (50:50) under vertical effective stress of 50 MPa. Under vertical effective stress, the ultrasonic device used to measure sonic velocity at different stress level. Mondol et al. (2007) and Mondol, (2009) suggested that the physical properties of mudstones vary significantly with different vertical effective stress, clay mineralogy and fluid content.

Marcussen et al. (2010) studied the sandstone lithology of the Etive Formation from 20 wells in northern North Sea. The velocity-depth trend is generated by experimental compaction of Etive sand. Marcussen et al. (2010) concluded that at shallow depth in mechanical compaction zone the experimental compaction trend show good agreement with natural compaction trend of the Etive sand formation.

The reference curves (Figure 3.11) are useful for interpretation of the compaction of sediments in mechanical compaction zone only. Furthermore, the curves can also be utilized in detection of overpressure zone and to estimate uplift.

3.4.7 Exhumation Estimation

The subsidence and uplift of the reservoir arise due to the tectonic and geologic evolution of the sedimentary basin. The reservoir properties are affected significantly during burial and uplift because the diagenetic processes of the siliciclastic rocks are extremely depth, temperature and time dependent. In reservoir evaluation the correction for uplift is crucial for better understanding of the reservoir properties in exploration prospective. In this study a simplistic approach used to estimate the maximum burial depth experienced by the reservoir rock. The experimental reference curves for Vp-depth data from published literature are used in uplift estimation. The Vp-depth (BSF depth) from studied wells plotted and compared with different experimental reference curves. The trend of Vp-depth of the study area in mechanical compaction zone assumed to match with one of the reference curves. Any mismatch (or high velocity) from reference curve in mechanical compaction zone may reveal upliftment in the area. The depth addition to compensate the mismatch between log derived data and reference curve gives the amount of upliftment. The shale data points ($V_{sh} \geq 0.75$) are used for this purpose.

The mechanical compaction is function of vertical effective stress with grain size, shape, sorting and mineralogy. The experimental reference curves are generated for different mineral composition. The well-known reference curve kaolinite-silt (50:50) suggested by Mondol, (2009) is very close to mineralogical composition of the mudrocks therefore the kaolinite-silt (50:50) is used in exhumation studies.

3.4.8 Uncertainties in exhumation studies

Several uncertainties are associated with exhumation studies by using such simplistic technique.

- In general velocity increase with depth and greatly depends on the grains sorting, shape, size and mineralogy in MC zone. The mineralogy and sediments architecture precisely depends on the depositional environment and basin history. The published curves are generated by performing experiments with different mineralogy and laboratory conditions.
- The comparison of the log derived data trend to the reference curve based on interpreter own observation and experience.
- The interpreter knowledge about the study area and tectonic evolution are also critical because the uplift is precisely affected by the tectonic and geologic evolution of the basin.
- The sedimentary basin not only includes sand and shales lithology. Other lithologies as carbonates and evaporates are also present and it is difficult to discriminate the other lithologies by using only standard derived trend. The presence of carbonate sequence can leads to misinterpretation of the transition zone and mechanical compaction regime.

3.5 Rock Physics Diagnostics

This part of the study focuses on rock physics cross-plotting technique called ‘‘Rock Physics Templates or Rock Physics Models’’ to characterize the reservoir and to achieve better image of reservoir. Rock physics models are key to construct link between geological parameters (porosity, lithology, saturation, shale content) and the seismic parameters (e.g., AI , V_p , V_s , and elastic moduli) (Avseth et al., 2009; Avseth et al., 2010; Chi and Han, 2009). The seismic parameters are sensitive to lithology and pore-fluid. The understanding of the variation in seismic/elastic parameters with change in geological parameters (lithology, porosity, cementation etc.) leads to generation of the rock physics model. Different rock physics models have been developed but all models contain some assumptions to simplify the physical appearance of the rock (Dr  ge, 2011). Rock physics models can either be used to interpret seismic parameters in term of reservoir parameters or/and to predict seismic properties from observed reservoir parameters (Avseth et al., 2009). For quantitative interpretation of the seismic data rock physics is the essential part (Avseth and Odegaard, 2004).

3.5.1 V_s Estimation

The shear wave velocity (V_s) has significant importance in rock physics study because of sensitivity of the V_s to lithology, fluid type and pore pressure. In most cases the V_s is not acquired during wireline logging. In this study, the database contains 20 well log data, acquired before 1990s and do not contain measured V_s from wireline logging. Only the well 34/7-27 contains acquired V_s for a small section (Table 3.1). The V_p and V_s are cross-plotted from well 34/7-27 (Figure 3.12). The concern here is to get a linear relation between V_p and V_s that can be used to estimate V_s in rest of wells to accomplish the interpretation.

The V_s is sensitive to fluids saturated rocks therefore to avoid the effect of hydrocarbon on velocity only the water saturated data points are included. In Figure 3.12 few data points marked in circle are scattered away from the data trend and show high V_p . With further analysis it has been observed that the high V_p data points are from thin carbonate intervals (Figure 3.13). It is difficult to avoid carbonate intervals from just only from petrophysical analysis.

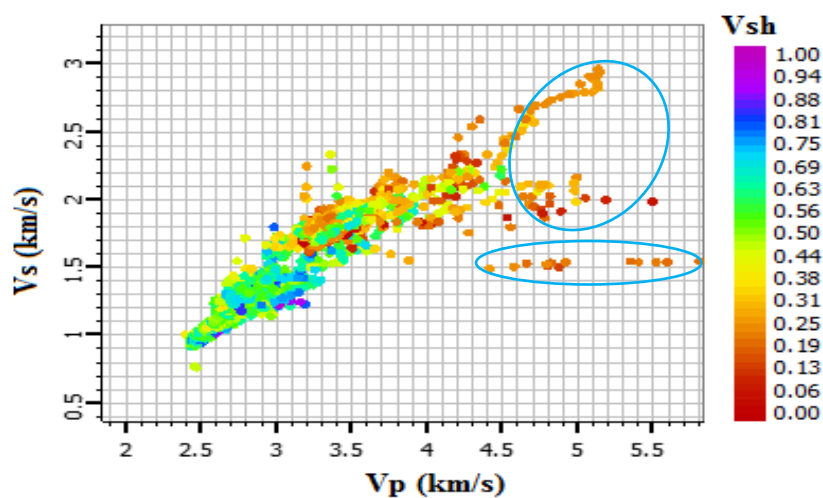


Figure 3.12: The V_p versus V_s crossplot of well 34/7-27. The high velocity data marked by light blue ellipses are carbonate intervals.

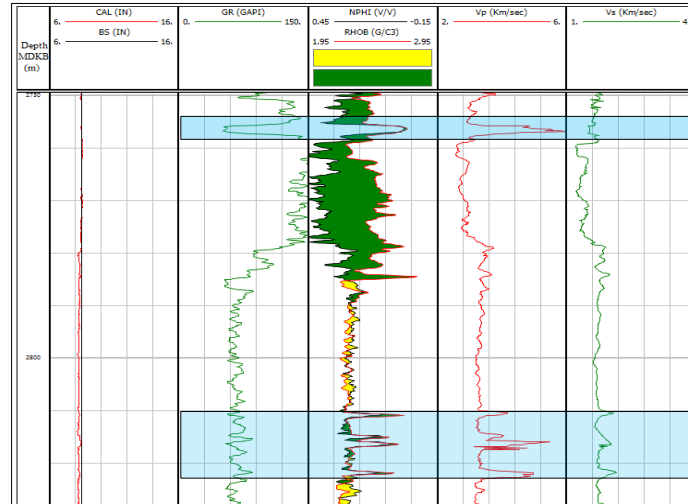


Figure 3.13: The log section from well 34/7-27. The high velocity carbonate intervals discussed in text are marked with light blue shading.

In order to find a linear relation of the V_p and V_s , the high velocity carbonate intervals are excluded by filtering the data with V_p . In Rider and Kennedy, (2011) the typical value of V_p for limestone is given 3.9-5.6 km/s. The following value is adapted and thin beds with V_p higher than 4 km/s are assumed as carbonate or carbonate cemented bed and excluded. Additionally the effect of the shales is taken into consideration by using two scenarios: (i) $V_{sh} \leq 0.5$; and (ii) $V_{sh} > 0.5$ (Figure 3.14). The results of regression relation for both scenarios are given in Table 3.6.

Table 3.6: V_p - V_s linear relations for two scenarios obtained from regression.

V_p - V_s relation (km/s)	Description
$V_s = 0.8857 \times V_p - 1.1874$	$V_{sh} \leq 0.5, S_w = 1$
$V_s = 0.8117 \times V_p - 0.9802$	$V_{sh} > 0.5, S_w = 1$

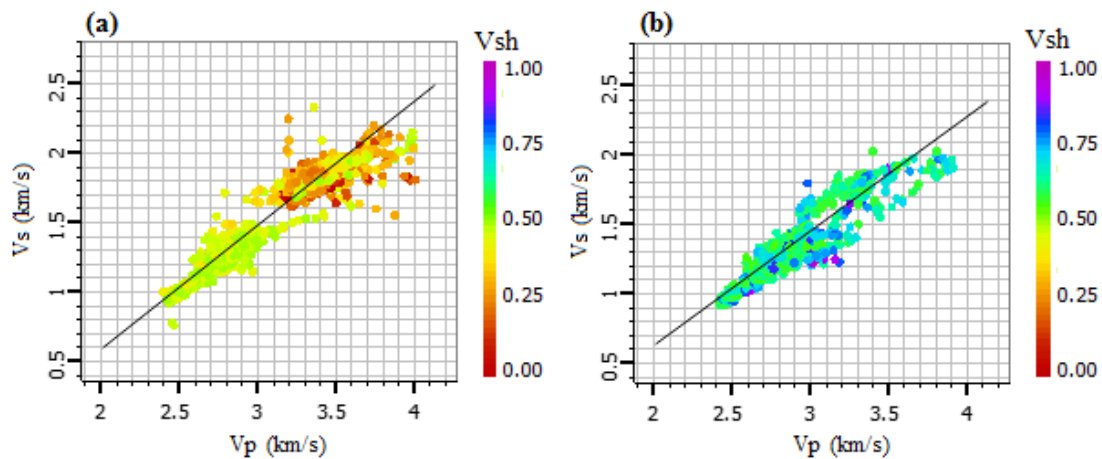


Figure 3.14: The V_p - V_s cross plot from well 34/7-27; (a) $V_{sh} \leq 0.5$, and (b) $V_{sh} > 0.5$.

The V_s estimation is challenging step in rock physics study. The unavailability of the shear wave data is common because of cost saving purpose or any other reason. Due to availability of the compressional wave data an alternate approach can be used to predict shear wave velocity (Greenberg and Castagna, 1992). Various workers suggested linear relation between V_p and V_s for different lithology by using different experimental data sets (Castagna, 1993; Castagna et al., 1985; Han et al., 1986; Krief et al., 1990; Mavko et al., 1998; Williams, 1990). The approach is applicable because same factors affect compressional and shear wave velocity in a similar way (Greenberg and Castagna, 1992).

The various empirical relations to predict shear wave velocity by using compressional wave velocity are shown in Table 3.7 and Figure 3.15. The empirical relations are given for different lithologies and conditions. The empirical relations for V_s prediction are derived for brine saturated (wet) sediments (Dvorkin, 2007).

Table 3.7: The published empirical relations for V_s estimation from V_p .

Author(s)	Description	Equation
Castagna et al. (1985)	Mudrock equation	$V_s = 0.862 \times V_p - 1.172$
Castagna, (1993)	Clastic rocks	$V_s = 0.804 \times V_p - 0.856$
Han et al. (1986)	Clay less than 0.25	$V_s = 0.754 \times V_p - 0.657$
Han et al. (1986)	Clay greater than 0.25	$V_s = 0.842 \times V_p - 1.099$
Krief et al. (1990)	Wet sand	$V_s = \sqrt{V_p^2 \times 0.4518 - 1.742}$
Mavko et al. (1998)	Unconsolidated sand	$V_s = 0.79 \times V_p - 0.79$
Williams, (1990)	Sand	$V_s = 0.846 \times V_p - 1.088$
Williams, (1990)	Shales	$V_s = 0.784 \times V_p - 0.839$

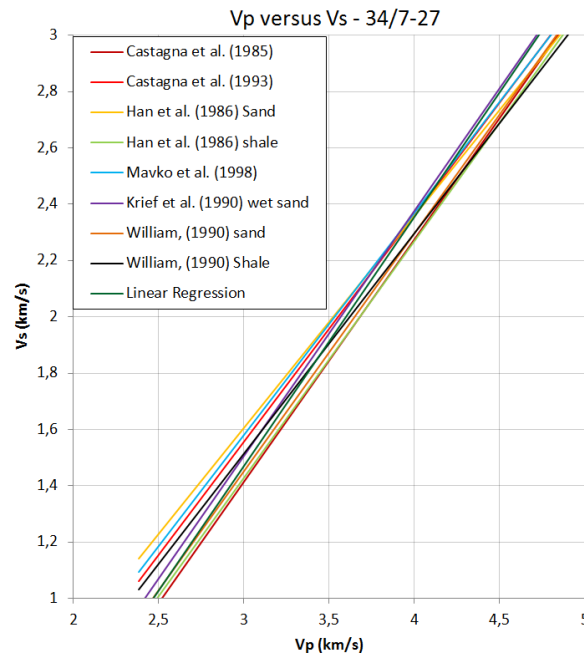


Figure 3.15: The linear V_p versus V_s trends of well 34/7-27. The V_s is estimated with linear equations from literature.

The published empirical relations are derived for certain data set and only applicable to rock from which they derived. The better approach is to use empirical relation from area being studied. The directly measured V_s from well 34/7-27 is compared with V_s calculated from empirical relations discussed above. The purpose of comparison is to find the best fit of the V_s from empirical equation to the directly measured V_s . The comparison is performed for both sand and shale cases. The close agreement between data and empirical relations from literature is observed in cross plot (Figure 3.16).

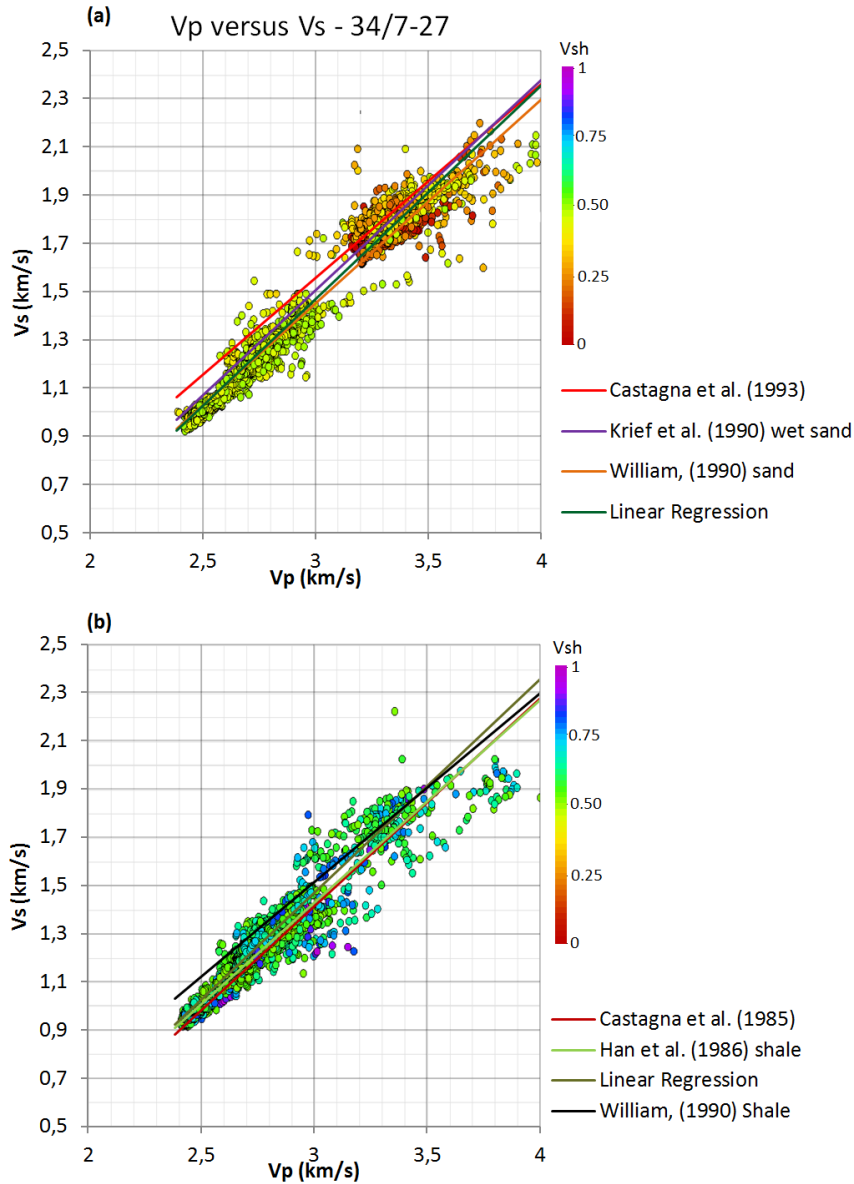


Figure 3.16: The V_p versus V_s crossplot overlaid by linear trend from literature data. The data is plotted from well 34/7-27 and categorized with shale volume as; (a) $V_{sh} \leq 0.5$; (b) $V_{sh} \geq 0.5$.

Limitations and Uncertainty in V_s Estimation

The shear wave velocity acquired during wireline logging is most reliable for rock physics interpretation. Unavailability of the V_s evolve lot of uncertainties, if the V_s is required for

rock physics approach to discriminate fluids, lithology. Following are the uncertainties of estimated V_s in this study.

- The linear regression of the V_p and V_s for brine saturated sand intervals is acquired from crossplot of V_p - V_s from well 34/7-27. The well 34/7-27 with directly measured V_s does not contain target reservoir of Lunde and Statfjord Formations.
- Alternative approach is to estimate V_s by using the empirical relations from published literature (see section 3.5.1). The empirical relations are suggested after performing set of experiments with different sediments and lithology. The type of the sediments, conditions and precautions utilized during experiment are not completely identical to natural rock/sediments which evolve uncertainty for estimated V_s from empirical relations.
- The uncertainty in V_s estimation arise uncertainty in other parameters such as bulk modulus, shear modulus, V_p/V_s ratio, shear impedance (I_s). Besides uncertainties the results shown and discussed in the chapter 6 are useful and comparable with published literature.
- In order to minimize uncertainty of the V_s estimated by using empirical relation, V_s is calculated by using linear regression from well 34/7-27 (discussed in section 3.5.1) and compared with V_s estimated from empirical relations (Figure 3.15).

3.5.2 Relationship between P and S – wave velocities

The ratio of compressional wave to shear wave velocity (V_p/V_s) is of significant importance for formation evaluation (Castagna et al., 1985). The experimental study by Pickett, (1963) introduced the use of the compressional to shear wave velocity plot for identification of different lithologies. In this study due to absence of shear sonic log the V_p - V_s cross-plot is may not reliable because shear wave velocity is calculated by using linear relation (explained earlier in section 3.5.1).

3.5.3 Relationship between velocity, porosity and clay

Porosity is the most influential reservoir parameter in hydrocarbon exploration and affected by several diagenetic process due to reservoir burial history. The introduction of the cement to sandstone during diagenesis increase velocity. The steep porosity-velocity trend observed due to variation in porosity by diagenetic processes while the trend is much flatter if porosity change is resulting from variation in clay content and sorting (Avseth et al., 2010).

The porosity affected by addition of clay content to sandstone is studied by Han et al. (1986) and presented model for varying clay content (Figure 3.17). The Han et al. (1986) model lines for consolidated sandstone are used in this study to observe the effect on porosity and velocity with varying clay content. The linear equations suggested by Han et al. (1986) are shown in Table 3.8 for different effective pressure.

The theory of Marion et al. (1992) is also applied to see the effect of clays on velocity and porosity. The theory from Marion et al. (1992) fits well with petrophysical analysis and the clay content interpretation.

Table 3.8: The empirical relations for velocity for different clay content suggested by Han et al. (1986); ϕ – porosity and C – clay content. The velocity is in km/s.

Effective Pressure	Equation
20 MPa	$V_p = 5.49 - 6.94 \phi - 2.17C$
	$V_s = 3.39 - 4.73 \phi - 1.18C$
30 MPa	$V_p = 5.55 - 6.96 \phi - 2.18C$
	$V_s = 3.47 - 4.48 \phi - 1.87C$
40MPa	$V_p = 5.59 - 6.93 \phi - 2.18C$
	$V_s = 3.52 - 4.91 \phi - 1.89C$

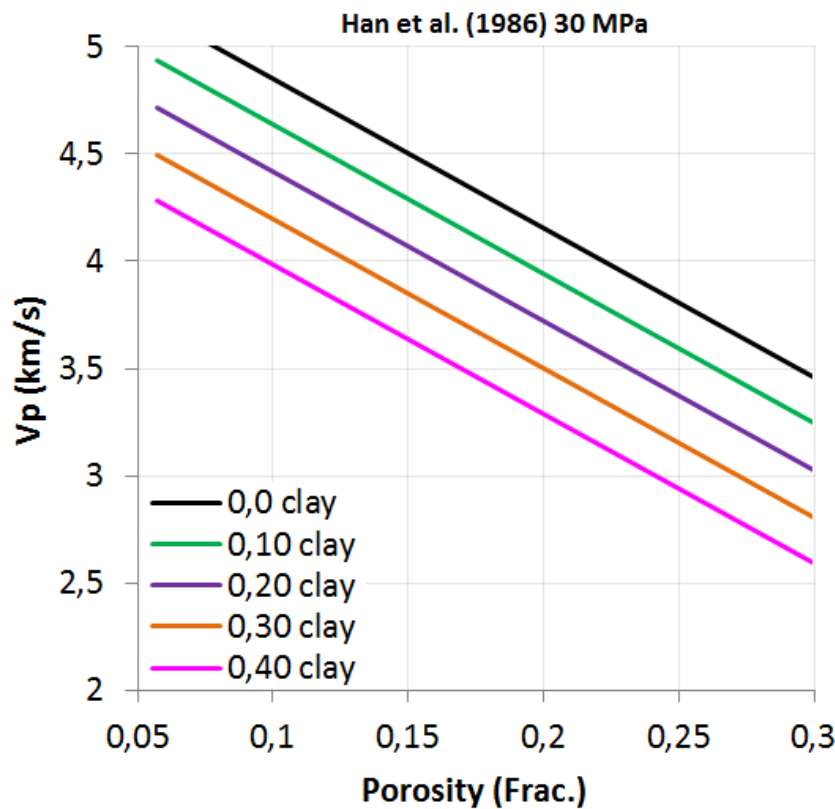


Figure 3.17: The Han et al. (1986) models for varying clay percentage in sandstones at 30 MPa effective pressure.

3.5.4 Rock physics diagnostics

Dvorkin and Nur, (1996), introduced rock physics diagnostic technique to understand rock microstructure from velocity-porosity relations. The effective-medium theoretical models are generated in rock physics diagnostic technique. The adjusting of data trend to theoretical curve assuming the microstructure of sediments is similar to that used in the model (Avseth et al., 2005).

3.5.5 Rock physics effective medium models

By knowing the mineralogical composition, elastic moduli of mineral constituent and porosity, only the upper and lower bound of the seismic velocities can be predicted. For better prediction of the seismic velocities the geometric details of mineral grains arrangement relative to each other must be known. Several models exist to predict rock microstructure from velocity-porosity relations.

Dvorkin and Nur, (1996), analysed data for two high porosity sands from North Sea and introduced theoretical models called Unconsolidated/Friable-sand model and Contact Cement model. Avseth et al. (2000) introduced constant cement model by analysing another data set of the North Sea. The constant cement model is mathematically combination of the contact cement model and friable sand model (Avseth et al., 2000). The cross-plot (Figure 3.18) with local validation of the model can estimate the amount of cement and degree of sorting (Avseth et al., 2009).

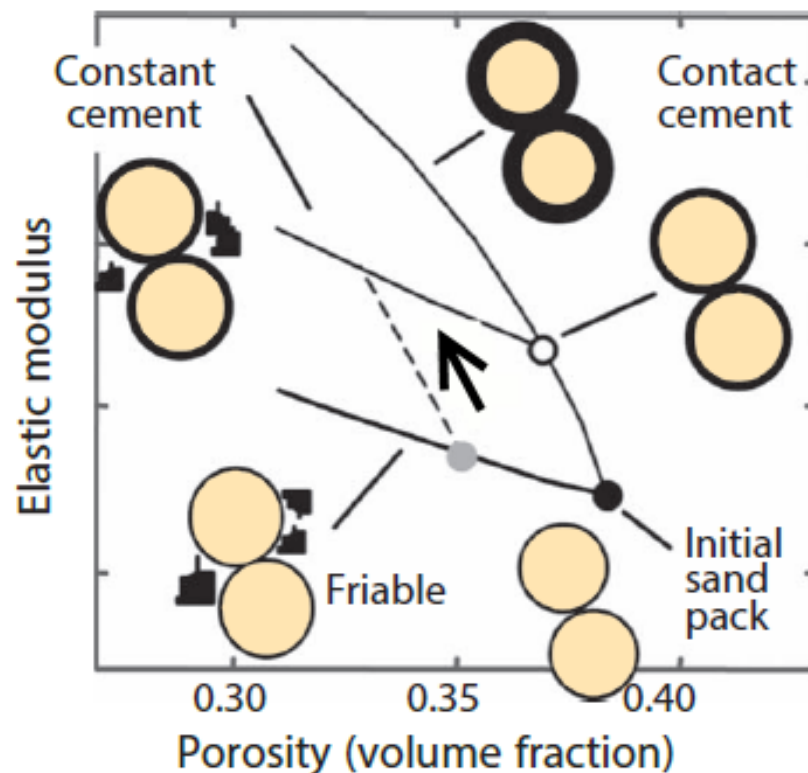


Figure 3.18: Schematic illustration of the effective medium models. The figure is adapted and modified from Avseth et al. (2005).

Friable-sand Model

Dvorkin and Nur, (1996) describe how the velocity and porosity change as a function of degree of sorting (Avseth et al., 2005; Avseth et al., 2010). The sands without contact cement are held together by confining pressure and mechanically unstable (Dvorkin and Nur, 1996).

The two end members are used for friable sand model. One end member is defined as well sorted identical sand grains with critical porosity. The other end member in friable-sand model is at zero porosity and has bulk (K) and shear (μ) moduli of the mineral grain. The

elastic moduli of dry high-porosity end member is computed by using Hertz-Mindlin theory (Mindlin, 1949). The equations are presented below:

$$K_{HM} = \left[\frac{n^2(1-\phi_c)^2\mu^2}{18\pi^2(1-\nu)^2} P \right]^{\frac{1}{3}} \dots\dots\dots (3.18)$$

$$\mu_{HM} = \frac{5-4\nu}{5(2-\nu)} \left[\frac{3n^2(1-\phi_c)^2\mu^2}{2\pi^2(1-\nu)^2} P \right]^{\frac{1}{3}} \dots\dots\dots (3.19)$$

where, K_{HM} – dry rock bulk modulus; μ_{HM} – dry rock shear modulus; ϕ_c – critical porosity; n – coordination number (number of contacts per grain); μ – shear modulus of solid phase; ν – Poisson's ratio of the solid phase; and P is the effective pressure.

The critical porosity is the highest possible porosity of sedimentary rock at the time of deposition. The well sorted end member typically contain critical porosity (ϕ_c) around 40 %, and coordination number can be approximated by following Equation 3.20 (Avseth et al., 2005).

$$n = 20 - 34\phi + 14\phi^2 \dots\dots\dots (3.20)$$

The elastic moduli of sand with varying degree of sorting and porosities between 0 and critical porosity (ϕ_c) can be calculated by using Hashin and Shtrikman, (1963) bound by following equations:

$$K_{dry} = \left[\frac{\frac{\phi}{\phi_c}}{K_{HM} + \frac{4\mu_{HM}}{3}} + \frac{1 - \frac{\phi}{\phi_c}}{K + \frac{4\mu_{HM}}{3}} \right]^{-1} - \frac{4}{3}\mu_{HM} \dots\dots\dots (3.21)$$

$$\mu_{dry} = \left[\frac{\frac{\phi}{\phi_c}}{\mu_{HM} + Z} + \frac{1 - \frac{\phi}{\phi_c}}{\mu + Z} \right]^{-1} - Z \dots\dots\dots (3.22)$$

where,

$$Z = \frac{\mu_{HM}}{6} \left(\frac{9K_{HM} + 8\mu_{HM}}{K_{HM} + 2\mu_{HM}} \right) \dots\dots\dots (3.23)$$

After computing the dry bulk modulus and shear modulus fluid substitution is required to perform for saturated rocks. The Gassmann's fluid substitution equation can be used to compute the elastic moduli of saturated rock (Equations 3.24 and 3.25).

$$K_{sat} = K^* + \frac{\left(1 - \frac{K^*}{K_s}\right)^2}{\frac{\phi}{K_{fl}} + \frac{1-\phi}{K_s} - \frac{K^*}{K_{s2}}} \dots\dots\dots (3.24)$$

$$\mu^* = \mu_d \dots\dots\dots (3.25)$$

where, K_{sat} – bulk modulus of saturated rock; K^* – dry rock framework bulk modulus; K_s – bulk modulus of the mineral matrix; K_{fl} – fluid bulk modulus; ϕ – porosity; μ^* – effective shear modulus of the fluid saturated rock; μ – shear modulus of dry rock.

The V_p and V_s can be calculated by using following equation:

$$V_p = \sqrt{\frac{K + \frac{4}{3}\mu}{\rho}} \dots\dots\dots (3.26)$$

$$V_s = \sqrt{\frac{\mu}{\rho}} \dots\dots\dots (3.27)$$

Contact cement model

Dvorkin and Nur, (1996), explain the high seismic velocity in high porosity sand. The initial cement on grains contact strengthens the whole grain framework and minimizes the effective stress driven compaction. The initial cement cause little decrease in porosity but the stiffening of the grain frame work results large increase in seismic velocity (Avseth et al., 2005). After grains contact cement the porosity reduction is purely function of cement precipitation. The sandstone is mechanically stable when cement grow at grains contact (Dvorkin and Nur, 1996).

Constant-cement Model

The constant cement model was introduced by Avseth et al. (2000) mathematically combination of the contact-cement model and friable-sand model (Avseth et al., 2005; Avseth et al., 2010). The model presume that sands with varying porosity have same amount of contact cement (Avseth et al., 2000; Avseth et al., 2010). The porosity reduction is only due to non-contact pore filling material (Avseth et al., 2005). The model is created by using contact cement model to compute velocity-porosity for well sorted sandstone with a given constant cement volume. The interpolation between two end members (high porosity and zero porosity end members) is obtained by using lower bond (Avseth et al., 2005).

The dotted curves in Figure 3.19 (upper) are friable sand model line generated for pure quartz sand at different effective pressure. The parameters used in generation of model are shown in Table 3.9. Moving to right in friable sand model lines correspond to cleaner and better sorted sand while moving to left correspond to more poorly sorted and clay rich sand (Avseth et al., 2005).

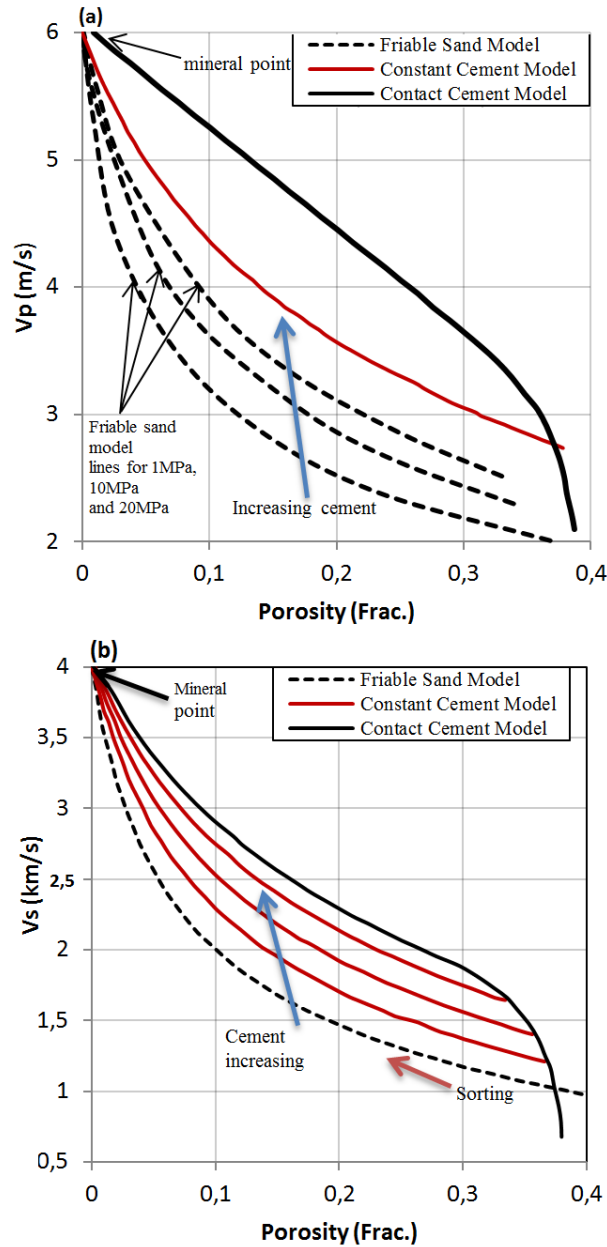


Figure 3.19: The effective medium models used in this study; (a) Friable sand model (black dotted lines) are produced for pure quartz sand at different effective pressure (1 MPa, 10 MPa & 20 MPa). Sediments of varying sorting will fall along black dotted line. The constant cement model line (red line, assuming 2 % quartz cement) is digitized from Avseth et al. (2005). The contact cement model line (continuous black line) is also digitized from Avseth et al. (2005). (b) The model lines are digitized from Avseth et al. (2010).

Elastic parameters used for model generation

In this study for the generation of the rock physics model/templates the elastic values of minerals are used from published literature and shown in Table 3.9. The elastic values are given in Mavko et al. (2009), but in this study, adapted from Hansen, (2016). The effective pressure is assumed from burial depth as 1MPa/100m.

Table 3.9: The elastic properties of minerals from published literature, adapted from Hansen, (2016).

Mineral	V _p (km/s)	V _s (km/s)	K (GPa) Bulk Modulus	μ (GPa) Shear Modulus	ρ (g/cm ³) Bulk density	ν Poisson's ratio
Quartz Carmichael, (1989)	6.05	4.09	37	44	2.65	0.08
Quartz with clay Han et al. (1986)	5.59	3.52	39	33	2.65	0.17
Clay Tosaya, (1982)	3.81	1.88	21.0	7.0	2.6	0.35

3.5.6 Estimation of cement volume

In siliciclastic rocks the effect of cementation increases with depth as a function of increasing temperature. The onset of cement starts after transition zone and then remains effective until temperature is greater than 60 °C. In terms of rock physical parameters the seismic velocity and density increase as a result of compaction and quartz cementation.

Marcussen et al. (2010), studied the effect of compaction and cementation on Eivie Formation sands from northern Viking Graben. The study suggested that at shallow depth the compaction is purely dependent on effective stress and experimental V_p-depth trend tie fully to trend from well log but at deeper depth deviation occur from experimental trend. The deviation is due to onset of quartz cementation which give rapid rise to seismic velocity after precipitation of small amount of cement. They found that increase in amount of quartz cement cause increase in P-wave velocity linearly with depth. The linear trend of increase in P-wave velocity and increasing quartz cementation can be used to guess approximately quartz cementation. The linear trend of velocity and quartz cement for Eivie Formation is digitized from Marcussen et al. (2010) and equation 3.28 is suggested to approximate quartz cement percentage:

$$V_p = 86.16 * Q + 2783 \dots\dots\dots (3.28)$$

where Q is quartz cement percentage and V_p is P-wave velocity (m/s).

3.5.7 Rock physics templates of V_p/V_s versus AI

The rock physics template was first introduced by Ødegaard and Avseth (2003). The template aids for identification of fluids and lithology from elastic inversion data. During elastic inversion of the seismic data, the typical output are V_p/V_s with AI and this is the main motivation for using rock physics template in V_p/V_s versus AI domain (Ødegaard and Avseth, 2003). The lithology and fluid content can be predicted by interpretation of the elastic properties inverted from seismic data along with rock physics template (Chi and Han, 2009).

The generation of the template involved three steps:

- Calculation of dry rock bulk modulus at critical porosity end member with pressure dependency by using Hertz-Mindlin theory. The other end member have zero porosity with bulk and shear moduli of mineral (Avseth et al., 2005).

- After calculation of dry rock bulk moduli for two end members, Hashin-Shtrikman bounds (upper or lower) is used for interpolation between two end members (Avseth et al., 2005).
- The obtained dry rock moduli will be used as input in Gassmann's equation to get moduli of brine saturated rock, which in turn use to find V_p and V_s .

During construction of rock physics template the geological factor of basin under study must be taken into consideration. Lithology, mineralogy, diagenetic cement, burial depth, pressure, temperature must be considered during generation of rock physics template (Avseth et al., 2005).

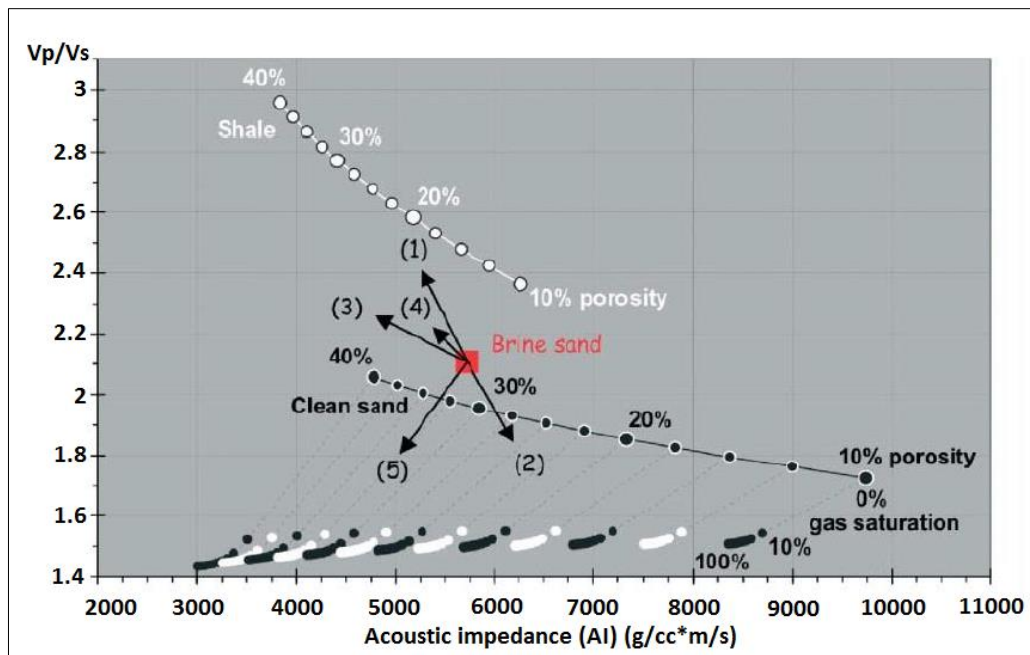


Figure 3.20: The conceptual rock physics template in term of V_p/V_s and AI . The template is modelled for well sorted, compacted arenite with effective pressure of 20 MPa. The arrows show various geologic trends; (1): increasing salinity, (2): increasing cement volume, (3): increasing porosity, (4): decreasing effective pressure and (5): increasing gas saturation. The figure is adapted from Ødegaard and Avseth, (2003).

The crossplot of V_p/V_s and AI superimposed with rock physics template allow us to discriminate various lithology and fluid content in reservoir. In crossplot shales show a different trend from sand and contain high V_p/V_s . The crossplot can be used to discriminate between hydrocarbon sand and brine sand. The conceptual rock physics template for V_p/V_s and AI crossplot is shown in Figure 3.20.

3.5.8 Lamda-rho versus Muo-rho

The Lamé parameters compressibility (λ) and shear rigidity (μ) are essential rock properties and easy to understand as compared to AI and velocities (Gray et al., 1999). The use of Lamé parameters for lithology identification and fluids discrimination was first introduced by

Goodway et al. (1997). The rock physics template used to discriminate lithology on the basis of LMR (Lamé parameters) is shown in Figure 3.21. In $\lambda\rho$ and $\mu\rho$ crossplot a good separation of gas sand from brine sand and shales can be detected (Goodway, 2001).

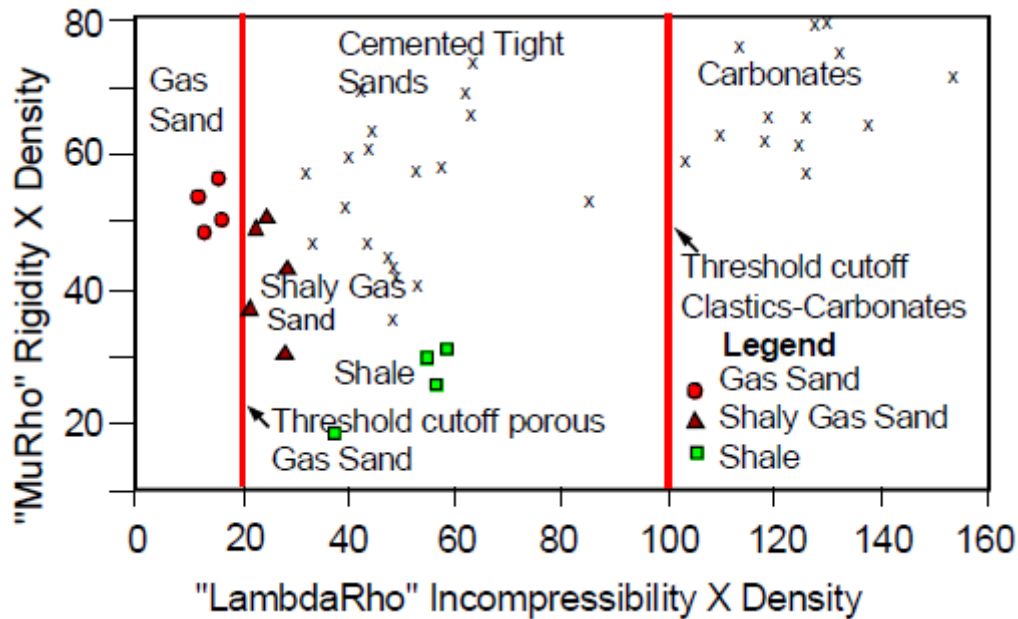


Figure 3.21: The LMR rock physics template for lithology discrimination and fluid identification. The figure is adapted from Goodway et al. (1997).

From the Lamé parameters for lithology identification the basic principle is the ratio between incompressibility and rigidity. In a case the material has incompressibility (λ) more than rigidity (μ), then anisotropic distribution of the stress deform shape and result large aspect ratio, this behaviour is usually found in shales, while in case where λ is equal to μ , the aspect ratio will be 1, this behaviour is identified in sand (Perez and Tonn, 2003). In case of fluid discrimination, the incompressibility (λ) for gas saturated rock is lower as related to brine saturated rock and the rock rigidity (μ) is comparatively unaffected (Dewar and Downton, 2002).

Chapter 4: Petrophysical analysis

Petrophysical analysis is one of the basic steps in evaluation and characterization of the reservoir rock. In this section results from the petrophysical analysis are presented.

4.1 Reservoir Rocks

4.1.1 Thickness and correlation of the reservoir rock

The thickness variation of the Lunde and Statfjord Formations across the Snorre field is observed by generating thickness contour maps (Figure 4.1 & Figure 4.2). The simple contour map is generated by using the formation top information given by NPD. Figure 4.1 shows the maximum thickness of the Lunde Formation in Snorre field is 1100-1150 m. All the wells drilled in Snorre field are not penetrated completely by Lunde Formation. Some wells are penetrated into top few meters of the Lunde Formation. The map could contain errors and uncertainties because only formation top information is not enough to measure thickness of certain horizon over a given area. The maximum thickness of the Statfjord Formation observed in Snorre field is 170 m (Figure 4.2). The Statfjord Formation is not encountered in north-eastern part of the field.

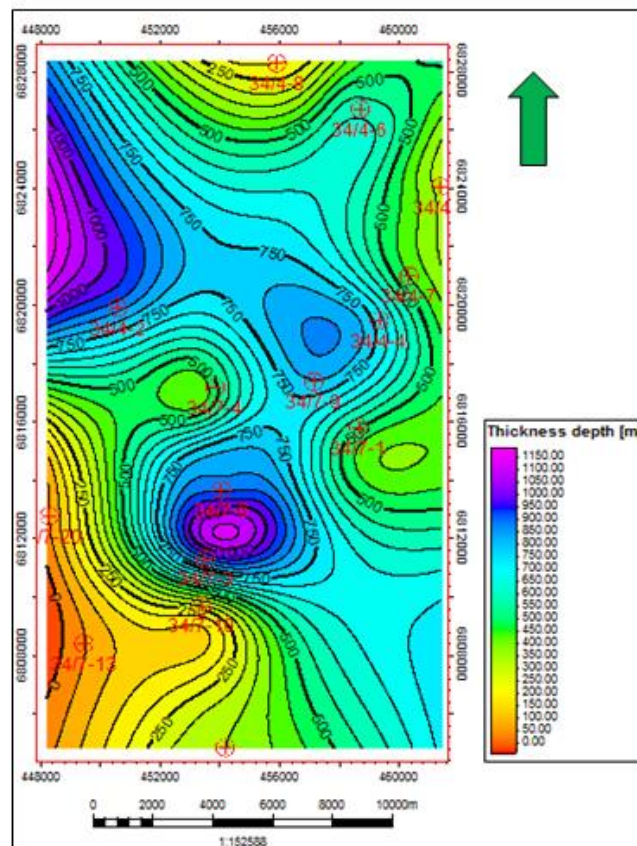


Figure 4.1: The thickness contour map of the Lunde Formation.

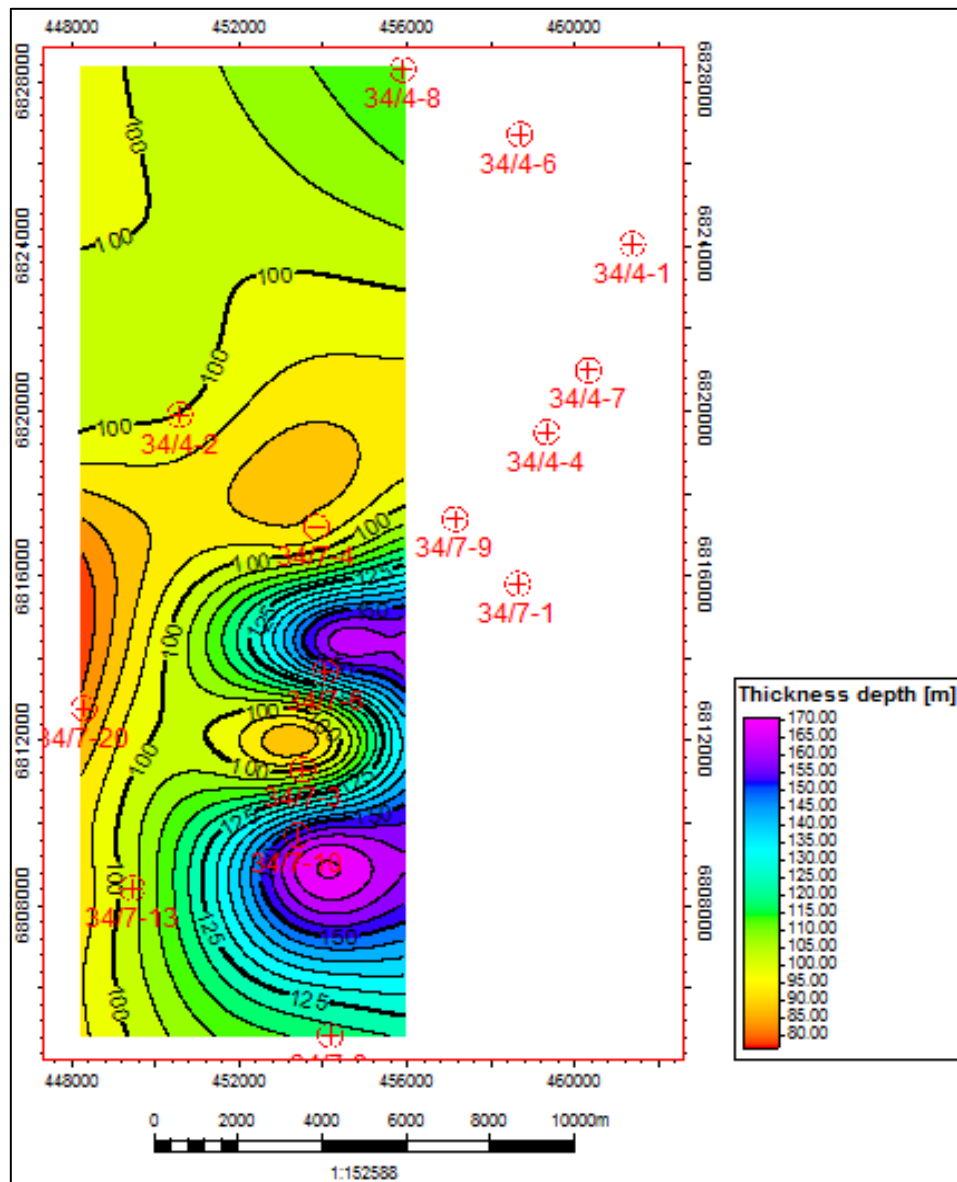


Figure 4.2: The thickness contour map of the Statfjord Formation.

Additionally the thickness variation and reservoir depth across the Snorre field is observed by the correlation of the reservoir along the wells. The correlation is carried by using Gamma Ray log and formation top information given on NPD's website (Figure 4.3 & Figure 4.4). The Statfjord Formation which is younger reservoir in Snorre field is not encountered in north-eastern wells. The Snorre field is located on the westward tilting fault blocks of the Tampen Spur area. During Cretaceous the uplifted eastern part of the westward tilting fault blocks were eroded and in Snorre blocks about 1200 m of sediments were eroded (Nystuen and Fält, 1995). The Statfjord Formation is encountered in all the wells from north to south (Figure 4.3). The thickness of the Statfjord Formation is not varying significantly within the wells on Snorre field. The principal reservoir Lunde Formation in the Snorre field is encountered by all wells. The Lunde Formation is not completely penetrated by wells on southwestern part therefore the thickness is unknown in this part (Figure 4.4). The Lunde Formation in some wells in south-western part of the Snorre field is not penetrated until base which is the possible reason for significant lower thickness.

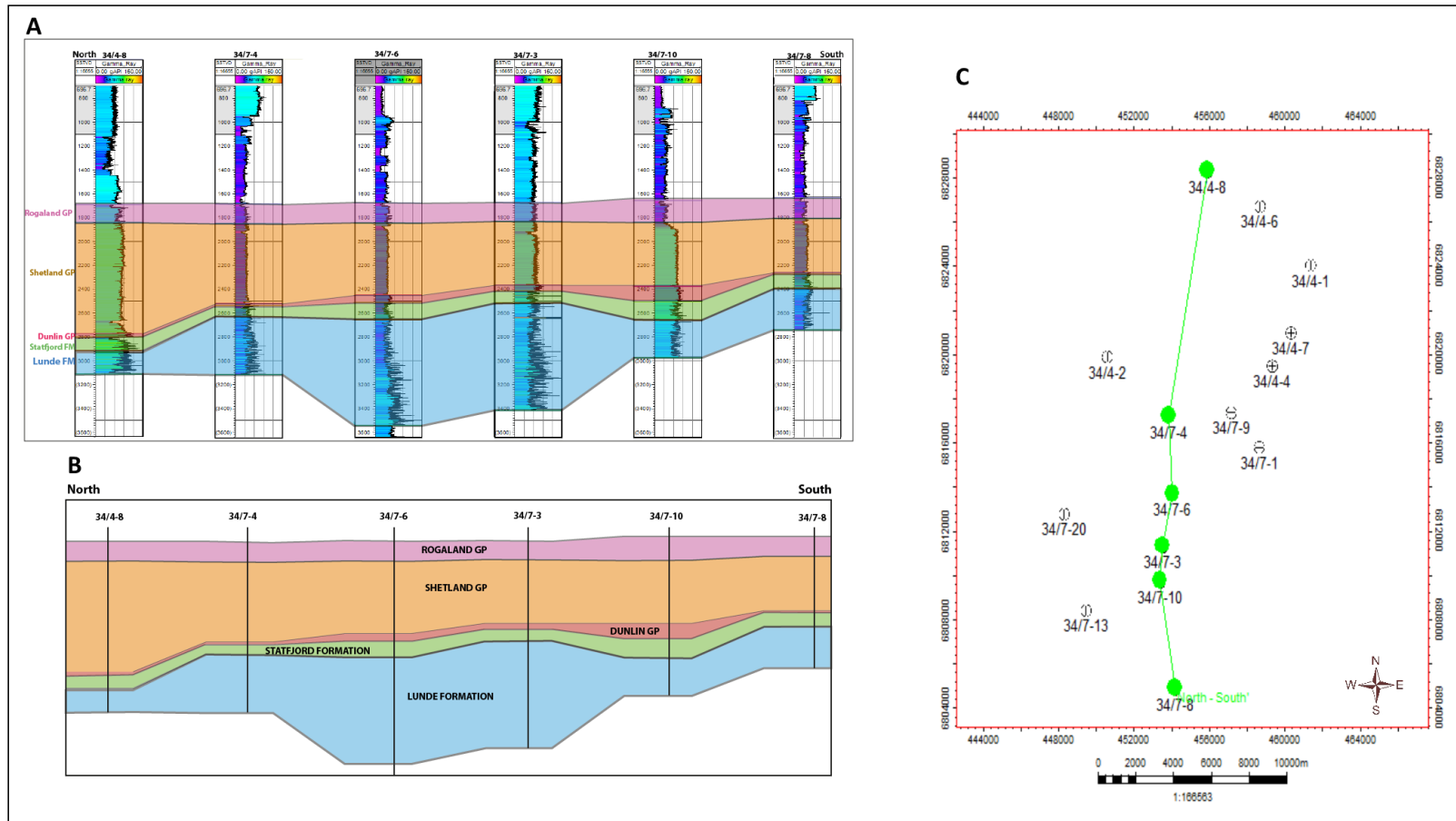


Figure 4.3: The stratigraphic correlation from N-S direction over the Snorre field; (A) shows the correlation using Gamma Ray log and formation top; (B) Schematic illustration of the thickness variation of the Lunde FM, Statfjord FM, Dunlin Gp, Shetland GP and Rogaland GP along N-S direction in the Snorre field; (C) The wells highlighted with green are used for correlation.

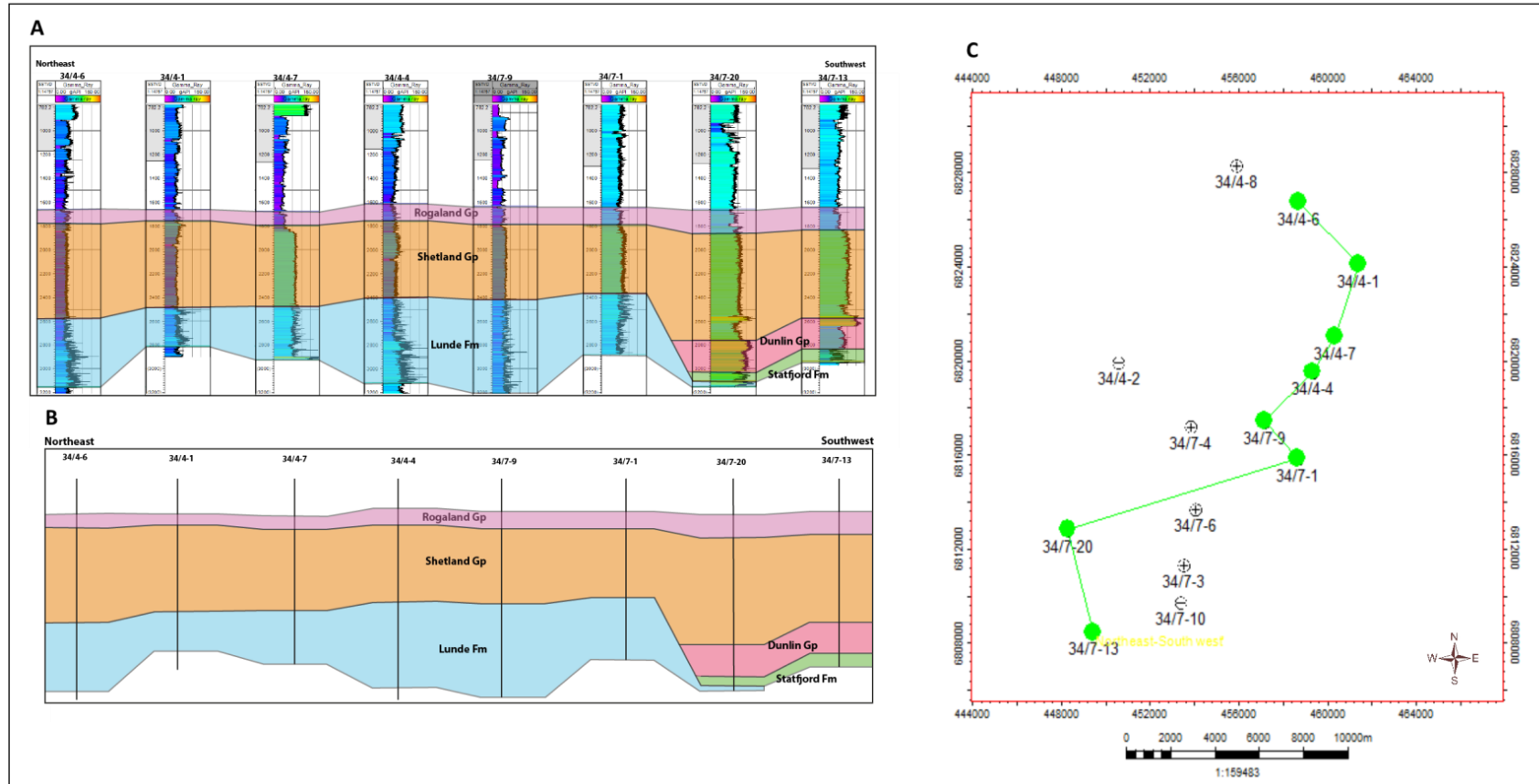


Figure 4.4: The stratigraphic correlation from NE to SW direction of the Snorre field; (A) The thickness of reservoir (Lunde and Statfjord Formations) and seal/cap rock (Shetland/Rogaland Groups) are shown by using gamma ray log and formation top information; (B) The schematic illustration of thickness variation along NE to SW direction; (C) The wells highlighted by green colour are used for NE-SW correlation starting from well 34/4-6 to well 34/7-13.

4.1.2 Shale Content in Reservoir rocks

The shale volume is the most complicated and important estimation in formation evaluation. The misinterpretation of the shale volume/shale content in the reservoir leads to uncertain results in other parameters such as porosity, permeability, water saturation subsequently net-to-gross and net pay zone calculation. The methodology used to calculate shale volume is discussed earlier in chapter 3 section 3.3.1 in detail. Here are presented shale volume results from reservoirs (Lunde and Statfjord Formations) from the study area.

Lunde Formation

The Lunde Formation is of fluvial origin and consists of fine to coarse grained sandstones, with siltstones, shales and marls (Detail description in chapter 2, section 2.3.1). The results from 14 wells are shown in Table 4.1 and also plotted as histogram in Figure 4.5a. The histogram shows mean value 0.28 and mode value 0.19 (Figure 4.5a).

Table 4.1: The shale volume calculated from 14 wells; Vsh – Shale volume, R.Top – Reservoir top (m), R.Bottom – Reservoir bottom (m).

Lunde Formation			
Well	R. Top (m)	R. Bottom (m)	Vsh
34/4-1	2507	2834	0.29
34/4-2	2696	3606	0.27
34/4-4	2425	3142	0.26
34/4-6	2576	3153	0.29
34/4-7	2502	2945	0.22
34/4-8	2913	3105	0.39
34/7-1	2391	2900	0.30
34/7-3	2512	3419	0.25
34/7-4	2627	3121	0.30
34/7-6	2654	3539	0.28
34/7-8	2417	2775	0.36
34/7-9	2442	3232	0.24
34/7-10	2683	3004	0.30
34/7-20	3128	3166	0.41

Statfjord Formation

The Statfjord Formation is not a main reservoir in the Snorre field but an important reservoir on Tampen Spur area. The shale volume histogram (Figure 4.5b) show the mean value is 0.27 and mode 0.13. The results from 8 wells containing Statfjord Formation are shown in Table 4.2. The presence of fine grained overbank facies and floodplain mudstones appear as flow barrier between channel sandstone bodies of the reservoir (Nystuen and Fält, 1995). Stacked

channel sandstone bodies can be identified from gamma ray log containing internal shale beds.

Table 4.2: The shale volume calculated from 8 wells containing Statfjord Formation; VshND – Shale volume, R.T – Reservoir Top (m), R.B – Reservoir Base (m).

Statfjord Formation			
Well	R. Top (m)	R. Bottom (m)	VshND
34/4-2	2596	2696	0.33
34/4-8	2799	2913	0.37
34/7-3	2414	2512	0.28
34/7-4	2536	2627	0.38
34/7-6	2510	2654	0.34
34/7-8	2299	2417	0.38
34/7-10	2531	2683	0.37
34/7-13	2859	2962	0.18

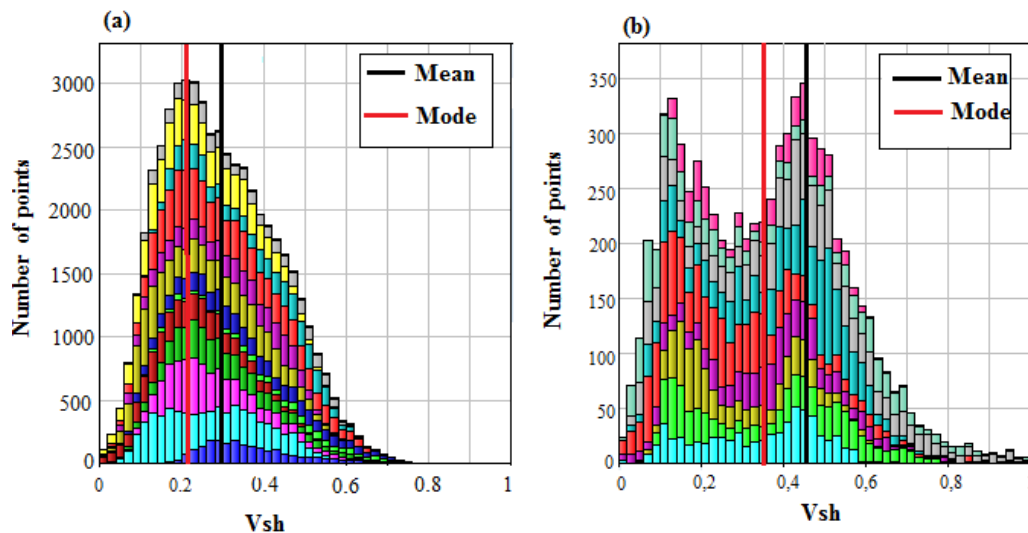


Figure 4.5: The shale volume histogram; (a) Lunde Formation, (b) Statfjord Formation. The mean and mode value are shown on histograms.

4.1.3 Porosity in Reservoir Sandstones

The porosity is the most desired parameter in hydrocarbon exploration. Porosity is expressed either in percentage (0 to 100 %) or fraction (0 to 1). The porosity in the reservoir rock depends on several factors from source to sink. The factors such as mineralogy of the parent rock, weathering, erosion, mode of transportation to the basin; influence deposition of the

reservoir rock and on other hand reservoir parameters. More specifically porosity is the function of grain size, grain shape, sorting, mechanical compaction and chemical compaction (burial diagenesis). The porosity in deeply buried reservoir reduced significantly by chemical compaction (quartz cementation). While at shallow depth mechanical compaction the grain crushing and reorientation reduce porosity.

Hydrocarbon exploration is a costly process especially offshore exploration. In order to reduce risk of failure, the precise estimation of the reservoir parameters (porosity, saturation, N/G) is required. With improvement in exploration techniques the risk of failure is reduced but still depends on the applicable method used for reservoir estimation. In case of the porosity estimation from well log data, several uncertainties are associated with every single log used for porosity estimation.

The most precise and reliable porosity is calculated from core samples. In the absence of core data combination of logs is preferred approach for porosity estimation. The single porosity log contains certain uncertainties with varied lithology. In wireline logging Neutron, Density and Sonic logs are widely used for porosity estimation. Neutron log measures porosity as a function of the hydrogen present in rock pores. The presence of hydrogen in rock matrix as in clay minerals evolves uncertainty and neutron log overestimate porosity. Neutron logs measure porosity accurately in limestone because limestone matrix is completely hydrogen free. In case of reservoir filled with gas neutron log underestimate porosity because gas contain less hydrogen as compared to oil and water. The limitations of certain logs with lithology and pore fluids are discussed in detail in chapter 3.

To minimize the limitations of porosity estimation using different logs, the standard industrial approach is the average porosity from density-porosity and neutron-porosity. The combination of neutron-porosity and bulk density log is also useful in lithology discrimination. The crossover of the neutron porosity log and bulk density log help in identification of the shales and gas zones. The average of neutron porosity and density porosity is used for further analysis.

Lunde Formation

The porosity results for Lunde Formation are shown in Table 4.3 and Figure 4.6. The results are shown from 14 wells. The mean value for true porosity (Φ_T) is 0.20 and mode 0.16 (Figure 4.6a), while the mean value for Φ_E (effective porosity) is 0.18 and mode value 0.14 (Figure 4.6b). The Lunde Formation has porosity more than 15 % except well 34/7-20. In well 34/4-2 the estimated porosity is more than 38 % which is actually not true. The bad borehole condition in well 34/4-2 observed from Calliper log (Appendix A.2), which leads to poor quality data. Additionally the well 34/4-20 and 34/4-8 penetrated only top of the Lunde Formation and the data quality is not reliable.

Table 4.3: The porosity calculated for Lunde Formation; PhiT – True porosity, PhiE – Effective porosity.

Well	Top Depth (m)	Base Depth (m)	PhiT	PhiE
34/4-4	2425	3142	0.20	0.18
34/4-2	2696	3606	0.38	0.36
34/4-1	2507	2834	0.16	0.13
34/4-6	2576	3153	0.16	0.15
34/4-7	2502	2945	0.18	0.17
34/4-8	2913	3105	0.15	0.12
34/7-1	2391	2904	0.20	0.17
34/7-3	2512	3419	0.17	0.16
34/7-4	2627	3121	0.18	0.15
34/7-6	2654	3539	0.16	0.14
34/7-8	2417	2775	0.20	0.16
34/7-9	2442	3232	0.19	0.17
34/7-10	2683	3004	0.16	0.14
34/7-20	3128	3166	0.11	0.09

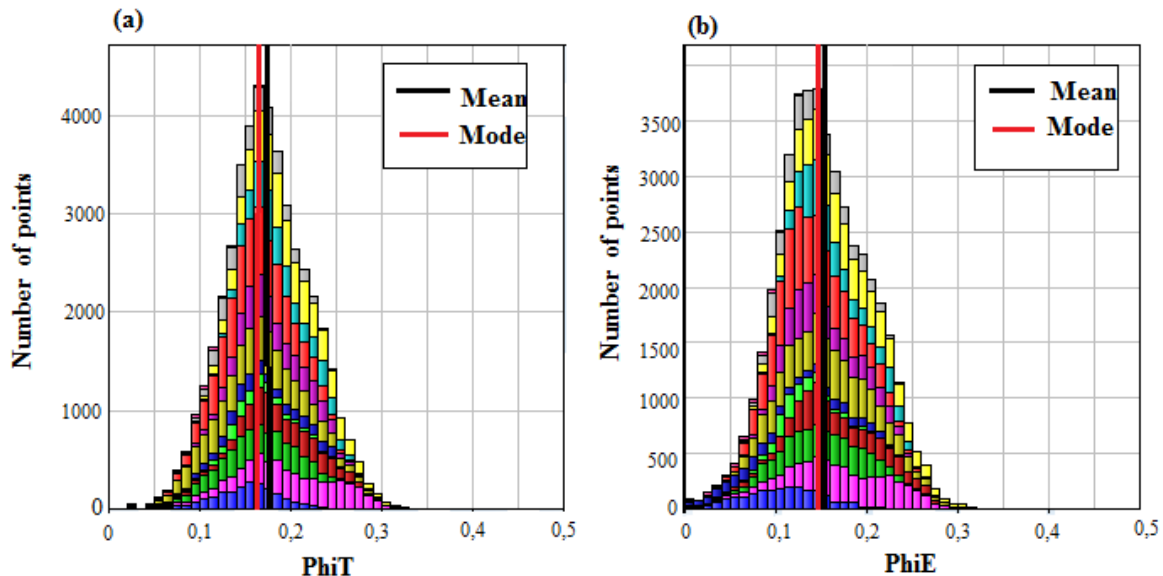


Figure 4.6: The porosity histograms for Lunde Formation; PhiT – True porosity, PhiE – Effective porosity.

Statfjord Formation

The porosity histogram is yet simple but quiet informative to see the porosity in zone of interest. The mean porosity value for Statfjord Formation using eight wells is 0.22 while the mode value is also 0.22 for the true porosity (PhiT) (Figure 4.7a). The effective porosity histogram shows mean value 0.19 and mode value 0.18 (Figure 4.7b). Statfjord Formation is not present along all the wells in Snorre field (discussed in section 4.1.1). The Statfjord Formation contains good porosity in most of the wells in Snorre field. The results of 8 wells are shown in Table 4.4.

Table 4.4: The calculated porosity of the Statfjord Formation; Φ_iT – true porosity, Φ_iE – effective porosity.

Well	Top Depth	Bottom Depth	Φ_iT	Φ_iE
34/4-2	2596	2696	0.21	0.20
34/4-8	2799	2913	0.21	0.10
34/7-3	2414	2512	0.29	0.23
34/7-4	2536	2627	0.22	0.18
34/7-6	2510	2654	0.23	0.22
34/7-8	2299	2417	0.23	0.19
34/7-10	2531	2683	0.20	0.20
34/7-13	2859	2962	0.21	0.19

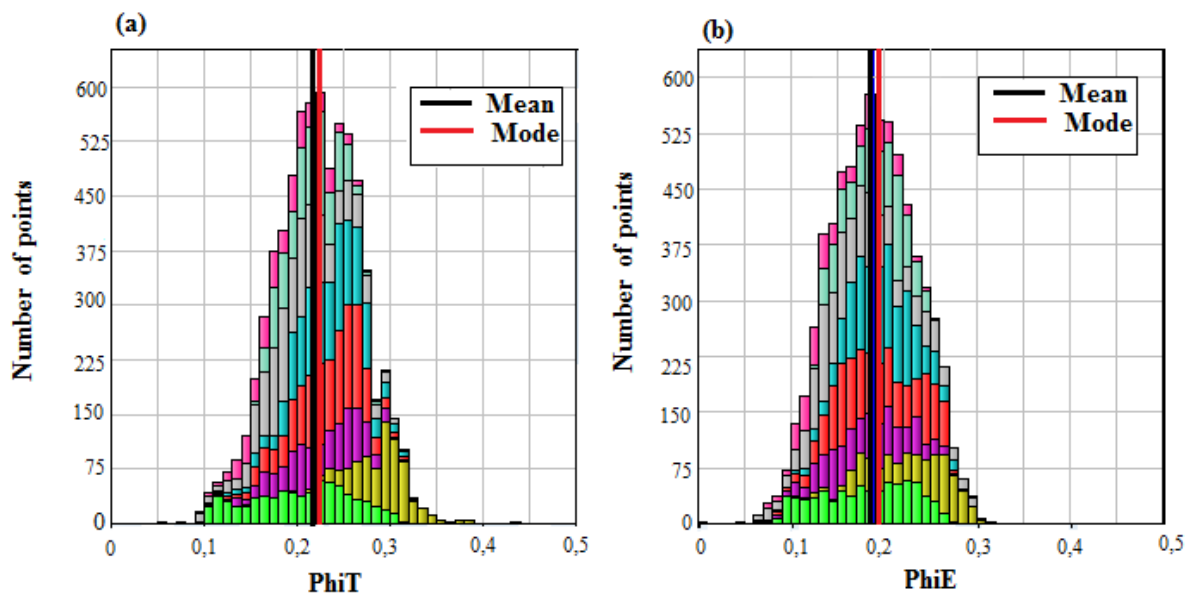


Figure 4.7: The porosity histograms for Statfjord Formation; Φ_iT – True porosity, Φ_iE – Effective porosity.

4.1.4 Saturation in Reservoir Sandstones

The electrical resistivity of the reservoir rock is an excellent tool to detect hydrocarbons in wells and additionally to quantify hydrocarbon saturations. The quantitative use of formation electrical resistivity was first introduced by Archie, (1942). The electrical resistivity logging affected by different factors such as bad bore hole condition, invasion of drilling mud into formation pores, salinity of the formation water. To avoid the effect of drilling fluid deep resistivity log use to calculate the water saturation in reservoir horizons. The deep resistivity log actually gives the true formation resistivity in uninvaded zone. The resistivity of the rock depends on porosity, salinity of pore water, hydrocarbon in pore spaces and temperature.

The water saturation calculation use to find the hydrocarbon saturation in the reservoir. Qualitatively the deep resistivity log can use to separate the hydrocarbon saturated zone from water saturated zone (Figure 4.8). The hydrocarbon saturation is calculated by using Equation 4.1 (Rider and Kennedy, 2011).

$$S_{hc} = 1 - S_w \dots\dots\dots (4.1)$$

In a reservoir zone if the water saturation is not 100%, then the hydrocarbons are present in reservoir (Rider and Kennedy, 2011). The Figure 4.8 shows the saturation of hydrocarbons in well 34/7-3. The reservoir zones are highlighted with blue rectangle. Four hydrocarbon zones named zone 1 to 4 respectively are observed in Statfjord Formation in well 34/7-3 (Figure 4.8). The shale layers present between the reservoirs intervals causing internal flow barrier for hydrocarbons. The water saturation calculated in four zones is given in Table 4.5. The reservoir zones also have good porosity. In zone 1 the water saturation is 0.3 then according to Equation 4.1, the hydrocarbon saturation is 0.7.

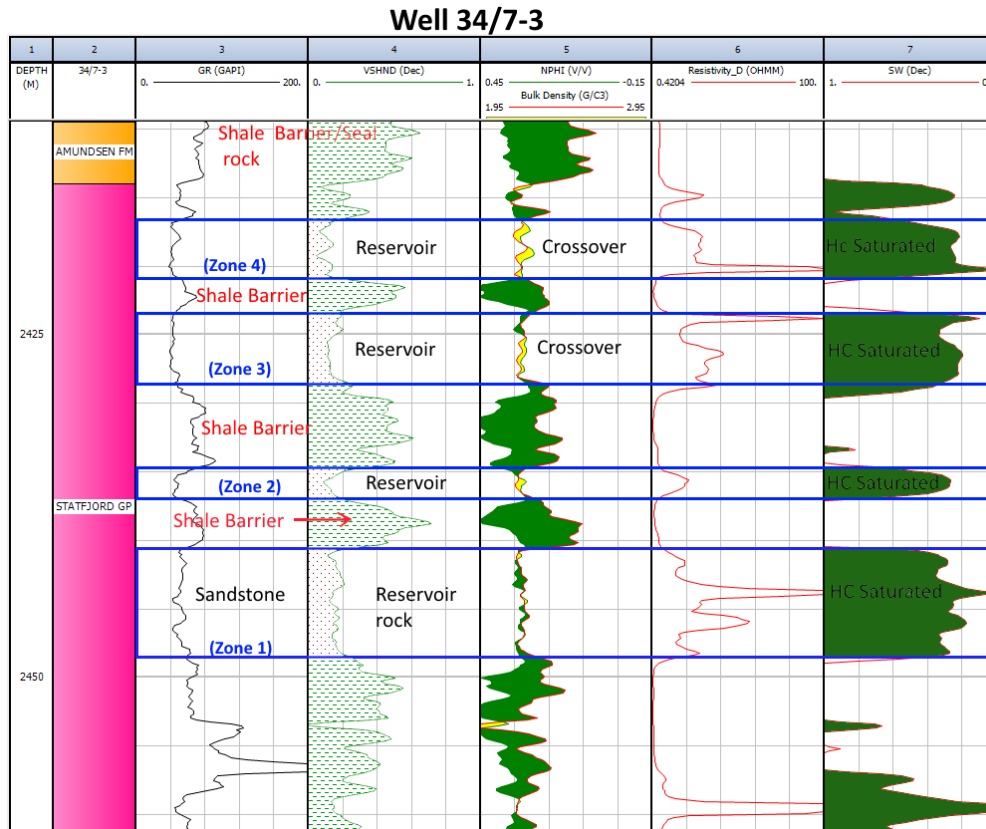


Figure 4.8: Log plot over hydrocarbon saturated zone from Statfjord Formation in well 34/7-3. The hydrocarbon saturated zones are marked by blue rectangle.

Table 4.5: The porosity and water saturation (S_w) of four hydrocarbon zones in well 34/7-13.

HC Zone	Depth interval (m)	Porosity (Frac)	S_w (Frac)
Zone 1	2440-2448	0.24	0.3
Zone 2	2434-2436	0.23	0.5
Zone 3	2423-2429	0.24	0.2
Zone 4	2416-2420	0.25	0.3

4.1.5 Permeability estimation

The estimated permeability plotted against effective porosity for Lunde Formation of well 34/4-1 is shown in Figure 4.9. The plot is colour coded by shale volume (V_{sh}). Two equations used for permeability estimation (see detail in section 3.3.6). The estimated permeability from both equations has difference. It has been observed that the permeability is increasing with increasing porosity in nearly linear trend. The decrease of permeability with increasing shale content can be seen in both plots in Figure 4.9. The presence of shale layers in sandstone act as fluid flow barrier. The presence of fine clay particles in pores also cause decrease in porosity and in turn permeability.

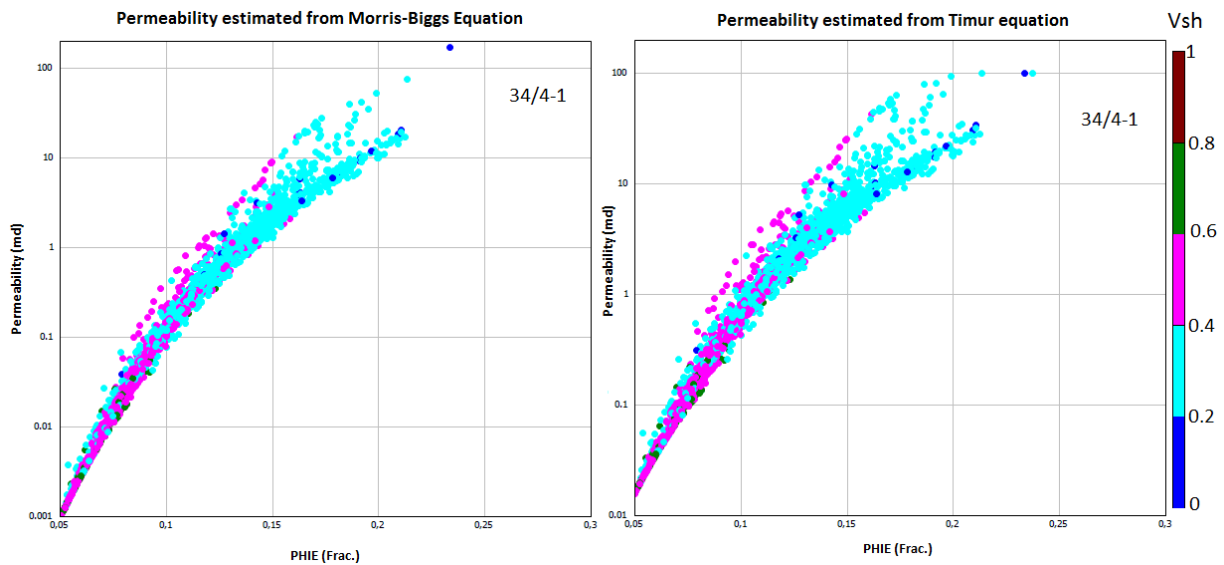


Figure 4.9: The permeability versus effective porosity crossplot of Lunde Formation of well 34/4-1. The permeability estimated by Morris-Biggs equation (left) and the estimated by Timur equation (right).

4.1.6 Net-to-Gross and pay thickness estimation

Net-to-Gross (N/G) is the ratio of total reservoir thickness to the net thickness which holds significant reservoir properties. It is the most quantitative parameter of the reservoir and greatly important in reservoir evaluation. The N/G is calculated by using the cutoffs values for porosity, shale volume and water saturation. After calculation of the N/G the net pay zone with producible hydrocarbon is calculated by using water saturation cut-off value.

The estimated gross reservoir thickness of Lunde and Statfjord Formations in net reservoir interval and net pay zones are given in Table 4.6 and Table 4.7 respectively. The cutoffs limits used are effective porosity 0.10 and shale volume 0.3. The N/G of Lunde Formation is good in most of the wells except few wells (34/7-8, 34/7-4, 34/4-8 and 34/4-20) where poor N/G are estimated. For Statfjord Formation the N/G is good only in two wells (34/7-13, 34/7-3).

Table 4.6: The estimated N/G values for Lunde Formation; Net(r) – Net reservoir interval, N/G – Net-to-gross ratio, $\phi(r)$ – average porosity in reservoir zone, $\phi(p)$ – porosity in pay zone, $S_w(R)$ – water saturation in reservoir zone in percentage, $S_w(P)$ – water saturation in pay zone in percentage.

Well	Formation	Gross Interval	Net(r)	N/G	Net Pay zone	$\Phi(r)$	$\Phi(p)$	$S_w(R)$	$S_w(P)$
34/7-1	Lunde	513	458	0.89	79	18	23	72	28
34/4-6	Lunde	576	421	0.73	27	16	21	85	54
34/4-7	Lunde	443	318	0.71	32	18	22	80	33
34/4-4	Lunde	717	417	0.67	78	23	23	37	37
34/4-1	Lunde	326	195	0.59	19	15	17	86	55
34/7-9	Lunde	781	461	0.59	43	19	26	75	33
34/7-3	Lunde	906	466	0.51	0	17	N/A	88	N/A
34/7-6	Lunde	885	427	0.48	0	16	N/A	98	N/A
34/7-10	Lunde	321	153	0.47	7	17	0.21	89	4
34/7-4	Lunde	493	204	0.41	0	16	N/A	90	N/A
34/7-8	Lunde	358	131	0.36	0	19	N/A	99	N/A
34/4-8	Lunde	192	29	0.15	0	15	N/A	96	N/A
34/7-20	Lunde	38	5	0.12	0	14	N/A	99	N/A

Table 4.7: The Net-to-gross value for Statfjord Formation; Net(r) – net reservoir interval, N/G – Net-to-gross ratio, $\phi(r)$ – average porosity in reservoir interval, $\phi(p)$ – average porosity in pay interval, $S_w(R)$ – water saturation in reservoir interval, $S_w(P)$ – water saturation in pay interval.

Well Name	Formation	Gross Interval	Net(r)	N/G	Net Pay Zone	$\Phi(r)$	$\Phi(p)$	$S_w(R)$	$S_w(P)$
34/7-13	Statfjord	103	82	0.79	0	19	N/A	99	N/A
34/7-3	Statfjord	98	57	0.58	48	25	25	36	29
34/7-8	Statfjord	74	29	0.39	14	20	23	53	30
34/7-6	Statfjord	143	54	0.38	38	22	23	42	25
34/4-8	Statfjord	114	41	0.36	0	0.18	N/A	97	N/A
34/7-10	Statfjord	151	44	0.29	29	20	20	42	27
34/7-4	Statfjord	91	24	0.26	15	20	19	44	29

4.1.7 Facies interpretation of reservoir rocks

The distribution of facies depends on basinal setting, depositional environment and climate with respect to age of formation. The Lunde and Statfjord Formations are deposited on alluvial plain with channel sand, non-channel sand and flood plain mudstones and shales. The upper most part of the Statfjord Formation marks transition from continental to marine environments. The marine part of the Statfjord formation is not encountered on wells in Snorre field (Jorde and Diesen, 1990; Nystuen et al., 1989). Due to limitations of other resources (e.g. seismic data, core section logging) the results contain some uncertainties. The published literatures e.g. (Hollander, 1987; Nystuen and Fält, 1995; Nystuen et al., 1989; Steel and Ryseth, 1990) are used to aid the facies interpretation. The main facies interpreted are fluvial channel sandstones, over bank deposits and floodplain mudstones.

Lunde Formation

As explained earlier the Lunde Formation is divided into three members. The Lower and Middle members of Ladinian-Carnian age has been interpreted as fluvial or estuarine channel sandstone (Hollander, 1987). The Upper member is the main reservoir in the Snorre field (Nystuen and Fält, 1995). The upper member consists of fluvial channel sandstones, non-channelized sands with silty overbank shales and floodplain mudstones (Hollander, 1987). Nystuen and Fält, (1995) define the channel sandstones, non-channel sandstones and floodplain mudstones with overall upward coarsening to upward finning succession in Lunde Formation on Tampen Spur area. The channel sandstone bodies are usually ranging in 3 m up to 30 m thickness and show blocky pattern on Gamma Ray curve (Nystuen and Fält, 1995). The Gamma Ray responses of Lunde Formation from well 34/4-1, 34/4-2 and 34/7-4 are plotted in Figure 4.10. The different facies are shown including single and multi-storey channel sands with over bank deposits and floodplain mudstones. The red arrow in Figure 4.10 shows the Gamma Ray log trend of coarsening upward and finning upward for individual small sequences. The small sequences are few meters thick. On the right side of logs for each well the higher order sequence is shown in blue colour with coarsening upward and finning upward trend. The high concentration of uranium from Spectral Gamma log confirms the presence of shales which are interpreted as flood plain mudstones and shales deposits. The presence of red palaeosol are observed in floodplain mudstone which represent the subaerial deposition of the mudstone (Nystuen and Fält, 1995).

Statfjord Formation

In Figure 4.11 the Gamma Ray log from interval of Statfjord Formation is plotted for well 34/7-13. The Statfjord Formation is divided into same depositional facies as Lunde Formation with single channel sandstone, multi-storey channel sandstones and floodplain mudstones deposits. The palaeosol are also observed in alluvial deposits of the Statfjord Formation (Nystuen and Fält, 1995), but it is not possible to identify the palaeosol beds from only Gamma Ray log response. The Figure 4.11 (left) shows the uppermost marine shales of Dunlin Group which act as seal/cap rock of Snorre field. The Dunlin Group in the Snorre field represent the transition of continental to marine environment in the Snorre field.

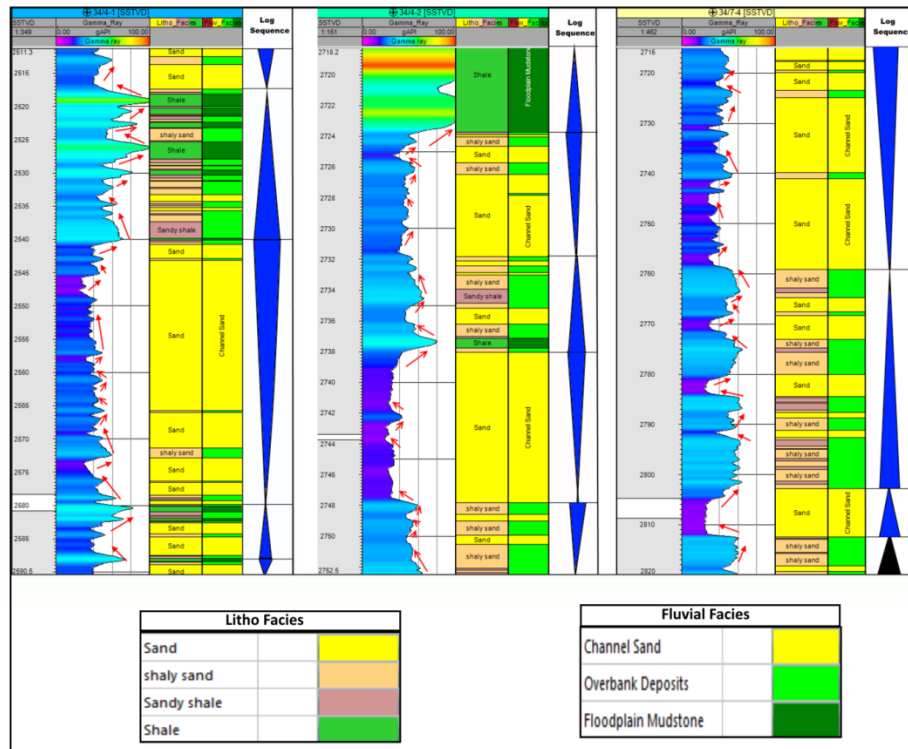


Figure 4.10: The facies marked along 3 wells (34/4-1, 34/4-2 and 34/7-4 from left to right respectively) for Lunde Formation. The red arrows shows individual sequence of coarsening upward and fining upward while the blue symbol show the major coarsening upward and fining upward along Gamma Ray log trend.

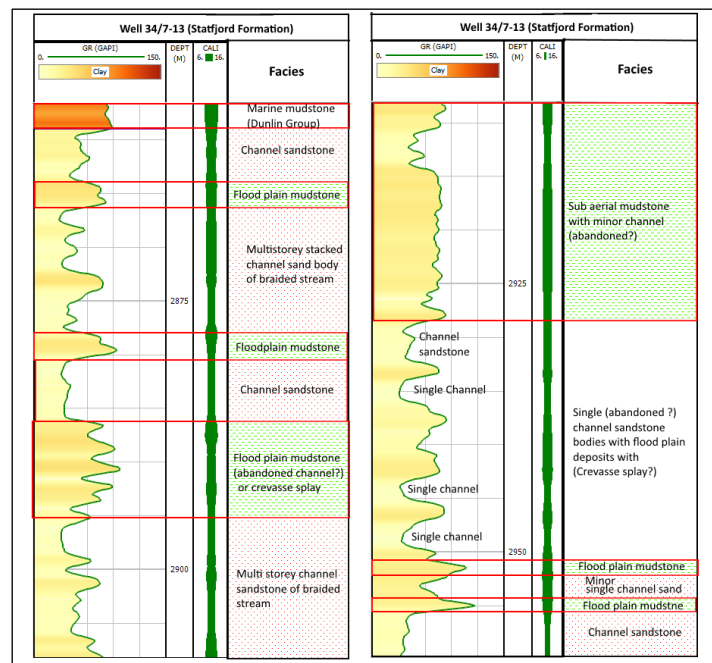


Figure 4.11: Gamma Ray log from Statfjord Formation for well 34/7-13. The different facies are marked along the log responses.

4.2 Cap rocks

The Jurassic shales of the Dunlin Group deposited as a result of marine transgression and can act as an efficient cap/seal for Snorre field. In Snorre field area the stratigraphic thickness of the Dunlin shales is very less and only restricted to the southwestern part of the field. The westward tilted blocks of Snorre field undergo intensive erosion on eastern shoulders in Cretaceous time and results the removal of Statfjord Formation and Dunlin Group of Jurassic age. Lower Cretaceous Cromer Knoll Group is thin marl/calcareous claystone horizon present in the Snorre field but the thickness does not exceed 20 m (Caillet, 1993). The thick shales sequence of Upper Cretaceous Shetland Group is efficient seal rocks for Snorre field.

4.2.1 Identification of Cap rock

The cap rock is identified by plotting Gamma Ray log, shale volume, neutron density cross plot with deep resistivity and water saturation (Figure 4.12). The well 34/4-7 is shown from north eastern part of the Snorre field, where the cap/seal rock is shales sequence from Shetland Group. The Shetland Group is highlighted with light red box in both wells. The density-neutron crossover clearly identifies shales in seal/cap rock of Shetland Group. The deep resistivity is very low in seal rock. The reservoir zones are marked by light blue box on both wells. In reservoir zone the distinctive crossover of density-neutron is observed. The well 34/7-3 is from southwestern part of the Snorre field where Jurassic shales of Dunlin group are present. The marine shales of Dunlin Group are a good seal rock but has limited occurrence over the Snorre field area. The Dunlin group is marked by light green box on Figure 4.12 (right) and show high Gamma Ray values with low resistivity.

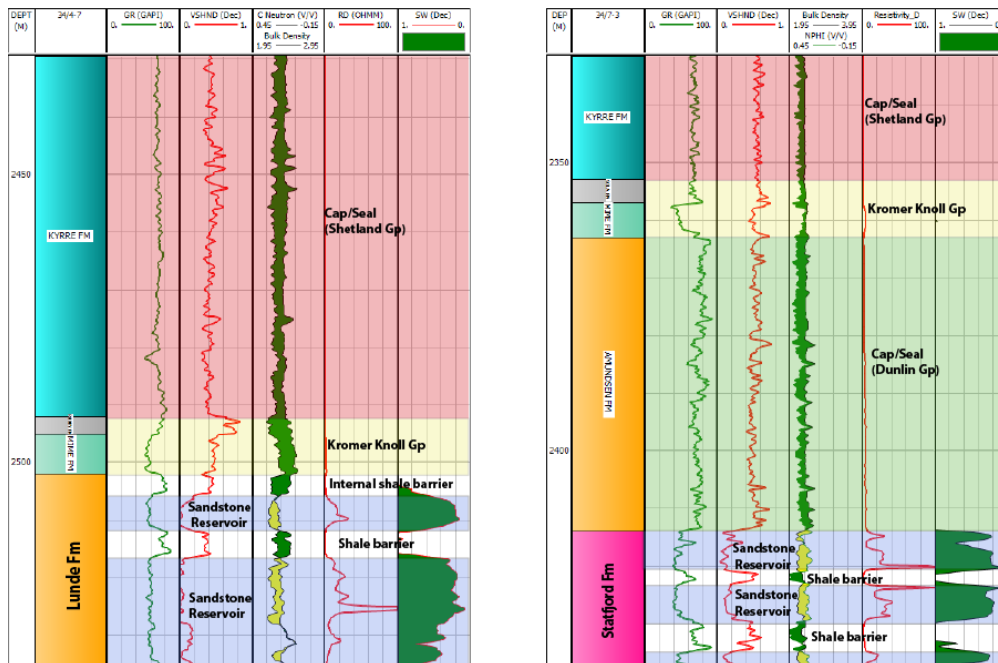


Figure 4.12: The composite log display of wells 34/4-7 (left) and 34/7-3 (right), show different reservoir sections (light blue colour) and their potential seals/cap rock (light red and light green colour).

4.2.2 Shale volume in cap rock

The estimated shale volumes for seal rocks in Amasuden Formation of the Dunlin Group and Kyree Formation of the Shetland Group are shown in Figure 4.13. The high shale volume in both rocks shows the capability of the rocks to be a seal/cap for hydrocarbons. The histogram (Figure 4.13a) show the mean value for Dunlin Group is 0.56 while the mode is 0.49. The data for Dunlin group is plotted from nine wells from southwestern part of the Snorre field. The Kyree Formation of the Shetland Group has mean and mode value of 0.55 (Figure 4.13b). The data for Kyree Formation is plotted from the 14 studied wells.

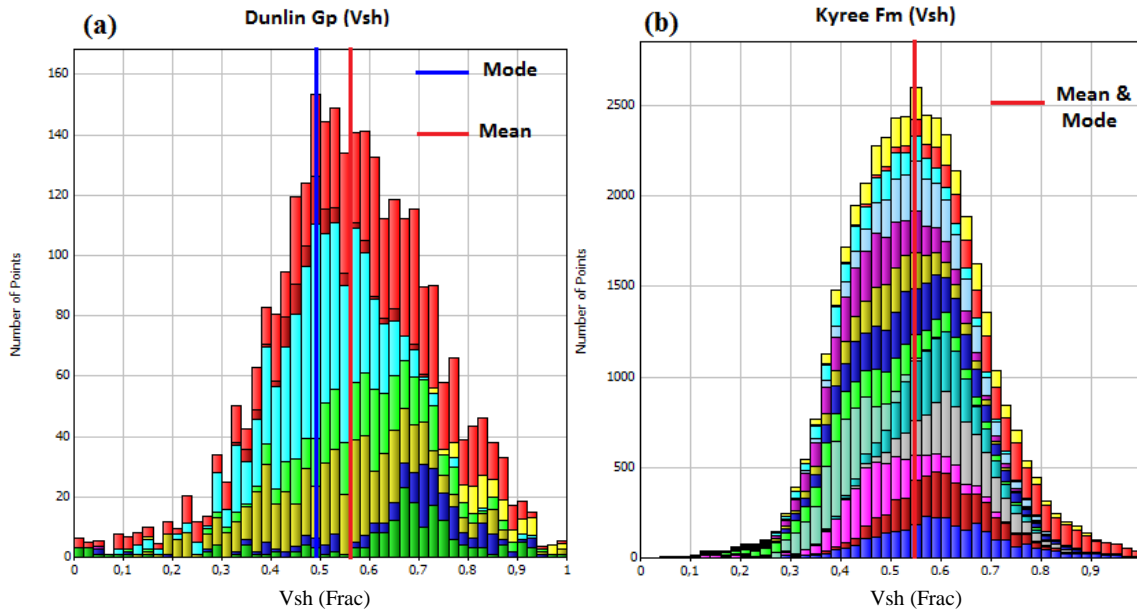


Figure 4.13: The shale volume histogram; (a) Amasuden Fm (Dunlin Gp), (b) Kyree Fm (Sheetland Gp).

4.2.3 Porosity in seal rock intervals

The effective porosity shows the interconnectivity of the pore spaces which in turn show the capability of the rock to transmit fluids. Shales are impermeable rocks and contain few pore interconnectivity therefore act as excellent cap/seal rock for hydrocarbons. The Dunlin Group effective porosity shows the mean and mode values of 0.05 and 0.005 respectively suggest good seals.

4.3 Discussion

The detailed petrophysical analysis of the Snorre field is discussed in this section. The main focus of discussion is Lunde and Statfjord Formations. The identification and interpretation of the petroleum system is the secondary target for the study and therefore not discussed in detail.

4.3.1 Overview of the data and reservoirs

A total 20 wells included in this study from the Snorre field and adjacent areas (Table 1.1). During log quality control the well 34/4-2 is observed with bad borehole conditions and data quality is not reliable (See Appendix A.2). The primary reservoir Lunde Formation is present in 14 wells (34/4-1, 34/4-4, 34/4-6, 34/4-7, 34/4-8, 34/7-1, 34/7-3, 34/7-4, 34/7-6, 34/7-8, 34/7-9, 34/7-10, 34/7-13 and 34/7-20) while Statfjord Formation is encountered only in 8 wells (34/4-8, 34/7-3, 34/7-4, 34/7-6, 34/7-8, 34/7-10, 34/7-13 and 34/7-20). The five wells (34/7-16, 34/7-19, 34/7-27, 34/7-28 and 34/7-32) do not contain either Lunde Formation or Statfjord Formation, therefore not included in petrophysical analysis but used in compaction study (further detail in chapter 5). Furthermore in well 34/7-20 only the top 38 meters of the Lunde Formation are drilled. Out of 15 wells in Snorre field only two wells are dry wells while rest contain hydrocarbons. The Lunde Formation contains oil in 11 wells while Statfjord Formation contains oil in 5 wells.

4.3.2 Source rock

Upper Jurassic Draupne Formation is the main source rock for the Tampen Spur area (Horstad et al., 1995). Gamma Ray log is used to identify the source rock (Beers, 1945; Passey et al., 1990). Organic rich shales contain high concentration of the Uranium which gives high Gamma Ray value. The higher Uranium concentration within the source rock can be detected by using Spectral Gamma log. Additionally the Resistivity log is also very high in organic rich shales. Rock matrix, solid organic matter and pore fluids are main component of the source rocks. On maturation of the source rock hydrocarbons are generated and occupied the pore spaces within the source rock. The electrical resistivity of the hydrocarbons is very high as compared to brine and therefore shows high resistivity for source rock in resistivity log response. The source rock Draupne Formation is not present in all of the wells included in this study. Horstad et al. (1995) suggested the oil migrated to Tampen Spur area is from different kitchen sources from different directions.

4.3.3 Reservoir rock

Formation evaluation

In the reservoir characterization, the petrophysical analysis is the vital step that provides important information about the subsurface formations that represent potential reservoir zones. The wireline logs are continuous recordings of the different reservoir parameters. In the absence of core and/or seismic data, the well logs are main source of information for evaluation of the subsurface rock (Moore et al., 2011). In industrial practice different kinds of geophysical logs such as radioactive, sonic, electrical, imaging etc. are used to get the reservoir information and to detect possible hydrocarbons zones. Additionally the well log information is used for calibration and correlation with seismic data. The well to well

correlation is advantageous practice to get the understanding of the subsurface formation over a certain area.

The identification of the lithology is the first step in petrophysical analysis and for the purpose Gamma Ray log which is measure of natural radioactivity from the rock formation is commonly used. Shales with high uranium content gives higher Gamma Ray value while clean sand lack radioactive elements and give low Gamma Ray. The sandstone with K-Feldspar content shows higher Gamma Ray value because of K (Potassium). The Spectral Gamma in such case is useful to get more confidence on interpretation because Spectral Gamma measures the individual concentration of the Uranium, Thorium and Potassium. In the case of the limestone it is difficult to identify from only Gamma Ray log but with the aid of Sonic log and Density-Neutron cross plot the discrimination between limestone and sandstone is possible. The shale volume is calculated from Gamma Ray by defining the shale and sand lines. The simple histogram (Figure 3.2) is utilized in this study for defining shale line and sand line. The accurate shale volume calculation is necessary because the calculation of the porosity, water saturation and other parameters rely on shale volume. The calculation of the shale volume is not direct measurement by logging tool rather it is calculated by using empirical relations (see section 3.3.1).

Further the porosity and water saturation are vital parameters of the reservoir. Bad bore hole condition is the most common reason for inaccuracy or uncertainty in porosity estimation from well logs (Moore et al., 2011). In the well 34/4-2, the bad bore hole condition is observed from calliper log and therefore the porosity calculated in reservoir rock (Lunde Formation) is 36 % (Table 4.3) actually not true due to bad borehole condition.

The calculation of the net-to-gross value by using certain cut-offs for lithology (shale and sand) leads to find the extent of the sand present in the formation. In practice cut-offs of shale volume and porosity are used to find N/G ratio. The net pay zone thickness is calculated by using additional water saturation cut-off value.

For economic production from a reservoir the continuity of the sandstone bodies is necessary. The primary factor is permeability or interconnectivity of the pores within sand bodies. The ability of the fluids to flow within reservoir is highly dependent on amount of clay present in reservoir, the porosity in the reservoir and the permeability in the reservoir (Badarinadh et al., 2002; Vardian et al., 2016).

Lunde Formation

The Lunde Formation is penetrated in 14 wells out of 20 wells included in this study (Table 1.1). The 5 wells in block 34/7 are not penetrated in Lunde Formation. Other wells are drilled beyond the boundary of the Snorre field. The stratigraphic thickness correlation is shown in Figure 4.3 and Figure 4.4. The base of Lunde Formation is not penetrated by most of the wells in southwestern part of the Snorre field and the exact thickness cannot be correlated. The eastern part of the Snorre field located on shoulder of the westward tilted fault blocks and due to erosion on eastern part of fault blocks the thickness is less.

The shale volume evaluation of the Lunde Formation is carried out by utilizing simple histogram plotted from data of 14 wells (Figure 4.5a). The average shale volume is 0.30 for 14 wells. The Lunde formation is interpreted as sand, shaly sand and shales on the basis of shale volume. The floodplain mudstone/shale intervals present between the channelized sandstone bodies and act as flow barrier for hydrocarbons. The saturation in the reservoir

intervals is an important aspect for hydrocarbon exploration. The water saturation in hydrocarbon filled zone of Lunde Formation is less and indicates that zones are filled with hydrocarbons. The higher resistivity value also confirms the presence of hydrocarbon. The continuous thick hydrocarbon column is not observed in Lund Formation in studied wells. The various reservoir zones are observed in Upper and Middle parts of the Lund Formation. The lower part of the Lunde Formation is mostly water saturated.

The estimation of net-pay thickness is important for economic aspect of the field. For the porosity the cut-off value 0.1 is used and it is assumed that the porosity below 0.1 is not effective for hydrocarbon production. The lowest value than 0.1 for effective porosity results low permeability which is main aspect of hydrocarbons flow within the reservoir. The cut-off value for shale volume is 0.3 and formation above the cut-off shale volume value is not clean sandstone. The water saturation cut-off used is 0.6 which means the reservoir zone with 0.4 hydrocarbons is not extractable. The water saturation in the pay zone is less than 50% in all the wells in which hydrocarbons are encountered in Lunde formation. The net-to-gross ratio for Lunde Formation in studied wells studied is divided into three categories with very good, moderate and poor. The four wells have very good N/G, greater than 0.6 while mostly wells lie in moderate category (N/G between 0.4 to 0.6) (Table 4.6). The wells 34/4-8 and 34/7-20 have very poor N/G value and the reason is only few top meters of Lunde Formation is penetrated and the gross thickness is very less (Table 4.6). In well 34/7-8 the top shaly part of the Lunde Formation is penetrated and N/G is 0.36. The overall observations during petrophysical analysis show that the Lunde Formation in Snorre field possesses very good to moderate net-to-gross value. The porosity in reservoir zone is good and range from 15 to 20% (Table 4.6).

Statfjord Formation

The Statfjord Formation is the secondary reservoir in the Snorre field. The formation is not encountered in many well. The Cretaceous erosion removes significant stratigraphic thickness in north-eastern part of Tampen Spur area. The Snorre field crosscuts by NE-SW and E-W trending fault (Nystuen et al., 1989). The stratigraphic thickness correlation along the Snorre wells is shown in Figure 4.3 and Figure 4.4. The thickness of Statfjord formation is 80 to 170 m in wells of the Snorre field (Sourced from formation top information for each well on NPD factpages). In late Cretaceous the area was subsided with deposition of marine marls or mudstones over Kimmerian unconformity (Nystuen et al., 1989). The Statfjord formation is overlain by marine Dunlin group which show the transgressive event due to subsidence of the area.

The shale volume in Statfjord Formation is high in most of wells (> 30%) except well 34/7-13 in which the shale volume is 18% with high N/G value. The Statfjord Formation is interpreted as channelized sandstone with overbank and flood plain mudstone deposited on alluvial plain (Nystuen and Fält, 1995). In the southwest of Snorre field the Statfjord Formation is more sand rich in as compared to Snorre field area which show the proximal to distal environment of the alluvial plane from southeast to northeast (Nystuen and Fält, 1995).

The sub division of the Statfjord Formation into Raude, Eriksson and Nansen member is not applied in Snorre field due to facie change from Statfjord field (Nystuen et al., 1989). The porosity in the Statfjord Formation is good to very good for hydrocarbon exploration. The average porosity is 0.22 in 8 wells in the Snorre field. The content of fluvial sandstone and post-depositional diagenetic processes controlled the reservoir potential of the Statfjord Formation (Ramm and Ryseth, 1996). The net-to-gross value of the Statfjord Formation in

Snorre field wells is not very high but the upper part of formation is more sand rich. Ramm and Ryseth, (1996) analysed the core section of Statfjord Formation from different areas of the North Sea and observed that the porosity in the Statfjord Formation decrease with increase depth. The depth of Statfjord Formation in Snorre field wells is not very deep (2000 to 3000 m) compared to other parts in the North Sea so porosity is relatively high.

The hydrocarbon zones in Statfjord Formation are occurring in channelized sandstones bodies. The water saturation in hydrocarbon saturated zones are less than 30% (Figure 4.8) which show the 70% of oil is present in zone with good production capability. The high resistivity value along low water saturated zones confirms the presence of hydrocarbons.

Facies Analysis of the Lunde and Statfjord Formations

The facies analysis is carried out by using Gamma Ray log and the coarsening and finning upward trend in the log utilized to understand the depositional trend. The log pattern depends on the grain size, mud sand ratio, sandstone bed thickness and give idea about depositional cyclicity (Nystuen et al., 1989). The different authors (Hollander, 1987; Nystuen and Fält, 1995; Nystuen et al., 1989; Steel, 1993; Steel and Ryseth, 1990; Vollset and Doré, 1984) studied Lunde and Statfjord Formations of the northern North Sea. The depositional environment is interpreted as fluvial setup on a large alluvial plane. During late Permian to early Triassic the rift basin originated due to active crustal stretching in northern North Sea (Nystuen et al., 1989). The central part of the basin was dominated by alluvial plane which was crossed by rivers and fluvial coarse deposition was dominated on rift margins (Nystuen et al., 1989).

The small scale finning upward and coarsening upward sequences are marked shown by red arrows and large scale sequence is marked by blue colour (Figure 4.10). Nystuen et al. (1989) interpreted the small sequence with up-ward finning as single fluvial channel sandstone or sheet flood sandstone and upward coarsening as crevasse splay.

Chapter 5: Compaction Study

In this chapter the results and discussion of compaction study are presented. The P-wave velocity, bulk density, bottom hole temperature (BHT) and published compaction trends for clastic rocks are utilized to perform compaction study of Snorre field.

5.1 General Velocity versus depth trends

The velocity data from the well log is very useful tool for identification of different lithology, facies, fluids and overpressure compartments along sedimentary basin (Storvoll et al., 2005). In normally subsided basin rock properties such as V_p , porosity and density change as a function of depth. The reason for changing rock properties is the effects of mechanical and chemical compaction of rocks. The mechanical compaction is stress dependent and active until certain depth depending on geothermal gradient. The start of chemical compaction minimizes the effect of mechanical compaction and sediments starts to compact by thermodynamically driven processes. The increasing effect of compaction leads towards more dense rocks which in turn gives rise to velocity and density. The rock with uniform lithology and hydrostatic pore pressure will show increase in density and velocity concurrently decrease in porosity as a function of burial depth. The overpressure mechanism in rocks works against effective stress and reduce the effect of mechanical compaction. The transition from mechanical compaction to chemical compaction gives a sharp rise to velocity due to precipitation of cement in grain contact. The early cement in transition zone gives strength to rock framework which in turn increases velocity.

The P-wave velocity from 19 wells is plotted as a function of depth to find the velocity trend of Snorre field (Figure 5.1). Only the data sorted for mudstones and shales ($V_{sh} \geq 0.75$) are plotted to find V_p -depth trend of mudstones and shales. For the interpretation of compaction trend and its deviation from normal, shale data is superior than sandstone because porosity of the shales is less affected by diagenetic processes (Japsen, 1999). The data points are colour coded with temperature extracted from BHT. The BSF (Below Sea Floor) depth is used in compaction study. The well log based V_p -depth trend compared with some reference trends e.g. (Mondol, 2009; Mondol et al., 2007) to understand the general compaction behaviour of rocks in the Snorre field (Figure 5.1). The two main compaction regimes mechanical compaction (MC, marked by black line) and chemical compaction (CC, marked by red line) are observed. The change from MC to CC is marked by narrow black ellipse and called transition zone (Figure 5.1). The increase in velocity from mechanical compaction to chemical is easily identifiable from transition zone along the data. The velocity trend below the transition zone in chemical compaction regime does not show significant variation and increase gently with increasing depth. The high velocity stringers are observed and marked with green polygon in Figure 5.1. The stringers show velocity ≥ 4500 m/s, interpreted as carbonates.

In mechanical compaction zone the data interval at shallow burial depth marked with light brown line show relatively high velocity. The data interval belongs to Nordland Group of the Miocene to Pleistocene age (Storvoll et al., 2005). The relatively high velocity increase of the shallow buried Nordland group is also reported by Storvoll et al. (2005) and Zadeh et al. (2016). Storvoll et al. (2005) reported this relatively high velocity interval as interval 1N from the northern North Sea. Excluding the high velocity interval of the Nordland Group and the

data marked by grey ellipse the velocity data from mechanical compaction regime follow at least one of the reference curve kaolinite-silt 50:50 from (Mondol, 2009). Furthermore, the data points marked with grey ellipse in Figure 5.1 show velocity inversion (lower reading than upper and lower part). These data points fall on the reference curve 100% smectite (Mondol et al., 2007). During mechanical compaction smectite rich mudstones and shales compact relatively less compared to other mudstones (Mondol et al., 2007; Zadeh et al., 2016). The smectite mudstones compact less due to the high specific surface area and mineral bound water associated with smectite (Storvoll et al., 2005). Figure 5.1 shows the velocity trend after transition zone starts to deviate from the reference curves indicates the chemical compaction zone.

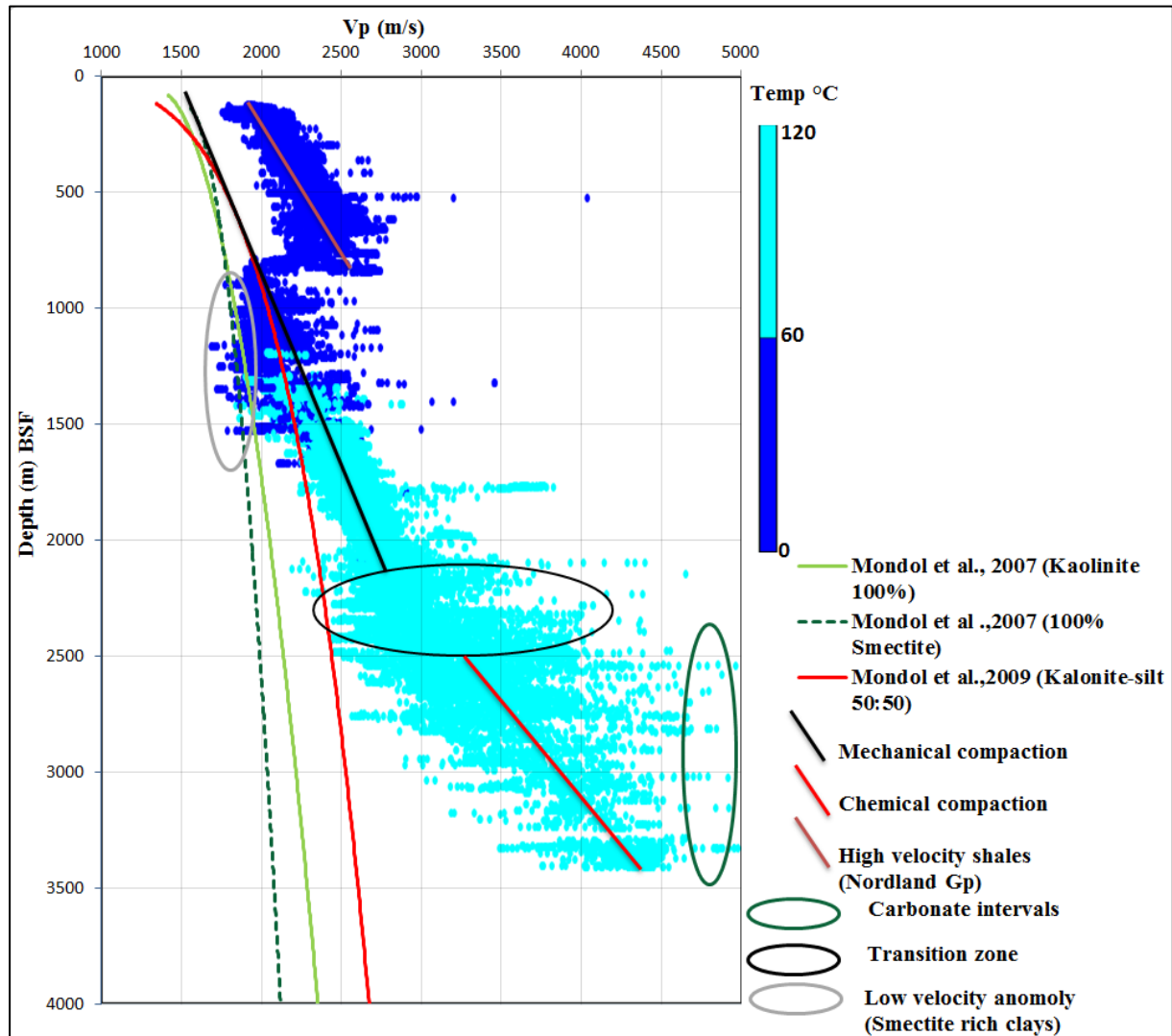


Figure 5.1: Velocity-depth trend for mudstones and shales ($V_{sh} \geq 75\%$) for studied 19 wells colour coded by present day temperature. One well (34/7-32) excluded due to absence of Vp data (Table 3.1).

5.2 Density versus depth trend

The bulk density data from 19 wells is plotted as a function of depth in Figure 5.2. Only the mudstones and shales ($V_{sh} \geq 0.75$) are included. The data is colour coded by temperature. The temperature data are acquired from BHT reported on NPD Factpages. The bulk density usually increases with increasing depth under hydrostatic pore pressure condition. In normally subsided basin, sediments undergo compaction due to increasing effective stress in mechanical compaction domain. Under chemical compaction at a certain limit the porosity become zero and sonic velocity approach the same value as sediment grain (Bowers, 1995). The divergence of the compaction dependent physical properties (e.g. low density, low velocity and high porosity) from normal trend mark the onset of overpressure (Bowers, 2002).

The mechanical and chemical compaction zones can also be observed from density-depth trend as same as velocity-depth trend. In mechanical compaction zone the density increase gradually. The sharp increase of density is not observed after transition zone. The data from Nordland Group show relatively high density trend and marked by brown line in Figure 5.2. The low density anomaly is observed in mechanical compaction zone and data points fall on experimental curve of smectite 100% (Mondol et al., 2007). The low density anomaly is marked by grey ellipse on Figure 5.2.

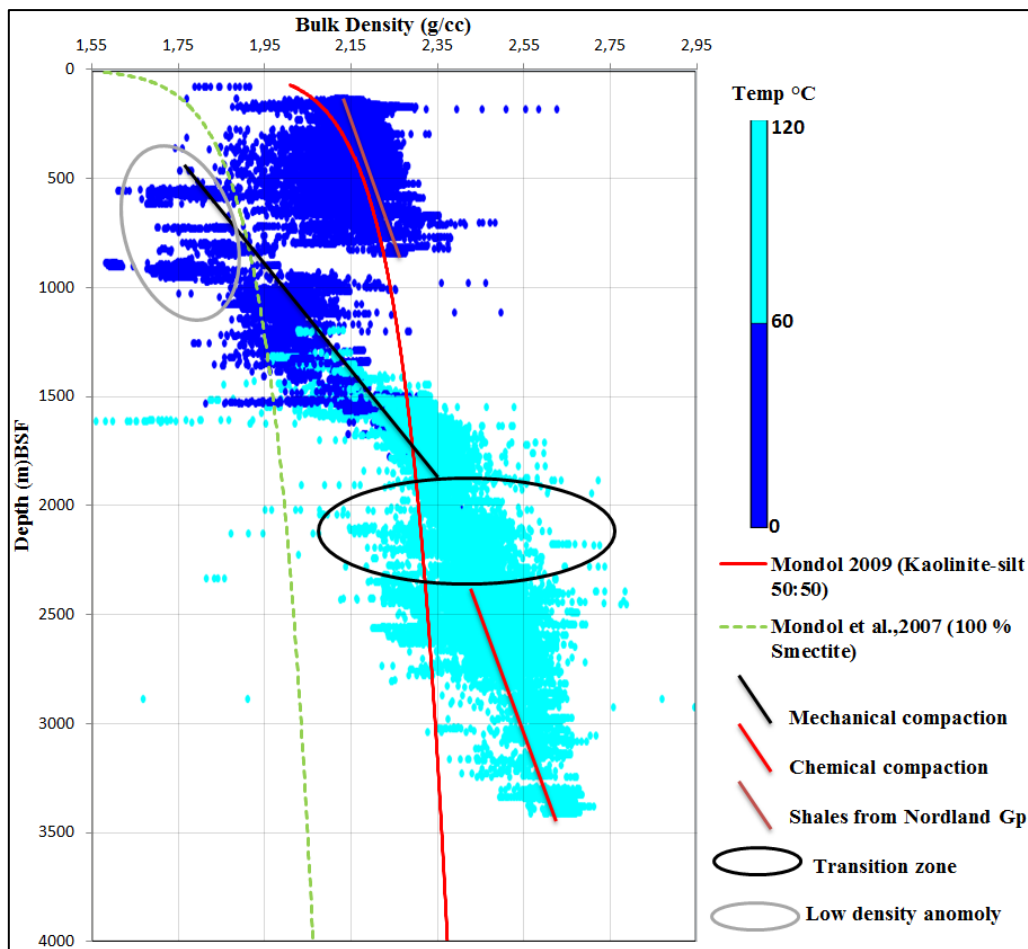


Figure 5.2: Density-depth plot from 19 wells. Data is colour coded by present day temperature.

5.3 Velocity versus density trend

The observation is further carried out by plotting V_p and bulk density (Figure 5.3). The data is plotted only for pure shales ($V_{sh} \geq 0.75$). The two different trends are easily identifiable and represent the mechanical and chemical compaction zones. The plot shows chemical compaction zone contains present day temperature greater than 60 °C. The high density and high velocity in chemical compaction zone represent the stiffness of sediments due to precipitation of cement. In mechanical compaction zone at low temperature the velocity increase at slower rate. However the increase in chemical compaction zone is sharp and significant.

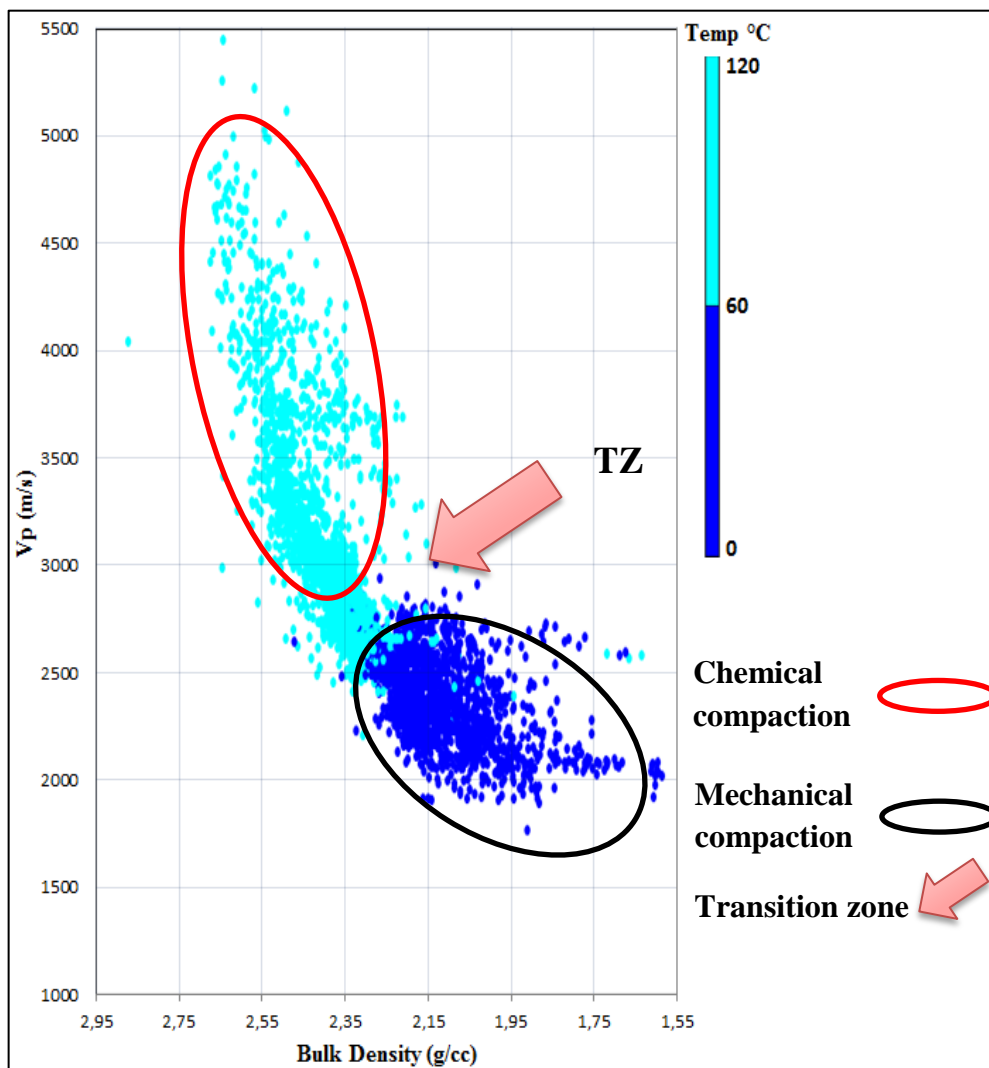


Figure 5.3: Velocity versus bulk density plot. Only for shales and mudstones data ($V_{sh} \geq 75\%$) are plotted from 19 wells and colour coded by present day temperature.

5.4 Trends from individual wells

In order to get better understanding, well 34/4-4 is chosen as the reference well to observe velocity trend individually. The Gamma Ray log is used additionally to control lithology. The Gamma ray-depth and Vp-depth trends are shown in Figure 5.4.

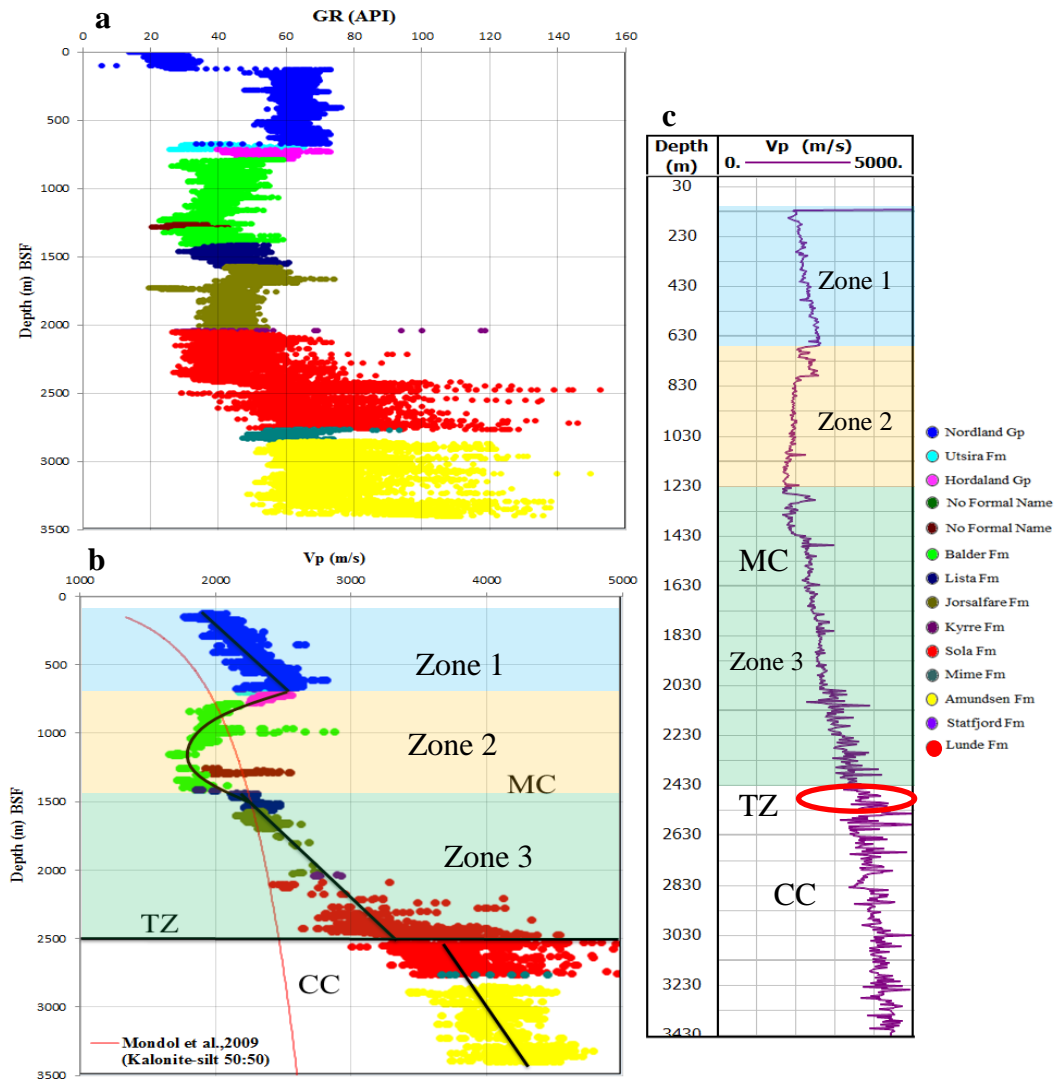


Figure 5.4: The Vp-depth trend of well 34/4-4; (a) GR-depth (b) Vp-depth colour coded by stratigraphic formations, (c) Vp log signature along the well. The zones are marked with different colour shading; TZ – transition zone, MC – mechanical compaction, CC – chemical compaction.

The velocity data is divided into three zones with different trends based on velocity gradient in mechanical compaction regime. The zone 1 shows relatively high velocity but the trend breaks at approximately 700 m (BSF) and decrease rapidly. The formation top colour code shows that the zone 1 is marine claystone of Nordland Group of Miocene age (See section 2.3.8). The zone 1 is marked by light blue shading. Zone 2 corresponds to significant decrease in velocity. The zone 2 is marked by light yellow shading (Figure 5.4). This zone has

relatively low gamma ray value as compared to zone 1. At the end of the zone 2 the velocity starts to increase until transition zone and marked as zone 3. The transition zone is marked at approximately 2500 m (BSF) and sharp increase in velocity is identified after start of chemical compaction. The transition zone lies in Lunde Formation.

The sharp increase in V_p after transition zone is due to onset of cementation. The high velocity stringers below transition zone different from normal trend are possible carbonate cemented zones. The low velocity intervals are also observed below the transition zone is interpreted as the presence of hydrocarbon that lower V_p . It is observed that the P-wave velocity above the transition zone is approximately less than 3000 m/s but after entering into chemical compaction regime the velocity exhibits more than 3000 m/s.

5.5 Transition from mechanical to chemical compaction

This section contains detailed analysis of the transition zone and the results for 14 wells with good data quality are shown in Table 5.1. An example of analysis for two wells 34/4-1 and 34/4-7 are given in Figure 5.5 which shows the change after transition zone. The velocity and density logs are used to identify the transition zone and the BSF depth is used in analysis. Only the shale data ($V_{sh} \geq 0.75$) is used to analyse the transition zone. The experimental curves of 50:50 kaolinite-silt (Mondol, 2009) and 100% smectite and kaolinite (Mondol et al., 2007) are used along plots as reference curves (Figure 5.5). The V_p -depth plot show clear change in velocity after the transition zone. The velocity increase is independent of lithology variation and obviously due to precipitation of cement. The results show that the transition zone for all wells is not at same depth. The transition occurs within same stratigraphic horizon in Lunde Formation except few wells (34/4-2 and 34/7-10) in which transition zone lie in Statfjord Formation (Table 5.1). In well 34/7-19, transition lie within Heather Formation. From transition zone, the data points move away from the reference curves. In Figure 5.6, the transition zone is observed in zoomed view to see the velocity variation. The velocity in mechanical compaction zone for both wells (34/4-1 & 34/7-1) shown in Figure 5.6 is less than 3000 m/s. After transition the velocity is greater than 3000 m/s.

Table 5.1: Approximate transition depth in the study area in different wells.

Well No.	TZ Depth (m) BSF	Formation
34/4-1	2100	Lunde Fm
34/4-2	2278	Statfjord Fm
34/4-4	2406	Lunde Fm
34/4-6	2276	Lunde Fm
34/4-7	2157	Lunde Fm
34/4-8	2410	Lunde Fm
34/7-1	2300	Lunde Fm
34/7-3	2304	Lunde Fm
34/7-4	2343	Lunde Fm
34/7-6	2328	Lunde Fm
34/7-8	2136	Lunde Fm
34/7-9	2300	Lunde Fm
34/7-10	2179	Statfjord Fm
34/7-19	2133	Heather Fm

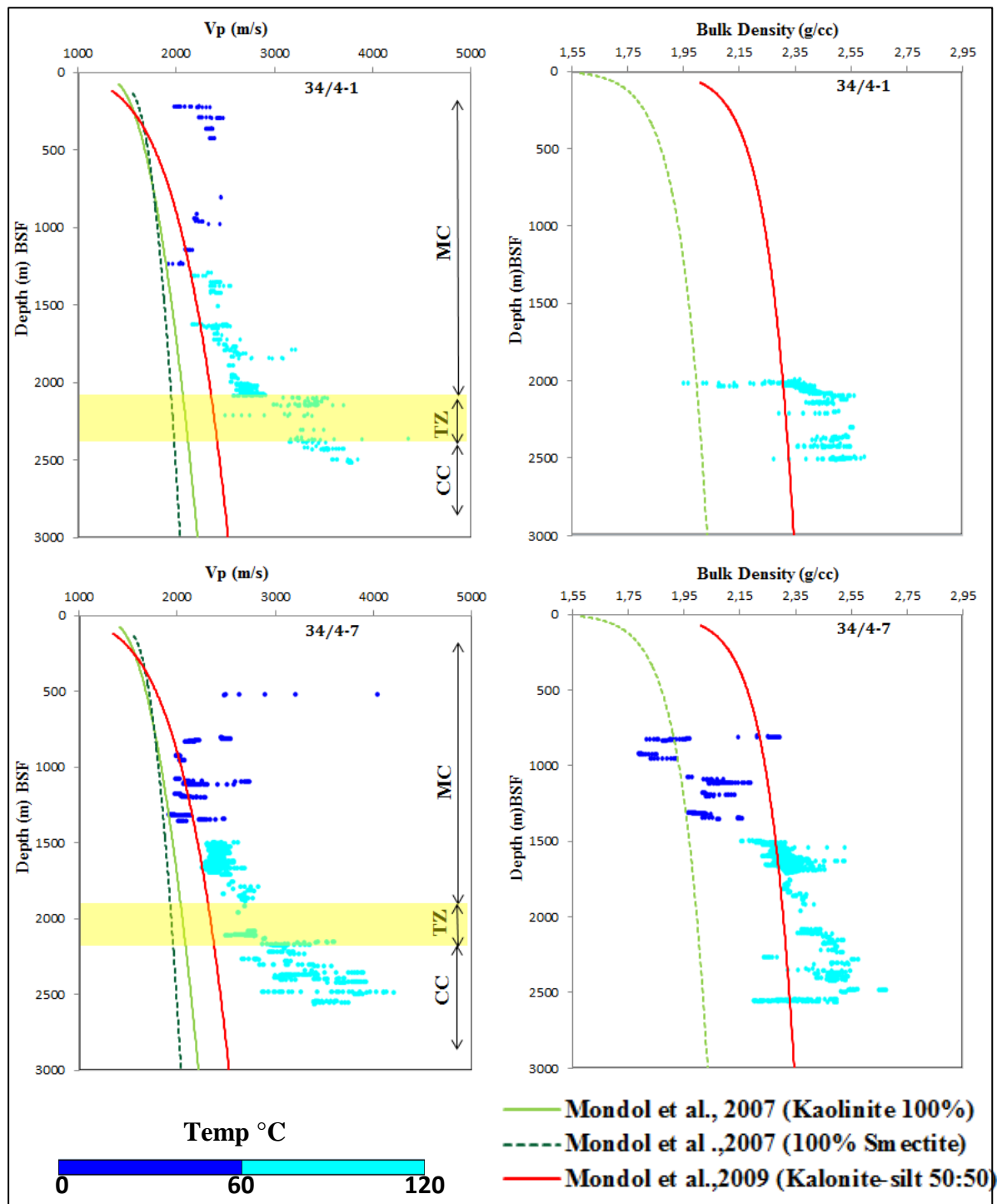


Figure 5.5: The Vp-depth data from well 34/4-1 and 34/4-7. The data plotted parallel with reference curves and colour coded by the present day temperature. The transition zone is marked with light yellow shading; MC – Mechanical compaction, CC – Chemical compaction, TZ – Transition zone.

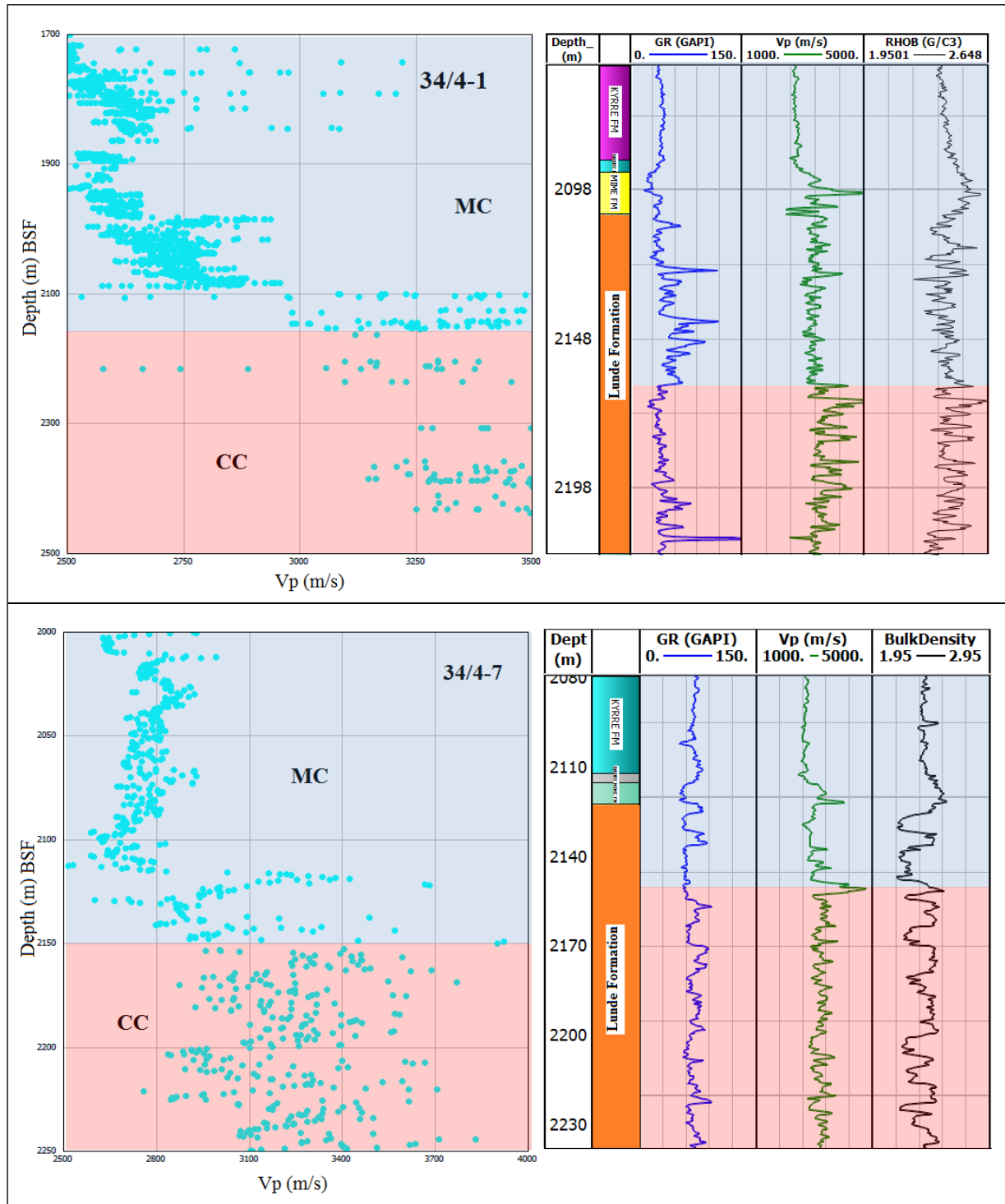


Figure 5.6: The zoomed view of the transition zone from well 34/4-1 and 34/4-7 with Gamma Ray log and density log; MC – Mechanical compaction, CC – Chemical Compaction.

5.6 Shale and Sand Compaction trend

Loose sediments lithified in sedimentary basins by various processes involving compaction, dissolution of grains and precipitation of cements (Bjørlykke et al., 1989). Sandstones and shales are most abundant lithology in a sedimentary basin. The sandstone and shales have

different mineralogical composition and both lithologies respond differently to various compaction processes. Due to higher porosity at the time of deposition clays and muds are altered more by mechanical compaction which results more changes in physical properties of mudstones with increasing burial depth (Mondol et al., 2007).

In Figure 5.7 the Vp data from 19 wells colour coded by present day temperature are plotted for sandy lithology only ($V_{sh} \leq 0.25$). The reference curve from Marcussen et al. (2010) is plotted to observe the compaction behaviour of sand. The plotted data also contain carbonate intervals and marked by red polygon (Figure 5.7). The sand data almost follow the reference sand line in mechanical compaction zone. After transition zone the data points move away from reference sand line. In mechanical compaction the data points marked with orange polygon show low velocity and fall below minimum velocity gradient line (Figure 5.7). The zone is possible over pressured sand and show low velocity. Over pressure mechanism has capability to lower the velocity. In chemical compaction zone the data points marked with grey polygon (Figure 5.7) also show lower velocity. The lower velocity is due to presence of hydrocarbons in sandstones of Lunde and Statfjord Formations.

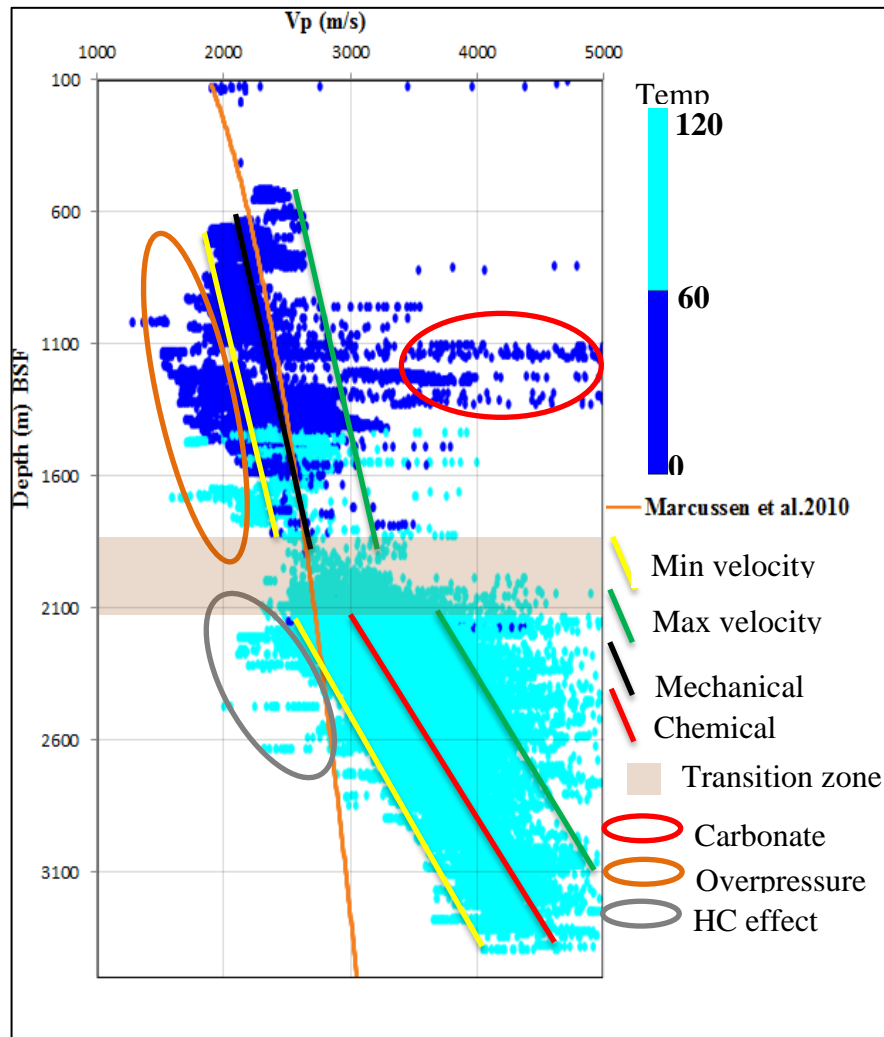


Figure 5.7: Velocity-depth trend of 19 wells sand data points. The data plotted only for sand lithology (V_{sh} cut-off ≤ 0.25).

In case of shales lithology the data points with shale volume greater than 0.75 are plotted as a function of depth and reference curves kaolinite-silt 50:50 (Mondol, 2009), Smectite 100% (Mondol et al., 2007) and Kaolinite 100 % (Mondol et al., 2007) are used to observe compaction trend. In mechanical compaction zone, the velocity-depth trend from 19 wells follows Mondol, (2009) (kaolinite-silt 50:50) reference curve but from transition zone clear deviation from reference curve is easily observable (Fig 5.8). The sharp increase of velocity after transition zone is easily observable for both shale and sandstone lithologies. The reference curves are generated by experimental studies and well explain the compaction of siliciclastic sediments under the influence of vertical effective stress. Therefore, the velocity trend in chemical compaction zone immediately deviates from reference curves after transition zone. The increase in velocity after transition zone is function of precipitation of the mineral cement.

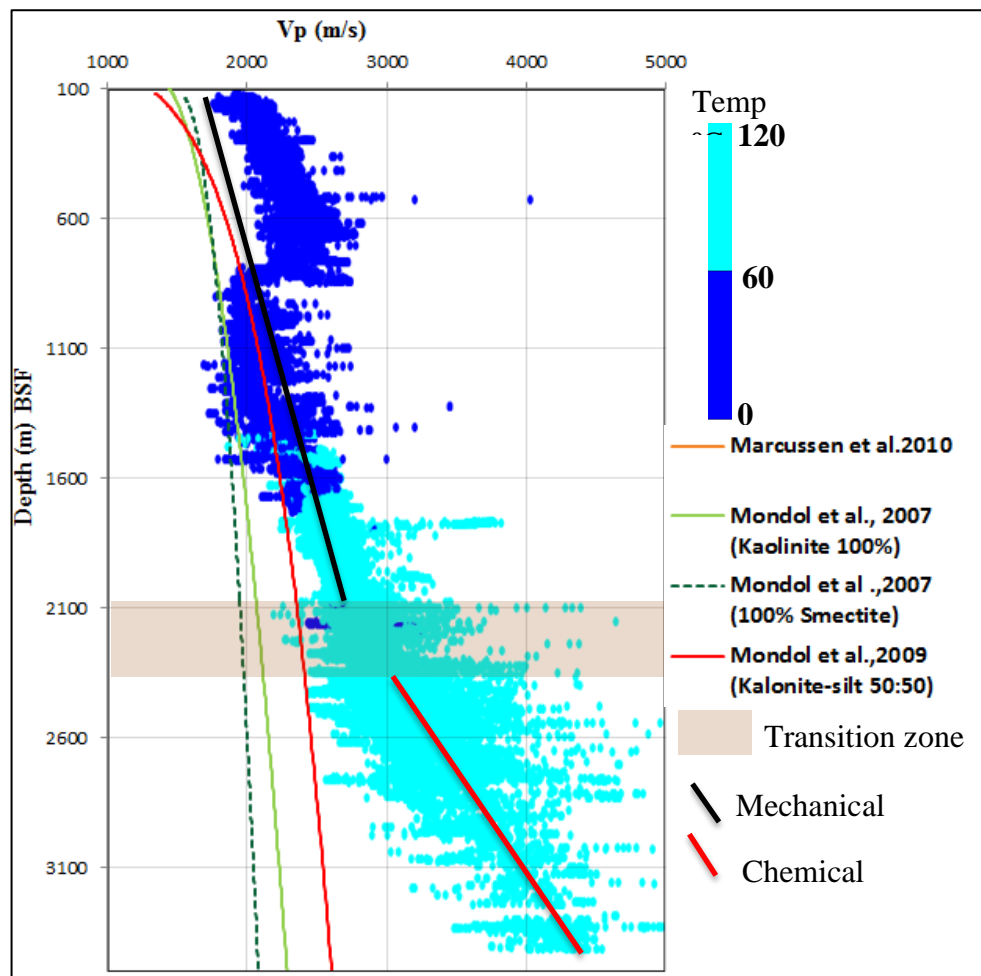


Figure 5.8: The velocity-depth trend for shale lithology ($V_{sh} \geq 0.75$). Data plotted from 19 wells.

The shale interval at shallow depth belongs to Nordland Group show rapid increase in velocity but the gradient break between 1000-1200 m depth (BSF) and then decrease. The lowest V_p value for shales in mechanically compacted part is 2300-2400 m/s and the approximately highest value is 2500-2700 m/s. In chemically compacted part the lowest average velocity for shales is 3000-3600 m/s and average highest value is 3800-4000 m/s.

5.7 Analysis of reservoir rock

As stated earlier, the reservoir intervals are present in both Lunde and Statfjord Formations in the Snorre field. Both formations also act as reservoir rock for many other fields on the Tampen Spur area. The stratigraphic thickness and other petrophysical parameters (V_{sh} , porosity and S_w etc.) are discussed earlier in chapter 4. In this section the compaction behaviour of the both reservoirs are analysed. The V_p data is plotted along with reference curve from Marcussen et al. (2010) to observe compaction trend (Figure 5.9). For compaction analysis only sand data points ($V_{sh} \leq 0.25$) are considered because the most of the hydrocarbon bearing zones belonged to sandstone lithology.

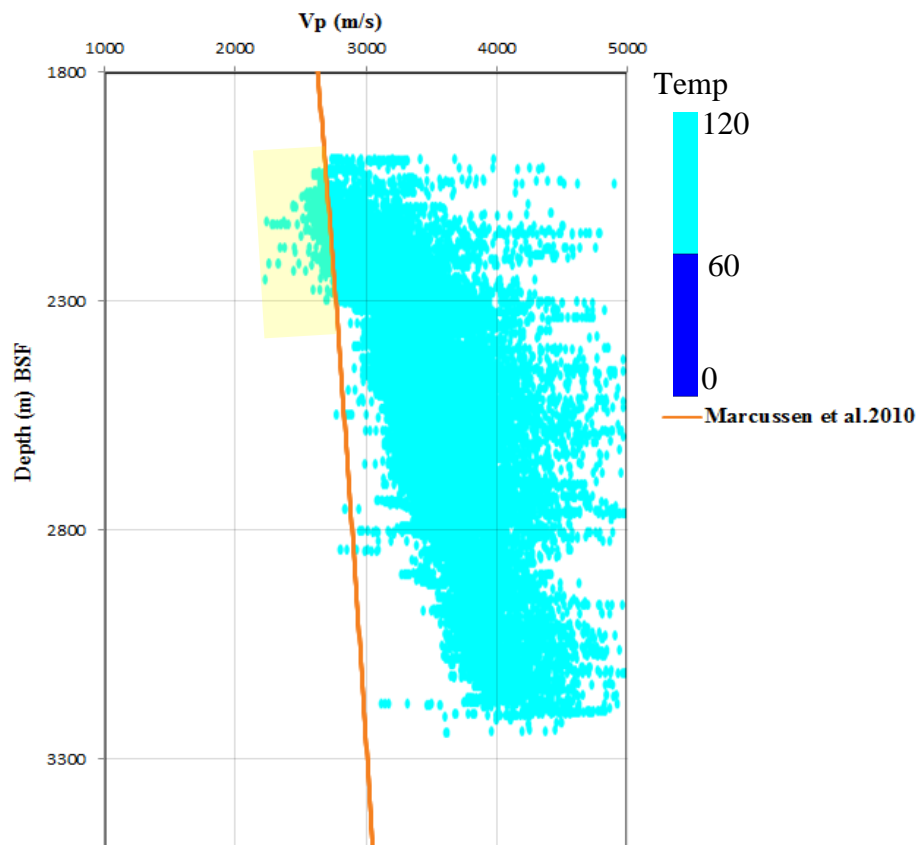


Figure 5.9: The velocity-depth data for reservoir interval (Lunde and Statfjord Formations). The reference sand trend from Marcussen et al. (2010) is also plotted. Data is plotted from 13 wells. The light yellow shading shows the presence of hydrocarbons. Data is colour coded by present day temperature.

In the Figure 5.9, upper part of the plot is showing close agreement with reference sand curve. The plotting of the data on the reference curve represent such part of the reservoir is present in mechanical compaction domain. The highlighted data on Figure 5.9 plotting below the reference curve. The low velocity in highlighted part of the reservoir is due to presence of the hydrocarbons to increase the sonic transit time or decrease the V_p . The presence of hydrocarbons are confirmed by plotting V_p -depth data and colour coded by water saturation in Figure 5.10.

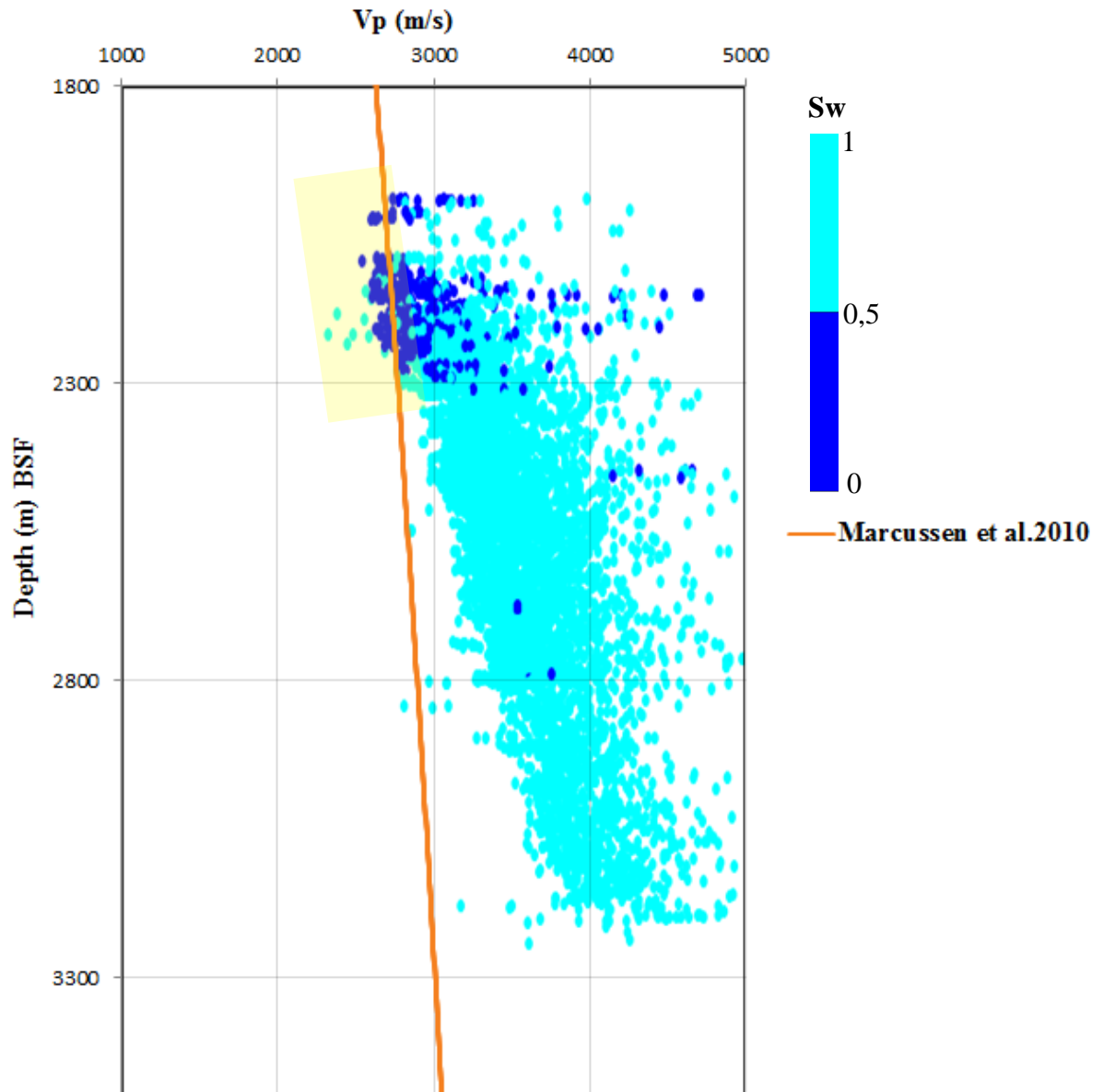


Figure 5.10: Vp-depth data for reservoir interval (Lunde and Statfjord Formations). Data colour coded by S_w (water saturation).

5.8 Time-temperature effect on compaction

For lithification of loose sediments into a sedimentary rock within basin, various factor involved. The most important factors during compaction of sediments in chemical compaction domain are time and temperature. The mechanical compaction of sediments undergo at shallow depth and starts immediately after burial without any effect of the temperature. At deep burial depth the compaction is temperature dependent because it is the function of the mineral cement precipitation. Other factors such as mineralogy, presence of catalyst, time also influence the chemical reaction. The temperature is most important as it is considered the

activation energy to start the chemical reaction (Storvoll and Brevik, 2008). The cement precipitation process in siliciclastic rocks is notably slow therefore time is also important for compaction of sedimentary rock.

The aim of this section is to observe the compaction in the study area by using present day temperature data. The result of all 14 wells with good data quality (presented in Table 5.2) and well 34/7-1 have been used for further study. In Figure 5.11 Vp-depth data plotted from well 34/7-1 and colour coded by present day temperature.

Table 5.2: Temperature in the transition zone in 14 wells utilized in Vp-depth plot.

Well Name	Temperature °C	Depth of TZ (m) (BSF)
34/4-1	70	2100
34/4-2	73	2278
34/4-4	74	2406
34/4-6	75	2276
34/4-7	75	2157
34/4-8	77	2410
34/7-1	70	2300
34/7-3	71	2304
34/7-4	51	2343
34/7-6	74	2328
34/7-8	70	2136
34/7-9	70	2300
34/7-10	76	2179
34/7-13	79	2414

The significant increase in velocity is observed for well 34/7-1 at temperature 70 °C (Figure 5.11). The increase is from approximately 2600 m/s to 3200 m/s after transition zone. The increase in density from approximately 2.3 g/cc to 2.5 g/cc is also observed when temperature reaches to 70 °C. The early cement at grains contact causes the grain framework to be stable and minimize the effect of the mechanical compaction. The precipitation of the mineral cement at grain contact gives sharp increase to velocity but on the other hand not cause significant porosity loss or density increment. The porosity reduction due to cementation is time dependent. With increase in temperature, burial depth and burial duration porosity loss increase. At deep burial depth the cementation is main porosity predator. After the onset of cement precipitation the porosity reduction will continue until the temperature is above 60°C.

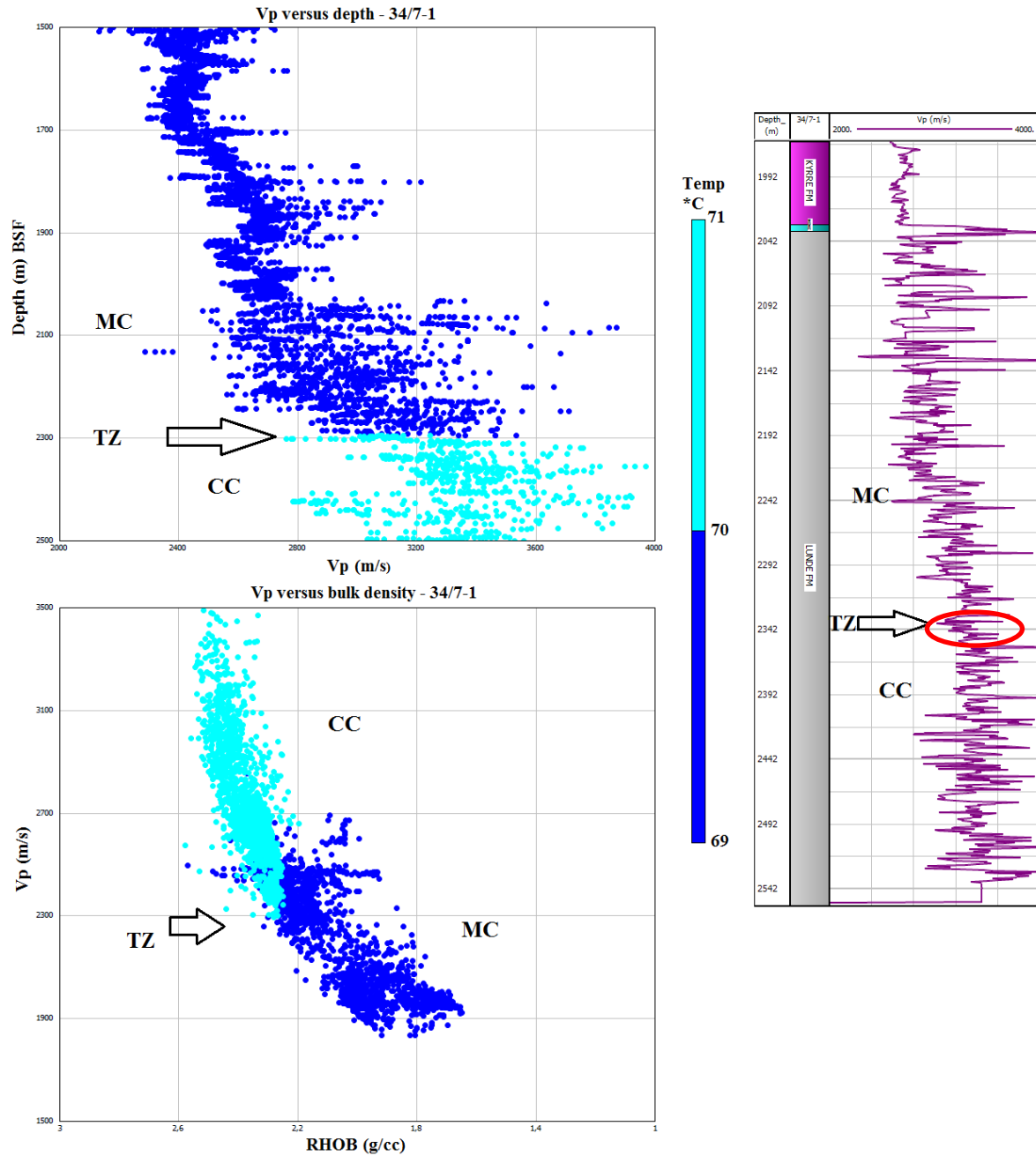


Figure 5.11: Vp, density and depth cross-plots colour coded by temperature from well 34/7-1. On right side the Vp signature from well 34/7-1 is also shown.

5.9 Compaction of reservoir rocks

The aim of this section is to investigate the reservoir units of Snorre field with respect to burial history and compaction processes act on them to change their properties. A general summary of compaction study of targeted reservoirs is shown in Table 5.3. The Statfjord Formation is penetrated by most of the studied wells experienced only by mechanical compaction. The Statfjord Formation penetrated by few other wells (34/4-2, 34/4-8, 34/7-10 and 34/7-13) located in the transition zone. Moreover, Statfjord Formation in one well 34/7-2 experienced both mechanical and chemical compaction. On other hand, in few wells, the

upper part of the Lunde Formation is situated in the mechanical compaction domain while the upper part of the Lunde Formation in most of the wells is in transition zone. The lower part of Lunde Formation of all wells is situated in the chemical compaction domain.

Table 5.3: The present locations of studied reservoir units (Lunde and Statfjord Formations) with respect to compaction processes.

Lunde Formation				
Well	Depth (m) BSF	TZ depth	The present location of the reservoir units with respect to compaction processes	
			Upper Lunde	Lower Lunde
34/4-1	2105 – 2403	2100	Within TZ	Chemical compaction
34/4-2	2350 – 3258	2278	Within chemical compaction	
34/4-4	2054 – 2773	2406	Within MC	Chemical compaction
34/4-6	2178 – 2754	2276	Within TZ	Chemical compaction
34/4-7	2122 – 2560	2157	Within TZ	Chemical compaction
34/4-8	2562 – 2712	2410	Chemical compaction	
34/7-1	2036 – 2547	2300	Within MC	Chemical compaction
34/7-3	2184 – 3082	2304	Within MC	Chemical compaction
34/7-4	2283 – 2770	2343	Within TZ	Chemical compaction
34/7-6	2320 – 3207	2328	Within TZ	Chemical compaction
34/7-8	2104 – 2438	2136	Within TZ	Chemical compaction
34/7-9	2086 – 2891	2300	Within TZ	Chemical compaction
34/7-10	2357 – 2660	2179	Chemical compaction	
34/7-20	2806 – 2846	2300	Chemical compaction	
Statfjord Formation				
34/4-2	2250 – 2350	2278	Within transition zone	
34/4-8	2411 – 2525	2410	Within transition zone	
34/7-3	2086 – 2184	2304	Within mechanical compaction	
34/7-4	2190 – 2283	2343	Within mechanical compaction	
34/7-6	2177 – 2320	2328	Within mechanical compaction	
34/7-8	1987 – 2104	2136	Within mechanical compaction	
34/7-10	2204 – 2357	2179	Within transition zone	
34/7-13	2451 – 2554	2414	Within transition zone	
34/7-20	2735 – 2846	2300	Within chemical compaction	

For further analysis the V_p data of Statfjord Formation from well 34/7-3 are plotted with the reference sand compaction curve suggested by Marcussen et al. 2010 (Figure 5.12a). In well 34/7-3 the Statfjord Formation is present within mechanical compaction domain (Table 5.3). The data points are plotting on the top of the reference sand compaction curve valid for mechanical compaction (Figure 5.12a). Similarly the V_p data of Lunde Formation are plotted with reference sand compaction curve (Figure 5.12b). The upper part of the formation is present in the mechanical compaction regime whereas the lower part is in the chemical compaction regime (Table 5.3). The Figure 5.12b shows that data from mechanically compacted part is plotting close to reference sand curve but after transition from mechanical to chemical compaction the data from lower part is deviating from reference curve.

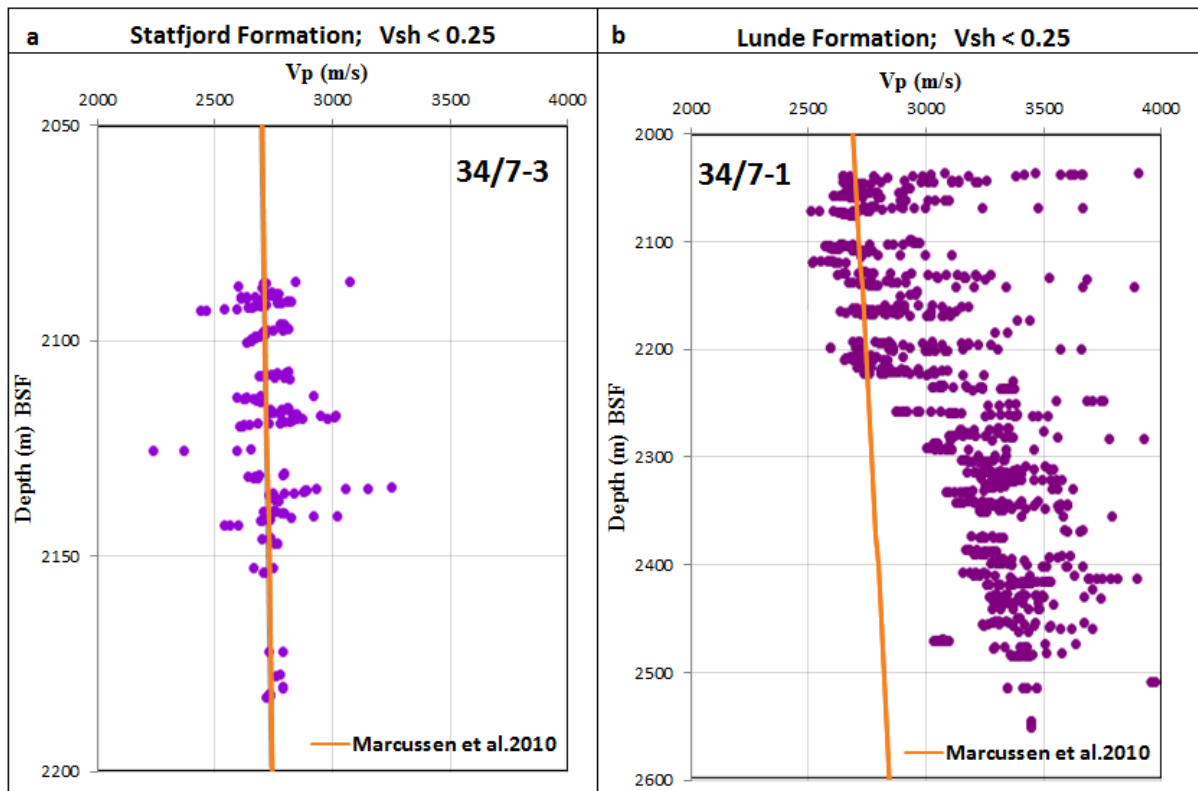


Figure 5.12: V_p -depth data of Statfjord Formation from well 34/7-3 (left) and Lunde Formation from well 34/7-1 (right). The data is plotted for sandstone ($V_{sh} < 0.25$).

5.10 Exhumation studies

The tectonic evolution of any sedimentary basin results subsidence and/or uplift of rocks in sedimentary basin. The consequences of the uplift, erosion, reburial and/or reuplift markedly affect the compaction of rock and affect whole petroleum system. In compaction studies for reservoir characterization, the exemption of the exhumation studies can establish lot of uncertainties in results. For exploration success understanding of the exhumation estimates is extremely important (Baig et al., 2016).

In this section the V_p -depth data from selected wells with good data quality are used to estimate any possible uplift in the study area. The BSF depth is used for exhumation studies. Furthermore, only shale data ($V_{sh} \geq 0.75$) is used to minimize uncertainties in uplift

estimation. It is explained earlier in chapter 3 section 3.4.7 that the mismatch between reference velocity-depth curve and velocity-depth data from studied well in mechanical compaction zone (high velocity compared to observe velocity for reference curve represents normally compaction) leads to upliftment in the area. The varieties of published reference curves are available in literature. The mechanical compaction depends on mineralogy and sediments architecture, it is most important to choose standard reference curve for exhumation studies. The mineralogical resemblance of the data set used for the reference curve and current data under study is necessary. In Figure 5.13 the data from 11 wells are plotted with different reference curves. The data is plotted before exhumation correction (left) and after exhumation correction (right). The exhumation correction is applied by using reference curve Mondol, (2009).

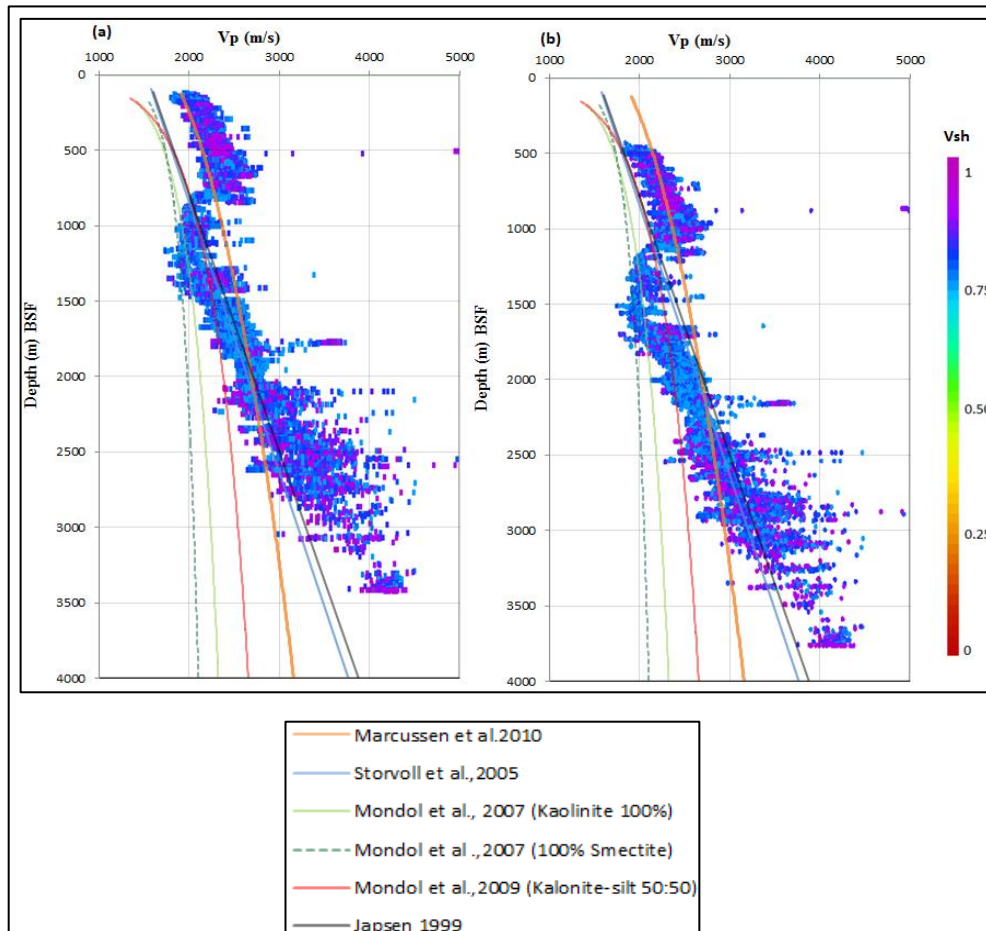


Figure 5.13: The Vp-depth data plotted from 11 wells with different published reference curves; (a) before exhumation (b) after exhumation. The uplift correction is applied from Mondol, (2009) kaolinite-silt 50:50.

The reference curve from Mondol, (2009) is used for uplift estimation. In well 34/7-1, (Figure 5.14) the uplift estimated by Kaolinite-Silt (50:50) reference curve Mondol, (2009) is 350 m. The results for exhumation for all wells are shown in Table 5.4. The example of wells (34/4-4, 34/4-6, 34/7-10 and 34/7-16) is shown in Figure 5.15.

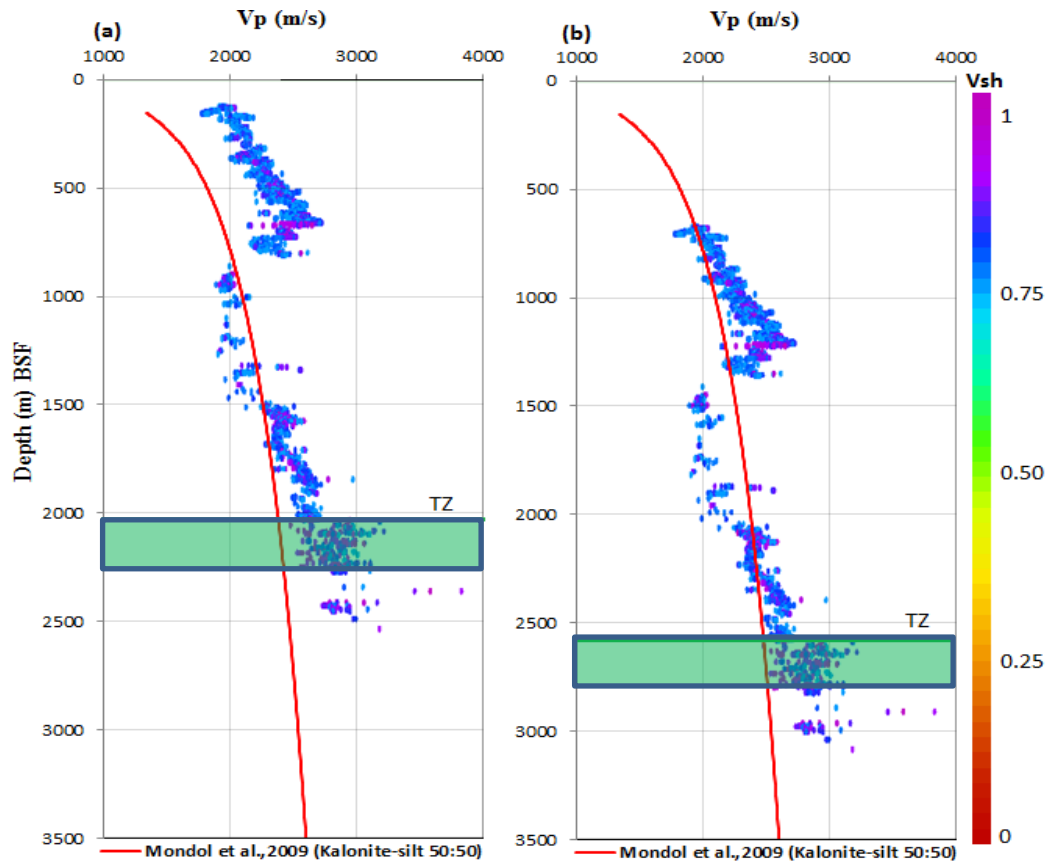


Figure 5.14: The V_p -depth data of Well 34/7-1; (a) data before exhumation correction (b) data after exhumation correction.

Table 5.4: The total estimated uplift (m) in different wells by using reference curve from Mondol, (2009).

Well	Estimated Uplift (m) from Mondol, (2009) kaolinite-silt 50:50
34/4-1	300
34/4-4	350
34/4-6	400
34/4-7	250
34/7-1	350
34/7-3	200
34/7-4	200
34/7-9	300
34/7-10	350
34/7-13	200
34/7-16	350
34/7-19	200

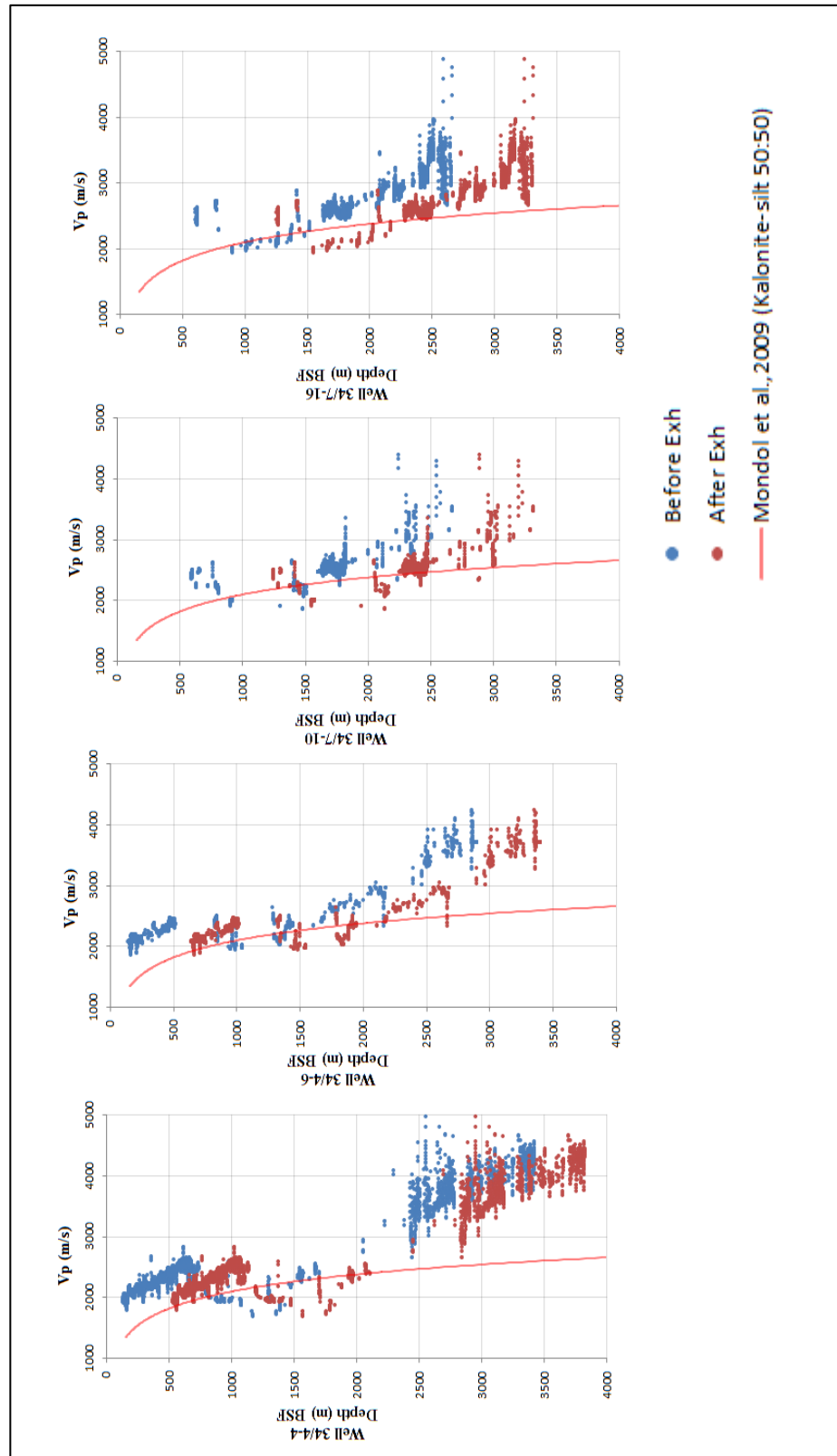


Figure 5.15: The Vp-depth data plotted from four wells. The data before exhumation and after exhumation are plotted. The correction is applied by kaolinite-silt (50:50) curve (Mondol, 2009).

5.11 Discussion

The burial and diagenetic history of reservoir has crucial impact for reservoir characterization. Reservoir properties strongly altered during compaction and burial diagenesis, provisional on type of compaction process. Siliciclastic rock undergo two type of compaction processes; mechanical compaction which is stress dependent without any chemical change of sediment while other type is chemical compaction which is governed by dissolution and precipitation of minerals. The temperature and burial history of reservoir is vital to understand the type of compaction regime which reservoir experienced.

In this study, the well log data of 19 exploration wells were utilized to observe compaction process experienced by Lunde and Statfjord Formations along Snorre field. The present day temperature is used as additional tool to differentiate between compaction regimes by using geophysical properties of rocks. Later approach has been made to estimate possible uplift in the study area.

5.11.1 Velocity, density trends with depth

The velocity-depth response of 19 wells plotted together shows increase with respect to burial depth (Figure 5.1). The data is exclusively plotted for shales ($V_{sh} \geq 0.75$). The increase of rock physical properties with depth is not along a single restricted trend. Excluding the velocity trend of top approximately 700 to 800 m (BSF) interval marked by brown line on Figure 5.1, the data is increasing along single confined trend with depth up to approximately 2100- 2400 m depth (BSF). The data up to approximately 700 to 800 m (BSF) is discussed in next section. The most noticeable change is observed from 2000-2400 m (BSF) and marked by black ellipse on Figure 5.1, where V_p increase abruptly. Above the abrupt increase of V_p (excluding data up to 700 to 800 m), the velocity data is following the reference curve (50:50 kaolinite-silt) of Mondol, (2009). The sudden shift of V_p below 2000-2400 m burial depth (BSF) dragged data points away from reference curves. This sudden shift of V_p is marked as onset of cement precipitation and the zone enclosed in black ellipse on Figure 5.1 is considered to be transition from pure mechanical compaction domain to chemical compaction. Above transition zone the compaction is governed by rearrangement and crushing of grains. The reduction in porosity occur due to compaction which results from grains reorientation and crushing (Bjørlykke, 1999). The driving force for mechanical compaction is vertical effective stress that increases with burial depth of the rocks. The vertical effective stress is the over burden pressure of overlying rocks. The close agreement of data with reference curve of Mondol, (2009) above transition zone confirms that sediments are compacted mechanically under vertical effective stress.

The depth of transition zone corresponds to temperature 70-100 °C and confirmed by colour coding by present day temperature in Figure 5.1. This temperature range is same as suggested by Bjørlykke, (1999) for onset of chemical compaction. The chemical compaction is thermodynamically driven process. Thermodynamically unstable minerals cause dissolution and precipitation of new minerals which are more stable at high temperature. Therefore, temperature is the key factor for chemical compaction domain. Once the chemical compaction domain approach, mechanical compaction is no more effective because the initial mineral cement cause stiffening of grain framework. The stiffening due to initial cement gives sharp response of velocity but on the other hand, porosity reduction is not significant. Therefore porosity-depth trend is not applicable to mark the onset of chemical compaction domain. The porosity reduction continues with continuation of cementation with respect to depth until

temperature is above 60 °C. The reference curve of Mondol, (2009) kaolinite-silt 50:50 represents the close lithology agreement to shales, and represents pure mechanical compaction for shales. The dragging of data away from the reference curve is argument for start of chemical compaction domain from depth of 2000 to 2400 m (BSF) in Figure 5.1.

Considering bulk density-depth trend (Figure 5.2), above the transition zone bulk density is increasing with considerably steep gradient. The mechanical compaction causes increase of density significantly. The net volume decrease is porosity loss during mechanical compaction domain. As compared to Vp-depth trend, density is not showing sharp increase after transition zone because initial cement cause the grain framework stiffening without making rock significantly dense. Below transition zone the bulk density increase progressively, with increasing cementation and burial depth. By plotting bulk density across velocity (Figure 5.3), is additional approach to mark transition zone. Figure 5.3 shows density increase in low temperature mechanical compaction domain while Vp increase is not significant. On other hand when temperature crosses the threshold limit for chemical compaction domain (70-90 °C), sudden velocity kick is observed.

Anomalies in Vp/density versus depth trends

In an ideal scenario velocity and density increase progressively with respect to depth and compaction domain without any observed anomaly. Besides temperature and depth several other factors has influence on compaction of siliciclastic rocks. The most common and important influencing factors are grain size, shape, mineralogy. The common minerals in mudstone are kaolinite, illite, smectite and chlorite out of which smectite is most fine grained mineral with large surface area (700 m²/g) and kaolinite is coarsest (Mondol et al., 2008b). One other factor that effect compaction is overpressure mechanism. The low permeability of shales can cause overpressure that work against vertical effective stress and reduce the effect of compaction in mechanical compaction domain.

Referring to Figure 5.1 and Figure 5.2, certain anomalies are observed from velocity-depth and density-depth trends which are necessary to discuss. First of all the velocity and density-depth trend of until 700 to 800 m burial depth (BSF) shows a steep increase and velocity reach up to 2500 m/s at approximately 800 m depth. This data is not showing any agreement with reference curves (Figure 5.1). The close interpretation reveals that these sediments belong to Nordland Group. This steep increase of velocity of Nordland Group sediments is also reported by Storvoll et al. (2005) and Zadeh et al. (2016) from other parts of the northern North Sea. The Miocene to Pleistocene Nordland Group sediments are marine sands and shales with glaciomarine sediments near top (Storvoll et al., 2005).

The other anomaly is marked by grey ellipse on Figure 5.1 and Figure 5.2. The data points of the Hordaland Group are showing low velocity, density and falling on 100% smectite reference curve from Mondol et al. (2007). The decrease in velocity is because of high smectite content in shales of Hordaland group. The high surface area and mineral bound water in smectite is the reason for low density for smectite as compared to other clay minerals. The interpretation is verified against Storvoll et al. (2005) and Zadeh et al. (2016). Both authors reported the decrease of velocity and density in Hordaland Group. The high smectite content in Cenozoic mudstones of the North Sea is reported by Berstad and Dypvik, (1982) which is quoted in Zadeh et al. (2016).

Below transition zone high velocity stringers are marked by green colour ellipse (Figure 5.1). The velocity stringers are showing velocity up to 5000 m/s. The stingers are due to presence

of carbonate cemented intervals in Lunde and Statfjord sandstones. The presence of carbonates in Lunde and Statfjord Formations are verified from published literature (Khanna, 1997; Morad et al., 1990; Morad et al., 2009; Muller, 1996).

5.11.2 Temperature and transition zone within the studied wells

The depth and temperature from which the effect of mechanical compaction became ineffective due to onset of mineral cement precipitation is called transition zone. Transition zone is not a single point or line; on the other hand it can range from meter to several meters. The temperature for onset of chemical compaction is 70-90 °C. In any sedimentary basin transition zone depth depends on geothermal gradient of the basin. In a basin like Gulf of Mexico with low geothermal gradient the transition zone could be occur at much deeper depth. The present day transition zone depth map of this study area is shown in Figure 5.16. The present day depth of transition zone ranges from 2000-2550 m (BSF) along different wells. The present day depth of transition zone is marked on the basis of abrupt increase in velocity. The increase of TZ depth from east to west can be observed from map (Figure 5.16). Although the difference of TZ depth is not very high but the structural complexity of the area can explain the difference of TZ along each well.

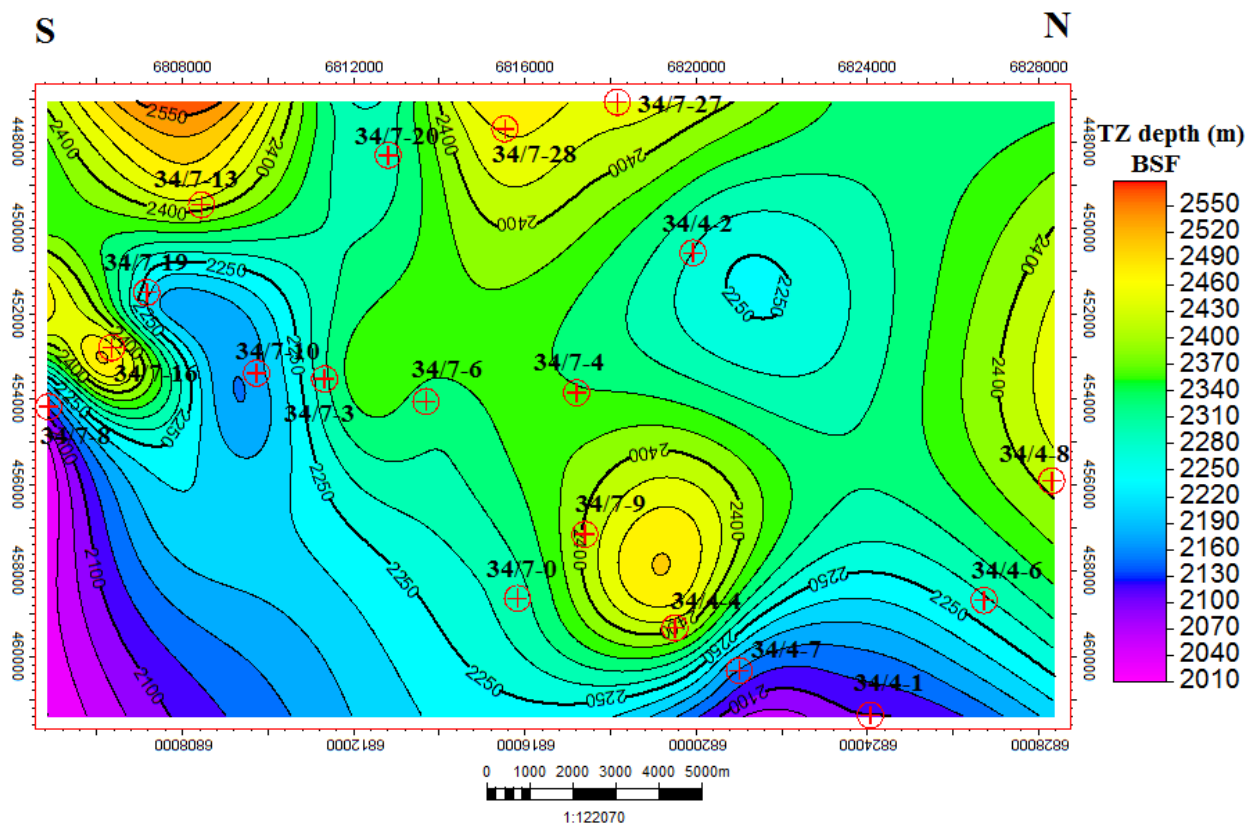


Figure 5.16: Present day transition zone depth map in the study area.

The geothermal gradient map calculated for each well by using bottom hole temperature is shown in Figure 5.17. The low geothermal gradient anomaly (22 °C/km) at well 34/7-4 is due to very low bottom hole temperature given by Norwegian Petroleum Directorate (NPD 2016). Comparing the transition zone depth map (Figure 5.16) and geothermal gradient map (Figure 5.17) it can be seen that the eastern part of field contain shallow TZ depth and high geothermal gradient compared to other parts. This assumes that the temperature for chemical

compaction in eastern part is attained prior than western part because of high geothermal gradient.

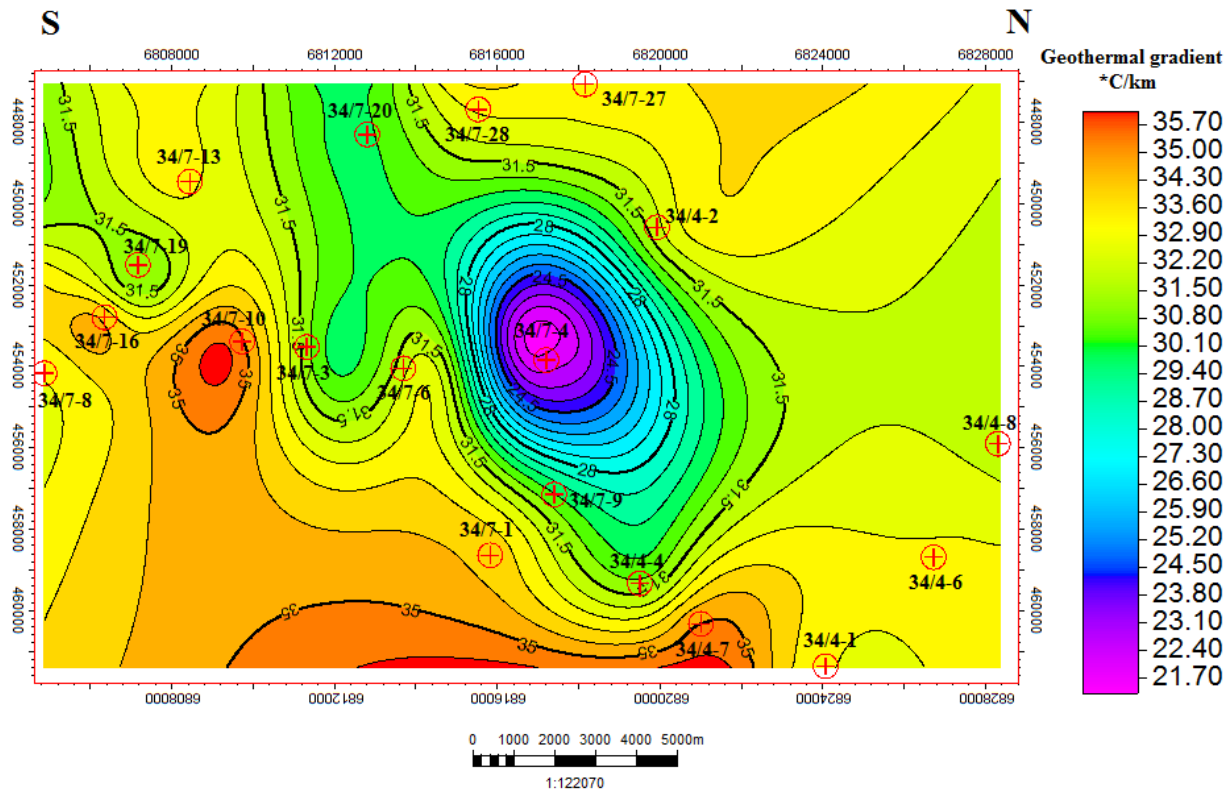


Figure 5.17: Geothermal gradient map within study area.

The Figure 5.18 shows the map of possible temperature at transition zone (TZ). Excluding the anomaly of low temperature at well 34/7-4, all the wells have temperature above 70 °C. The temperature can be assumed as lower threshold for onset of cement in study area. The interpretation of temperature higher than 70 °C at transition zone gives more confidence that sharp Vp increase picked from each well is purely due to mineral cement precipitation. The temperature data of this study relies on bottom hole temperature provided by NPD. Error and uncertainties could present in temperature because of incorrect BHT data, but still observation is valid to understand the temperature range experienced by reservoir in the Snorre field. The transition zone has been identified in Lunde Formation for mostly wells which is principal hydrocarbon reservoir of Snorre field. The transition zone data is useful to distinguish the reservoir properties of Lunde Formation in mechanically compacted part and chemically compacted part. Later the rock physics study will be aided from temperature and depth information of two compaction regimes of the Lunde Formation.

The actual paleogeothermal gradient is unknown. The temperature experienced by reservoirs in past can be different from current temperature. Such limitations evolve some uncertainties about the interpretation of transition zone depth and actual temperature at the time of onset of the quartz cementation but still the results are useful to understand the compaction domain experienced by the reservoir. In aspect of the reservoir quality the compaction domain of the reservoir is of great importance.

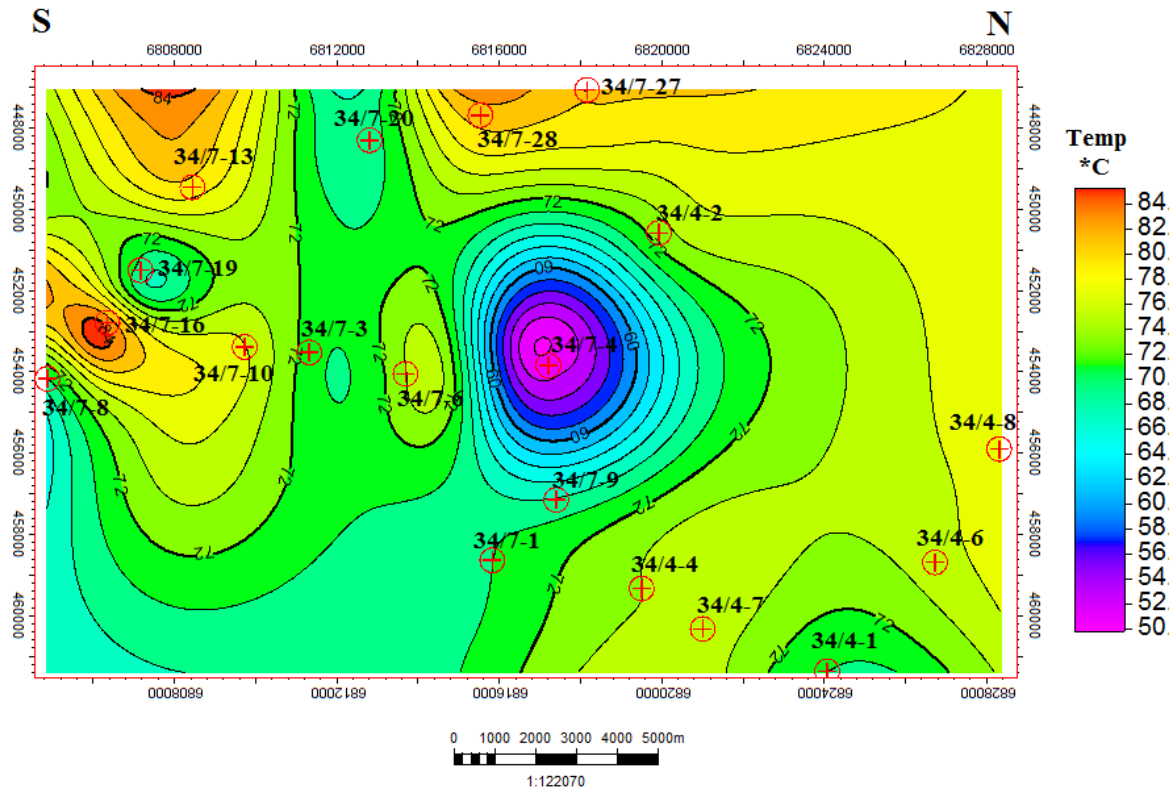


Figure 5.18: The possible present day temperature at transition zone within the study area.

5.11.3 Effect of overpressure

The overpressure in sedimentary rock refers to pore pressure greater than hydrostatic pressure. The overpressure is generated due to quick burial of low permeable rocks because fluids cannot escape rapidly during burial. This mechanism benefits sediments to retain high porosity, as overpressure holds vertical effective stress along with sediment grains. In term of rock physical properties overpressured compartments along sedimentary basin shows velocity reversal (lower than actual trend) and also decrease of bulk density. The mechanism is most common in mudrocks because of low permeability. Other reasons for overpressure are hydrocarbon generation and migration, compression from tectonic forces, maturation of kerogen, addition of water from mineral structure to pore water.

In this study the presence of overpressure is recognized in Hordaland Group sediments. As discussed earlier the smectite rich sediments of Hordaland Group show velocity reversal due to certain properties of smectite mineral. The low permeability of smectite can generate overpressure at quite shallow depth (Storvoll et al., 2005). In case of bulk density-depth relation (Figure 5.2), the data marked with grey ellipse is plotting below the experimental curve of brine saturated 100 % smectite suggested by Mondol et al. (2007). This is referred as presence of overpressure which causes lowering of bulk density. In Figure 5.7, the velocity reversal for sand data points ($V_{sh} \leq 0.25$) is observed in same area along V_p -depth plot. The data points within the light orange ellipse show lower value than the minimum velocity gradient line. The overpressure mechanism is also reported by Zadeh et al. (2016) for Hordaland Group from northern, North Sea. Referring to Figure 5.7, velocity reversal can be seen in another zone which is marked by a grey ellipse. The depth of this zone is below 2000 m (BSF) which corresponds to burial depth of hydrocarbon filled reservoirs of the Snorre

field. This shows the reservoir is overpressured due to presence of hydrocarbons. In Figure 5.9 all the data points of the Lunde and Statfjord Formations are plotted from 13 wells and experimental compaction curve of sand suggested by Marcussen et al. (2010). The shaded data below the experimental curve is another argument for possibility of overpressure in reservoir sandstones. The presence of hydrocarbon also cause decrease in V_p as compared to brine.

The petrophysical analysis reveals that the Lunde and Statfjord Formations are single and multi storey channel sandstone bodies with fine grained overbank deposits and floodplain mudstones. The presence of carbonate intervals with in the reservoir sandstones is reported by Morad et al. (1990), Morad et al. (2009), Muller, (1996) and Khanna, (1997). The internal shale layers and completely carbonate cemented intervals cause internal flow barrier which leads to overpressure.

5.11.4 Uplift estimation

The uplift estimation is important for reservoir understanding because it gives the actual depth and temperature history of the reservoir and source rock. The controlling factor for cement precipitation and source rock maturation is temperature which is dependent on burial depth. The effect of uplift on rock properties is significant in uplifted basin like Barents Sea, but North Sea is a subsiding Sea therefore any estimated uplifted is assumed to be related to rotated fault blocks and structures.

5.12 Uncertainties

The change from mechanical compaction to chemical compaction is marked by picking the abrupt increase in V_p which assumed as onset of quartz cementation and grain framework stiffening. The abrupt increase could be lithologic effect and in such case transition zone would be marked wrong. The careful interpretation is required in presence of carbonate cemented intervals close to expected transition zone boundary. The high V_p in carbonates is a lithologic effect rather than cement effect. In current study the transition zone is marked from abrupt V_p increase aided with present day temperature and geothermal gradient. The geothermal gradient is calculated from bottom hole temperature. Any error in bottom hole temperature can lead miscalculation of geothermal gradient and also transition zone. The compaction curves used for comparison are generated for certain mineralogy. The discrepancy between composition of data set used for generation of reference curve and composition of data under study can lead to uncertainties in results. Difference of the paeogeothermal gradient from current geothermal gradient also evolves some uncertainties because paeogeothermal gradient is actually responsible for onset of cementation.

Chapter 6: Rock Physics Diagnostics

In this chapter the results of the rock physics diagnostics are presented and discussed by utilizing various rock physics templets (RPTs). Rock physics templets/models from published literature are utilized to interpret the effect of clay, cement, porosity and pore fluid on seismic parameters (e.g. V_p , V_s , IP, LMR). The utilized models from published literature are discussed in detail and presented in chapter 3.

6.1 Effect of clay on V_p

The relationship between V_p and porosity of the clean sandstones are studied and documented by Wyllie et al. (1956) and Raymer et al. (1980). These studies did not take into account the effect of the clay content on P-wave velocity in sandstone. The velocity of sandstones is related to mineralogy, pore geometry, compaction, cementation, pore pressure and temperature. The effect of clay content on porosity and velocity is studied by Han et al. (1986) and presented a model for varying clay content (see section 3.5.3). The large part of the scatter in velocity-porosity relationship of sandstones are associated with clay content (Marion et al., 1992).

The porosity and velocity data from selected wells are plotted to study the effect of clay for Lunde and Statfjord Formations. The Figure 6.1 shows the crossplot of V_p versus porosity of well 34/7-8 (Lunde Formation) and 34/7-10 (Statfjord Formation) respectively, colour coded by shale volume (V_{sh}).

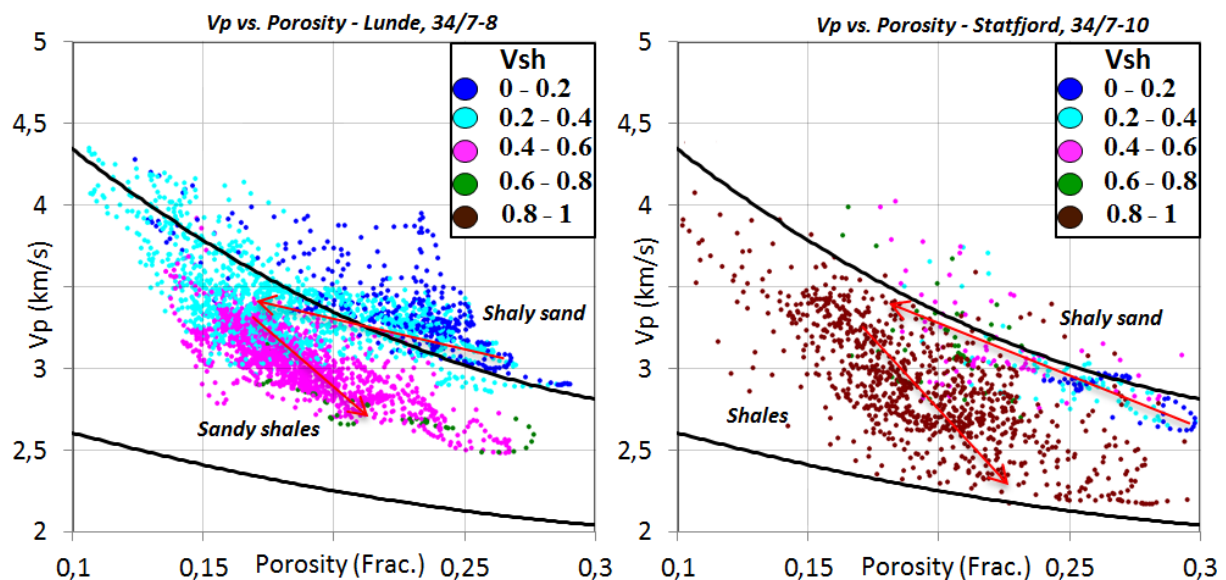


Figure 6.1: The porosity and velocity (V_p) crossplot for Lunde Formation (left) and Statfjord Formation (right). The crossplot is colour coded by shale volume to observe the effect of shale on porosity and velocity. The overlaid upper curve is clean sandstone line (2 % quartz cement) and lower curve is clay line assuming 80% clay and 20 % quartz. The overlaid curves are digitized from Avseth et al. (2005).

The increase of velocity with decreasing porosity is observed in data points with shale volume less than 0.4. The data points are assumed as shaly sand. The trend line of shaly sand is showing decrease in porosity with increasing velocity in linear fashion. In shaly sand the fine grained clay particles fill the pore spaces and reduce porosity which causes seismic velocity to increase. But when the shale volume is higher than 0.4 the decrease in velocity with increasing porosity trend is observed. The data points with shale volume greater than 0.4 are assumed as sandy shale. The inverted V-shaped trend suggested by Marion et al. (1992) is observed (Figure 6.1).

According to Marion et al. (1992), the clay particles are located in sand pore spaces and cause to stiffen the pore filling material in shaly sand, which cause increase in seismic velocity. On the other hand in sandy shales the velocity decrease with increase in clay content because of transition from grain supported to clay supported matrix (Marion et al., 1992). The point at which velocity starts to decrease due to increase in clay fraction is transition from shaly sand to sandy shale (Avseth et al., 2005). The clean sand data points in Lunde Formation are plotted above the clean sandstone line with 2 % cement which shows that the cement is more than 2 % in Lunde Formation. The burial depth of the Lunde Formation in well 34/7-8 range from 2417- 2775 m (MDKB) suggest the Lunde Formation experienced chemical compaction. In Statfjord Formation the clean sandstone data points are clustered below the 2 % clean sandstone line.

In addition to theory from Marion et al. (1992), the model suggested by Han et al. (1986) is also utilized to observe the effect of clays on velocity and porosity. Han et al. (1986) suggested linear relation between velocity and clay content below 0 and 50 percent. In Figure 6.2 the data points from Lunde Formation and Statfjord Formation are crossplotted for V_p and porosity.

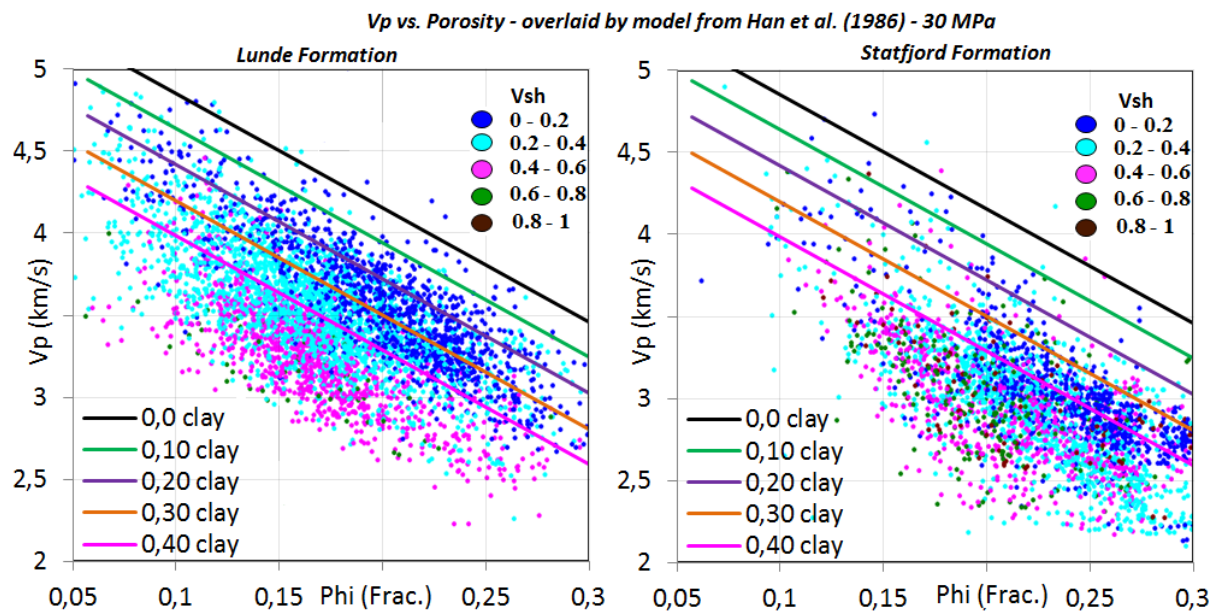


Figure 6.2: The V_p -porosity crossplot overlaid by empirical line suggested by Han et al. (1986) for 30 MPa confining pressure. On left the Lunde Formation from 14 wells is plotted, while on right Statfjord Formation from 8 wells is plotted.

The data points are overlaid by linear empirical model suggested by Han et al. (1986) for 30 MPa effective pressure (which correspond to 3000 m burial depth, assuming pressure 1MPa/100m and hydrostatic pore pressure). The Lunde and Statfjord Formations in study area are buried to depth range of 2000-3500 m (MDKB). The data points were colour coded by shale volume calculated by combination of neutron-density crossplot. Furthermore, only water sand saturated data is used to avoid the effect of the hydrocarbon on velocity (Figure 6.3).

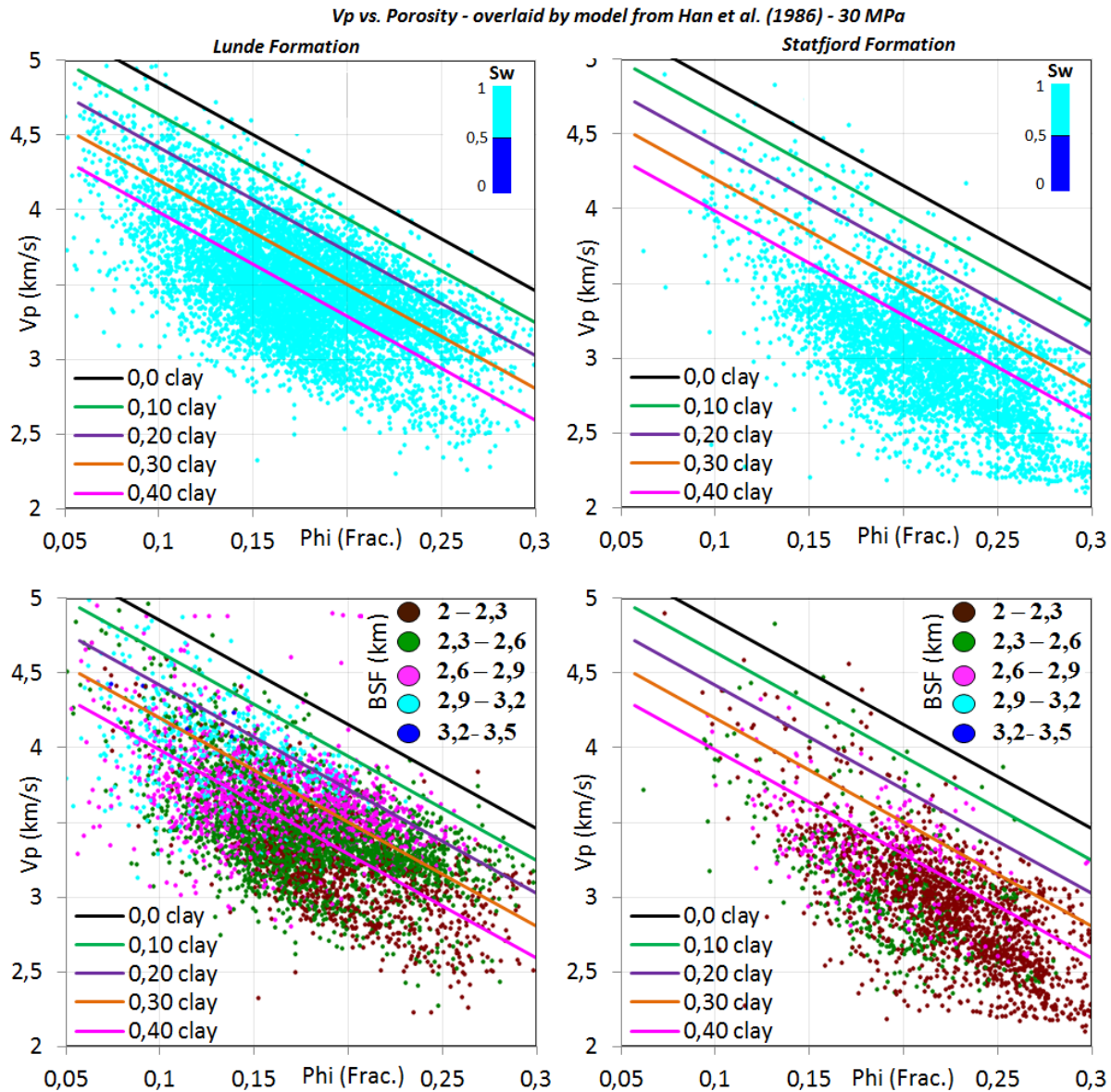


Figure 6.3: The Vp-porosity crossplot overlaid by Han et al. (1986) clay line for 30 MPa confining pressure. Crossplot is colour coded with S_w (upper) and burial depth (lower).

The decrease in velocity with increasing clay fraction is observed in both Lunde and Statfjord Formations. The data points are not plotted completely inside the model. For Lunde Formation the data points with shale volume greater than 40% are falling below the empirical line of 0.4 (Frac) clay and the data points with shale volume from 0-40% are falling between 0.2 and 0.4 (Frac) clay lines. However for Statfjord Formation mostly data points are falling

below the clay line of 0.4 (Frac) in high porosity area. The mismatch of data points with empirical lines can possibly be misleading of shale volume due to uncertainties associated in V_{sh} calculation. The diagenetic effect on velocity with increasing depth is also observed in Lunde Formation. With increasing depth the velocity in Lunde Formation is increasing with decreasing porosity (Figure 6.3). The increase is due to diagenetic cement because with depth temperature increase and conditions for cementation become more favourable. In Statfjord Formation the velocity increase with depth is not observed because the thickness of the Statfjord Formation is less.

6.2 V_p/V_s versus AI

The crossplot of V_p/V_s versus AI is commonly used to discriminate lithology, porosity and type of fluids present in reservoir. In rock physics interpretation the main limitation in this study is the absence of shear sonic data in all of the wells except well 34/7-27, which contain partially measured shear wave data (Table 3.1). The well 34/7-27 does not contain the Lunde and Statfjord Formations which are main focus of this study. Because of availability of the shear sonic data, initially the V_p/V_s and AI is plotted with overlying rock physics template of well 34/7-27 (Figure 6.4).

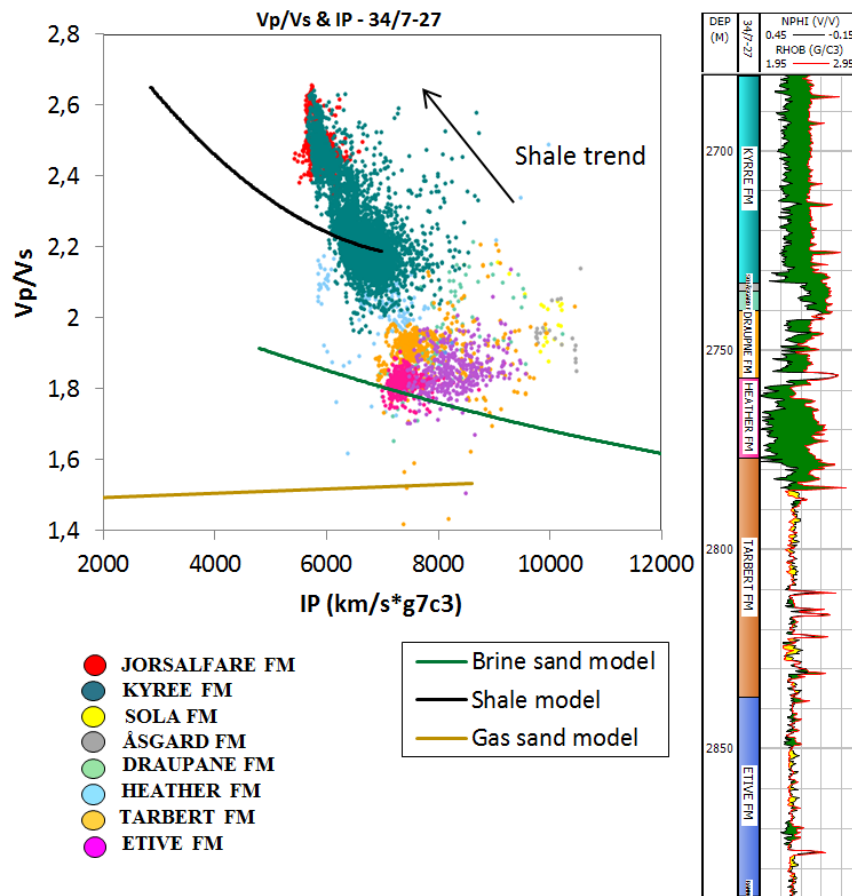


Figure 6.4: Crossplot of V_p/V_s versus IP (P-impedance) of data points from well 34/7-27, overlying the rock physics template modelled for 25 MPa pressure (assumed from depth as 1MPa/100m). The log section of neutron-density is also shown to discriminate between sand and shales.

The effective pressure is suggested from the burial depth as 1MPa/100m assuming hydrostatic pore pressure. The burial depth of the sand interval is 2777 m (MDKB) in well 34/7-27. The well contains water saturated sand intervals of Tarbert Formation and Etive Formation with very good reservoir quality. The sand intervals are overlying shales of the Heather, Draupane, Åsgard and Kyree Formations. In Figure 6.5, a good discrimination between clean sand and shale data points is observed. The shale data points are plotting along different trend than sand data points that are plotting near the brine saturated quartz sand model.

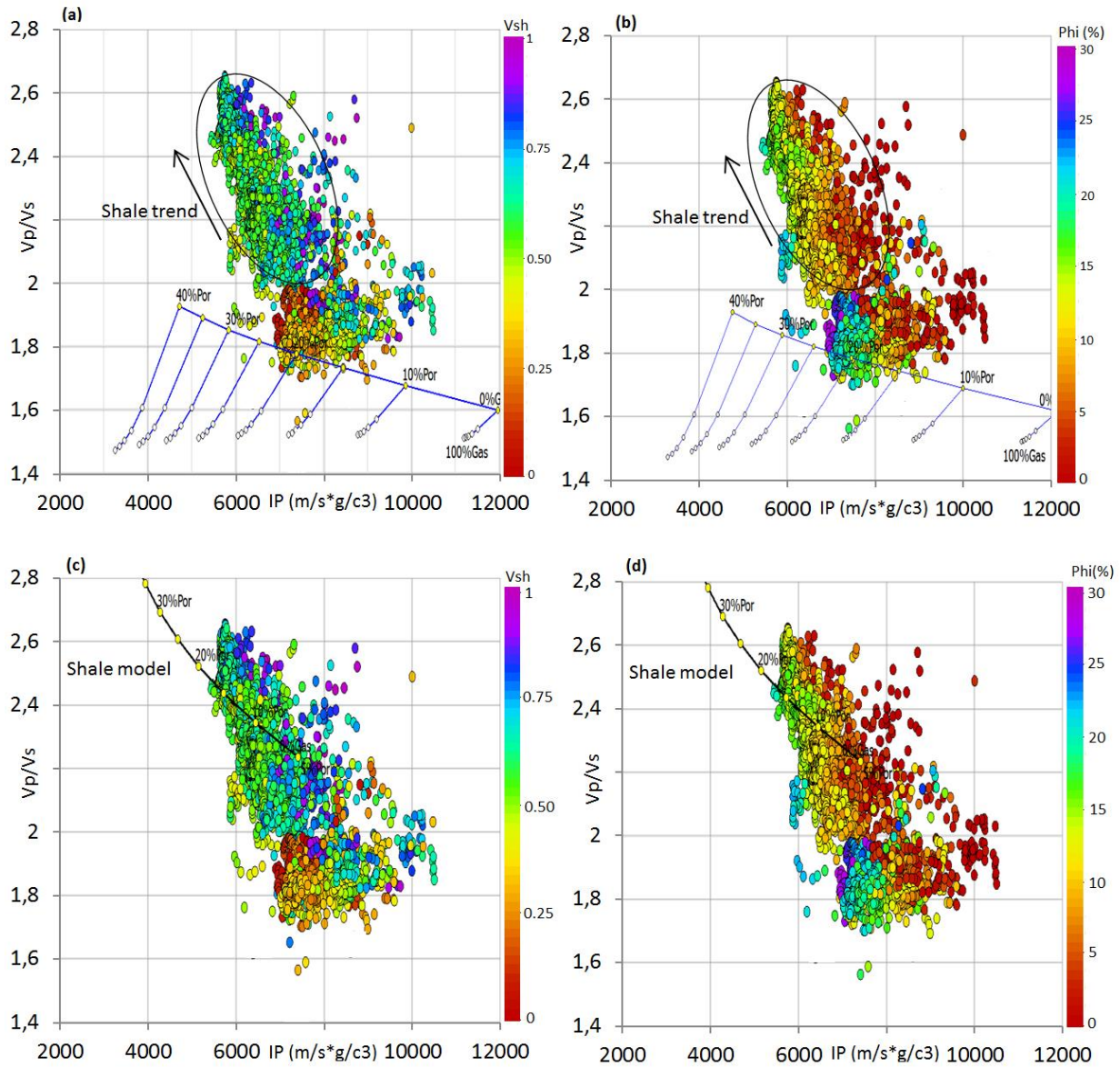


Figure 6.5: The V_p/V_s versus AI crossplot of well 34/7-27; (a) data points colour coded by shale volume overlaid on quartz sand model, (b) data points colour coded by porosity and overlaid on quartz sand model, (c) data points colour coded by shale volume and overlaid on pure shale model line, (d) data points are colour coded by porosity and overlaid on pure shale model line.

The shale data points are not falling on the shale model line but plotted close to the line (Figure 6.5). The applicability of the template depends on the geological input of the area. For example if the shale line is modelled for smectite rich shales, it will be not applicable for

kaolinite-rich shales. In Figure 6.5, the maximum shales data points are from Kyree Formation and few data points from Jorsalfare Formation. The detail mineralogical investigation of above mentioned formations is beyond the scope of this study. Therefore it is interpreted that the difference of shale data trend from model line is due to mineralogical difference of the shales and model input. The brine sand trend commonly have general validity but shale trend is more basin specific (Ødegaard and Avseth, 2003).

For further analysis only Etive Formation is selected from well 34/7-27 to study the effect of fluids on Vp/Vs and AI . The Etive Formation is 100% brine saturated sand for in situ case. The Vp/Vs versus AI crossplot for in situ case is shown in Figure 6.6, colour coded by shale volume (left) and porosity (right). The brine sand data points sit above the theoretical brine sand model line. The fluid substitution is performed for two scenarios; (a) 100% oil saturated; (b) 100% gas saturated for the Etive Formation.

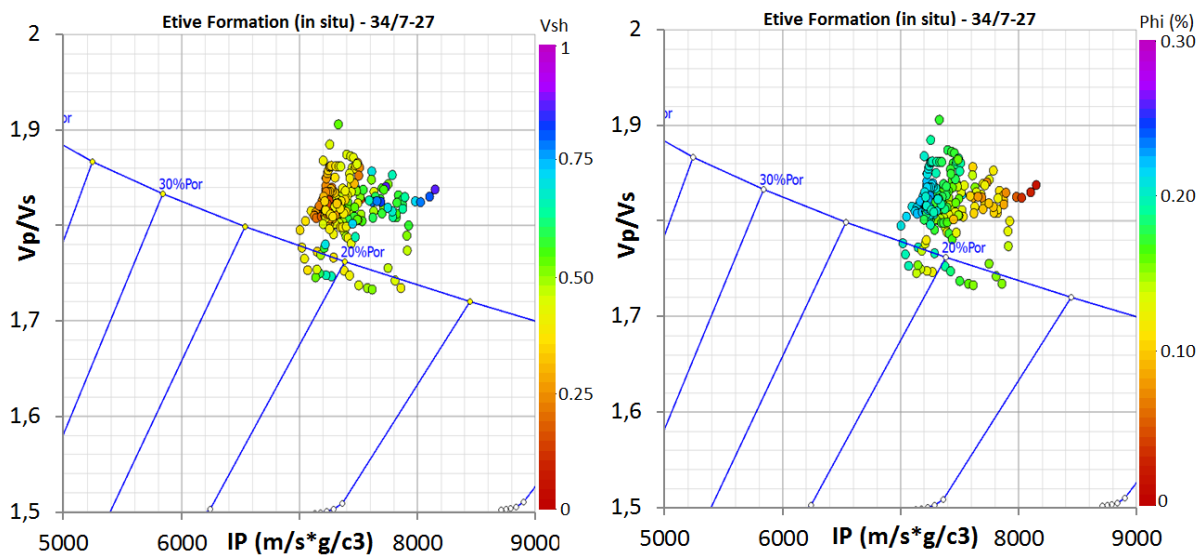


Figure 6.6: The Vp/Vs versus AI crossplot of the Etive Formation from well 34/7-27. The crossplot is colour coded by shale volume (left) and porosity (right).

In Figure 6.7, the Vp/Vs versus AI crossplot is shown for oil saturated scenario (upper) and gas saturated scenario (lower) respectively. The colour coding for crossplot is shale volume (left) and porosity (right). The dramatic decrease in Vp/Vs is observed for both oil and gas scenarios. The fluid substituted data points shifted below the brine saturated line. In term of porosity the data points are plotting between the model porosity lines of 20 and 25%. Few data points remain unaffected after fluid substitution and sitting above the sand model line (Figure 6.7). These data points are possible carbonate intervals. Another factor is cementation that effect Vp/Vs significantly. The Vp/Vs ratio in unconsolidated sand is more affected with respect to fluids as compared to well consolidated sand. The Etive Formation is present at 2800 m depth (MDKB). The depth corresponds to chemical compaction regime as quartz cementation tends to occur at temperature 80 °C. Despite of presence in chemical compaction zone a strong response of fluids is observed in Vp/Vs versus AI crossplot (Figure 6.7).

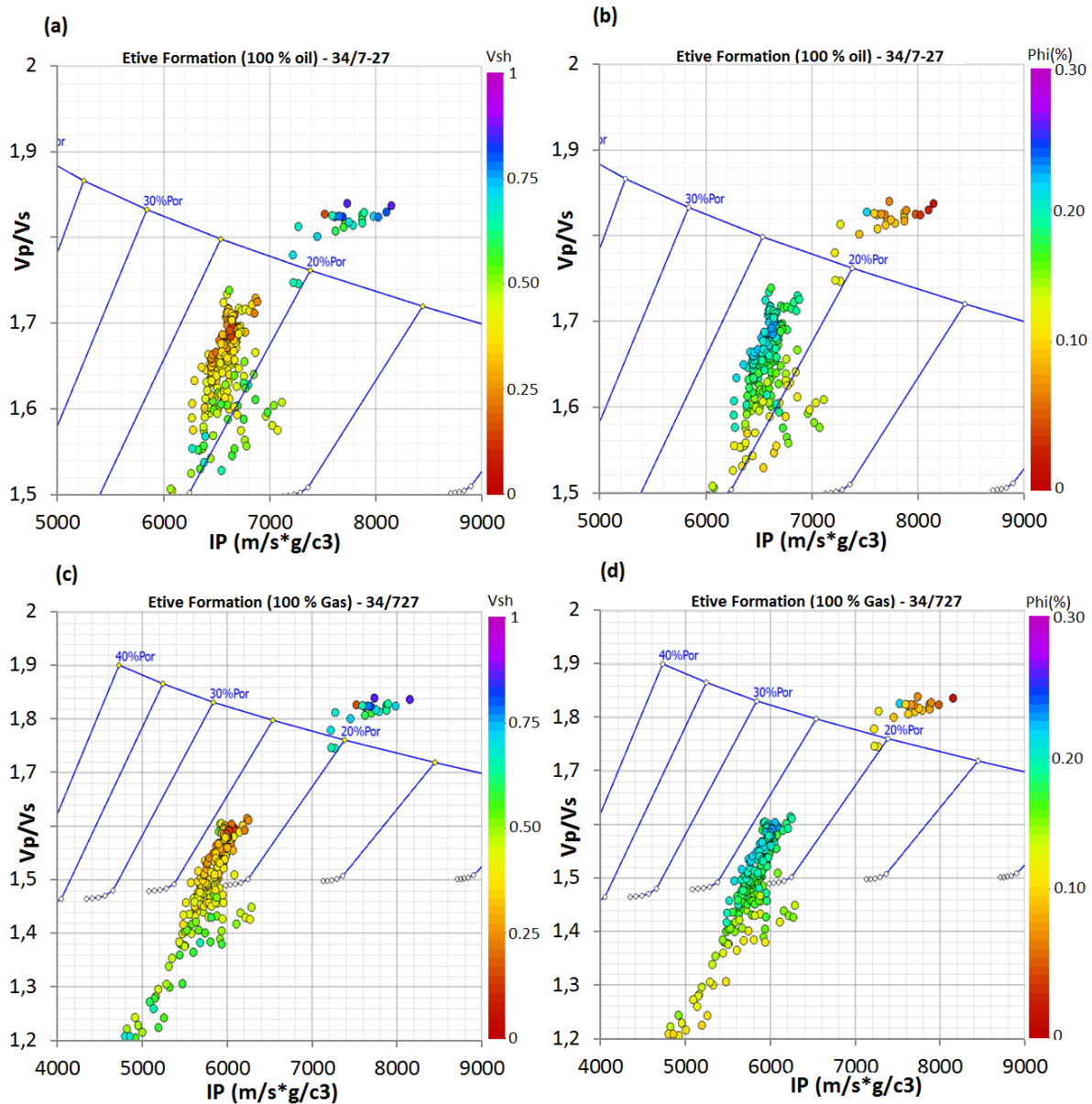


Figure 6.7: The V_p/V_s versus AI crossplot of Etive Formation after performing fluid substitution from well 34/7-27; (a & b) 100 % oil saturated scenario, (c & d) 100 % gas saturated scenario.

Statfjord Formation

The V_p/V_s versus AI crossplot of the Statfjord Formation is shown in Figure 6.8. The data are plotted from for wells 34/4-8, 34/7-4, 34/7-8 and 34/7-13. The entire Statfjord Formation is plotted with colour code of shale volume (Figure 6.8). Due to absence of measured shear sonic data, the estimated V_s are utilized as input. Instead of wider spread of data as expected with measured V_s , by using estimated V_s the data is falling along a narrow trend. The decrease in V_p/V_s and increasing AI is observed along the narrow trend of the data. The two different data clusters are observed on the basis of the shale volume. The cluster of sand data points with low shale volume (marked by ellipse on Figure 6.8) is showing high AI with low V_p/V_s .

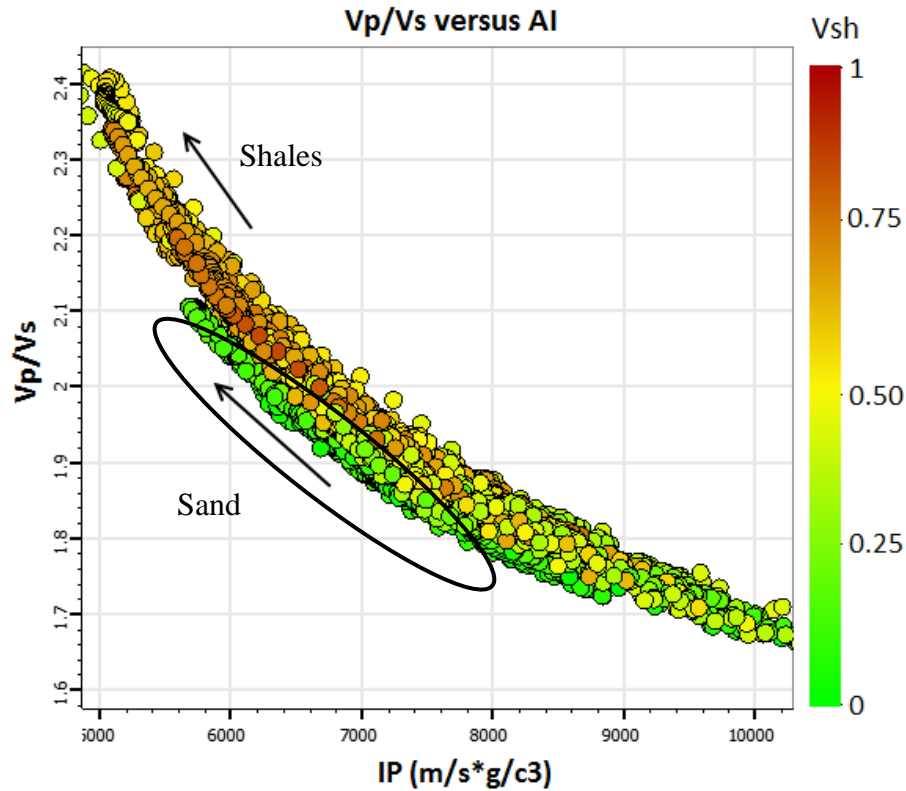


Figure 6.8: The V_p/V_s crossplot of the Statfjord Fm. Data from four wells is plotted.

The well 34/4-8 is selected for further analysis. To study the V_p/V_s and AI by using standard rock physics template, the crossplot for Statfjord Formation from well 34/4-8 is plotted with overlying rock physics template. The burial depth of the Statfjord Formation (2700-2900m; MDKB) corresponds to 27 to 29 MPa effective pressure. Therefore, the input of effective pressure used for model is 28 MPa. The pore fluid pressure is assumed as hydrostatic. Additionally two scenarios are considered for generation of model line; (a) 100 % quartz sand, (b) 80% quartz plus 20 % clay. In Figure 6.9, the crossplot is overlaid by 100% quartz sand model line (left) and 80% quartz plus 20% clay model line (right). In first scenario the data points are plotting above the 100% quartz sand model line. In case of 80% quartz and 20% clay, the data points are falling on model line in low V_p/V_s domain and high AI but increasing V_p/V_s the data deviating from the model line.

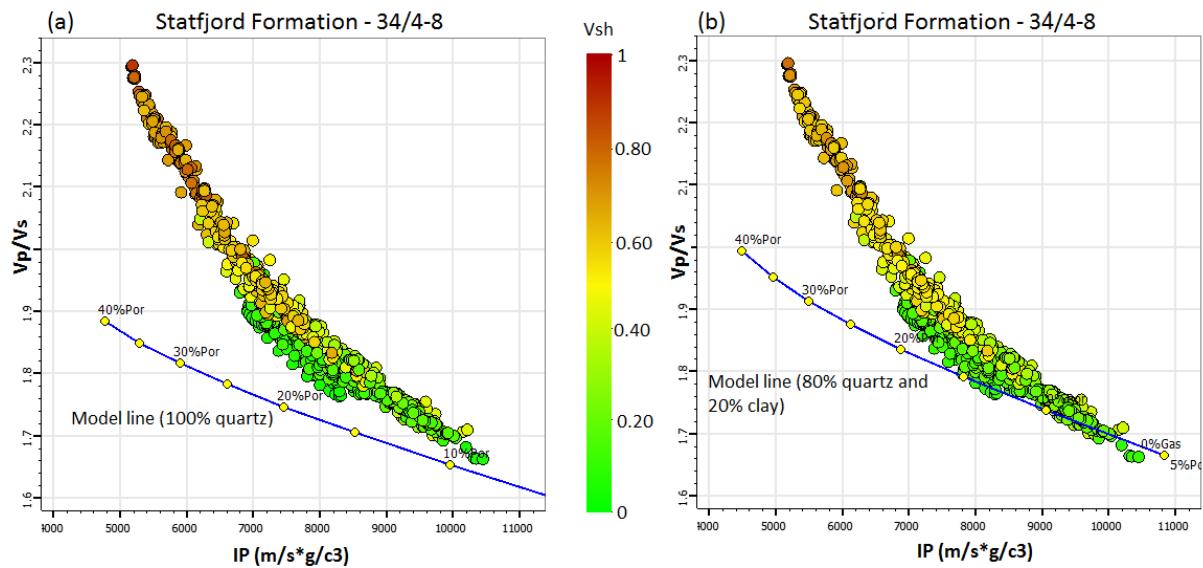


Figure 6.9: The V_p/V_s crossplot of Statfjord Formation from well 34/4-8. The crossplot is overlaid by rock physics template; (a) the model line is generated for 100 % quartz sand, (b) the model line is generated for 80% quartz and 20% clay.

The interpretation is that pure quartz sand model is not valid for Statfjord Formation in well 34/4-8. The rock physics template is useful when local geological factors (mineralogy, clay content, fluids content etc.) are taken into consideration in generation of the template. The clay content must be taken into consideration during analysing velocity ratio. The increase of clay content cause increase of velocity ratio (Hornby and Murphy, 1987). In Statfjord Formation the increase in V_p/V_s with increasing clay content is observed in well 34/4-8 (Figure 6.9).

For further analysis porosity is also taken into consideration and only sand data points are analysed by filtering the data with shale volume ($V_{sh} < 0.25$). An attempt has been done to calculate the cement volume by using study of Marcussen et al. (2010). The calculated cement volume is used for colour coding in crossplot to understand its effect on velocity ratio. In Figure 6.10 the V_p/V_s versus AI crossplot from Statfjord Formation for pure sand data points are plotted and colour coded with porosity (left) and cement volume (right). The crossplot is overlaid by rock physics template (80% quartz and 20% clay). In low V_p/V_s domain the porosity is low and cement volume is high. Increasing porosity shows increasing V_p/V_s while increasing cement shows decrease in V_p/V_s . The maximum value of V_p/V_s observed is 1.9 with AI 7000 (m/s*g/cc). The interpretation is presence of cement decrease porosity with increasing density which causes high AI but low V_p/V_s . The slight underestimation of the porosity by model line is also observed.

The absence of directly measured V_s exhibits some limitations in interpretation of V_p/V_s versus AI crossplot. The effect of hydrocarbon is not easy to understand by using estimated V_s because separation between brine sand and hydrocarbon sand is not clear as we can see by using directly measured V_s . In this study, due to the absence of shear sonic data results discussed earlier can contain significant uncertainties but major findings are still comparable with published literature.

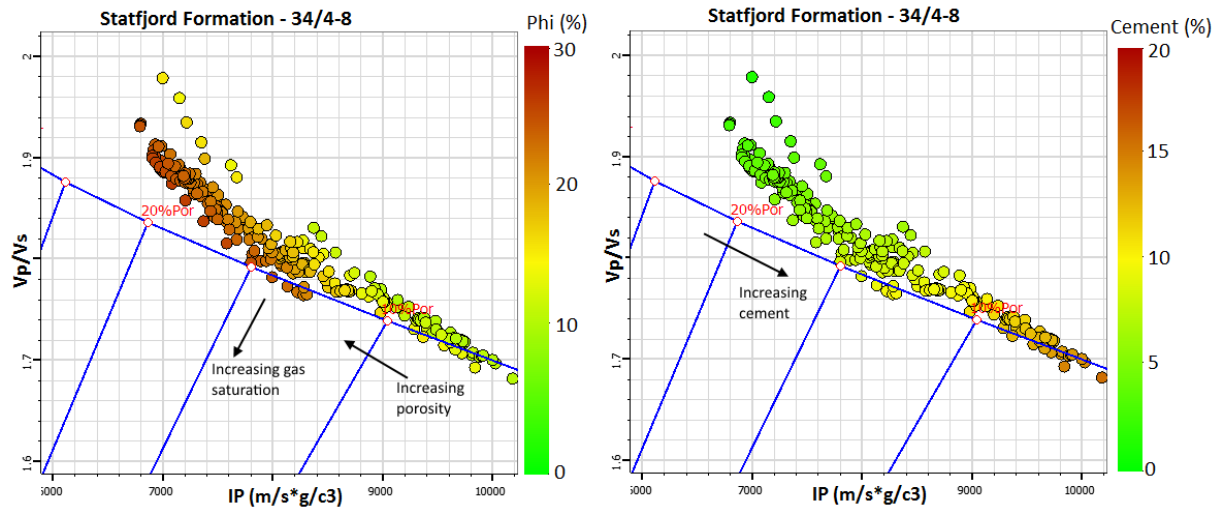


Figure 6.10: The V_p/V_s versus AI crossplotted from Statfjord Formation for well 34/4-8. The data is sorted by shale volume ≤ 0.25 . The data is colour coded with porosity (left) and cement volume (right).

A slightly different trend is observed for Statfjord Formation in well 34/7-8 (Figure 6.11). The pure sand data points show maximum V_p/V_s value 2.1 with AI between 5000 – 6000 $m/s \cdot g/cc$ (Figure 6.11). The burial depth of the Statfjord Formation of well 34/7-8 is between 2200 and 2300 m (MDKB). In well 34/7-8 the Statfjord Formation is at shallower depth than in well 34/4-8 and subjected to lower temperature which in turn cause less cementation. Due to less cementation the effect of V_p/V_s is higher as compared to well 34/4-8. Porosity is also significantly higher in shallow buried Statfjord Formation.

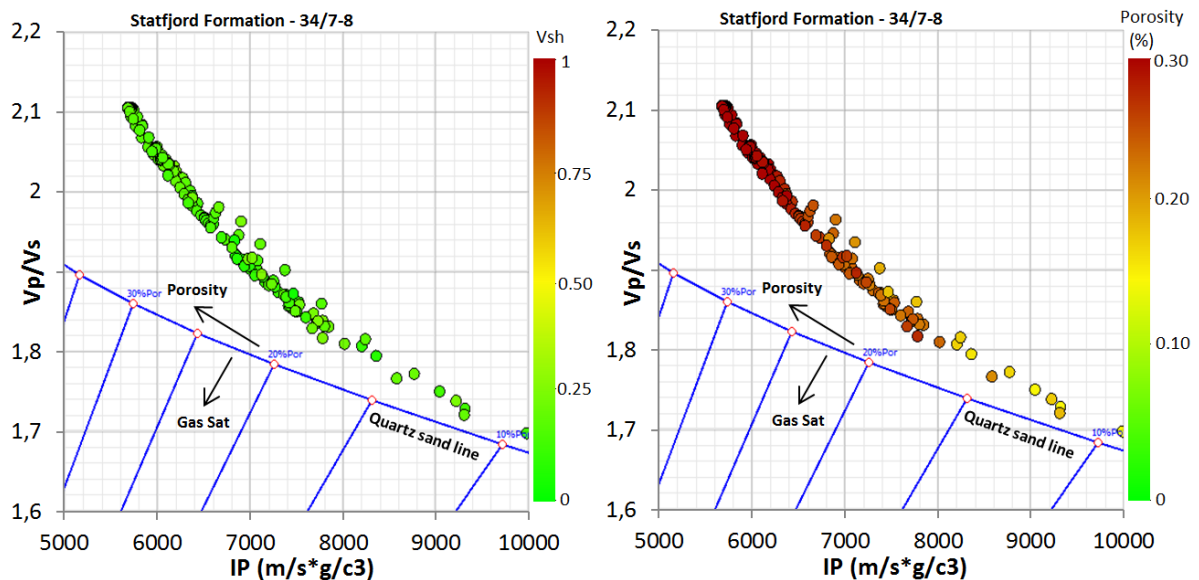


Figure 6.11: The V_p/V_s and AI crossplot of Statfjord Formation of well 34/7-8. The data points are sorted by shale volume ($V_{sh} \leq 0.25$). The colour coding is V_{sh} (left) and porosity (right).

Lunde Formation

The crossplot V_p/V_s versus AI of Lunde Formation, from well 34/7-6 colour coded with shale volume is shown in Figure 6.12. A good discrimination between shales and sandstone lithologies can be observed with respect to shale volume. The crossplot is overlaid by rock physics template of brine saturated pure quartz sand. The pressure input is 25 MPa for model assumed from burial depth of Lunde Formation (2200-3000 m MDKB).

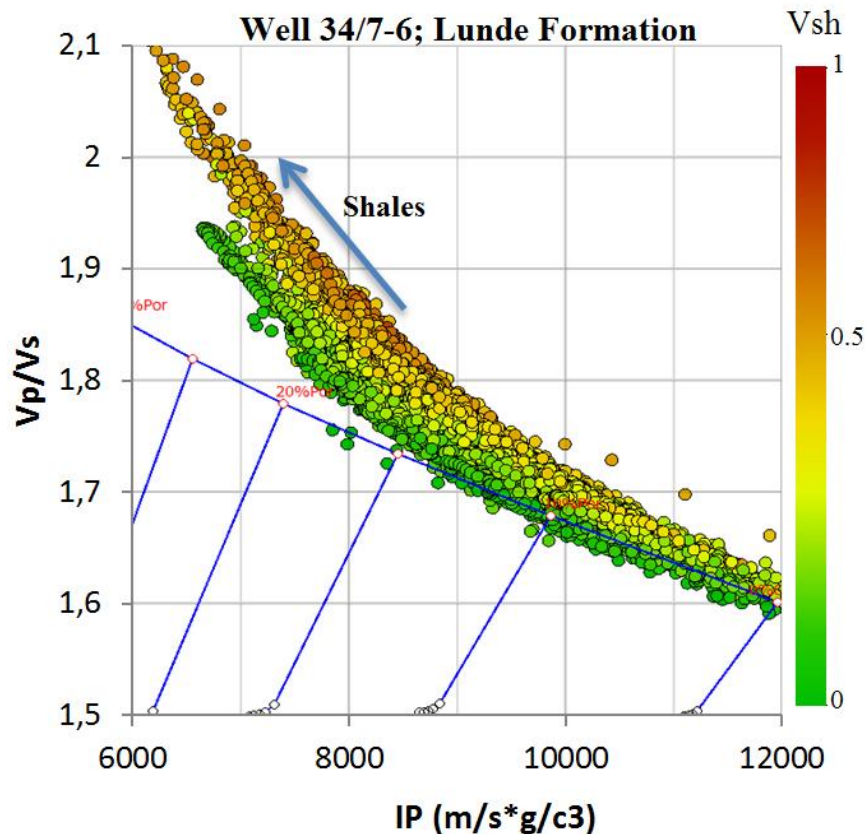


Figure 6.12: The V_p/V_s versus AI crossplot for the Lunde Fm from 34/7-6. The data is colour coded with shale volume (V_{sh}).

The further interpretation is carried out by using the data for sandstones ($V_{sh} \leq 0.25$) in Figure 6.13. The colour coding of burial depth (left) and estimated cement volume (right) is used as additional tool in crossplots. The Figure 6.13 shows that deeply buried and cemented data points are plotting on model line. The increase of cement volume caused decrease in V_p/V_s with increase in AI . The two data clusters from same well are because of different burial depth. The stiffening of sand due to cement decreases the pore fluid sensitivity. Different RPTs even used for same stratigraphic horizons at different burial depth (Ødegaard and Avseth, 2003).

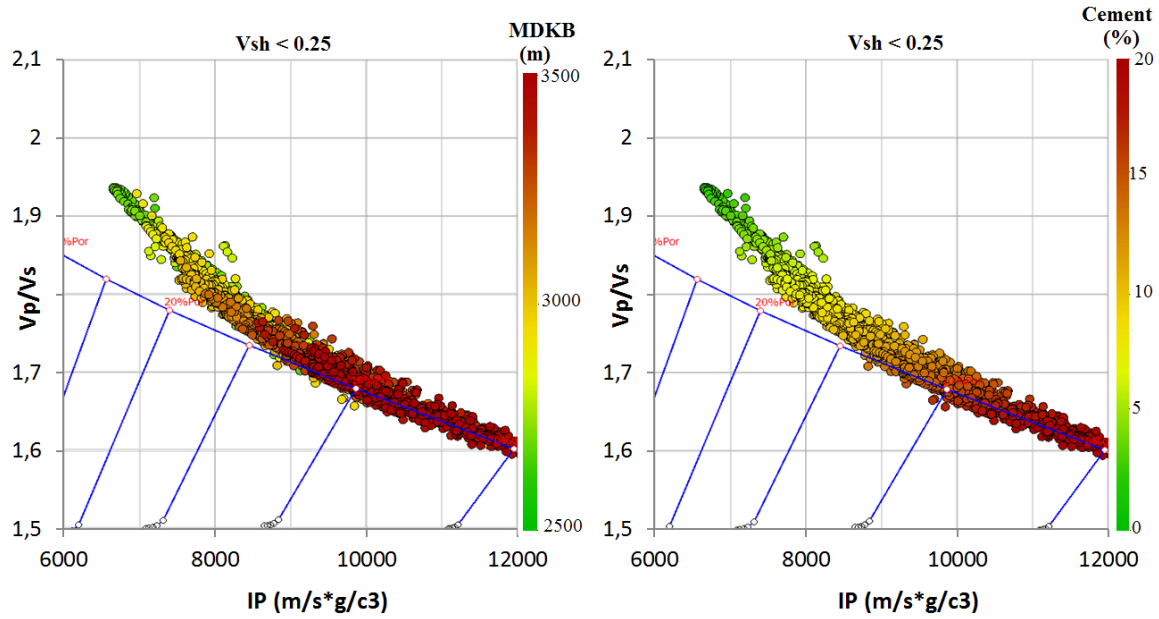


Figure 6.13: V_p/V_s and AI crossplot of Lunde Formation of well 34/7-6; colour coded by burial depth (left) and cement volume (right). The data is plotted for only sandstone ($V_{sh} \leq 0.25$).

6.3 Rock physics cement models

The change in rock microstructure effect the porosity and seismic velocity. The stiffness of sediments is not only reliant on porosity and mineralogy but also rock microstructures show a part for stiffening (Avseth et al., 2000). The rock physics effective medium models are used to assume microstructure of rocks from velocity-porosity relation. The effective medium model theoretical curves adjusting with data trend assume that microstructure of sediments is same as that are used for theoretical model curve (Avseth et al., 2005). In this study the rock physics effective medium models (Friable Sand Model, Constant Cement Model and Contact Cement Model) are utilized to understand the rock microstructures (sorting and cement volume). The model used in this study is described in detail in section 3.5.5.

Lunde Formation

The seven wells are selected from different parts of the Snorre field to apply the rock physics cement model. The depth of Lunde Formation in selected wells ranges from 2000 to 3500 m (MDKB). For the first sight of analysis the V_p versus porosity (upper) and V_s versus porosity (lower) data from selected wells are plotted together with overlying rock physics cement models presented in Figure 6.14. In fact Lunde Formation is fluvial deposited channel sandstone with interbedded shales and mudstones. To avoid shales, initially data is filtered with shale volume less than 50%. The cement model is purely designed for clean sandstone.

A wide spread of data is observed in both V_p -porosity (upper) and V_s -porosity (lower) presented in Figure 6.14. The data with higher shale volume is falling below the cement model lines in V_p -porosity crossplot. The data points up to certain fraction of shale volume are plotting on friable sand model lines which reveal that the plotting intervals are compacted under the effective stress and porosity reduction with increase in seismic velocity is controlled by changing in sorting. The sand data points are also plotting above the constant cement

model line which means the plotting intervals are cemented with more than 2% cement volume. Both diagenetic controlled and sorting control trend of decreasing porosity and increasing seismic velocity is observed for Lunde Formation from plotted 7 wells. It is not easy to make a clear interpretation from combined wells; therefore close interpretation of each well is required because diagenetic trend can be controlled by burial depth and temperature.

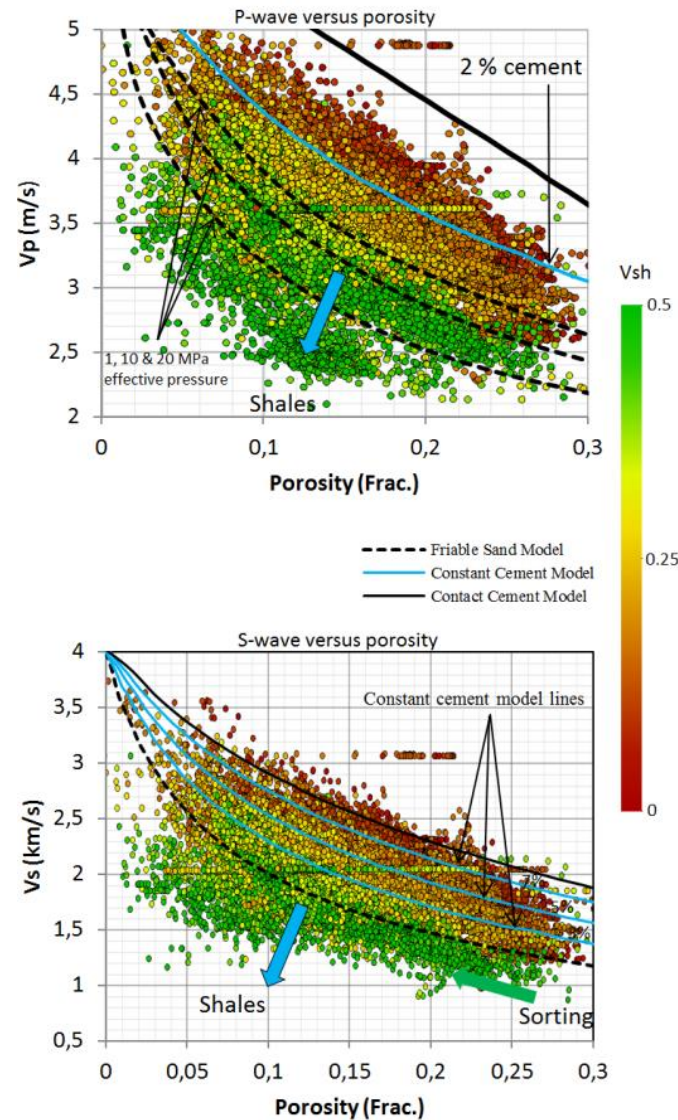


Figure 6.14: The V_p -porosity crossplot (upper) and V_s -porosity crossplot (lower) of Lunde Formation with overlying rock physics effective medium models. The data is plotted from six selected wells (34/4-7, 34/4-8, 34/7-1, 34/7-3, 34/7-4, 34/7-6 and 34/7-8) across the Snorre field. The data is filtered by using shale volume ($V_{sh} \leq 0.5$). The colour coding in both plots is shale volume.

In case of V_s versus porosity crossplot overlaid by rock physic effective medium models, the sand data points are plotting on constant cement model line. The constant cement model lines are digitized from Avseth et al. (2010). The lines are representing cement volume of 3, 5 and 7% from lower to upper one respectively (Lower plot in Figure 6.14). Few clean data points are also plotting on contact cement model line. The contact cement model line is digitized from Avseth et al. (2005).

For the close interpretation, well 34/7-1 is selected (Figure 6.15) because the well contain good reservoir intervals. The burial depth of the Lunde Formation in well 34/7-1 is ranging from 2300 to 2900 m (MDKB).

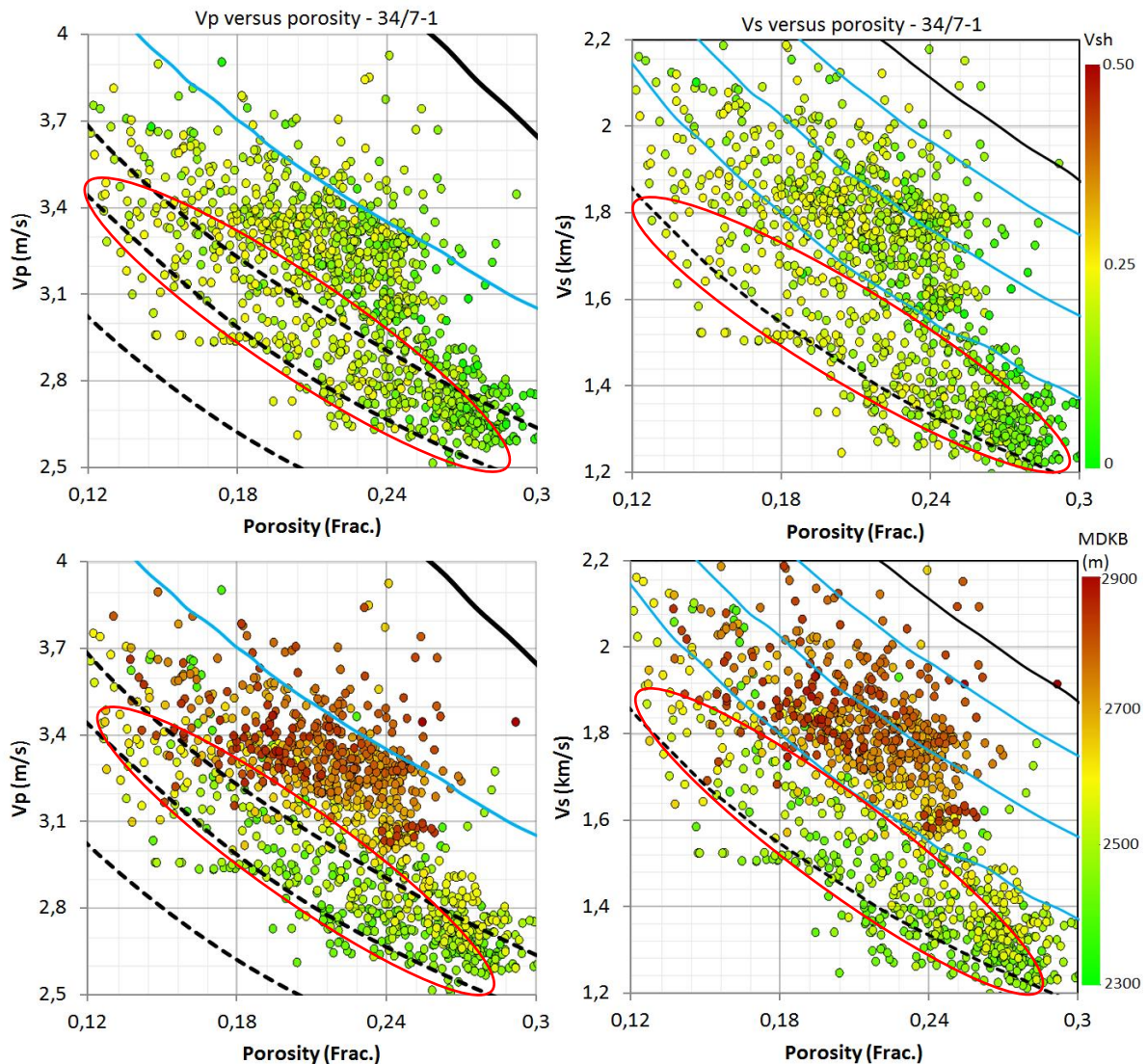


Figure 6.15: The Vp versus porosity (left) and Vs versus porosity (right) crossplots of Lunde Formation from well 34/7-1. The crossplots are overlaid with rock physics cement models. The colour coding used is Vsh (upper) and burial depth (lower).

Overall two data trends are observed from crossplots of well 34/7-1. The data marked with red ellipse is from shallow burial depth and plotting on the friable sand model lines (Figure 6.15). While the other data points are falling on constant cement model lines. This shows that from shallower part of the well 34/7-1, the porosity and velocity change is controlled by change in sorting under vertical effective stress. With increasing depth temperature increase which result increase in cement volume. The plotting of data on constant cement model lines indicate that the change in porosity in deeper part of the well is more diagenetic controlled.

Another well 34/7-6 is used for close interpretation (Figure 6.16). The burial depth of Lunde Formation in this well is range from 2654-3539 m (MDKB). The Lunde Formation is relatively deeper in this well than well 34/7-1.

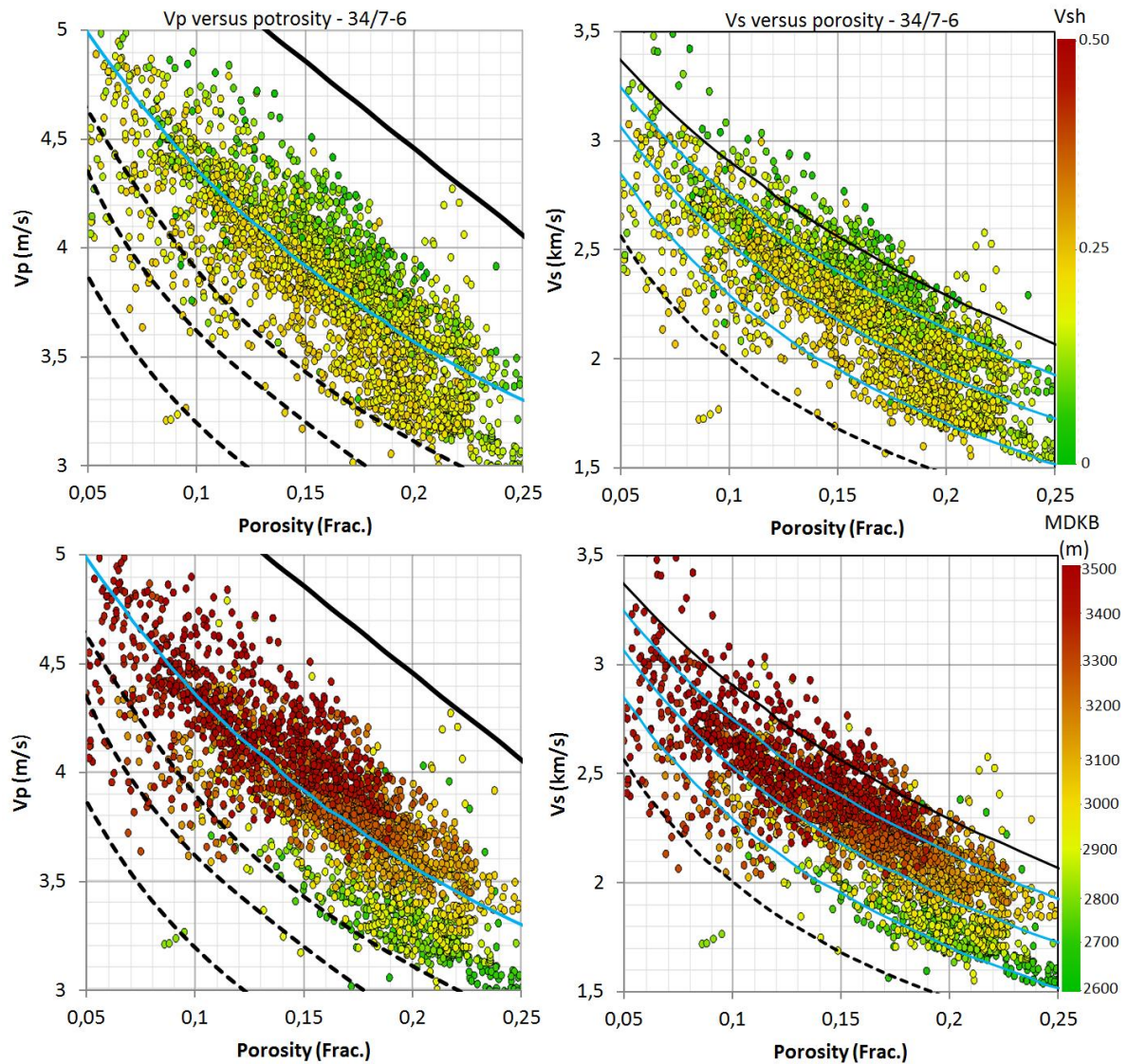


Figure 6.16: The Vp versus porosity (left) and Vs versus porosity (right) crossplot for Lunde Formation from well 34/7-6. The crossplot overlaid by rock physics cement model and data points are colour coded with Vsh (upper) and burial depth (lower).

In Figure 6.16, for the Vp versus porosity crossplot (left) most of the data are plotted around the constant cement model line, while few data points are in between friable sand model lines and constant cement model lines. The data points plotting on constant cement model lines are from burial depth more than 3000 m (MDKB). The shallow depth data points are not plotting on constant cement model line which means the portion of the Lunde Formation at shallow depth is not as much cemented as compared to deeply buried part. The deeper part of the Lunde Formation on constant cement line reveals that the portion is cemented and porosity and seismic velocity trends are diagenetically controlled.

In V_s versus porosity crossplot (right) the data is plotting on the constant cement model lines and with increasing depth the data is moving towards higher cement percentage model line (Figure 6.16). The V_s versus porosity crossplot suggesting 3 to 9% cement volume for Lunde Formation in this well. The cement volume suggested by rock physics cement model lines must be verified by cement volume from point counting results of the thin sections. In this way the applicability of the model to the area under study can be establish.

Statfjord Formation

For the initial analysis six wells with good data quality are selected for rock physics diagnostics to interpret effect of rock microstructures (sorting and cement) on porosity and velocity. The Statfjord Formation are plotted for P-wave velocity versus porosity (left) and S-wave velocity crossplots (right), overlaid by rock physics effective medium models in Figure 6.17. The data discriminated by shale volume is less than 0.5. The burial depth of the Statfjord Formation in plotted wells range from 2200 to 3000 m (MDKB). Both plots are colour coded with shale volume (Figure 6.17). A wide spread of data is observed in both plots. In case of V_p versus porosity the data with higher shale volume are plotting on and below the friable sand model lines. The data points with low shale volume are plotting on friable sand line of 20 MPa and some data points are plotting on constant cement model line. The constant cement model line is adapted from Avseth et al. (2005), which assume 2% cement for clean sand.

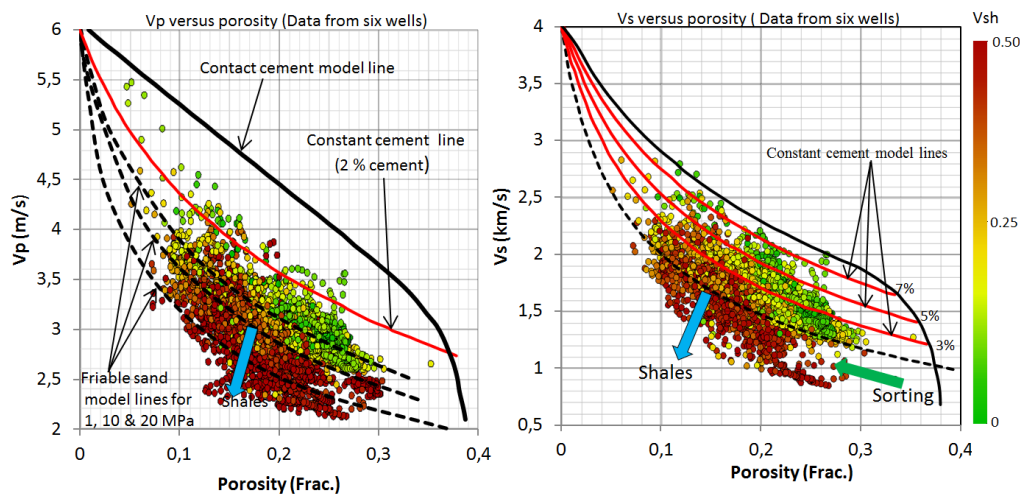


Figure 6.17: The V_p -porosity (left) and V_s -porosity crossplot of the Statfjord Formation overlaid by rock physics cement models. Data is plotted from six wells (34/4-8, 34/7-3, 34/7-4, 34/7-6, 34/7-8 and 34/7-13).

The rock physics models assume that if the data falls on theoretical cement model lines the rock is cemented (Avseth et al., 2010). The red lines in V_s versus porosity crossplot are constant cement model lines and representing cement percentage 3, 5 and 7% respectively from lower to upper one (Figure 6.17). In case of V_s versus porosity the sand data is plotting on constant cement model lines representing 3 to 7% cement. From the first sight of the data from six wells it has been observed that clean sand data points are showing close relation to friable sand lines in V_p versus porosity cross plot. But in case of V_s versus porosity data showing close settlement with constant cement model line of 3 to 5% cement volume. The interpretation is the reservoir contains both diagenetic controlled and sorting controlled trend. The expected cement could be between 1 to 7% but the close analysis is required.

For further analysis the data from six wells sorted with shale volume less than 25% and plotted together with cement models and colour coding of burial depth (Figure 6.18). It has been observed the clean sand data points are plotting on friable sand model lines in Vp-porosity crossplots. Few data points with deep burial depth are plotting above the friable sand model lines. This shows that the clean sand intervals of the Statfjord Formation in the plotted wells are not very much cemented and porosity change is controlled by change in sorting.

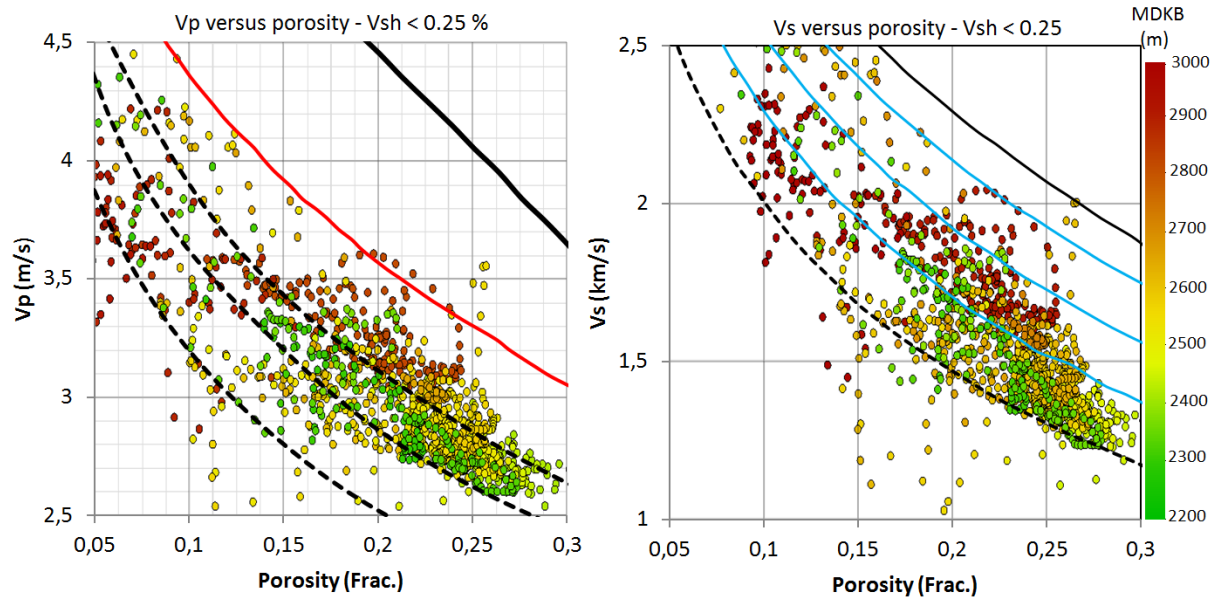


Figure 6.18: The Vp-porosity (left) and Vs-porosity (right) crossplot for Statfjord Formation from six wells. Data is sorted by $V_{sh} \leq 0.25$ and colour coded with depth (MDKB).

In case of Vs versus porosity the clean sand data points are plotted between friable sand model line and constant cement model line for 3% cement volume. The data from deeper depth are plotted between constant cement model lines for 3 and 5% cement respectively. The difference in Vp-versus porosity and Vs versus porosity is due to different parameters used for generation of both models. The Vs-porosity model is digitized from Avseth et al. (2010) while the constant cement model for Vp-porosity crossplot is acquired from Avseth et al. (2005). Furthermore, the Vs in plotted wells is not measured directly and calculated by using published literature. The calculated Vs contain itself some uncertainties. All of these factors together are possible reason for different plotting of data on both models in Figure 6.18. The interpretation made for Statfjord Formation is that the porosity change is more controlled by change in sorting. Less diagenetic effect is present in Statfjord Formation as compared to deeply buried Lunde Formation. For Statfjord Formation in plotted wells the cement estimated for this study is 1 to 5%.

The equation acquired from study of Marcussen et al. (2010) (Eq 3.28) for calculation of cement volume (see section 3.5.6). The estimated cement volume for Statfjord Formation is compared with cement estimated by using rock physics cement models. A good comparison of cement volume estimated by using Eq 3.28 and cement volume suggested by rock physics model is observed for Statfjord Fm (Figure 6.19). The Equation 3.28 suggested the 0 to 5% cement volume for clean sand data points of the Statfjord Formation.

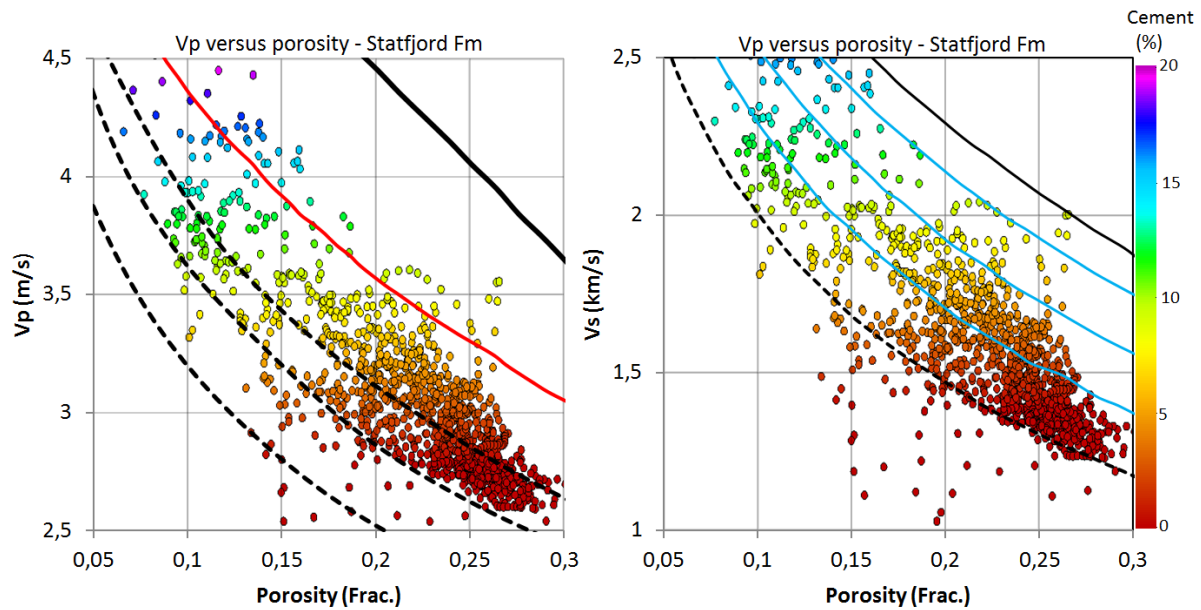


Figure 6.19: The V_p versus porosity (left) and V_s versus porosity (right) plots of the Statfjord Formation from six selected wells are plotted with rock physics effective medium models. The crossplots are colour coded by cement volume.

6.4 Lamda-Rho versus Mu-Rho (LMR)

The Lambda-Rho (incompressibility) and Mu-Rho (rigidity) crossplot is useful for lithology identification and fluids discrimination. The parameters (λ , μ & ρ) can be derived from seismic and well log data, therefore technique is most useful for hydrocarbon detection. Prestack seismic CMP gather are inverted to extract LMR parameters (λ & μ) and combined with density to get $\lambda\rho$ and $\mu\rho$ (Inichinbia et al., 2014).

In general the incompressibility of the rock (λ) decreases with gas saturation and the rigidity (μ) is unaffected. The effect is more pronounced in high porosity sand. This moves the gas saturated sand in lower $\lambda\rho$ domain.

The LMR is very useful when the measured shear sonic data from well log is available. Little information can be extracted by using estimated shear sonic as compared to directly measured shear sonic. As explained earlier the absence of shear sonic data for targeted Lunde and Statfjord Formations insert noticeable limitation in rock physics interpretation of this research.

Lunde Formation

The well 34/7-6 is selected for interpretation of the LMR. In Figure 6.20, the whole Lunde Formation is plotted from well 34/7-6. The burial depth of the Lunde Formation in well 34/7-6 range from 2600-3500 m (MDKB). The well is proven to be brine saturated from petrophysical analysis. The Figure 6.20 shows majority of the data points are located in sand zone with shale data points located below sand in crossplot as expected. A slight distinction is observed between sand and shale points. It is clear a little a can be extracted from LMR if the directly measured shear wave data is not present.

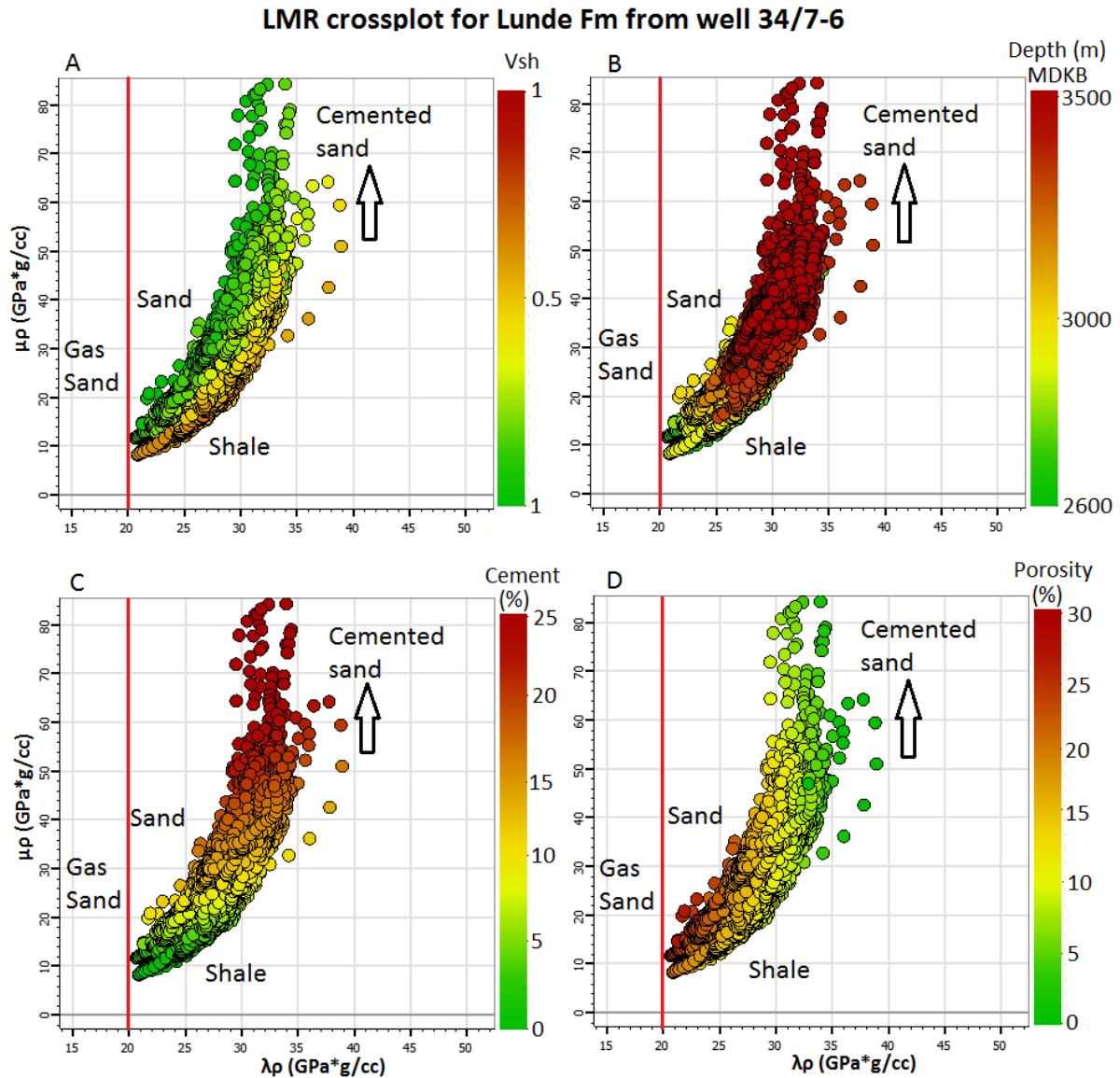


Figure 6.20 The Lamda-Rho versus Mu-Rho crossplot of the Lunde Formation from well 34/7-6. The red line on the left side of the each plot is threshold line for gas saturated zone from Goodway et al, (1997). The crossplots are colour coded by; (A) Shale volume, (B) burial depth (MDKB), (C) cement volume and (D) porosity.

There is no data point below the threshold of gas saturated zone. It has been observed that rigidity of sand is increasing with depth. The increase in rigidity is greater than incompressibility. Figure 6.20B shows that the value of Mu-Rho start to increase from the value of 25 GPa*g/cc, when burial depth increase from 3000 m (MDKB). The maximum value attain by Mu-Rho is 80 GPa*g/cc until 3500 m burial depth. On the other side the change in Lamda-Rho is not as high as Mu-Rho. The maximum value attain by Lamda-Rho is 35 GPa*g/cc. Due to increase of depth, the temperature increase and which favour the cementation process. Due to cementation the bulk density increases with increase in value of Lamda-Rho and Mu-Rho. The decrease in porosity with increasing in depth, cement and LMR shows that deeply buried Lunde Formation reservoir sandstone is tight cement sand.

Another well 34/7-1 is interpreted for Lamda-Rho versus Mu-Rho crossplot for Lunde Formation. The burial depth of the Lunde Formation in this well is relatively shallower than the previously interpreted well. The burial depth ranges from 2400 to 2900 m (MDKB).

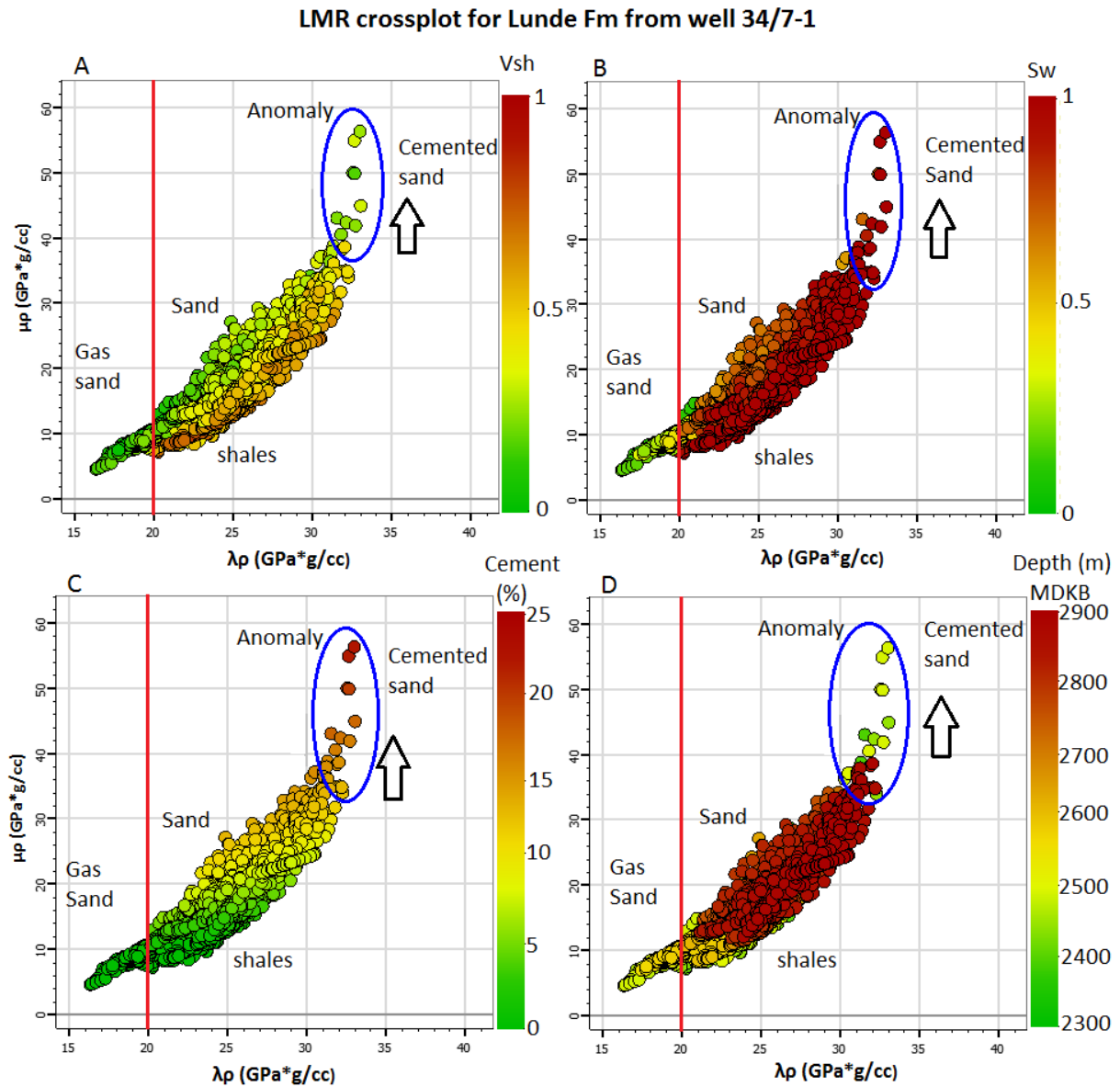


Figure 6.21: The LMR crossplot of Lunde Formation from 34/7-1, colour coded by; (A) shale volume, (B) water saturation, (C) cement volume and (D) burial depth.

In Figure 6.21, the anomaly is observed and marked with blue ellipse. The data points in blue ellipse are from shallower depth (Fig 6.21D) but show higher value for Lamda-Rho and Mu-Rho. The interpretation is that such small intervals are possibly calcite cemented and showing high value for LMR. Furthermore in this well data points are plotting below the threshold line of gas sand zone. The colour coding of water saturation (Fig 6.21B) shows the data below the threshold line of the gas saturated zone is hydrocarbon bearing data. The decrease in incompressibility is due to presence of the hydrocarbons.

Furthermore, the maximum value of Muo-Rho in this well is 40 GPa*g/cc (excluding calcite cemented points) which is less than previously interpreted well (34/7-6). The reason for such

gap for same formation in two different wells is different burial depth. The shallower burial depth in well 34/7-1, contain lower temperature and less favourable condition for quartz cement. This make the data points in well 34/7-1 plotting in unconsolidated less cemented sand zone of LMR crossplot.

Statfjord Formation

The well 34/4-8 is chosen to study LMR crossplot for Statfjord Formation. The reservoir is proven brine saturated in well 34/4-8. The burial depth of the Statfjord Formation in well 34/4-8 ranges from 2800 to 2900 m (MDKB). The Figure 6.22 shows range of data in Mu-Rho domain while little stretch is observed along Lamda-Rho. Most of the data points are plotting in sand zone. The increase in rigidity ($\mu\rho$) is observed with increase in depth. No data points below gas sand threshold line of the Goodway et al. (1997) are observed in the crossplot (Figure 6.22).

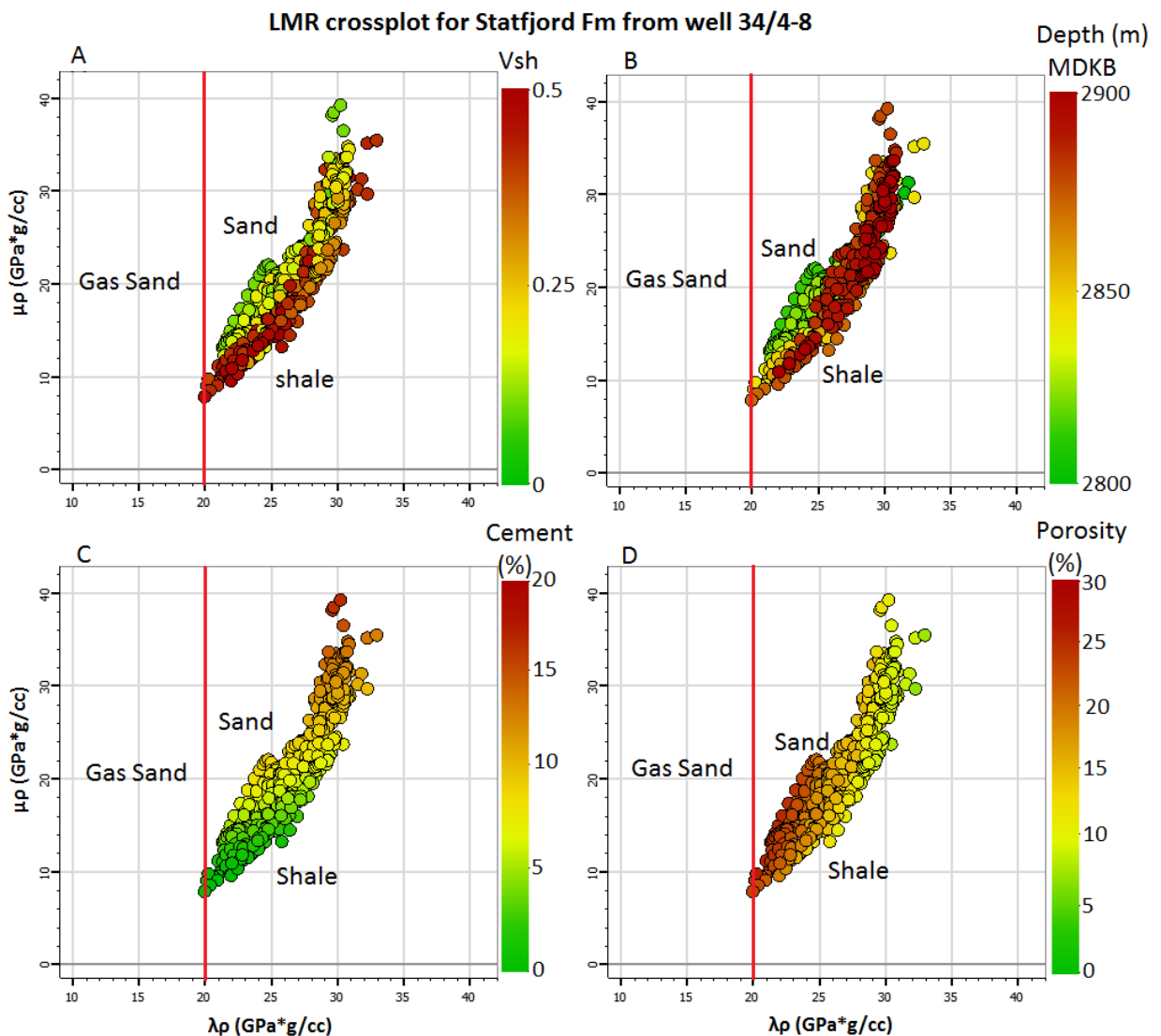


Figure 6.22: The LMR crossplot of Statfjord Formation from well 34/4-8. The crossplots are colour coded by; (A) Vsh, (B) burial depth, (C) cement volume and (D) porosity.

6.5 Discussion

In reservoir characterization for hydrocarbon exploration prospect, the depositional and diagenetic trends of rock physical properties must be taken into consideration. The effect of geological factors such as sand-shale ratio, degree of sorting, cement volume, clay content on rock physical properties can be well studied by using rock physics templates/models. The understanding and application of rock physics models make it easier to extract additional information about subsurface hydrocarbon reservoirs which benefits to reduce exploration risks. The quantitative seismic interpretation is additional advantage of the rock physics model in prospect evaluation. All these advantages of the rock physics techniques/models make it most valuable and researchable field in hydrocarbon industry. The ability to predict geological properties by using elastic properties of rocks is the basic motivation for rock physics modelling.

In this study different rock physics models are applied to observe the change in rock physical trends of the Lunde and Statfjord Formations. The discussion of the each model applied is given below.

6.5.1 Effect of clay on porosity and velocity

The Figure 6.1 illustrates two data trends indicated by arrow heads in the Vp-porosity crossplot. The two different data trends are because of different shale content. The cluster of data with increase in velocity and decreasing porosity is sand which contains small clay particles located in pore spaces. The finer particles cause to decrease in porosity linearly with increasing clay content. This trend is seen up to certain fraction of the shale volume. The reversing of the trend appears with decreasing velocity and increasing porosity when shale volume exceeds more than 40%. The point from which decrease in velocity appear is possible point of transition from grain-supported sediments to matrix-supported sediments. This point is suggested by Marion et al. (1992), the critical clay point (Figure 6.23). The increase of the clay content from sand porosity cause sand grains to be disconnected (Avseth et al., 2005), which is possible reason for velocity decrease in shaly sediments. The increase of shale volume from shaley sand to pure shales cause drop in velocity. The inverted V-shaped Yin-Marion shaly sand model (Avseth et al., 2005; Marion et al., 1992) is possible explanation of the two velocity-porosity trends observed in Figure 6.1. The fine clay particles in pore spaces of the sand cause stiffening and porosity lost.

The constant cement model line in Figure 6.1 is another explanation of high velocity in sand data points. The data containing less than 40% shale volume are captured by constant cement model line assuming 2% quartz cement and also plotting above the line. The increase in velocity from right to left the along constant cement line is because of settlement of fine grain particles in pore spaces with constant cement of 2 %. The data above the line are expecting more cement than 2% volume. The thin section observation for analysis of fine clay particles settlement in pore spaces could be more useful to understand the effect of clay on velocity and porosity of sandstone.

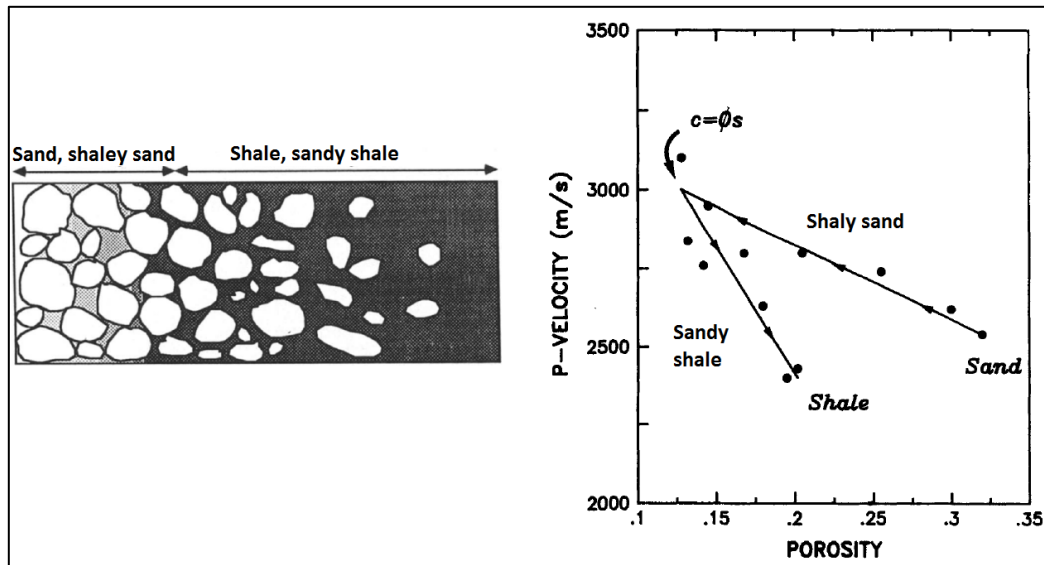


Figure 6.23: Schematic illustration of the grain supported to clay-supported sediments (left). The inverted V-shaped model for shaly sand and sandy shale (right) is suggested by Marion et al. (1992). The model shows increase in velocity with decreasing porosity from sand to shaly sand due to settlement of fine clay particles in pore spaces of sand and decrease in velocity after transition from shaly sand to sandy shale and pure shales. The figure is adapted from Marion et al. (1992).

Figure 6.2 shows effect of clay in velocity-porosity domain by using model from Han et al. (1986). The model lines are representing steep gradient of velocity-porosity relation with respect to different clay fraction. The top most line in Han's model (0 clay content) represents the diagenetic trend for clean sand. The other contours of Han et al. (1986) model represent the velocity-porosity trend with different clay content values. The data superimposing on each model line are assumed to have the clay fraction of the model line. By examining the Figure 6.2 (left) for Lunde Formation, the data points with shale volume more than 40% are plotting below the model line of 0.4 clay content. Few data points are plotting on model line of 0.1 clay content. By interpolating clay volume from model lines only, the Lunde Formation is showing no data points with clay content less than 0.1, since all the data points are plotting below model line of 0.2 clay content. The interpretation shows discrepancy between shale volume suggested from Han's model lines and shale volume from petrophysical analysis. The difference could be because of following reasons;

- The uncertainties associated with shale volume can lead to misinterpretation of the shale volume from petrophysical analysis.
- Porosity estimated from well logs also contains uncertainties since most reliable porosity can be estimated from core samples absent in this study.
- The effective pressure for Han's model used in this study is 30 MPa assumed from burial depth of reservoir as 1MPa/100 m. The assumed effective pressure may not be accurate because it is assumed from overburden rocks.
- The Han's model lines are explaining the certain percentage of clay content within sandstone, while the colour coding of the data in Figure 6.2 is the shale volume from neutron-density combination.

All these factors together could possibly the reason for deviation of data from Han's model lines. By analysing Figure 6.3 (Vp-porosity crossplot of Lunde Formation colour coded with

depth), it can be seen that the data points in the domain of high velocity and low porosity are from the burial depth of 2.9 to 3.2 km (BSF). This depth corresponds to temperature of chemical compaction domain which effect both velocity and porosity. All such factors and uncertainties should be considered for concluding clay affect from Han's model line. The empirical relations of Han et al. (1986) are applicable to data from which they are derived and extrapolation to other condition may not be straight forward (Avseth et al., 2005).

6.5.2 Rock physics cement models

The effect of the rock microstructures on velocity and porosity is studied by using rock physics effective medium models for Lunde and Statfjord Formations. The porosity reduction in sandstones as function of change in sorting and increase of cement volume is examined. The rock physics effective medium models help to predict that the porosity reduction is either due to change in sorting of grains or/and due to cementation. Change in sorting refers to addition of small clay particles between sand grains that cause reduction of porosity with stiffening of sediments under vertical effective stress.

In Figure 6.15, the data points plotting on friable sand model lines (data marked with red ellipse). The slightly increase in shale volume moving the data points towards left in plot to high velocity area. While the other data points plotting above the friable sand model line and close to constant cement model. The increase of depth moving these data points towards constant cement model line.

By the theory of rock physics effective medium models the data on friable sand model line is losing porosity with addition of fine particles (clay and/or silt size particles) between sand grains under vertical effective stress. The presence of authigenic pore filling kaolinite in sandstones of Lunde and Statfjord Formations is reported by study of Khanna, (1997) and is reported as dominant pore filling mineral. In Lunde Formation sandstone average point count of kaolinite are higher (8.63%) than Statfjord samples (7.82%) (Khanna, 1997). The pore filling authigenic kaolinite is sourced from dissolution of feldspar and mica by meteoritic water flushing.

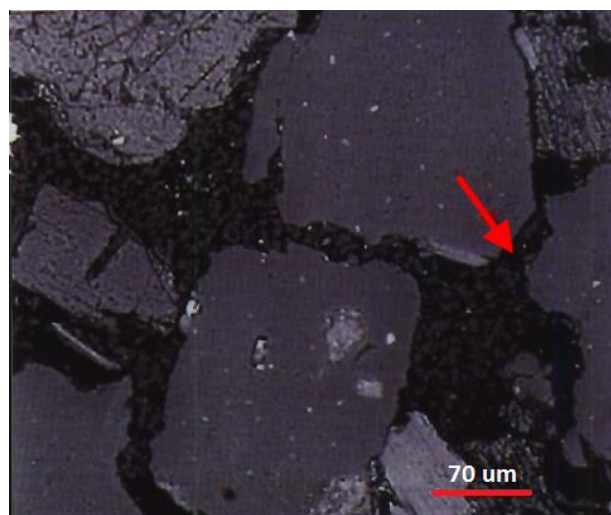


Figure 6.24: Pore filling kaolinite in Lunde Formation from well 34/7-A5H at burial depth of 2936.82 m. The figure is adapted from Khanna, (1997).

The authigenic pore filling kaolinite is incompletely to completely filling the pore space and best developed in absence of cement (Khanna, 1997). The presence of pore filling secondary minerals could be possible reason of moving data points towards low porosity and high velocity area along friable sand model line. The example of pore filling kaolinite in Lunde Formation is also shown in Figures 6.24 and 6.25.

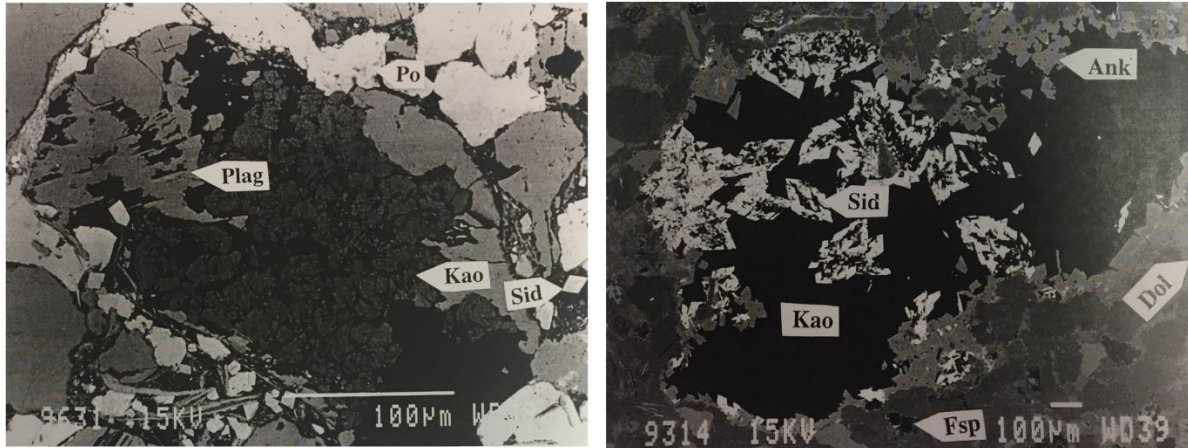


Figure 6.25: The SEM picture showing pore filling kaolinite in Lunde Formation from well 34/4-1 at burial depth 2575 m (left) and at burial depth 2524 m (right); Kao – kaolinite, Plag – plagioclase, Sid – siderite, Dol – dolomite, Fsp – feldspar, Ank – ankerite. The figure is adapted from Muller, (1996).

The other cluster of data close to constant cement model line shows some diagenetic effect (i.e. precipitation of the cement) for porosity loss and velocity increase. The question arises why two different data clusters are observed in same well with different trend? The possible reason of the two data clusters is burial depth and different temperature. In well 34/7-1, plotted in Figure 6.15, the 520 m thick Lunde Formation is buried to approximated depth range of 2034 to 2552 m (MDBSF). The geothermal gradient at well 34/7-1 is 34 °C/km (Figure 6.26), which shows temperature at the top of the Lunde Formation (BSF) is approximately 67 °C, while at the bottom (2552 BSF), temperature is approximately 87.5°C. The shifting of data points towards high velocity is starting from depth of 2250 m (BSF) (Figure 6.26) and temperature is 78 to 80 °C. The onset of quartz cementation starts in basin like North Sea at the temperature of 80 to 100°C (Bjørlykke and Jahren, 2010). The cement precipitation moved data points above the friable sand model line in Figure 6.15. The diagenetic clay minerals present in sandstone of the Lunde Formation are pore-filling kaolinite, smectite, mixed layer chlorite-smectite and chlorite (Khanna, 1997; Morad et al., 1990). The quartz cement could be sourced from smectite to illite transformation which liberates silica but detail analysis is required to find the source of cement for Lunde Formation. By temperature around 70-80 °C smectite dissolves and exchanged by mixed layered minerals and illite (Bjørlykke and Jahren, 2010).

The rock physics model in Vp-porosity domain suggesting 1 to 2% cement because data cluster which shows diagenetic trend is plotting between friable sand model line of 20 MPa which assume 1% quartz cement (Avseth et al., 2005) and constant cement model line of 2% quartz cement. But the Vs-porosity domain is assuming cement from 3 to 5%. The discrepancy between two models is because of different parameters used for generation of models.

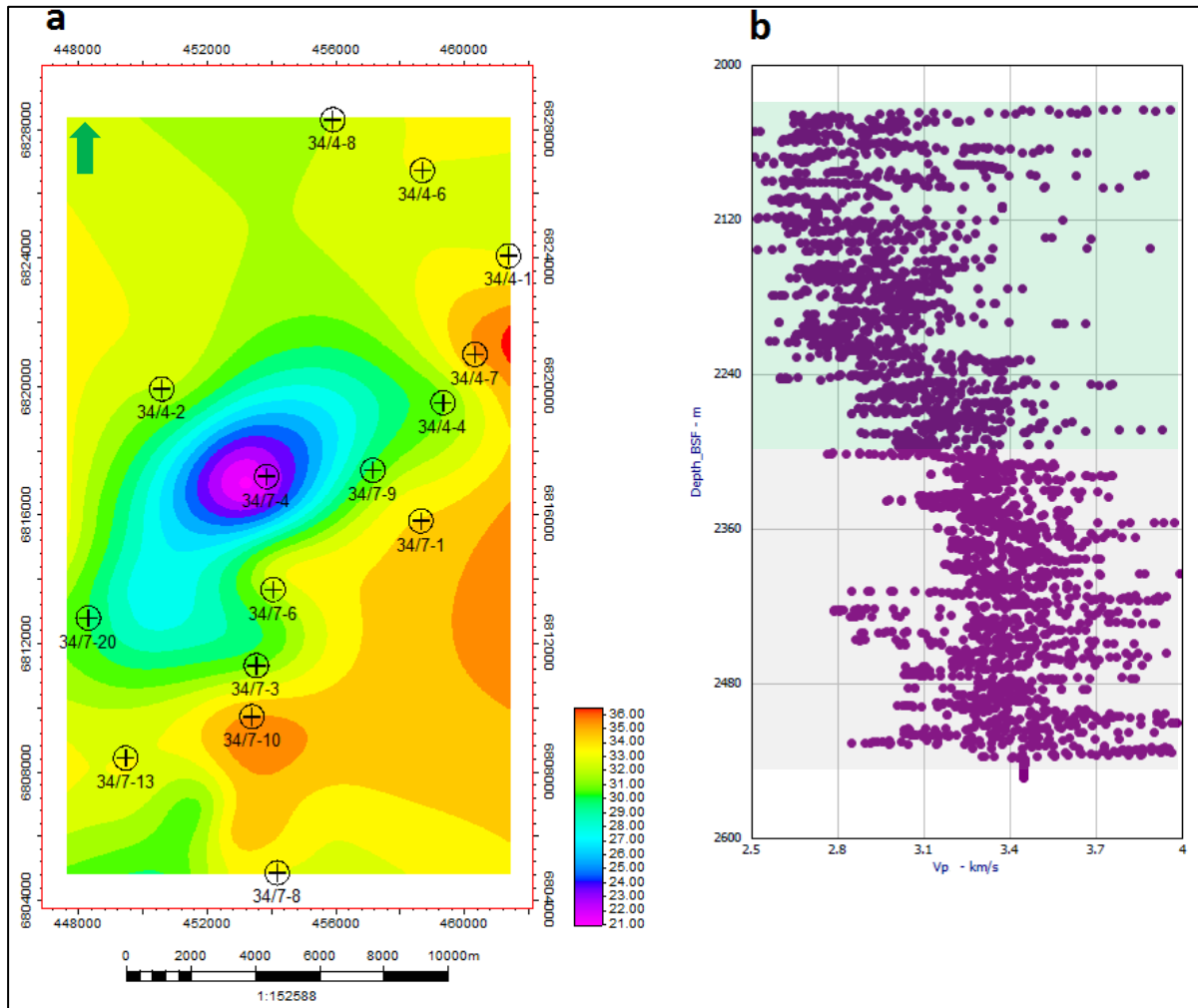


Figure 6.26: The geothermal gradient map of the Snorre field (left) and Velocity-depth trend of Lunde Formation from well 347-1(right). The light green shaded data (right) is plotting on friable sand model line in Figure 6.15, while the light grey shaded data plotting close to constant cement model line.

Another aspect is presence of carbonate cement. The study of the Morad et al. (1990, 2009) reported the presence of calcite cement in Lunde Formation in the Snorre field. The carbonate cement are calcite but dolomite and ankerite are also present (Morad et al., 1990; Morad et al., 2009). The study of Muller, (1996) also reported presence of calcite and dolomite in Lunde Formation from different wells of the Snorre field. The carbonate cement containing mostly calcite, minor dolomite is observed in Lunde Formation and lower part of Statfjord Formation (Khanna, 1997). The carbonate cement is largely pore filling (Khanna, 1997). The presence of calcite cement and quartz overgrowth could possibly taking part in porosity reduction with velocity increase and plotting data on constant cement model line. The example of pore filling calcite cement in Lunde and Statfjord Formations is shown in Figure 6.27.

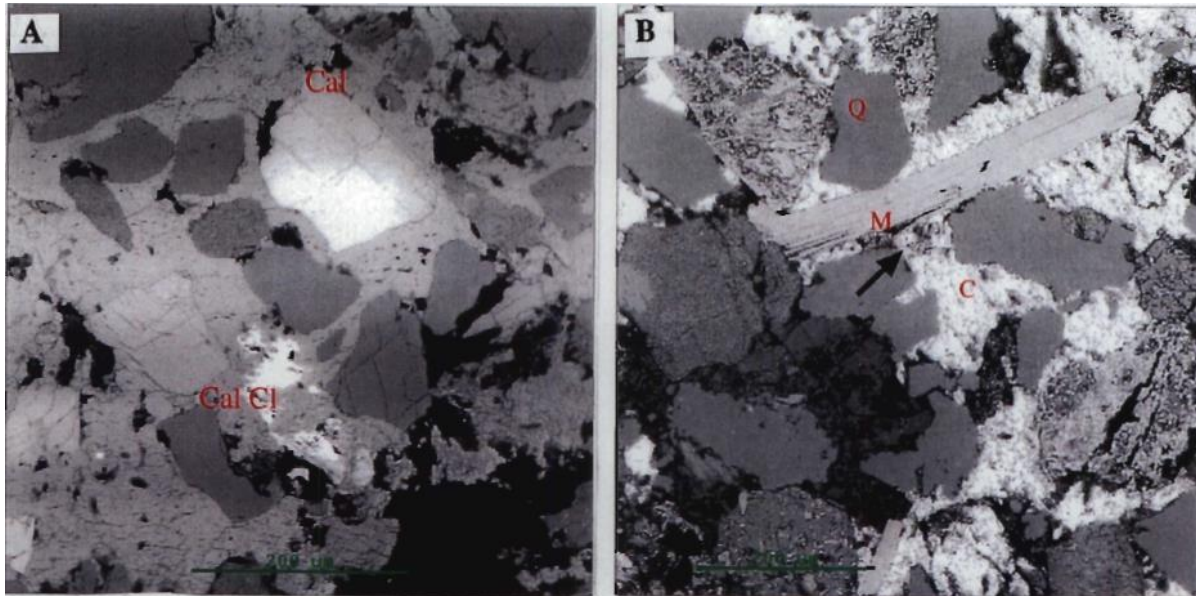


Figure 6.27: Backscatter image of calcite cement in Statfjord Fm (left) from well 34/7-8 (2341 m burial depth) and Lunde Formation (right) from well 34/7-P13 (3684 m burial depth) in the Snorre field. The figure is adapted from Khanna, (1997).

In well 34/7-6, most of the data is plotting on and above constant cement model (Figure 6.16). This well is considerably deeper than well 34/7-1 discussed earlier. Due to deep burial the temperature is high and effect of cement is more prominent, with very few data points plotting in between friable sand model line and constant cement model line. The study of Muller, (1996) confirms the presence of quartz overgrowth in Lunde Formation at deep burial depth (Figure 6.28).

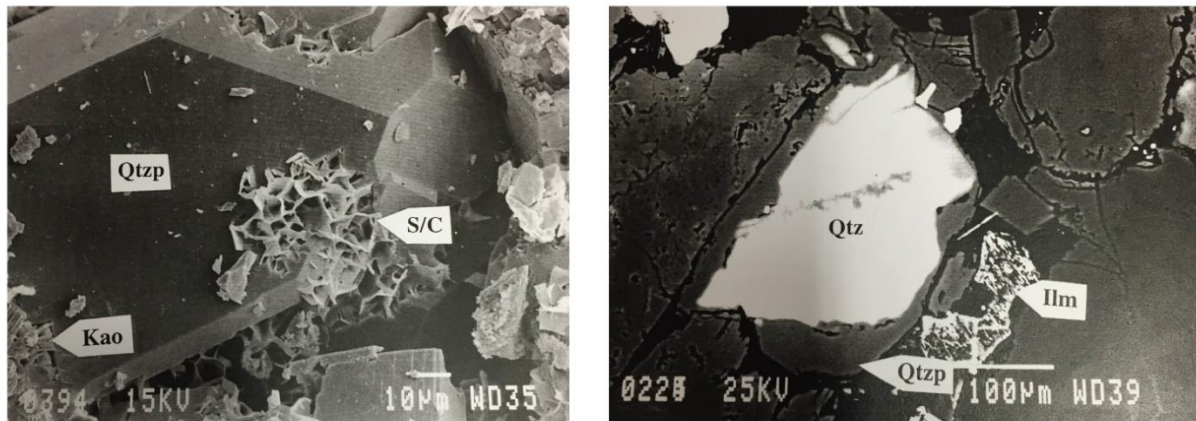


Figure 6.28 SEM images of Lunde Formation from well 34/7-7 at burial depth of 3329 m (left) and 34/4-7 at burial depth of 3328 (right) showing quartz overgrowth; Qtz – quartz grain, Qtzp – quartz overgrowth, Kao – kaolinite and Ilm – ilmenite. The figure is adapted from Muller, (1996).

The rock physics cement model results are comparable with published literature (Khanna, 1997; Morad et al., 1990; Morad et al., 2009; Muller, 1996). The pore filling minerals are causing stiffening of sand grains and plotting on friable sand model lines. The confirmation of the presence of pore filling kaolinite in SEM images of Lunde and Statfjord Formations

confirm the applicability of friable sand model. The effect is more prominent in shallow buried parts and in absence of quartz overgrowth and other cement (e.g. calcite, dolomite). The presence of quartz overgrowth and pore filling calcite cement is possible reason for diagenetic controlled trend of velocity and porosity from deep burial depth. Sandstones of Statfjord Formation is less affected by calcite cement and quartz overgrowth as compared to Lunde Formation and exhibit better reservoir properties (Khanna, 1997).

The models used in this study are generated for simplistic quartz sand saturated with brine. During generation of model the elastic properties of other minerals and rock fragments present in sandstone must be taken into consideration. The verification of the cement from rock physics model against thin sections is necessary (Avseth et al., 2010). The stiffening effect due to carbonate cement (e.g. Calcite, dolomite, siderite) can lead to overestimation of quartz cement assumed from rock physics model.

6.5.3 Effect of lithology and fluid sensitivity

The V_p/V_s versus AI crossplot with overlying rock physics template is excellent tool for lithology discrimination and identification of fluid. In Figure 6.4, the lithology is discriminated very well between overlying cap shales and underlying sandstones reservoirs. The increasing V_p/V_s for shales reflect its sensitivity to clays. The brine sand model shows much flatter trend for V_p/V_s as compared to shales. The deviation of data above brine sand line is due to presence of clay and called clay effect by Ødegaard and Avseth, (2003), while falling below sand model is called gas effect. The idealized brine saturated pure quartz sand model is used in this study for interpretation, but applicability of the template is practically dependent on the geological input for model generation. In Figure 6.6 the brine saturated sandstone data points of Eive Formation from well 34/7-27 sitting above the model line but fluid substitution for oil and gas scenario (100%) drag data down with decreasing V_p/V_s (Figure 6.7). This sensitivity of fluids is more prominent in loose/unconsolidated sands than consolidated/cemented sands.

The limitation of this study is absence of measured shear wave information for Lunde and Statfjord Formations, which make it challenging to extract much information from V_p/V_s and AI crossplot by using estimated shear wave. In Figure 6.9a, data from Statfjord Formation from well 34/4-8 falling above the quartz model line which reflects the effect of clay. The presence of clays moved data above the brine saturated pure quartz sand. But in other scenario (Figure 6.9b) the sandstone data is showing good agreement with 80% quartz and 20% clay model line. The agreement is until certain fraction of shale volume. From petrophysical analysis it is interpreted that the reservoir of Statfjord Formation is channel sandstone interbedded with shales. The deviation of data points from sandstone model with shale volume greater than 40% confirm different trend of shales in V_p/V_s versus AI crossplot. This reflects good lithology discrimination between sandstone and shales using V_p/V_s and AI crossplot for Statfjord Formation. The sandstone data points plotting above the quartz sand model line is showing presence of clay in sandstones of Statfjord Formation. The thin section observation of Statfjord Formation by Khanna, (1997) discussed in above section confirms the presence of clays in sandstones of Statfjord Formation.

The effect of cement on V_p/V_s versus AI crossplot is tested by using the estimated cement volume as colour coding (Figure 6.10). The increase in cement volume move data in high AI area because of increase in density due to precipitation of cement. Cementation is directly dependent on burial depth and temperature of the rocks. During lithology and fluid

interpretation from V_p/V_s versus AI plot, the depth and cementation factor should be considered. The presence of diagenetic cement shift the brine saturated data points to the area where hydrocarbon saturated data points are expected in V_p/V_s versus AI crossplot (Ødegaard and Avseth, 2003). The slight under estimation of the porosity from rock physics template is either due to misinterpretation of porosity from petrophysical analysis or/and because of using more generalized elastic parameters for model generation. The fluid separation is not easy to detect from V_p/V_s versus AI crossplot if the estimated V_s is used as input. By using estimated V_s the close narrow trend of V_p/V_s is observed. The estimated V_s itself contain some uncertainties, depends on which linear equation used to estimate V_s .

6.5.4 LMR ($\lambda\rho$ versus $\mu\rho$) crossplot

The incompressibility ($\lambda\rho$) of rock is sensitive to rock pore fluids while rigidity ($\mu\rho$) is concerned with rock fabric and lithology (Goodway et al., 1997). The rigidity is resistance to shape change without any change in volume and in case of shales rigidity is low because they can slide over each other (Gray and Andersen, 2000).

By analysing Figure 6.20 for Lunde Formation the separation between shales and sandstone from LMR crossplot is observed. The separation is not very clear because the estimated shear wave information is used. The high incompressibility ($\lambda\rho$) and low rigidity ($\mu\rho$) of shales fall them below sand in crossplot of LMR comparable to template suggested by Goodway et al. (1997). The steep increase of rigidity for Lunde Formation in Figure 6.20 is observed. This steep increase is argued by stiffening of grains framework with onset of cement. On other hand incompressibility is also increasing but the increase is less as compared to rigidity. The argument that cements cause to increase LMR value is supported by decrease in porosity with respect to burial depth. The maximum value of rigidity ($\mu\rho$) at 3500 m burial depth for Lunde Formation in well is approximately 80 GPa*g/cc (Figure 6.20B). Due to cement increase of density occur which in turn increase $\mu\rho$.

6.6 Uncertainties in rock physics diagnostics

The following are some uncertainties related to rock physics study and necessary to discuss, because the results are influenced by uncertainties and limitations.

- The rock physics model used in this study are produced by assumption of pure brine saturated quartz sand. The model is valid for well-rounded, well sorted quartz sand but in case of presence of clay minerals and rock fragments the validity/limitation should be considered. During generation of effective medium model the elastic value of all mineral constituents of sandstone should be considered.
- The constant cement model and contact cement model are used from published literature. The mineralogical input of both models is different from mineralogy of currently studied horizons. Therefore, the exact cement volume cannot be estimated.
- The input of effective pressure is assumed from overburden stress considering hydrostatic pore pressure due to lack of pore pressure data in studied reservoirs.
- For cement model generation the type of cement must be taken into consideration. Currently studied Lunde and Statfjord Formations contain carbonate cement (calcite, siderite dolomite). The quartz cement precipitated from clay mineral transformation but the model used is not calibrated for occurrence of quartz cement.

- The elastic properties of arkose sandstones and quartz arenite are different, therefore should be taken into consideration during rock physics template generation.
- The absence of measured V_s evolves uncertainties for V_p/V_s versus AI and LMR crossplots. The estimated V_s is used in absence of measured V_s , but variety of linear relations are available in literature to estimate V_s from V_p . All the equations are generated for certain data set and lithology; it is challenging to find which equation fit best for data under study.
- In rock physics plotting the third dimension or z-axis (colour coding) is powerful tool for extraction of much more information. In this study the parameters used for colour coding are mostly derived from petrophysical analysis. Any misinterpretation in petrophysical analysis due to uncertainties of petrophysical interpretation can mislead rock physics interpretation.

Chapter 7: Summary and Conclusions

This study is aimed to understand the reservoir properties of the Statfjord and Lunde Formations of the Snorre field. The field is located on the Tampen Spur area in northern North Sea. Tampen Spur is a structural high, located northwest of Viking Graben and consists of rotated fault blocks. The field is located in blocks 34/4 and 34/7, under production licence PL05 and PL089. The field was discovered in 1979 with discovery of oil in well 34/4-1. The Lunde Formation is the principal reservoir and the Statfjord Formation is secondary reservoir of the Snorre field. The hydrocarbons are trapped within structural traps and production is aided by water and gas injection.

A suite of well log data from 20 exploration wells in the Snorre field and the surrounding areas are used to conduct the study. Within the 20 wells, five wells (34/4-2, 34/4-8, 34/7-27, 34/7-28 and 34/7-32) are dry while rest of the wells content oil. The Lunde Formation is encountered in 14 wells (34/4-1, 34/4-2, 34/4-4, 34/4-6, 34/4-7, 34/4-8, 34/7-1, 34/7-3, 34/7-4, 34/7-6, 34/7-8, 34/7-9, 34/7-10, 34/7-20), while the Statfjord Formation is encountered along 9 wells (34/4-2, 34/4-8, 34/7-3, 34/7-4, 34/7-6, 34/7-8, 34/7-10, 34/7-13 and 34/7-20). From well to well correlation it has been observed that the Statfjord Formation is not present in north-eastern part of the Snorre field. The uplift of rotated fault blocks during the Kimmerian tectonic phase, cause erosion of uppermost Triassic and Jurassic strata.

The Lunde and Statfjord Formations were deposited on large alluvial plain during thermal subsidence phase of permo-triassic rifting episode of the North Sea. The main interpreted facies are multi-storey and single channel sandstone bodies with fine grained overbank and floodplain mudstone deposits. These facies are interpreted with the aid of published literature and Gamma Ray log trends. The Statfjord Formation is divided into sub members in other discovered fields of the Tampen Spur (e.g. Statfjord and Gullfaks) but subdivision is not applied in the Snorre field. The maximum thickness of the Lunde Formation encountered in wells in the Snorre field is approximately 1100m in well 34/4-2, while the maximum thickness of the Statfjord Formation in the Snorre field is 144m in well 34/7-6.

In order to characterize the reservoir petrophysical analysis, compaction study and rock physics diagnostics were performed. Due to absence of seismic data, thin section analysis several uncertainties evolve in this study. The results produced but utilizing only well log data are still valuable and in many cases comparable with published literature.

In petrophysical analysis shale volume, porosity, net-to-gross reservoir, water saturation and permeability are estimated. The lithology is identified from Neutron-Density and Gamma Ray log, while Caliper is used to check borehole conditions. The shale content in Statfjord Formation is higher than the underlying Lunde Formation. The sandstone of Statfjord Formation preserves higher porosity as compared to the Lunde Formation. The channel sands with fining upward sequence exhibit good porosity which show decrease towards finer overbank deposits. The internal shale layers cause barrier for fluid flow within reservoirs. The correlation of the channel sand within the studied wells is not straightforward if we use only well log data.

In compaction study data fall with the mechanical and chemical compactions are evaluated by comparing the well log trends with published compaction trends. The geothermal gradient is calculated by using bottom hole temperature which used to confirm the transition zone depth with respect to present day temperature. The temperature history and transition zone depth

help to find the reservoir location in mechanically or chemically compacted zones. The start of chemical compaction in the Snorre field wells is observed from temperature $>70^{\circ}\text{C}$ and the transition zone is mostly located in the Lunde Formation. The presence of carbonate intervals are also observed in both reservoirs (Lunde and Statfjord Formations). It is also verified by published literature. The uplift estimation is performed by using the 50:50 silt-kaolinite curve published by Mondol, (2009). The study area is located in subsiding basin and the calculated uplift is related to rotated fault block geometry and footwall uplift.

The rock physics diagnostics using rock physics effective medium model are used to predict cement in Statfjord and Lunde sandstones. The effective medium models also utilized to predict the change in rock physical properties with respect to rock microstructures. Furthermore, the presence of clays and their influence on rock properties (e.g. porosity and velocity) is studied using Han et al. (1986) and Marion et al. (1990) models. The crossplot of V_p/V_s and AI is utilized to distinguish lithology between shale and sand. The effect of fluids was also part of consideration in V_p/V_s versus AI crossplot. In addition, LMR crossplot is utilized to differentiate lithology and fluids. The main limitation for V_p/V_s versus AI or LMR crossplot was absence of measured V_s (shear wave) data for all wells that penetrated both Statfjord and Lunde Formations.

The following conclusions are drawn from integrated studies of petrophysical analyses, compaction history and rock physics diagnostics.

- The Lunde Formation (principal reservoir) contains significant thickness but the thickness of the Statfjord Formation is very thin due to erosion of the Kimmerian tectonism formed unconformity. The Statfjord Formation sandstone contains high porosity. The highest effective porosity 18% for the Lunde Formation and 23% for the Statfjord Formation is calculated from petrophysical analysis. The highest net-to-gross is 0.89 for the Lunde Formation in well 34/7-1 and 0.79 for the Statfjord Formation in well 34/7-13. No any specific trend of net-to-gross observed from well to well over the field.
- The hydrocarbon saturation is observed in channel sandstone with shale barrier between sandstone bodies. The vertical connectivity of the channel sandstone bodies is very limited. This is the reason for injection aided production from the Snorre field.
- Facie correlation from well to well is not possible to study by using just only well log data. The core section logging along with well log can be used to find the continuity of channel sandstone body which can help to understand better the flow of hydrocarbons within the reservoirs.
- Compaction analysis shows the transition of mechanical compaction to chemical compaction occur within the Lunde Formation.
- The temperature at transition zone is $70\text{--}80^{\circ}\text{C}$, which shows the onset of quartz cementation in the Lunde Formation. The Statfjord Formation is present above transition zone in wells 34/7-3, 34/7-4, 34/7-6 and 34/7-8. In the well 34/7-20, the Statfjord Formation is present within chemical compaction. The sharp increase of V_p is not observed in the Statfjord Formation in most of the wells. This could be reason of high porosity in the Statfjord Formation as compared to the Lunde Formation. Besides quartz cementation, pore filling carbonate cement is identified in Lunde Formation, which is close agreement with several authors. The carbonate cement is also observed in the Statfjord Formation prompting porosity and permeability reduction in both reservoirs. The high V_p values also confirm the presence of carbonate cemented

intervals above and below the transition zone. The carbonate cement is may be sourced during early diagenesis.

- The overpressure is observed in the hydrocarbon saturated Lunde and Statfjord Formations. The overpressure also works against effective stress and help to preserve porosity.
- The estimated uplift in several wells in the Snorre field is related to rotated fault block geometry.
- The rock physics cement models correspond data from two compaction regimes; data plotted on friable sand model correspond to position above the transition zone while data from chemical compaction zone is plotting on constant cement model line.
- As expected the cement percentage increase with depth and temperature. The increasing cement volume moving data points in high velocity and low porosity area along constant cement model lines.
- The presence of carbonate cements is also a possible reason for plotting data on cement model lines especially in the case of the Statfjord Formation which is present above the transition zone in most of the wells. The absolute percentage of cement volume cannot be estimated from rock physics cement model. The applicability of model lacking mineral calibration may not be precise.
- The V_p/V_s versus AI impedance crossplot shows good lithology discrimination for shales and sandstones for both Lunde and Statfjord Formations. The effect of fluids is not conclusive because the estimated V_s in crossplot is used. By using estimated V_s the separation for HC saturated data is not clear. The presence of diagenetic cement moved data points in low V_p/V_s and high AI area of crossplot. This reflects the stiffening of grain framework and reduces the effect of V_p/V_s . The presence of clay in sandstone shift data points towards shale trend. The calibration of template with mineralogy is crucial for its applicability.
- Shales are discriminated from sand because of low incompressibility of shales. The increase of rigidity of sand is observed with increasing cement and burial depth.

Reference list

- Adeoti, L., Ayolabi, E., and James, P., 2009, An integrated approach to volume of shale analysis: Niger Delta example, Offshore Field: World Applied Sciences Journal, v. 7, no. 4, p. 448-452.
- Archie, G. E., 1942, The electrical resistivity log as an aid in determining some reservoir characteristics: Transactions of the AIME, v. 146, no. 01, p. 54-62.
- Avseth, P., Dvorkin, J., Mavko, G., and Rykkje, J., 2000, Rock physics diagnostic of North Sea sands: Link between microstructure and seismic properties: Geophysical Research Letters, v. 27, no. 17, p. 2761-2764.
- Avseth, P., Jørstad, A., van Wijngaarden, A.-J., and Mavko, G., 2009, Rock physics estimation of cement volume, sorting, and net-to-gross in North Sea sandstones: The Leading Edge, v. 28, no. 1, p. 98-108.
- Avseth, P., Mukerji, T., and Mavko, G., 2005, Quantitative seismic interpretation.
- Avseth, P., Mukerji, T., Mavko, G., and Dvorkin, J., 2010, Rock-physics diagnostics of depositional texture, diagenetic alterations, and reservoir heterogeneity in high-porosity siliciclastic sediments and rocks—A review of selected models and suggested work flows: Geophysics, v. 75, no. 5, p. 75A31-75A47.
- Avseth, P., and Odegaard, E., 2004, Well log and seismic data analysis using rock physics templates: First break, v. 22, no. 10, p. 37-43.
- Badarinadh, V., Suryanarayana, K., Youssef, F. Z., Sahouh, K., and Valle, A., 2002, Log-derived permeability in a heterogeneous carbonate reservoir of Middle East, Abu Dhabi, using artificial neural network, Abu Dhabi International Petroleum Exhibition and Conference, Society of Petroleum Engineers.
- Badley, M., Price, J., Dahl, C. R., and Agdestein, T., 1988, The structural evolution of the northern Viking Graben and its bearing upon extensional modes of basin formation: Journal of the Geological Society, v. 145, no. 3, p. 455-472.
- Baig, I., Faleide, J. I., Jahren, J., and Mondol, N. H., 2016, Cenozoic exhumation on the southwestern Barents Shelf: Estimates and uncertainties constrained from compaction and thermal maturity analyses: Marine and Petroleum Geology, v. 73, p. 105-130.
- Beers, R. F., 1945, Radioactivity and organic content of some Paleozoic shales: AAPG Bulletin, v. 29, no. 1, p. 1-22.
- Berstad, S., and Dypvik, H., 1982, Sedimentological evolution and natural radioactivity of Tertiary sediments from central North Sea: Journal of Petroleum Geology, v. 5, no. 1, p. 77-88.
- Bjørlykke, K., Hoeg, K., and Haque Mondol, M., 2010, Introduction to geomechanics: stress and strain in sedimentary basins: Petroleum geoscience: from sedimentary environments to rock physics, p. 281-298.
- Bjørlykke, K., Jahren, J., Mondol, N. H., Marcussen, O., Croize, D., Peltonen, C., and Thyberg, B., 2009, PS Sediment Compaction and Rock Properties.
- Bjørlykke, K., 1999, Principal aspects of compaction and fluid flow in mudstones: Geological Society, London, Special Publications, v. 158, no. 1, p. 73-78.
- Bjørlykke, K., 2010, Compaction of sedimentary rocks including shales, sandstones and carbonates, Petroleum Geoscience, Springer, p. 329-337.

- Bjørlykke, K., and Jahren, J., 2010, Sandstones and Sandstone Reservoirs: Petroleum Geoscience, p. 113-140.
- Bjørlykke, K., Ramm, M., and Saigal, G. C., 1989, Sandstone diagenesis and porosity modification during basin evolution: *Geologische Rundschau*, v. 78, no. 1, p. 243-268.
- Bowers, G. L., 1995, Pore pressure estimation from velocity data: Accounting for overpressure mechanisms besides undercompaction: *SPE Drilling & Completion*, v. 10, no. 02, p. 89-95.
- Bowers, G. L., 2002, Detecting high overpressure: *The Leading Edge*, v. 21, no. 2, p. 174-177.
- Bowman, M., 2009, *Cenozoic: Petroleum Geology of the North Sea: Basic Concepts and Recent Advances*, Fourth Edition, p. 350-375.
- Bukovics, C., and Ziegler, P. A., 1985, Tectonic development of the Mid-Norway continental margin: *Marine and Petroleum Geology*, v. 2, no. 1, p. 2-22.
- Caillet, G., 1993, The caprock of the Snorre Field, Norway: a possible leakage by hydraulic fracturing: *Marine and Petroleum Geology*, v. 10, no. 1, p. 42-50.
- Cant, D., 1992, Subsurface facies analysis: *Facies Models, Response to Sea Level Changes*. Geol. Assoc. Canada, p. 27-45.
- Castagna, J. P., 1993, Petrophysical imaging using AVO: *The Leading Edge*, v. 12, no. 3, p. 172-178.
- Castagna, J. P., Batzle, M. L., and Eastwood, R. L., 1985, Relationships between compressional-wave and shear-wave velocities in clastic silicate rocks: *Geophysics*, v. 50, no. 4, p. 571-581.
- Chamock, M., Kristiansen, I., Ryseth, A., and Fenton, J., 2001, Sequence stratigraphy of the lower jurassic dunlin group, northern North Sea: *Norwegian Petroleum Society Special Publications*, v. 10, p. 145-174.
- Chi, X.-g., and Han, D.-h., 2009, Lithology and fluid differentiation using a rock physics template: *The Leading Edge*, v. 28, no. 1, p. 60-65.
- Christiansson, P., Faleide, J., and Berge, A., 2000, Crustal structure in the northern North Sea: an integrated geophysical study: *Geological Society, London, Special Publications*, v. 167, no. 1, p. 15-40.
- Chuhan, F. A., Kjeldstad, A., Bjørlykke, K., and Høeg, K., 2002, Porosity loss in sand by grain crushing—Experimental evidence and relevance to reservoir quality: *Marine and Petroleum Geology*, v. 19, no. 1, p. 39-53.
- Chuhan, F. A., Kjeldstad, A., Bjørlykke, K., and Høeg, K., 2003, Experimental compression of loose sands: relevance to porosity reduction during burial in sedimentary basins: *Canadian Geotechnical Journal*, v. 40, no. 5, p. 995-1011.
- Clavier, C., Hoyle, W., and Meunier, D., 1971, Quantitative interpretation of thermal neutron decay time logs: part I. Fundamentals and techniques: *Journal of Petroleum Technology*, v. 23, no. 06, p. 743-755.
- Cluff, S. G., and Cluff, R. M., 2004, Petrophysics of the Lance sandstone reservoirs in Jonah field, Sublette County, Wyoming.
- Dalland, A., Worsley, D., and Ofstad, K., 1988, A Lithostratigraphic Scheme for the Mesozoic and Cenozoic and Succession Offshore Mid-and Northern Norway, Oljedirektoratet.
- Dewar, J., and Downton, J., 2002, Getting unlost and staying found—a practical framework for interpreting elastic parameters: *CSEG, Expanded Abstracts*.
- Downie, R., 2009, *Devonian: Petroleum Geology of the North Sea: Basic Concepts and Recent Advances*, Fourth Edition, p. 85-103.
- Dresser Atlas, 1982, *Well Logging and Interpretation Techniques: The Course for Home Study*, Dresser Industries, Incorporated.

- Dræge, A., 2011, A diagenetic rock physics approach for siliciclastics: The Leading Edge, v. 30, no. 12, p. 1368-1375.
- Dvorkin, J., 2007, Yet another Vs equation, Volume 26, p. 1570-1574.
- Dvorkin, J., and Nur, A., 1996, Elasticity of high-porosity sandstones: Theory for two North Sea data sets: Geophysics, v. 61, no. 5, p. 1363-1370.
- Dvorkin, J., and Nur, A., 2002, Critical-porosity models: MEMOIRS-AMERICAN ASSOCIATION OF PETROLEUM GEOLOGISTS, p. 33-42.
- Ellis, D. V., and Singer, J. M., 2007, Well logging for earth scientists, Springer Science & Business Media.
- Emery, D., and Myers, K., 2009, Sequence stratigraphy, John Wiley & Sons.
- Erratt, D., Thomas, G., and Wall, G., 1999, The evolution of the central North Sea Rift, Geological society, london, petroleum geology conference series, Volume 5, Geological Society of London, p. 63-82.
- Ezekwe, N., 2010, Petroleum reservoir engineering practice, Pearson Education.
- Faleide, J. I., Bjørlykke, K., and Gabrielsen, R. H., 2015, Geology of the Norwegian continental shelf, Petroleum Geoscience, Springer, p. 603-637.
- Faleide, J. I., Kyrkjebø, R., Kjennerud, T., Gabrielsen, R. H., Jordt, H., Fanavoll, S., and Bjerke, M. D., 2002, Tectonic impact on sedimentary processes during Cenozoic evolution of the northern North Sea and surrounding areas: Geological Society, London, Special Publications, v. 196, no. 1, p. 235-269.
- Fisher, M., and Mudge, D., 1998, Triassic: Petroleum Geology of the North Sea: Basic Concepts and Recent Advances, Fourth Edition, p. 212-244.
- Fjellanger, E., Olsen, T. R., and Rubino, J. L., 1996, Sequence stratigraphy and palaeogeography of the Middle Jurassic Brent and Vestland deltaic systems, northern North Sea: Norsk Geologisk Tidsskrift, v. 76, p. 75-106.
- Færseth, R., 1996, Interaction of Permo-Triassic and Jurassic extensional fault-blocks during the development of the northern North Sea: Journal of the Geological Society, v. 153, no. 6, p. 931-944.
- Færseth, R., Gabrielsen, R., and Hurich, C., 1995, Influence of basement in structuring of the North-Sea basin, offshore southwest Norway: Norsk Geologisk Tidsskrift, v. 75, no. 2-3, p. 105-119.
- Gabrielsen, R. H., Faleide, J. I., Pascal, C., Braathen, A., Nystuen, J. P., Etzelmuller, B., and O'Donnell, S., 2010, Latest Caledonian to Present tectonomorphological development of southern Norway: Marine and Petroleum Geology, v. 27, no. 3, p. 709-723.
- Glennie, K., 2009, Petroleum Geology of the North Sea: Basic concepts and recent advances, John Wiley & Sons.
- Goodway, B., 2001, AVO and Lamé constants for rock parameterization and fluid detection: CSEG Recorder, v. 26, no. 6, p. 39-60.
- Goodway, B., Chen, T., and Downton, J., 1997, Improved AVO Fluid Detection And Lithology Discrimination Using Lamé Petrophysical Parameters; “ $\lambda\rho$ ”, $\mu\rho$, $\lambda\mu$ Fluid Stack”, From P And S Inversions, 1997 SEG Annual Meeting, Society of Exploration Geophysicists.
- Gray, D., Goodway, B., and Chen, T., 1999, Bridging the Gap-Using AVO to Detect Changes in Fundamental Elastic Constants, 61st EAGE Conference and Exhibition.
- Gray, F. D., and Andersen, E., 2000, Case Histories-Inversion for Rock Properties, 62nd EAGE Conference & Exhibition.
- Greenberg, M., and Castagna, J., 1992, Shear-wave velocity estimation in porous rocks: Theoretical formulation, preliminary verification and applications: Geophysical prospecting, v. 40, no. 2, p. 195-209.

- Han, D.-h., Nur, A., and Morgan, D., 1986, Effects of porosity and clay content on wave velocities in sandstones: *Geophysics*, v. 51, no. 11, p. 2093-2107.
- Hansen, J. A., 2016, Reservoir characterization of the Triassic-Jurassic succession of the Bjarmeland Platform, Norwegian Barents Sea. Examples from the Caurus, Arenaria and Obesum discoveries: Master's thesis, University of Oslo, Norway.
- Hashin, Z., and Shtrikman, S., 1963, A variational approach to the theory of the elastic behaviour of multiphase materials: *Journal of the Mechanics and Physics of Solids*, v. 11, no. 2, p. 127-140.
- Hollander, N. B., 1987, Snorre. In: A.M Spencer et al. (Editors), *Geology of the Norwegian oil and gas fields: Graham and Trotman*, London, p. 307-318.
- Hornby, B. E., and Murphy, W. F., 1987, V P/V S in unconsolidated oil sands: Shear from Stoneley: *Geophysics*, v. 52, no. 4, p. 502-513.
- Horstad, I., Larter, S., and Mills, N., 1995, Migration of hydrocarbons in the Tampen Spur area, Norwegian North Sea: a reservoir geochemical evaluation: *Geological Society, London, Special Publications*, v. 86, no. 1, p. 159-183.
- Hoversten, G. M., Newman, G., Morrison, H., Gasperikova, E., and Berg, J.-I., 2001, Reservoir characterization using crosswell electromagnetic inversion: A feasibility study for the Snorre field, North Sea: *Geophysics*, v. 66, no. 4, p. 1177-1189.
- Inichinbia, S., Sule, P. O., Ahmed, A. L., Hamza, H., and Omudu, L. M., 2014, Fluid and lithology discrimination of Amangi hydrocarbon field of the Niger Delta using Lambda-Mu-Rho technique.
- Isaksen, D., and Tonstad, K., 1989, A revised Cretaceous and Tertiary lithostratigraphic nomenclature for the Norwegian North Sea, Norwegian Petroleum Directorate.
- Jackson, C. A., Kane, K. E., and Larsen, E., 2010, Structural evolution of minibasins on the Utsira High, northern North Sea; implications for Jurassic sediment dispersal and reservoir distribution: *Petroleum Geoscience*, v. 16, no. 2, p. 105-120.
- Japsen, P., 1999, Overpressured Cenozoic shale mapped from velocity anomalies relative to a baseline for marine shale, North Sea: *Petroleum Geoscience*, v. 5, no. 4, p. 321-336.
- Jorde, K., and Diesen, G., 1990, The Snorre field-A major field in the northern North Sea: *AAPG Bulletin (American Association of Petroleum Geologists);(USA)*, v. 74, no. CONF-9010204--.
- Justwan, H., and Dahl, B., 2005, Quantitative hydrocarbon potential mapping and organofacies study in the Greater Balder Area, Norwegian North Sea, *Geological Society, London, Petroleum Geology Conference series, Volume 6, Geological Society of London*, p. 1317-1329.
- Kennedy, M., 2015, *Practical petrophysics*, Elsevier.
- Ketzer, J. M., Morad, S., Nystuen, J. P., and De Ros, L. F., 2002, The role of the Cimmerian Unconformity (Early Cretaceous) in the kaolinitization and related reservoir-quality evolution in Triassic sandstones of the Snorre Field, North Sea: *International Association of Sedimentologists Special Publications*, no. 34, p. 361-382.
- Khanna, M., 1997, Kaolinitization of Upper Triassic-Lower Jurassic sandstones of the Tampen Spur area, North Sea: implications for early diagenesis and fluid flow.
- Krief, M., Garat, J., Stellingwerf, J., and Ventre, J., 1990, A petrophysical interpretation using the velocities of P and S waves (full-waveform sonic): *The Log Analyst*, v. 31, no. 06.
- Larionov, V., 1969, *Borehole radiometry: Nedra, Moscow*, v. 3rd ed.
- Lervik, K., 2006, Triassic lithostratigraphy of the northern North Sea Basin: *NORSK GEOLOGISK TIDSSKRIFT*, v. 86, no. 2, p. 93.
- Lervik, K., Spencer, A., and Warrington, G., 1989, Outline of Triassic stratigraphy and structure in the central and northern North Sea, *Correlation in Hydrocarbon Exploration*, Springer, p. 173-189.

- Løseth, H., Raulline, B., and Nygård, A., 2013, Late Cenozoic geological evolution of the northern North Sea: development of a Miocene unconformity reshaped by large-scale Pleistocene sand intrusion: *Journal of the Geological Society*, v. 170, no. 1, p. 133-145.
- Marcussen, Ø., Maast, T. E., Mondol, N. H., Jahren, J., and Bjørlykke, K., 2010, Changes in physical properties of a reservoir sandstone as a function of burial depth—The Etive Formation, northern North Sea: *Marine and Petroleum Geology*, v. 27, no. 8, p. 1725-1735.
- Marion, D., Nur, A., Yin, H., and Han, D.-H., 1992, Compressional velocity and porosity in sand-clay mixtures: *Geophysics*, v. 57, no. 4, p. 554-563.
- Mavko, G., Mukerji, T., and Dvorkin, J., 1998, *The Rock Physics Handbook: Tools for Seismic Analysis in Porous Media*, 329 pp, Cambridge Univ. Press, Cambridge, UK.
- Mavko, G., Mukerji, T., and Dvorkin, J., 2009, *The rock physics handbook: Tools for seismic analysis of porous media*, Cambridge university press.
- Mindlin, R., 1949, Compliance of elastic bodies in contact: *J. of Appl. Mech.*, v. 16.
- Mohebbi, A., Kamalpour, R., Keyvanloo, K., and Sarrafi, A., 2012, The prediction of permeability from well logging data based on reservoir zoning, using artificial neural networks in one of an Iranian heterogeneous oil reservoir: *Petroleum Science and Technology*, v. 30, no. 19, p. 1998-2007.
- Mohn, K., and Osmundsen, P., 2008, Exploration economics in a regulated petroleum province: the case of the Norwegian Continental Shelf: *Energy Economics*, v. 30, no. 2, p. 303-320.
- Mondol, N. H., 2009, Porosity and permeability development in mechanically compacted silt-kaolinite mixtures, 2009 SEG Annual Meeting, Society of Exploration Geophysicists.
- Mondol, N. H., 2015, *Well Logging: Principles, Applications and Uncertainties*, Petroleum Geoscience, Springer, p. 385-425.
- Mondol, N. H., Bjørlykke, K., and Jahren, J., 2008a, Experimental compaction of clays: relationship between permeability and petrophysical properties in mudstones: *Petroleum Geoscience*, v. 14, no. 4, p. 319-337.
- Mondol, N. H., Bjørlykke, K., Jahren, J., and Høeg, K., 2007, Experimental mechanical compaction of clay mineral aggregates—Changes in physical properties of mudstones during burial: *Marine and Petroleum Geology*, v. 24, no. 5, p. 289-311.
- Mondol, N. H., Jahren, J., Bjørlykke, K., and Brevik, I., 2008b, Elastic properties of clay minerals: *The Leading Edge*, v. 27, no. 6, p. 758-770.
- Moore, W. R., Ma, Y. Z., Urdea, J., and Bratton, T., 2011, Uncertainty analysis in well-log and petrophysical interpretations.
- Morad, S., Bergan, M., Knarud, R., and Nystuen, J. P., 1990, Albitization of detrital plagioclase in Triassic reservoir sandstones from the Snorre Field, Norwegian North Sea: *Journal of Sedimentary Research*, v. 60, no. 3.
- Morad, S., De Ros, L., Nystuen, J., and Bergan, M., 2009, Carbonate diagenesis and porosity evolution in sheet-flood sandstones: evidence from the Middle and Lower Lunde Members (Triassic) in the Snorre Field, Norwegian North Sea: *Carbonate Cementation in Sandstones: Distribution Patterns and Geochemical Evolution*, p. 53-85.
- Morris, R., and Biggs, W., 1967, Using log-derived values of water saturation and porosity, SPWLA 8th Annual Logging Symposium, Society of Petrophysicists and Well-Log Analysts.
- Muller, R., 1996, *Den diagenetiske utviklingen an Lundeforformasjaonen; Nordlig Nordsjø*. Master's thesis, University of Oslo, Norway

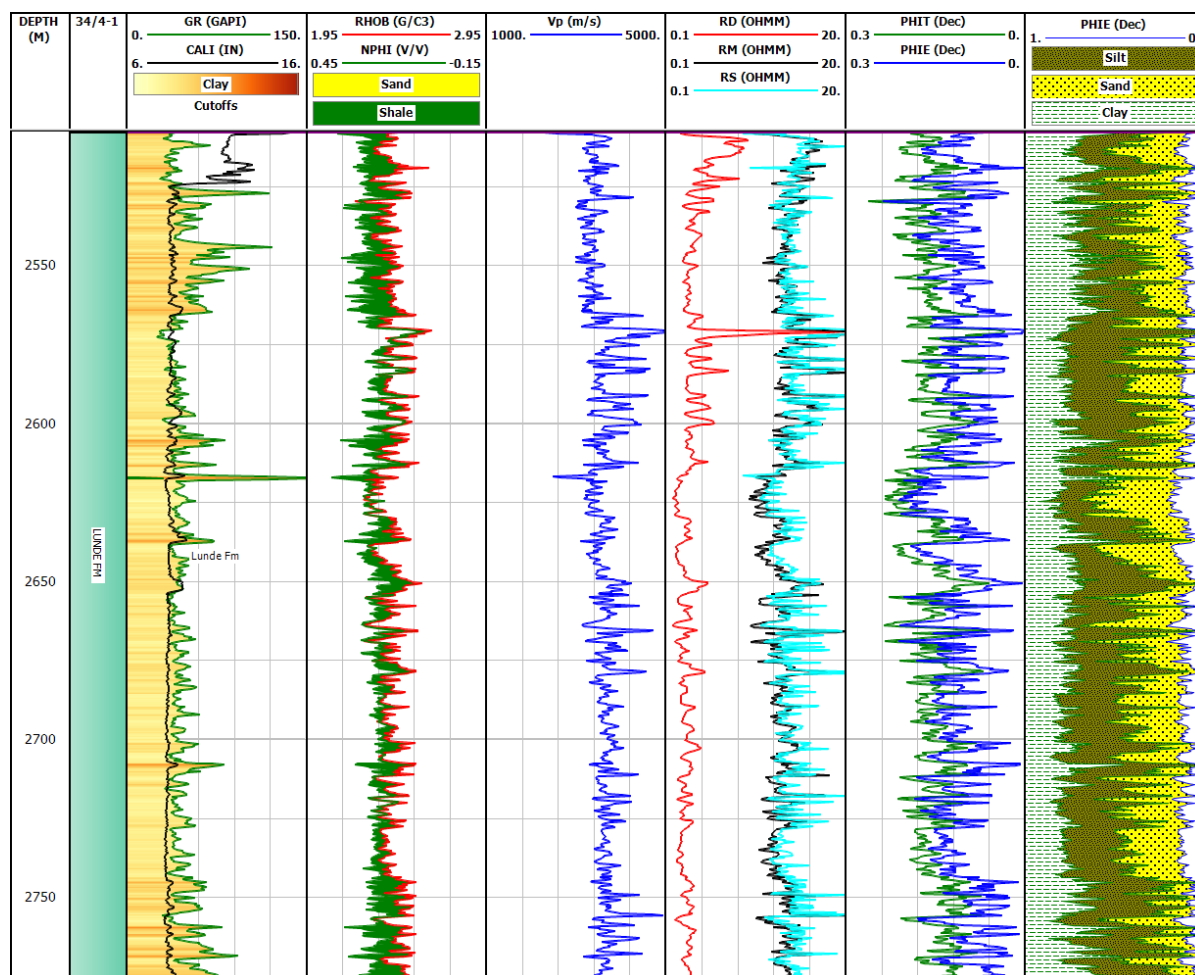
- Nottvedt, A., Gabrielsen, R., and Steel, R., 1995, Tectonostratigraphy and sedimentary architecture of rift basins, with reference to the northern North Sea: *Marine and Petroleum Geology*, v. 12, no. 8, p. 881-901.
- NpdFactmaps, 2016, [Online]. Norwegian Petroleum Directorate. Available: http://gis.npd.no/factmaps/html_21/. [Accessed 28. November. 2016].
- NpdFactPages, 2016, [Online]. Norwegian Petroleum Directorate. Available: <http://factpages.npd.no/FactPages/Default.aspx?culture=en>. [Accessed 28. November. 2016].
- Nystuen, J. P., and Fälth, L.-M., 1995, Upper Triassic-Lower Jurassic reservoir rocks in the Tampen Spur area, Norwegian North Sea: Norwegian Petroleum Society Special Publications, v. 4, p. 135-179.
- Nystuen, J. P., Knarud, R., Jorde, K., and Stanley, K. O., 1989, Correlation of Triassic to Lower Jurassic sequences, Snorre field and adjacent areas, northern North Sea, *Correlation in Hydrocarbon Exploration*, Springer, p. 273-289.
- Odinsen, T., Christiansson, P., Gabrielsen, R. H., Faleide, J. I., and Berge, A. M., 2000, The geometries and deep structure of the northern North Sea rift system: Geological Society, London, Special Publications, v. 167, no. 1, p. 41-57.
- Passey, Q., Creaney, S., Kulla, J., Moretti, F., and Stroud, J., 1990, A practical model for organic richness from porosity and resistivity logs: *AAPG bulletin*, v. 74, no. 12, p. 1777-1794.
- Perez, M. A., and Tonn, R., 2003, Reservoir Modelling and Interpretation with Lamé's Parameters: A Grand Banks Case Study: Presented at CSPG/CSGE Convention.
- Pickett, G. R., 1963, Acoustic character logs and their applications in formation evaluation: *Journal of Petroleum technology*, v. 15, no. 06, p. 659-667.
- Ramm, M., and Ryseth, A. E., 1996, Reservoir quality and burial diagenesis in the Statfjord Formation, North Sea: *Petroleum Geoscience*, v. 2, no. 4, p. 313-324.
- Ravnås, R., Nøttvedt, A., Steel, R., and Windelstad, J., 2000, Syn-rift sedimentary architectures in the Northern North Sea: Geological Society, London, Special Publications, v. 167, no. 1, p. 133-177.
- Raymer, L., Hunt, E., and Gardner, J. S., 1980, An improved sonic transit time-to-porosity transform, SPWLA 21st annual logging symposium, Society of Petrophysicists and Well-Log Analysts.
- Richards, P., 1992, An introduction to the Brent Group: a literature review: Geological Society, London, Special Publications, v. 61, no. 1, p. 15-26.
- Rider and Kennedy, 2011, The geological interpretation of well logs.
- Ryseth, A., 2001, Sedimentology and palaeogeography of the statfjord formation (Rhaetian-Sinemurian), North Sea: Norwegian Petroleum Society Special Publications, v. 10, p. 67-85.
- Sclater, J. G., and Christie, P., 1980, Continental stretching: an explanation of the post-mid-Cretaceous subsidence of the central North Sea basin: *Journal of Geophysical Research*, v. 85, no. B7, p. 3711-3739.
- Smith, P., Berg, J. I., Eidsvig, S., Magnus, I., Verhelst, F., and Helgesen, J., 2001, 4-D seismic in a complex fluvial reservoir: The Snorre feasibility study: *The Leading Edge*, v. 20, no. 3, p. 270-276.
- Steel, R., 1993, Triassic-Jurassic megasequence stratigraphy in the Northern North Sea: rift to post-rift evolution, Geological Society, London, Petroleum Geology Conference series, Volume 4, Geological Society of London, p. 299-315.

- Steel, R., and Ryseth, A., 1990, The Triassic—Early Jurassic succession in the northern North Sea: megasequence stratigraphy and intra-Triassic tectonics: Geological Society, London, Special Publications, v. 55, no. 1, p. 139-168.
- Stieber, S., 1970, Pulsed Neutron Capture Log Evaluation-Louisiana Gulf Coast, Fall Meeting of the Society of Petroleum Engineers of AIME, Society of Petroleum Engineers.
- Storvoll, V., Bjørlykke, K., and Mondol, N. H., 2005, Velocity-depth trends in Mesozoic and Cenozoic sediments from the Norwegian Shelf: AAPG bulletin, v. 89, no. 3, p. 359-381.
- Storvoll, V., and Brevik, I., 2008, Identifying time, temperature, and mineralogical effects on chemical compaction in shales by rock physics relations: The Leading Edge, v. 27, no. 6, p. 750-756.
- Timur, A., 1968, An investigation of permeability, porosity, and residual water saturation relationships, SPWLA 9th annual logging symposium, Society of Petrophysicists and Well-Log Analysts.
- Torskaya, T. S., Jin, G., and Torres-Verdin, C., 2007, Pore-level analysis of the relationship between porosity, irreducible water saturation, and permeability of clastic rocks, SPE Annual Technical Conference and Exhibition, Society of Petroleum Engineers.
- Torsvik, T. H., Carlos, D., Mosar, J., Cocks, L. R. M., and Malme, T. N., 2002, Global reconstructions and North Atlantic paleogeography 440 Ma to recent: BATLAS—Mid Norway plate reconstruction atlas with global and Atlantic perspectives, p. 18-39.
- Vardian, M., Nasriani, H., Faghihi, R., Vardian, A., and Jowkar, S., 2016, Porosity and permeability prediction from well logs using an adaptive neuro-fuzzy inference system in a naturally fractured gas-condensate reservoir: Energy Sources, Part A: Recovery, Utilization, and Environmental Effects, v. 38, no. 3, p. 435-441.
- Vollset, J., and Doré, A. G., 1984, A revised Triassic and Jurassic lithostratigraphic nomenclature for the Norwegian North Sea, Oljedirektoratet.
- Whipp, P., Jackson, C., Gawthorpe, R., Dreyer, T., and Quinn, D., 2014, Normal fault array evolution above a reactivated rift fabric; a subsurface example from the northern Horda Platform, Norwegian North Sea: Basin Research, v. 26, no. 4, p. 523-549.
- Williams, D. M., 1990, The acoustic log hydrocarbon indicator, SPWLA 31st Annual Logging Symposium, Society of Petrophysicists and Well-Log Analysts.
- Wyllie, M., and Rose, W. D., 1950, Some theoretical considerations related to the quantitative evaluation of the physical characteristics of reservoir rock from electrical log data: Journal of Petroleum Technology, v. 2, no. 04, p. 105-118.
- Wyllie, M. R. J., Gregory, A. R., and Gardner, L. W., 1956, Elastic wave velocities in heterogeneous and porous media: Geophysics, v. 21, no. 1, p. 41-70.
- Yielding, G., Badley, M. E., and Roberts, A. M., 1992, The structural evolution of the Brent Province: Geological Society, London, Special Publications, v. 61, no. 1, p. 27-43.
- Zadeh, M. K., Mondol, N. H., and Jahren, J., 2016, Compaction and rock properties of Mesozoic and Cenozoic mudstones and shales, northern North Sea: Marine and Petroleum Geology, v. 76, p. 344-361.
- Ziegler, P., 1975, The geological evolution of the North Sea area in the tectonic framework of North-Western Europe: NorgesGeol Unders, v. 316, p. 1-27.
- Ziegler, P., 1977, Geology and hydrocarbon provinces of the North Sea: GeoJournal, v. 1, no. 1, p. 7-32.
- Ziegler, P., 1992, North Sea rift system: Tectonophysics, v. 208, no. 1, p. 55-75.
- Ødegaard, E., and Avseth, P., 2003, Well log and seismic data analysis using rock physics templates: First break 22.10 (2004): 37-43.

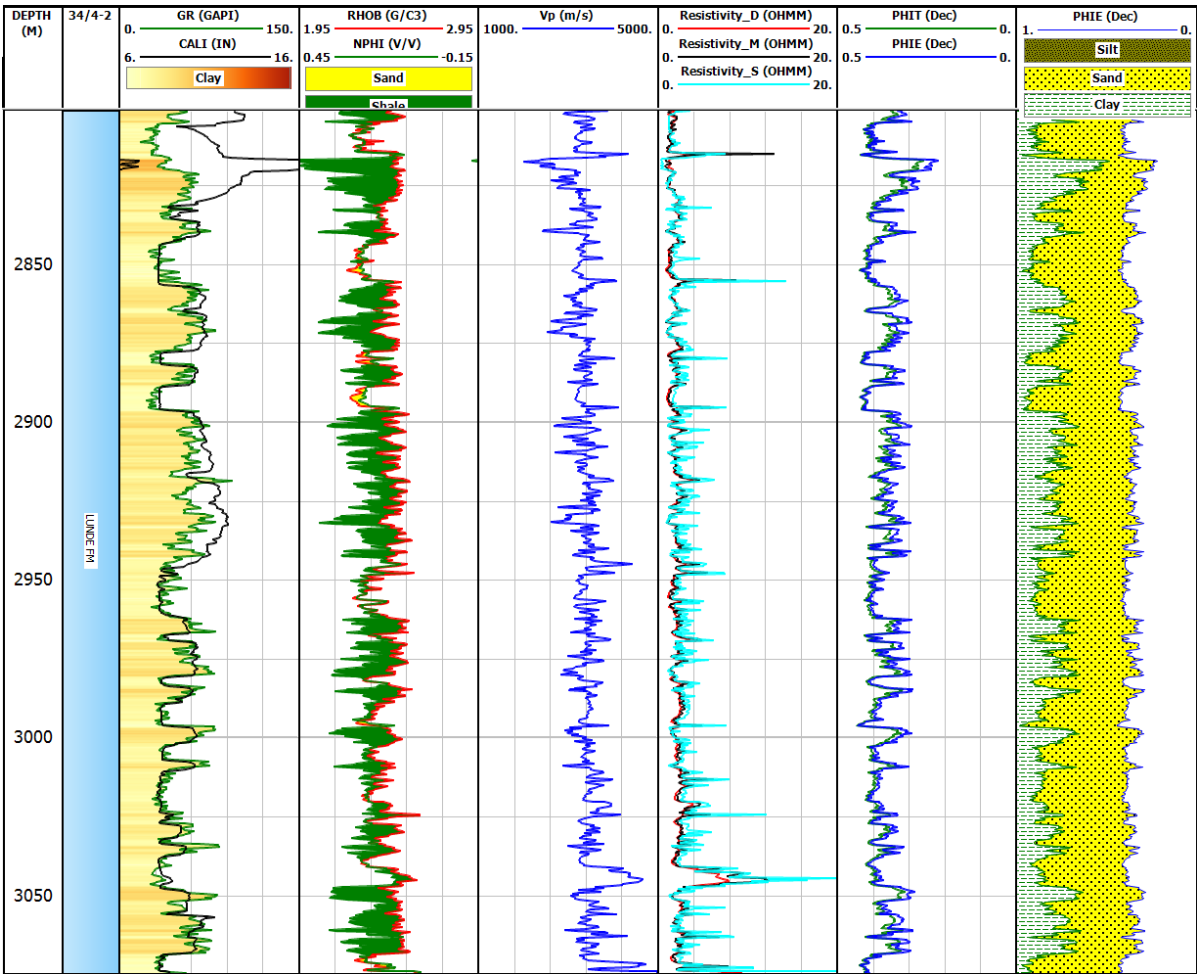
Appendix A. Composite log displays

Lunde Formation

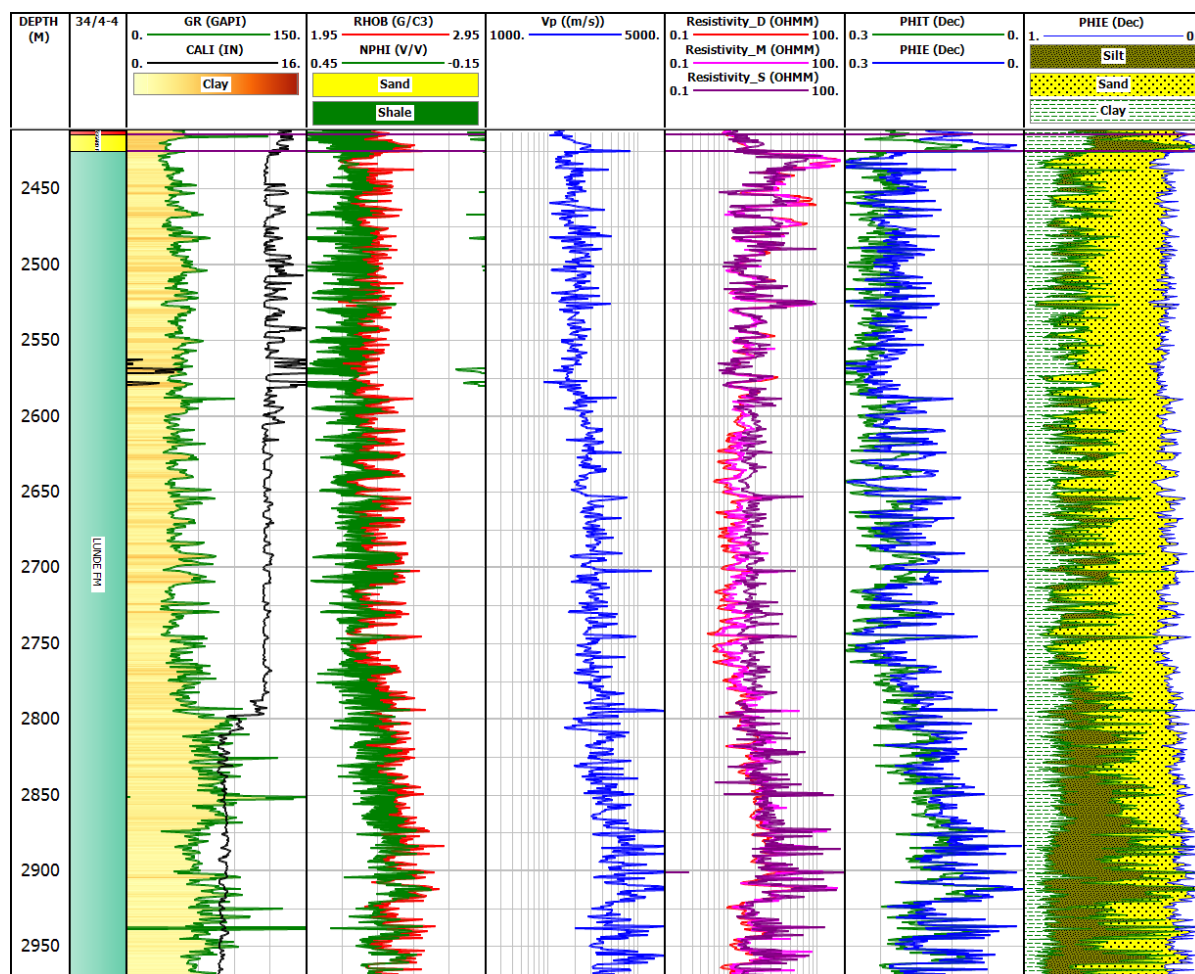
The depth is shown in meters and referenced from kelly bushing.



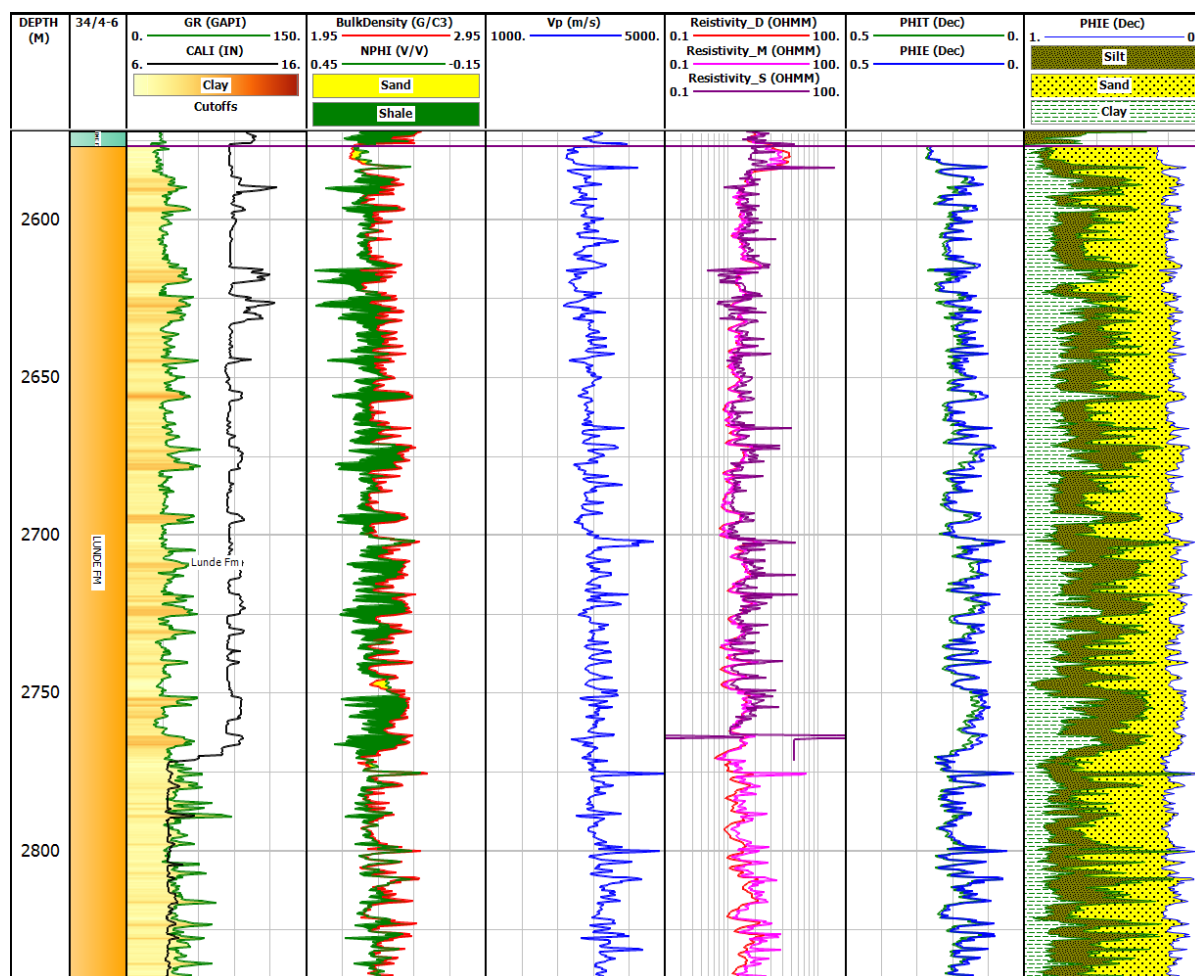
A.1: Composite log display of Lunde Formation, well 34/4-1.



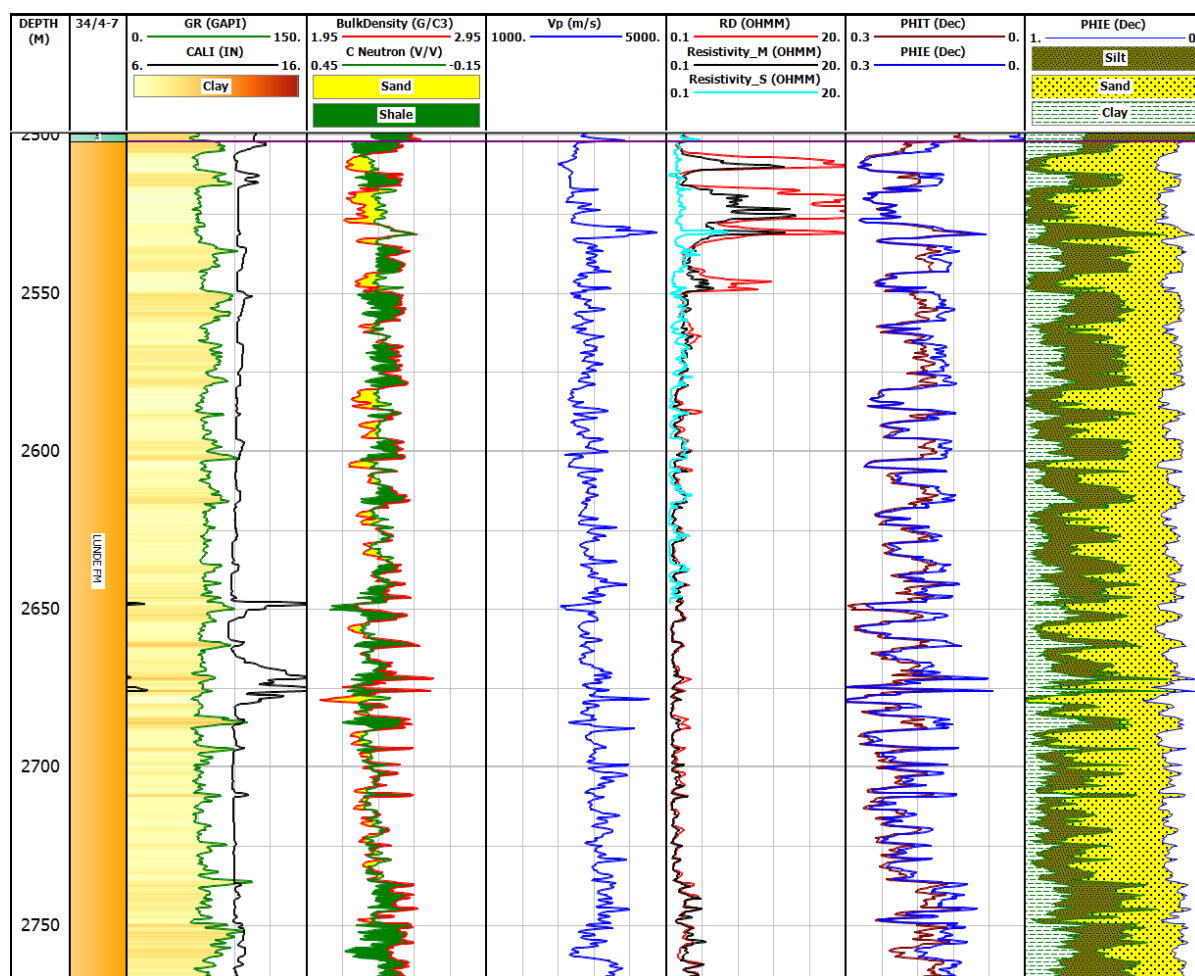
A.2: Composite log display of the Lunde Formation, well 34/4-2.



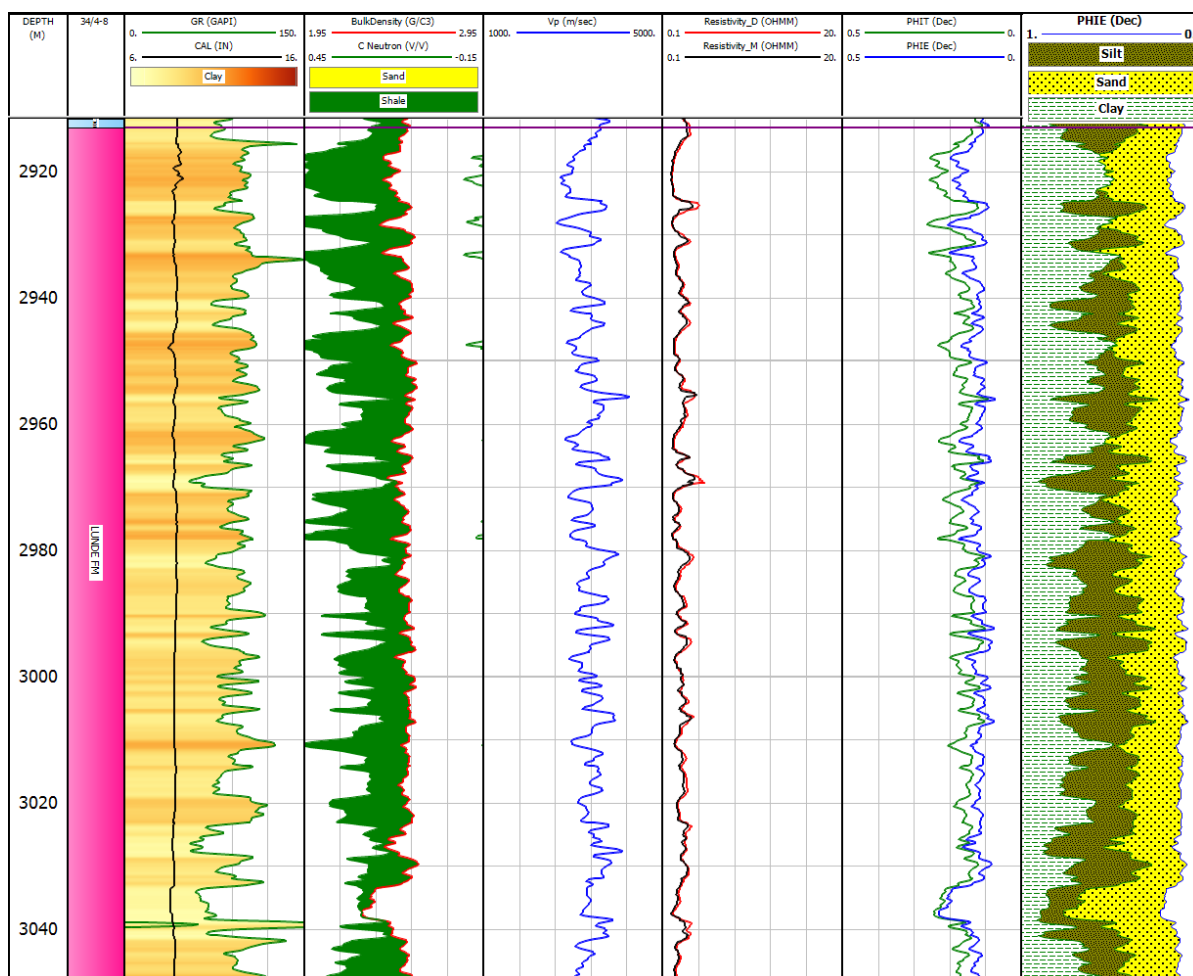
A.3: Composite log display of the Lunde Formation, well 34/4-4.



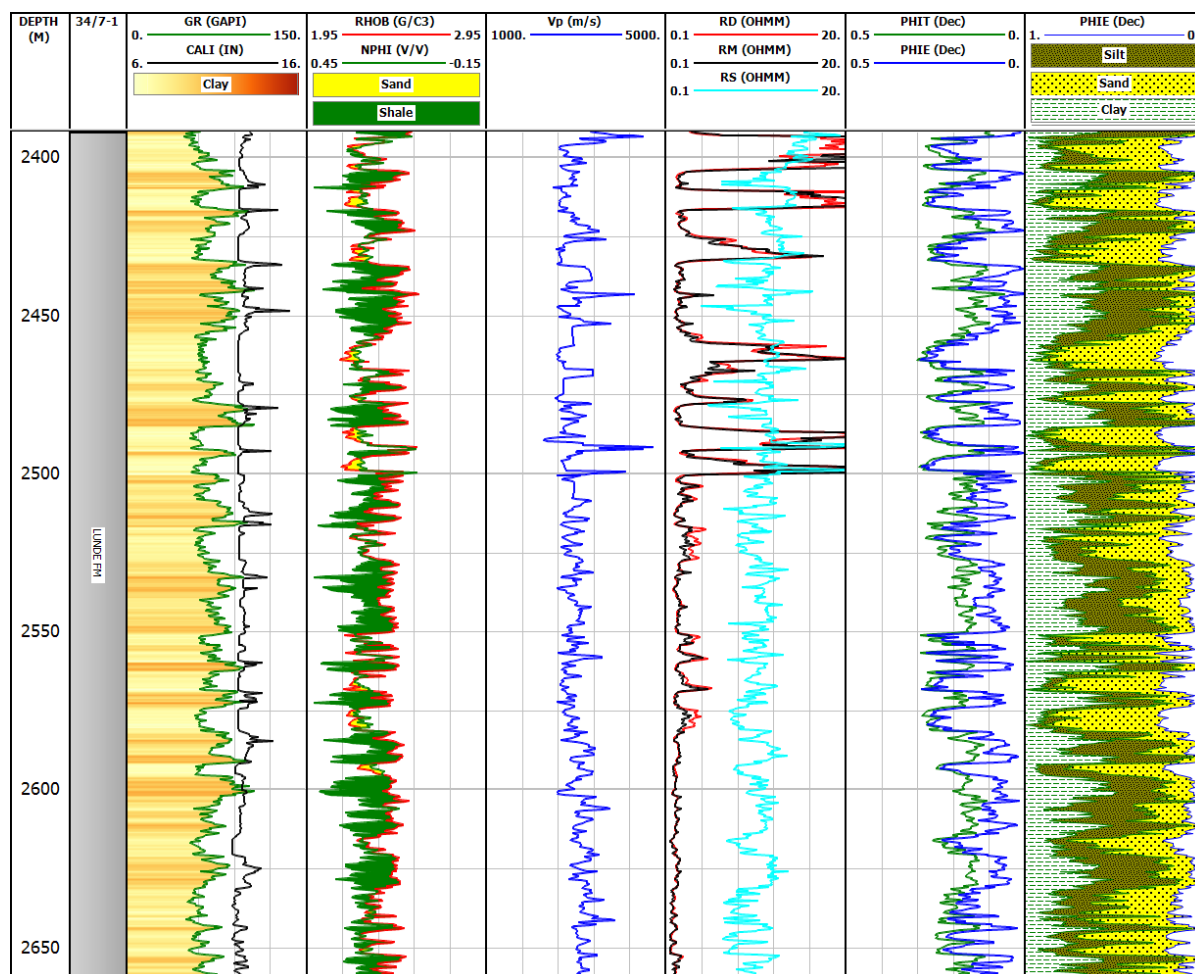
A.4: Composite log display of Lunde Formation, well 34/4-6.



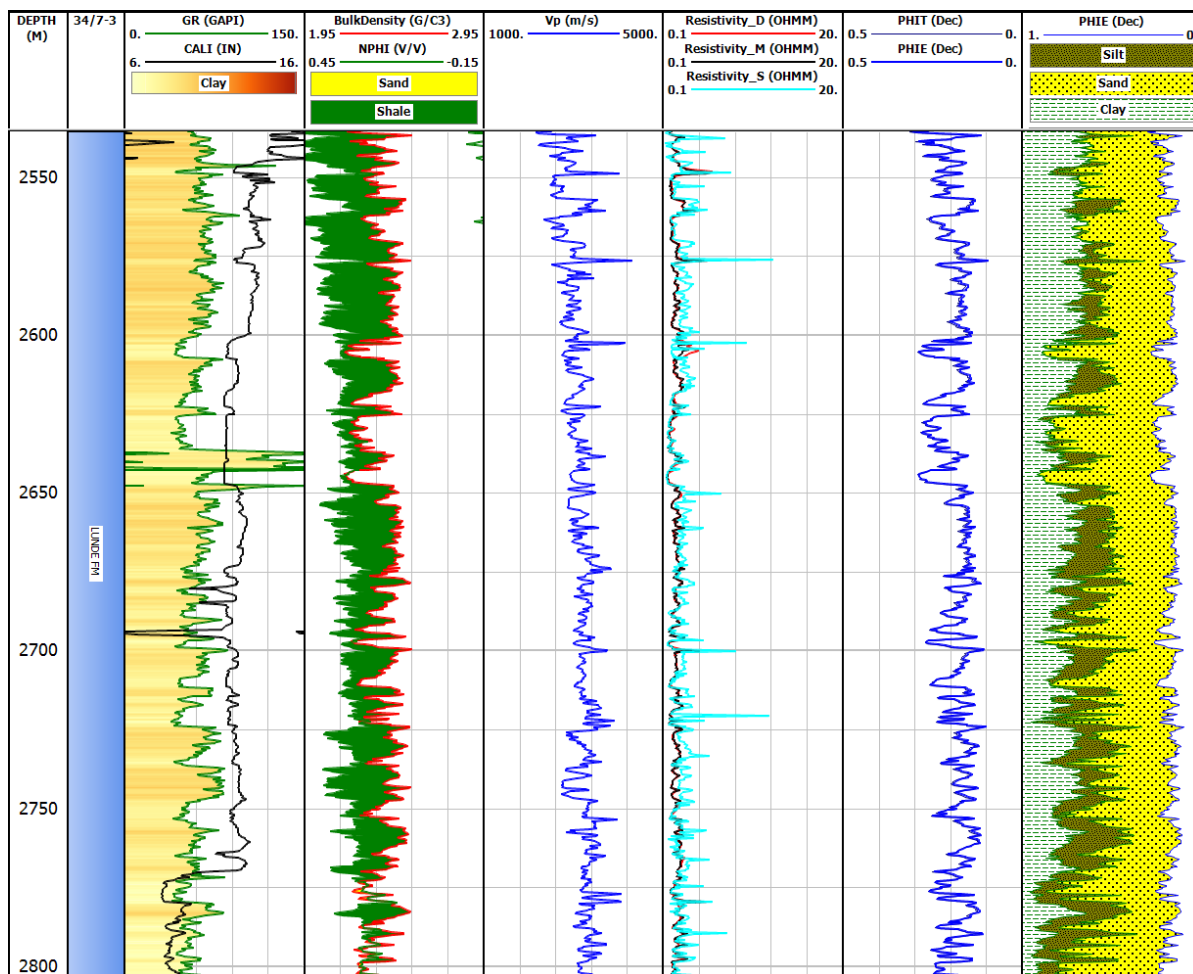
A.5: Composite log display of Lunde Formation well 34/4-7.



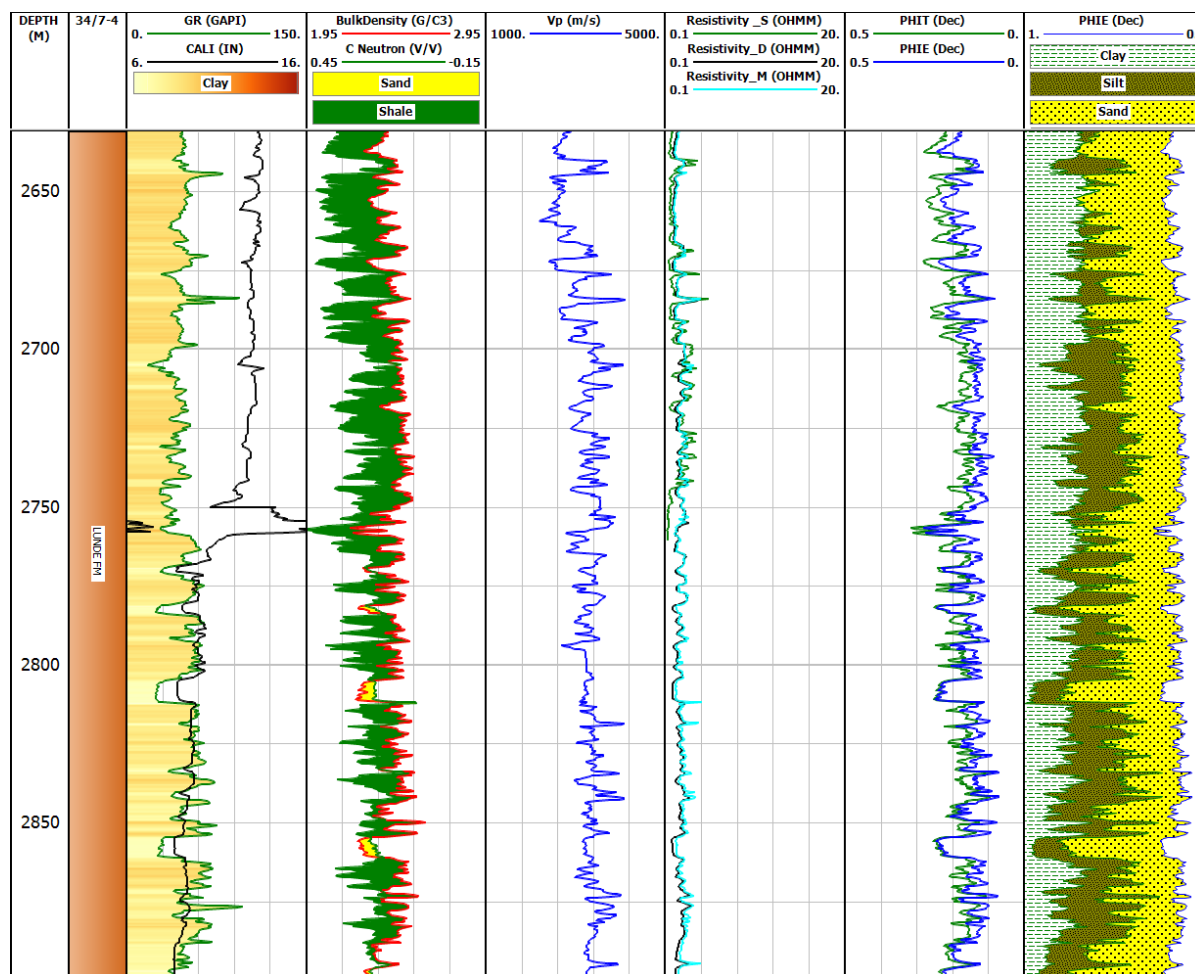
A.6: Composite log display of Lunde Formation well 34/4-8.



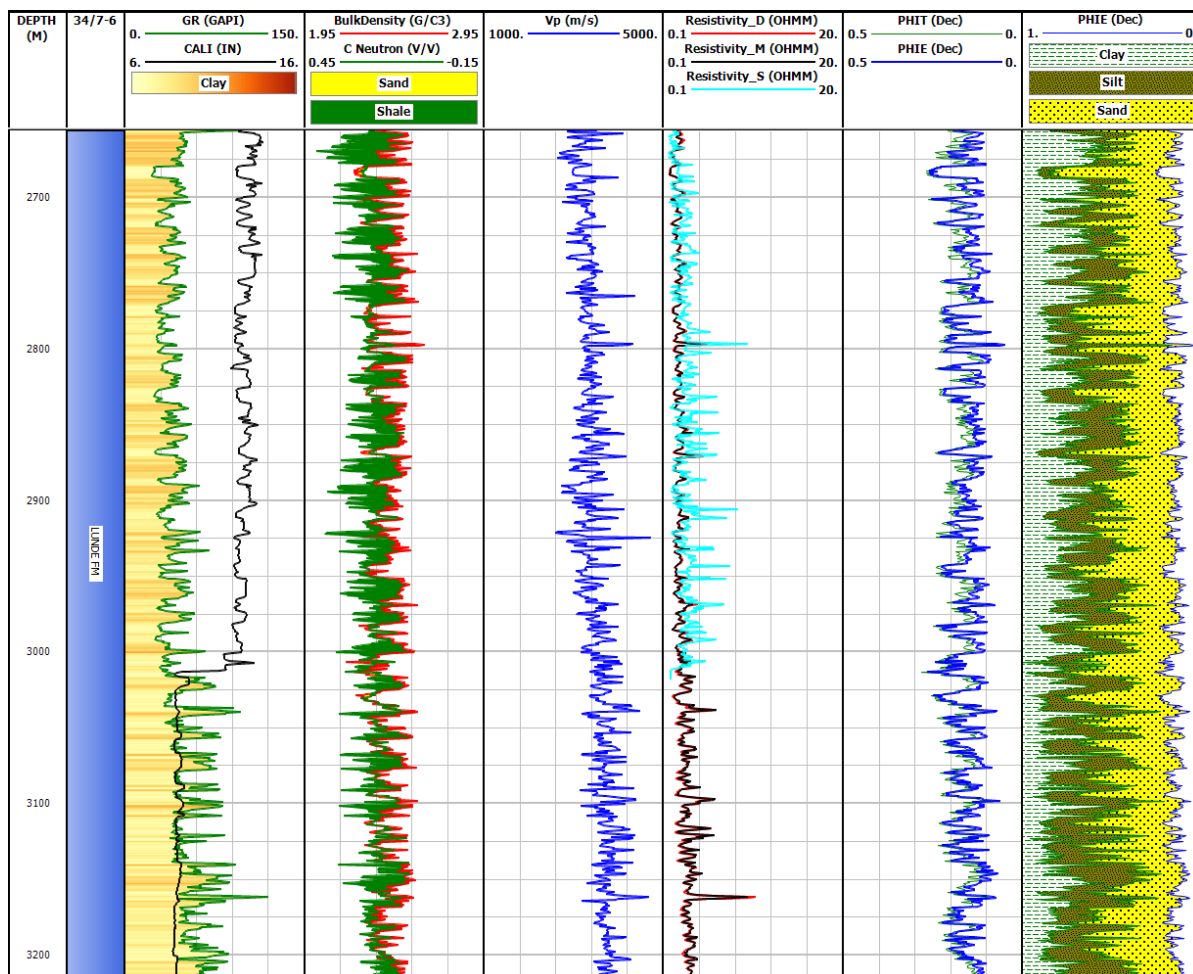
A.7: Composite log display of Lunde Formation well 34/7-1.



A.8: Composite log display of Lunde Formation well 34/7-3.

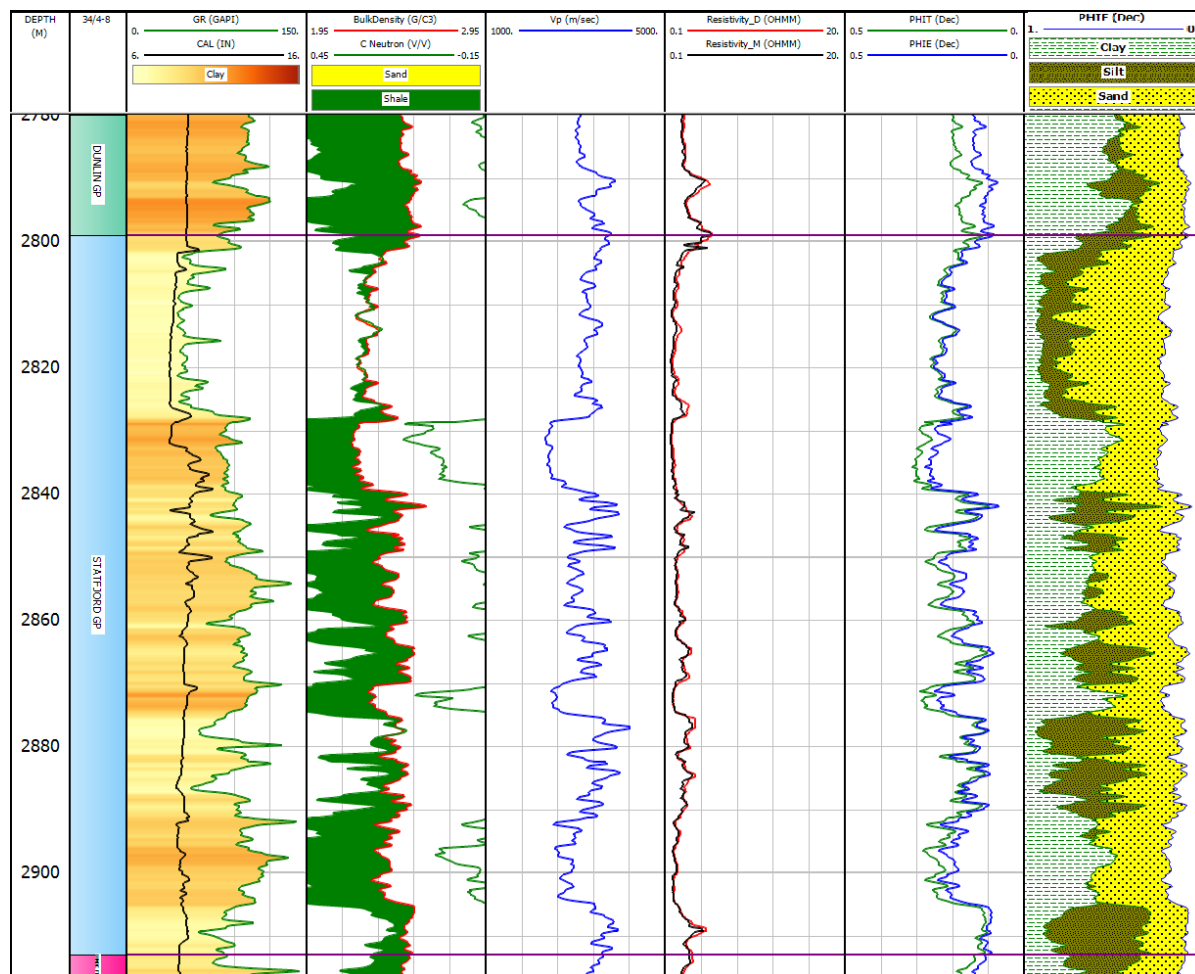


A.9: Composite log display of Lunde Formation well 34/7-4.

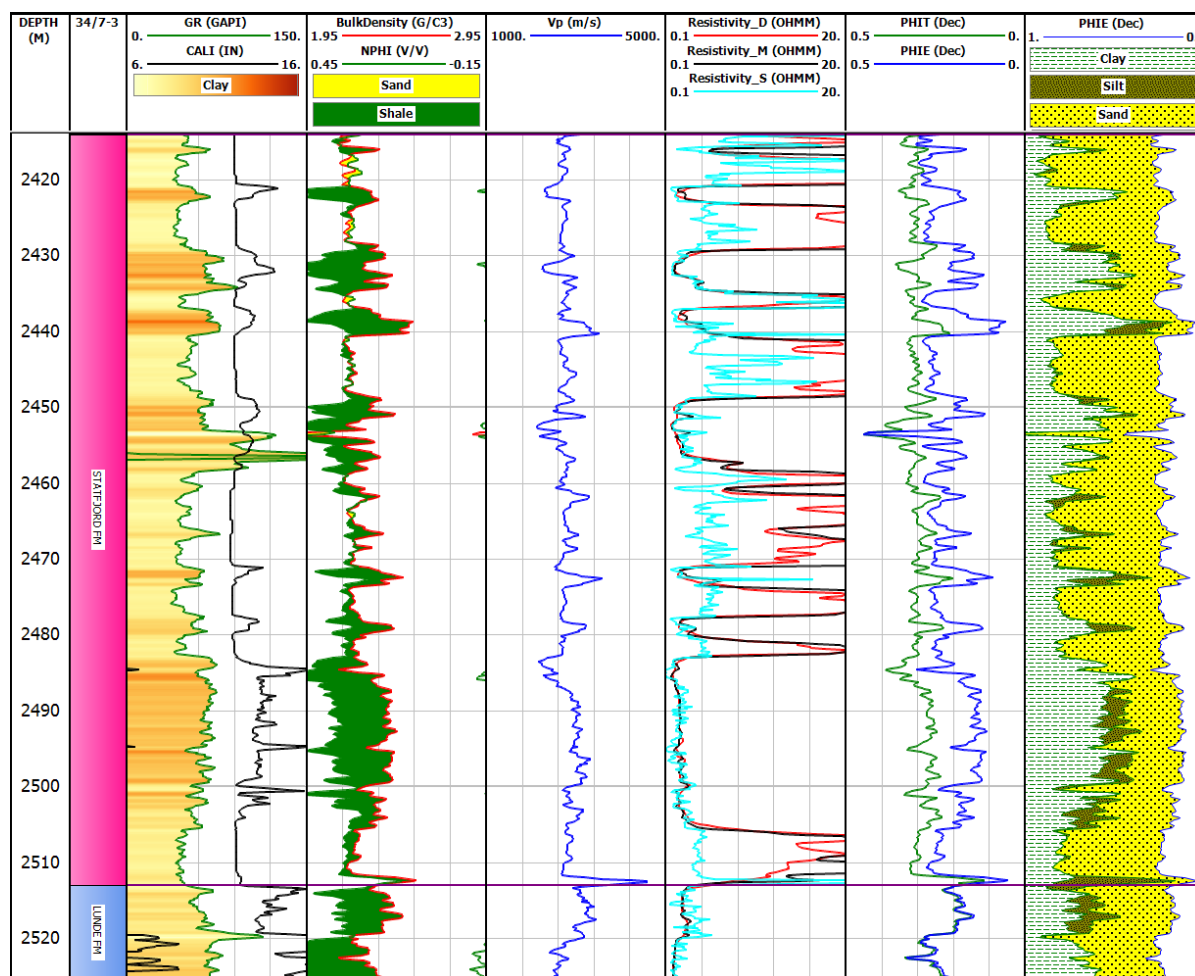


A.10: Composite log of Lunde Formation, well 34/7-6.

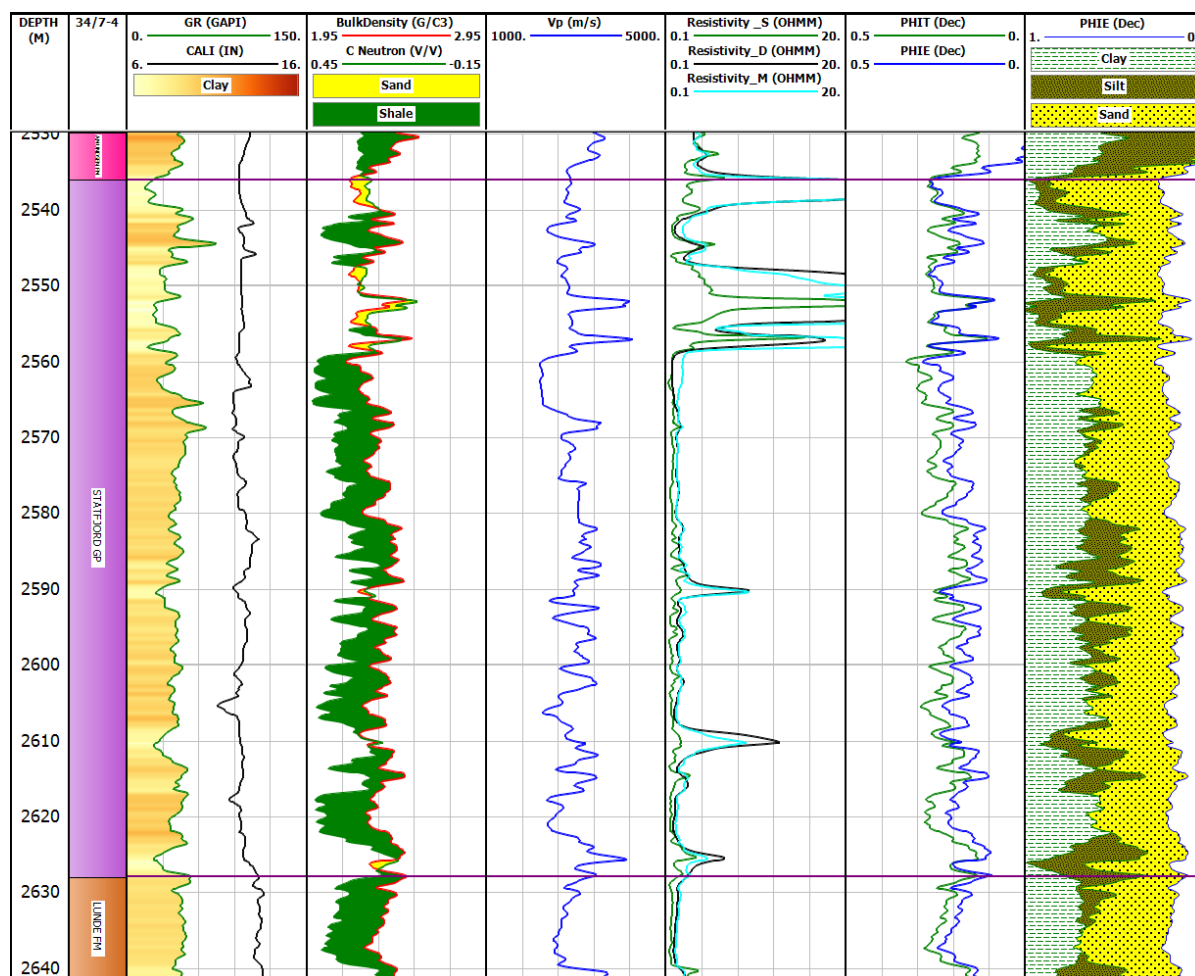
Statfjord Formation



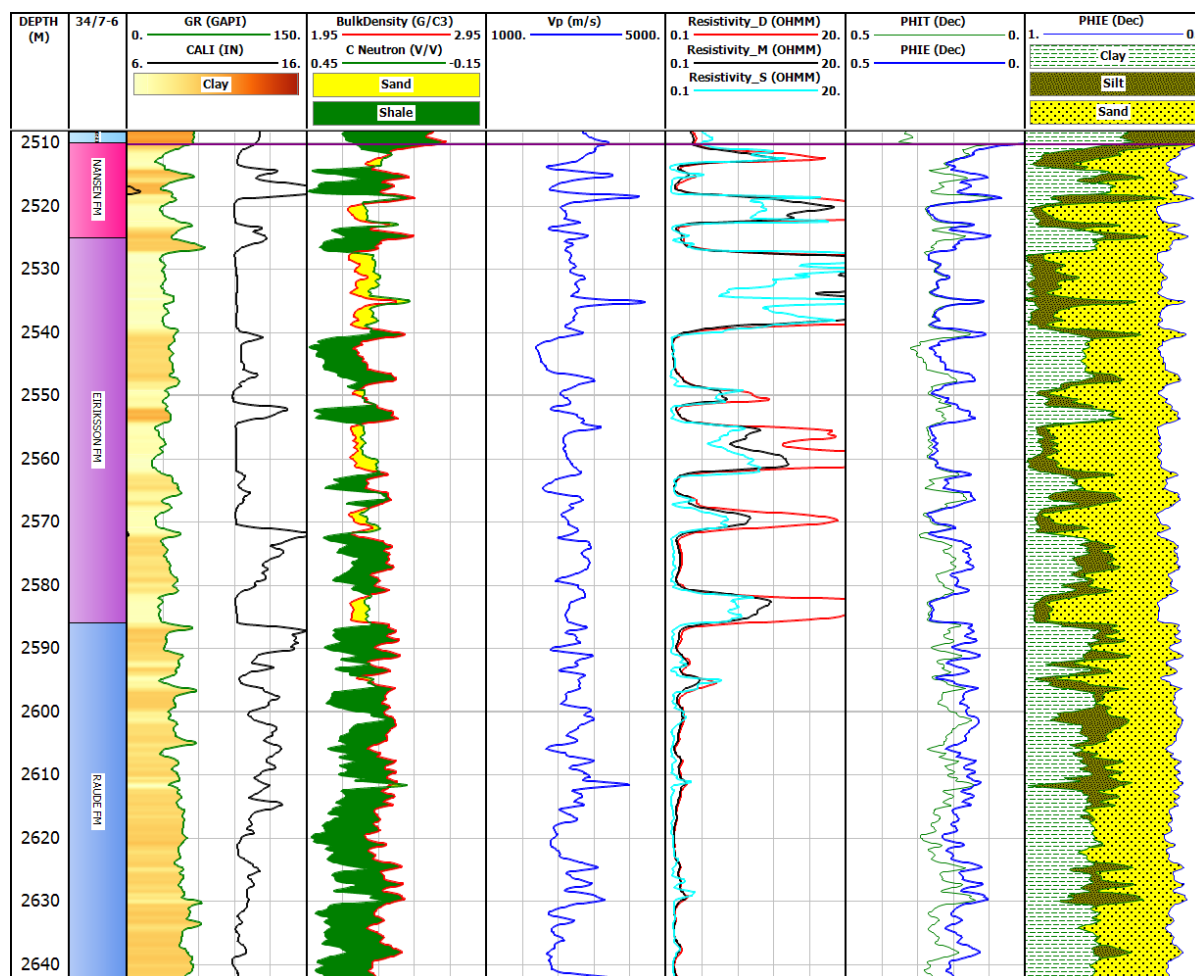
A.11: Composite log of Statfjord Formation, well 34/4-8.



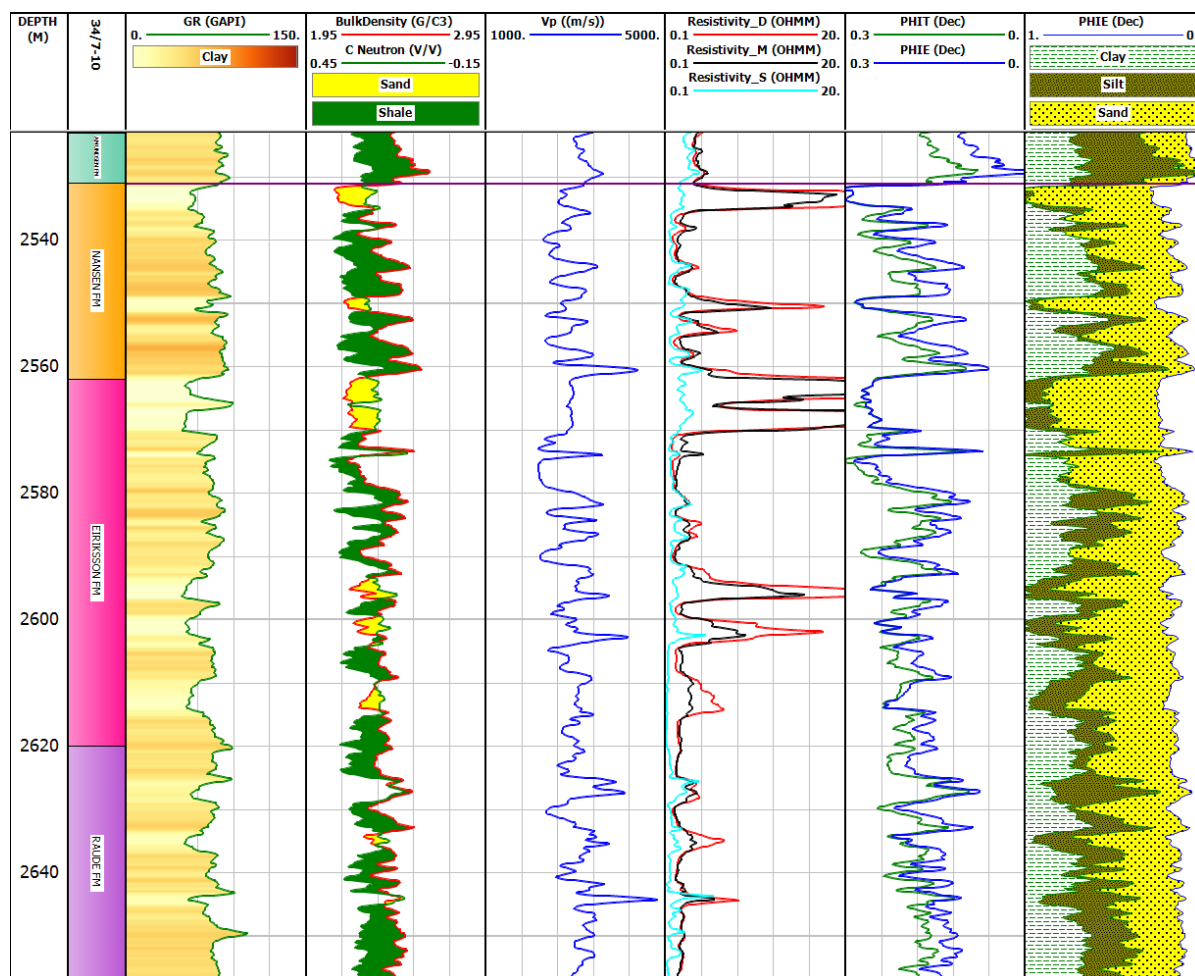
A.12: Composite log of Statfjord Formation, well 34/7-3.



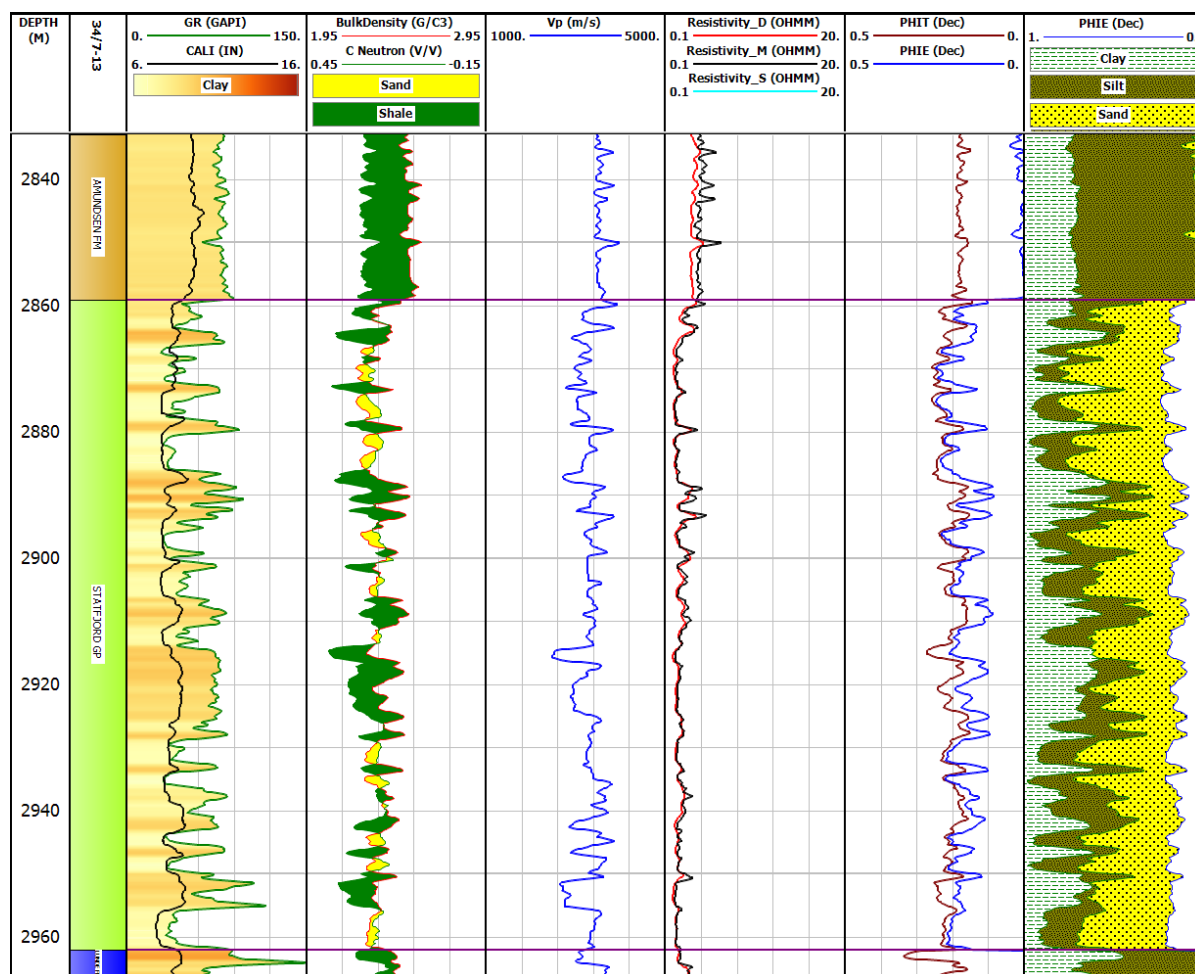
A.13: Composite log of Statfjord Formation, well 34/7-4.



A.14: Composite log of Statfjord Group, well 34/7-6.

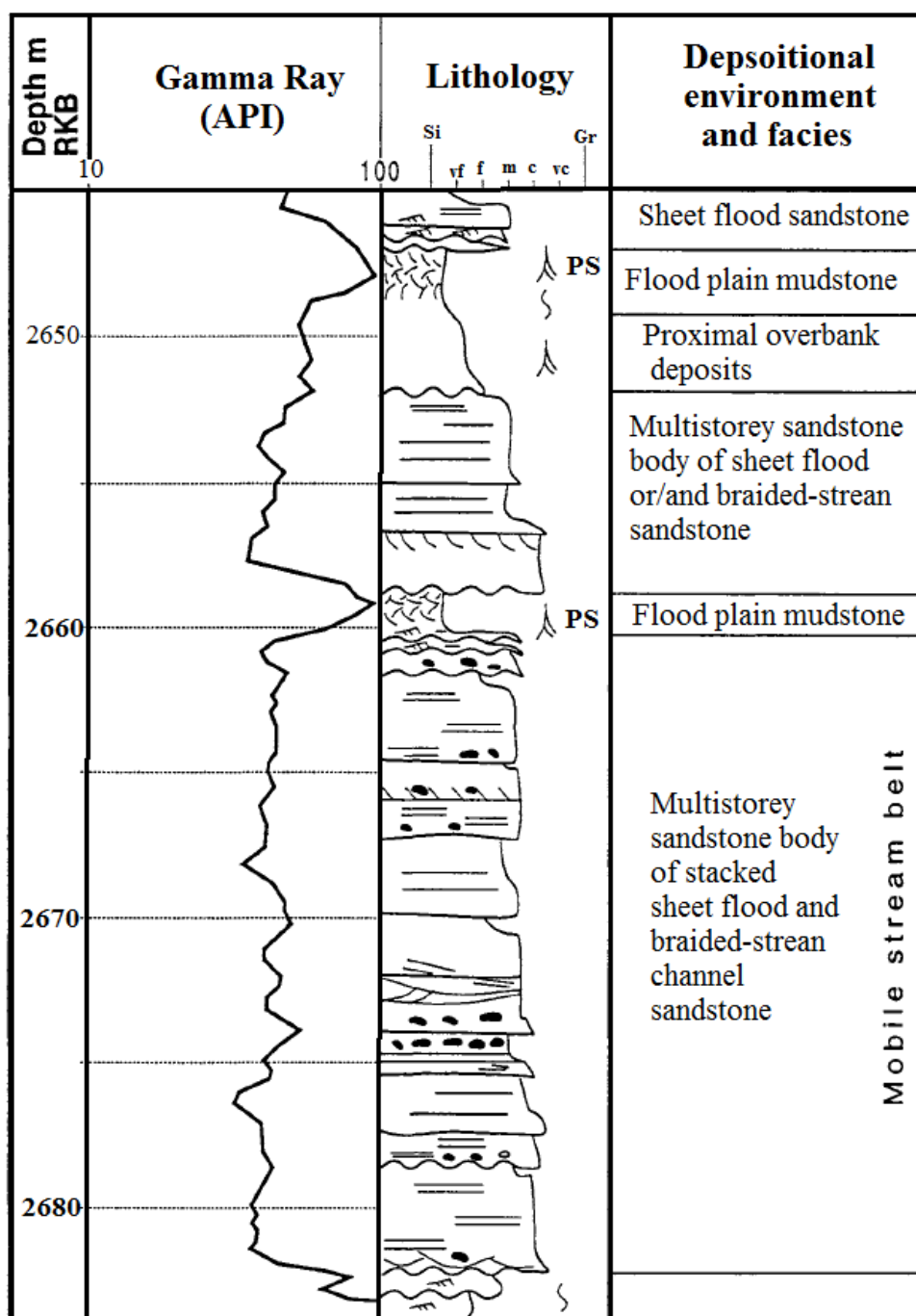


A.15: Composite log of Statfjord Group, well 34/7-10

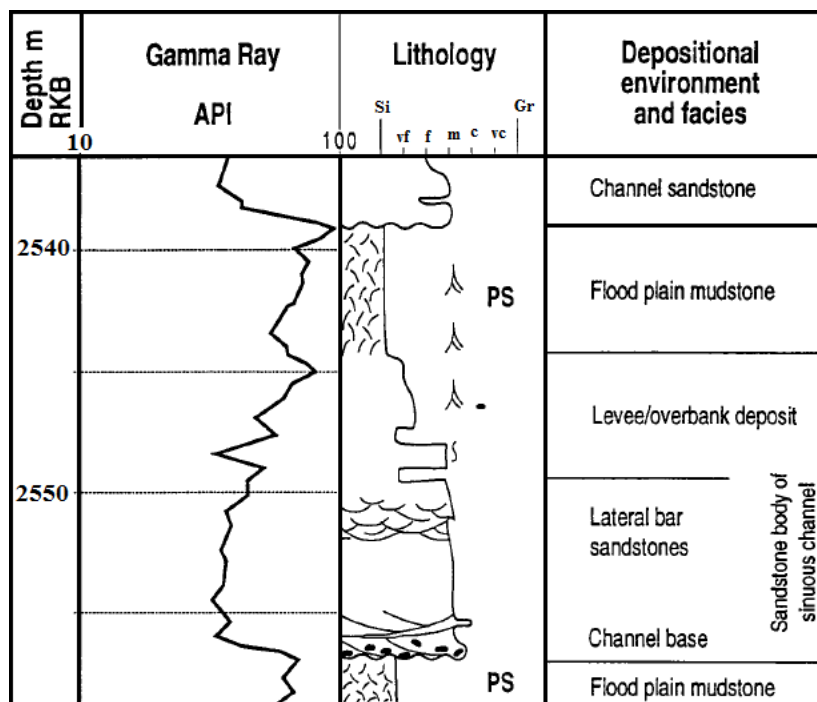


A.16: Composite log of Statfjord Formation, well 34/7-13.

Appendix B. Interpreted facies from published literature



B.1: The facies in Lunde Formation from well 34/4-7. Figure adapted from Nystuen and Fält, (1995).



B.2: The facies in Lunde Formation from well 34/7-9. The figure adapted from Nystuen and Fält, (1995).

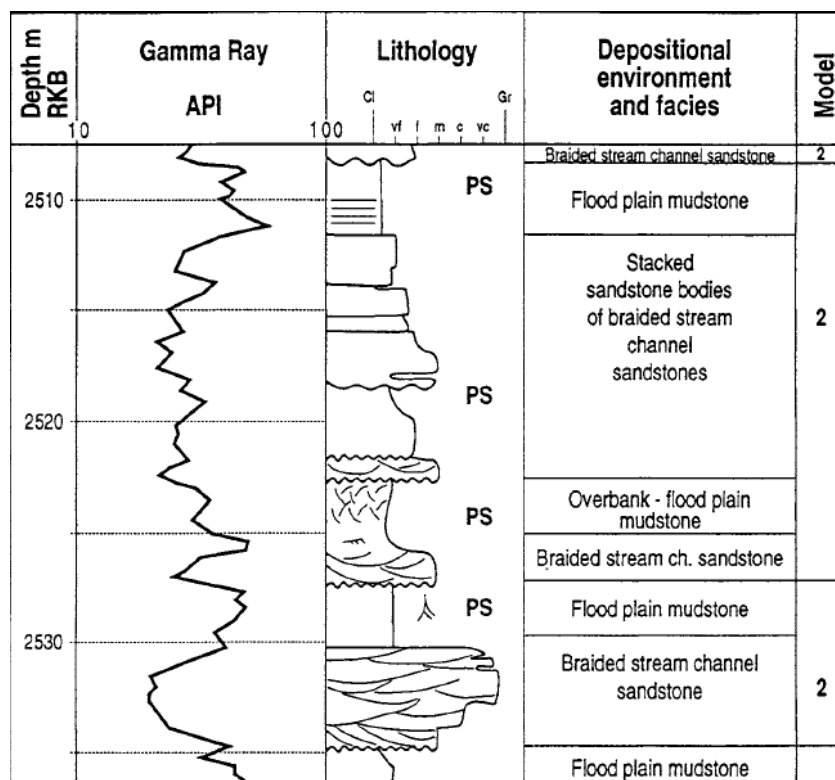
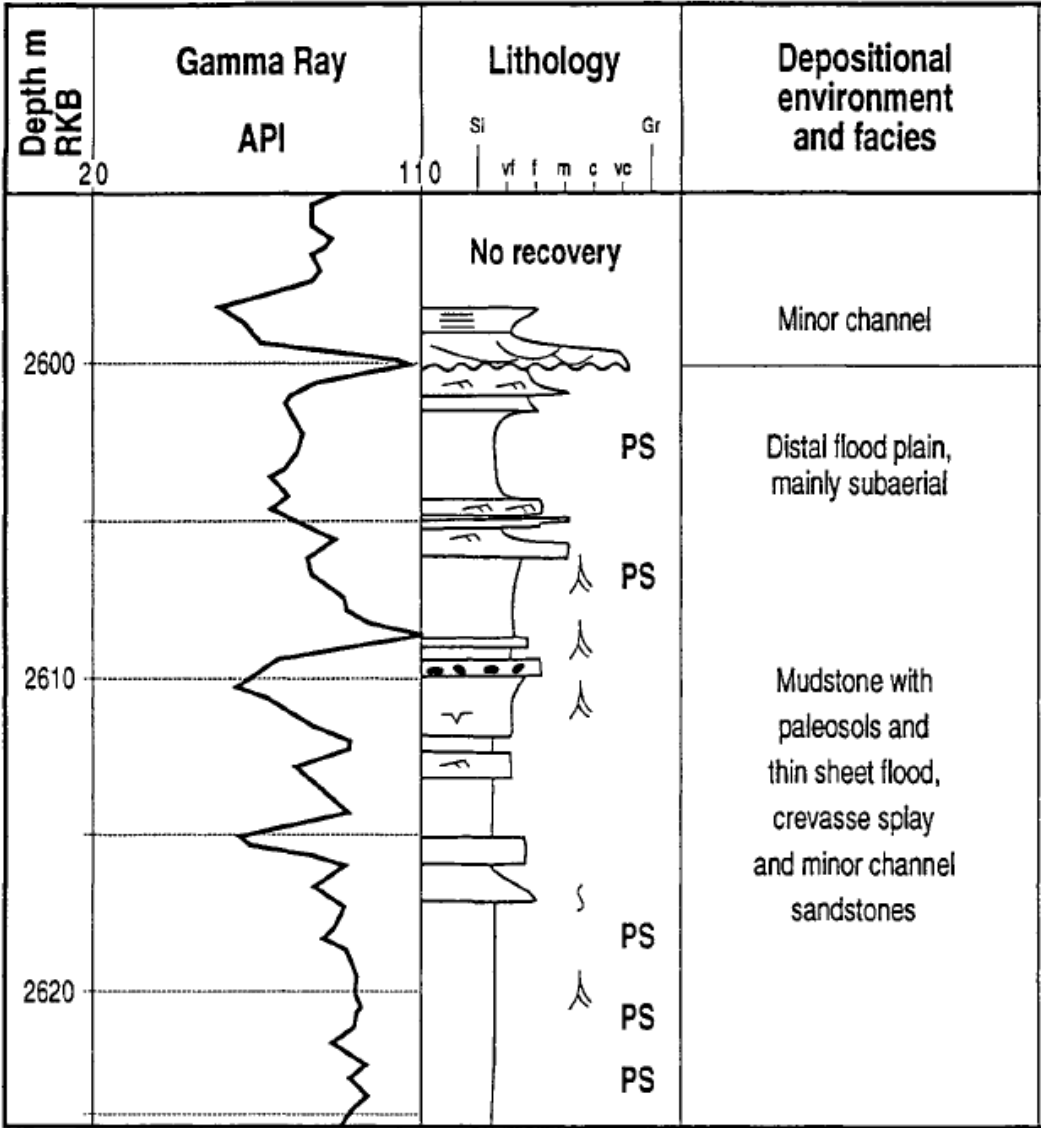


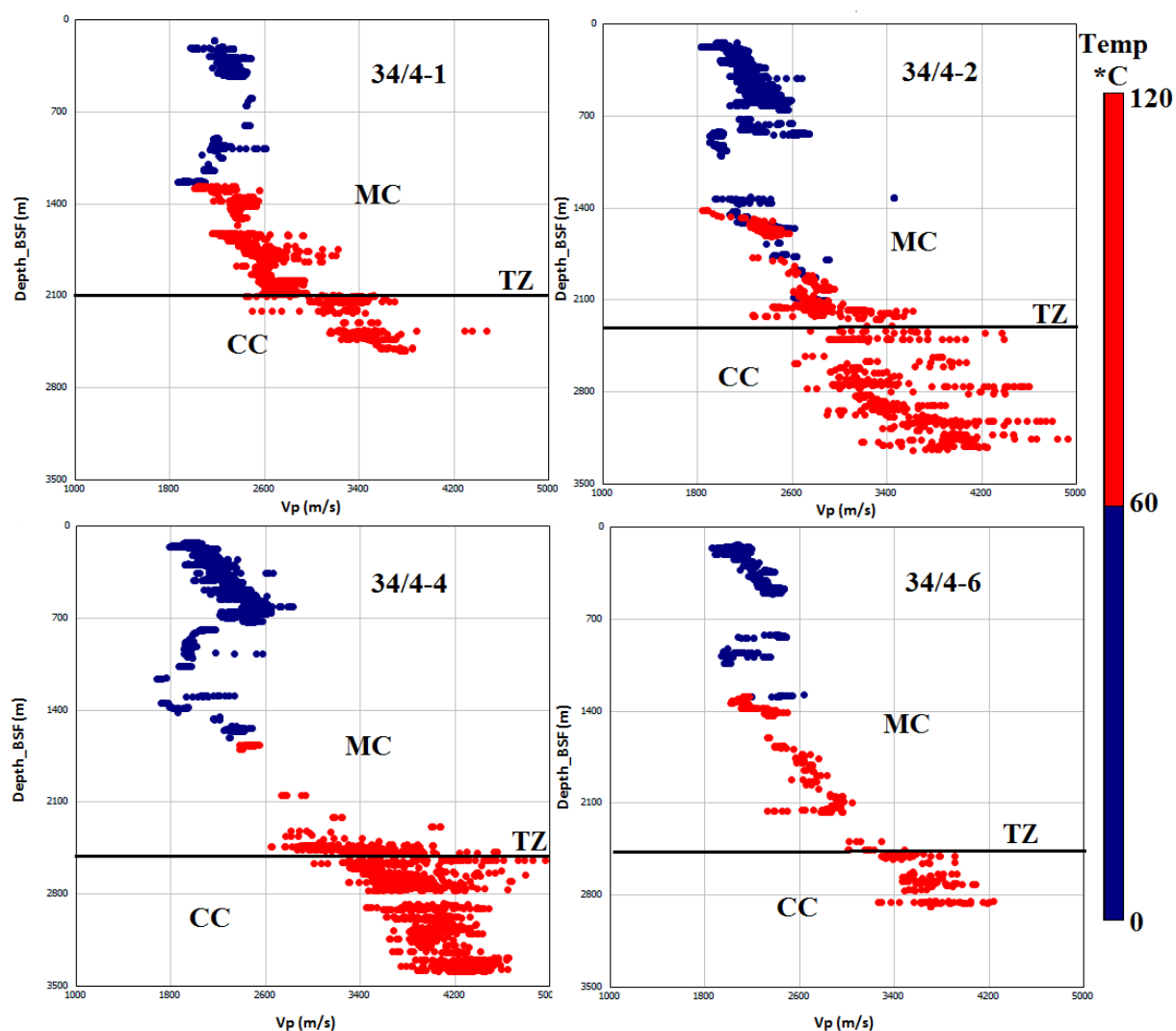
Figure B.3: The facies in Lunde Formation from well 34/4-1. Figure adapted from Nystuen and Fält, (1995).



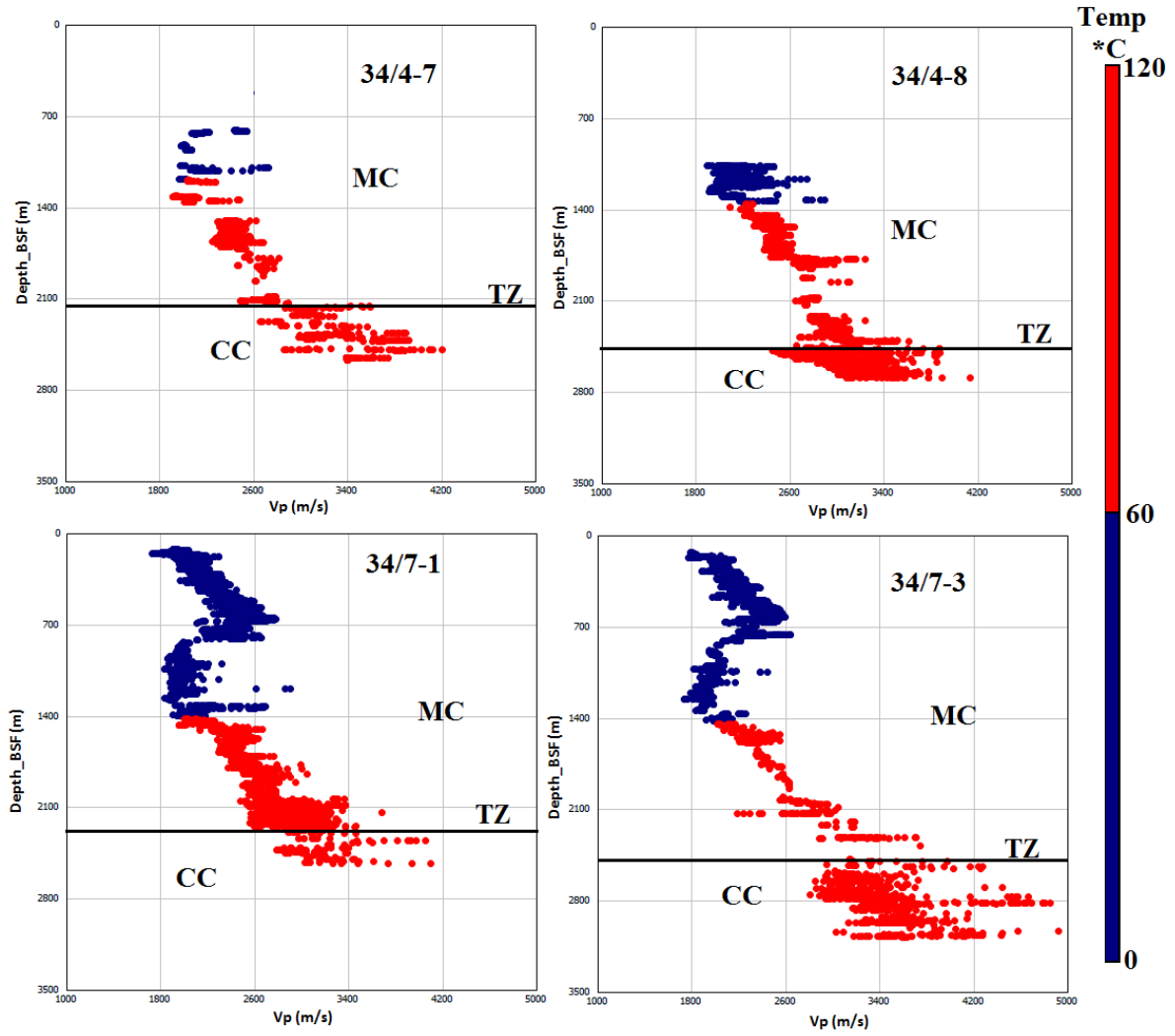
B.4: The facies interpreted in Statfjord Fm from well 34/7-10. Figure adapted from Nystuen and Fält, (1995).

Appendix C. Velocity-depth trend

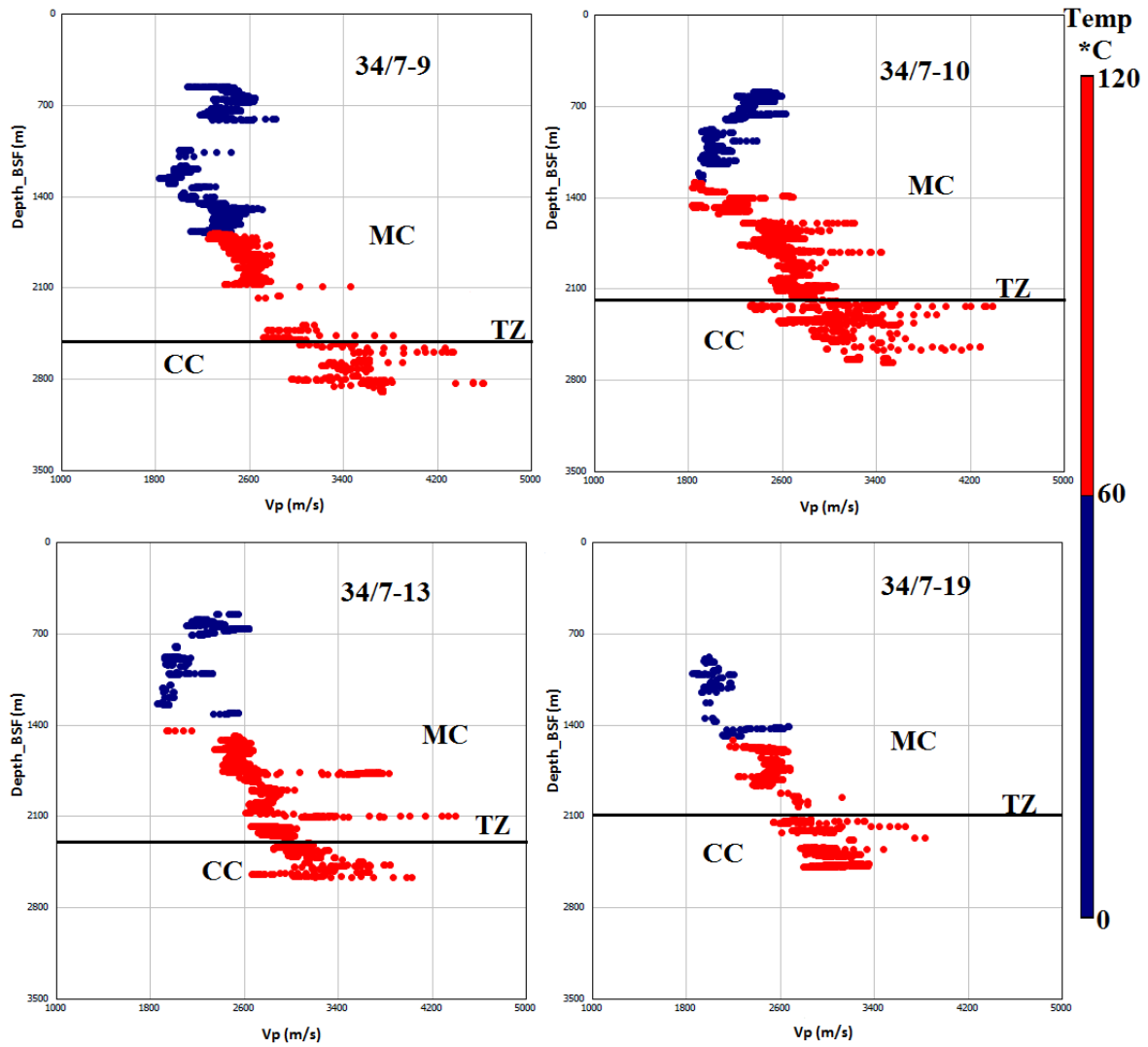
Velocity-depth trend from each well showing mechanical compaction zone, chemical compaction zone and transition zone.



C.1: The velocity-depth trend from well 34/4-1, 34/4-2, 34/4-4 and 34/4-6. MC – mechanical compaction, CC – chemical compaction and TZ – transition zone.



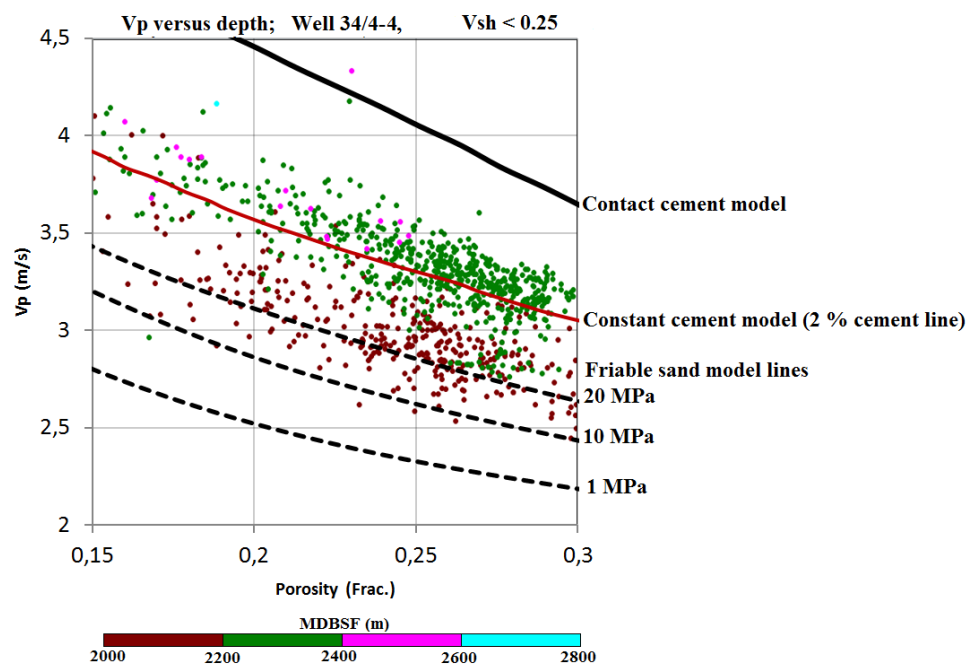
C.2: Velocity-depth trend of well 34/4-7, 34/4-8, 34/7-1 and 34/7-3. MC – mechanical compaction, CC – chemical compaction and TZ – transition zone.



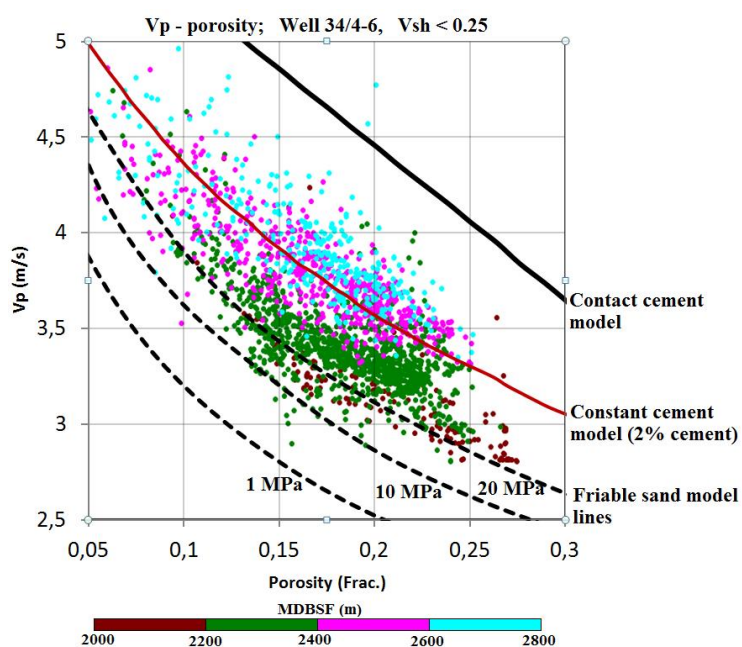
C.3: The velocity-depth trend from well 34/7-9, 34/7-10, 34/7-13 and 34/7-19. MC – mechanical compaction, CC – chemical compaction and TZ – transition zone.

Appendix D. Rock physics plots

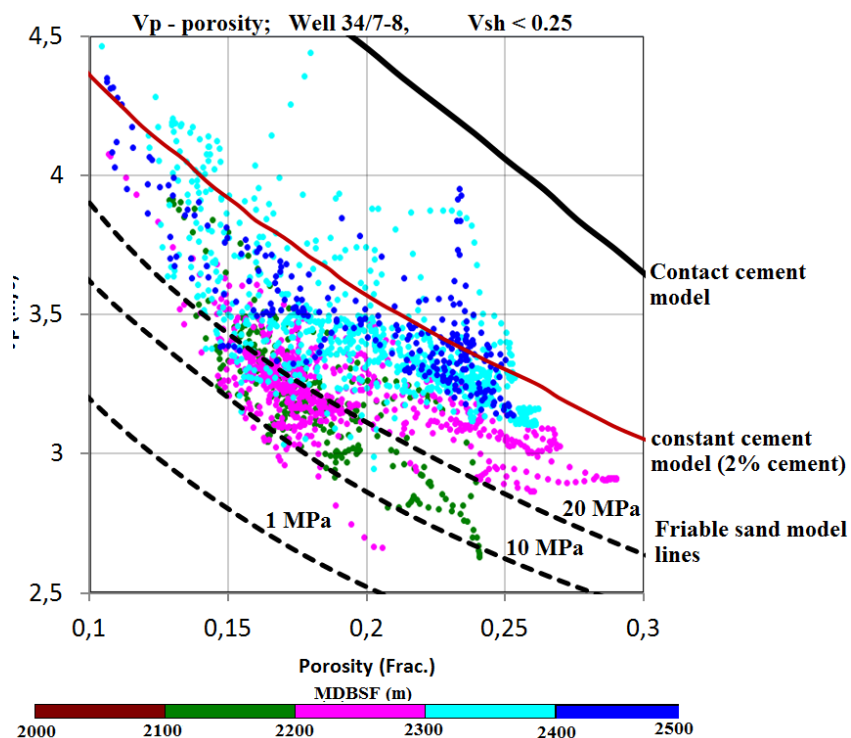
Cement model for Lunde Formation



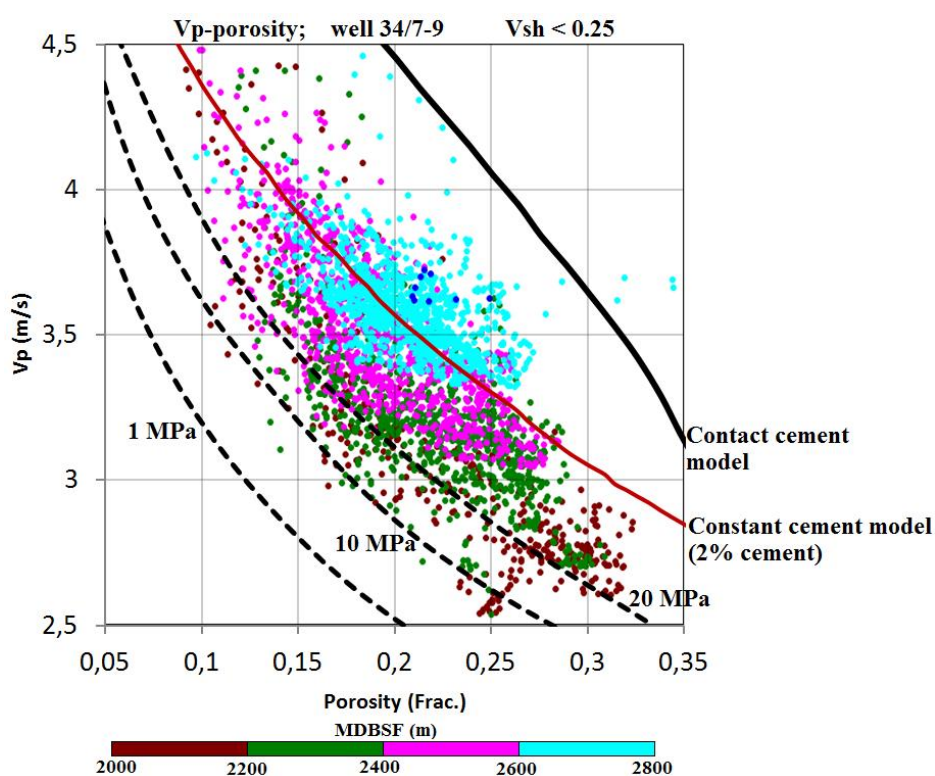
D.1: Vp-porosity crossplot for Lunde Fm with rock physics cement model from well 34/4-4.



D.2: Vp-porosity crossplot for Lunde Fm with rock physics cement model from well 34/4-6.

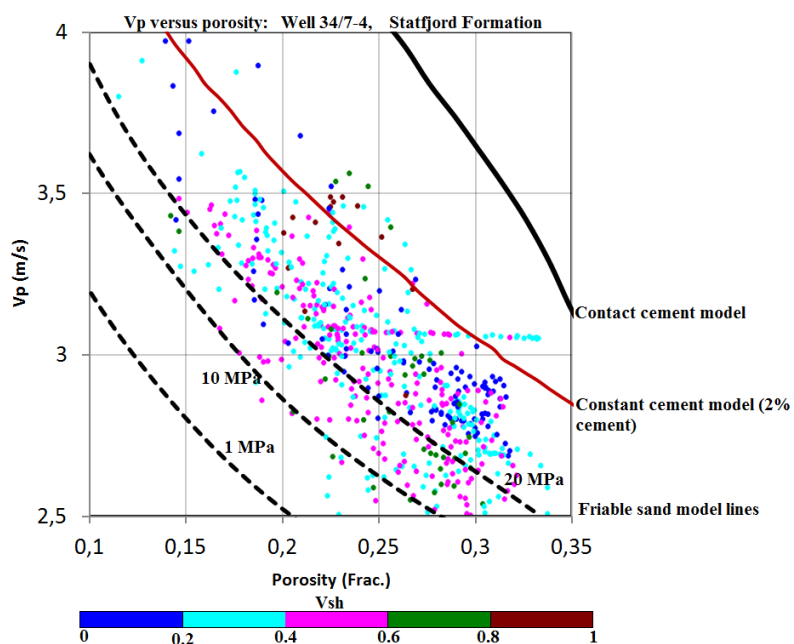


D.3: Vp – porosity from well 34/7-8 for Lunde Fm, with rock physics cement model.

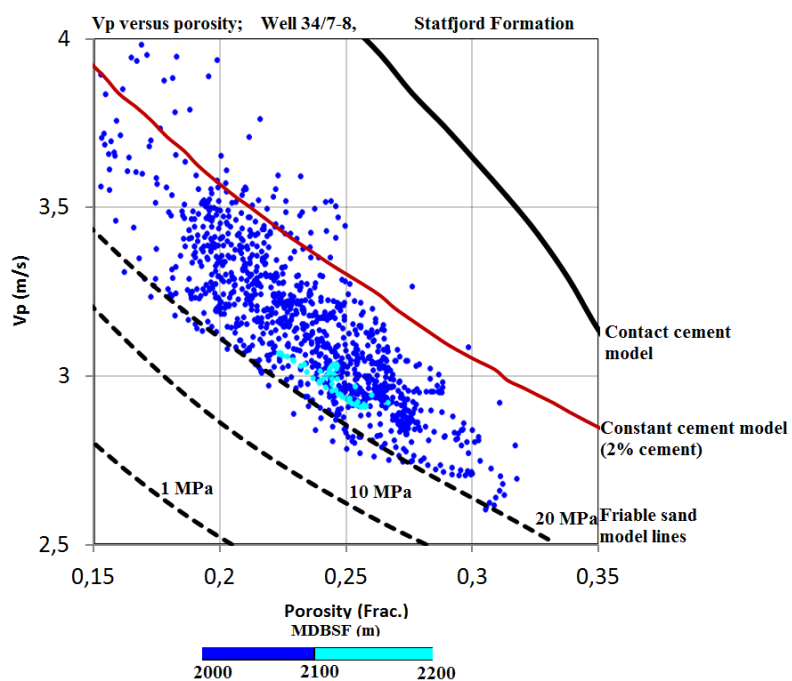


D.4: Vp-porosity for Lunde Fm from well 34/7-9, with rock physics cement model.

Cement model for Statfjord Fm



D.5: Vp-porosity crossplot of Statfjord Fm from well 34/7-4, overlaid by rock physics cement model.



D.6: Vp-porosity crossplot of Statfjord Fm from well 34/7-8, overlaid by rock physics cement model.